National Library of Canada
Bibliothèque nationale du Canada

Canadian Theses Service
Service des thèses canadiennes

Ottawa, Canada
K1A 0N4

NOTICE

The quality of this microform is heavily dependent upon the quality of the original thesis submitted for microfilming. Every effort has been made to ensure the highest quality of reproduction possible.

If pages are missing, contact the university which granted the degree.

Some pages may have indistinct print especially if the original pages were typed with a poor typewriter ribbon or if the university sent us an inferior photocopy.

Reproduction in full or in part of this microform is governed by the Canadian Copyright Act, R.S.C. 1970, c. C-30, and subsequent amendments.

AVIS

La qualité de cette microforme dépend grandement de la qualité de la thèse soumise au microfilmage. Nous avons tout fait pour assurer une qualité supérieure de reproduction.

S'il manque des pages, veuillez communiquer avec l'université qui a conféré le grade.

La qualité d'impression de certaines pages peut laisser à désirer, surtout si les pages originales ont été dactylographiées à l'aide d'un ruban usé ou si l'université nous a fait parvenir une photocopie de qualité inférieure.

La reproduction, même partielle, de cette microforme est soumise à la Loi canadienne sur le droit d'auteur, SRC 1970, c. C-30, et ses amendements subséquents.

NL-339 (r. 88/04) c

Canada

National Library of Canada
Bibliothèque nationale du Canada

Canadian Theses Service
Service des thèses canadiennes

Ottawa, Canada
K1A 0N4

The author has granted an irrevocable non-exclusive licence allowing the National Library of Canada to reproduce, loan, distribute or sell copies of his/her thesis by any means and in any form or format, making this thesis available to interested persons.

The author retains ownership of the copyright in his/her thesis. Neither the thesis nor substantial extracts from it may be printed or otherwise reproduced without his/her permission.

L'auteur a accordé une licence irrévocable et non exclusive permettant à la Bibliothèque nationale du Canada de reproduire, prêter, distribuer ou vendre des copies de sa thèse de quelque manière et sous quelque forme que ce soit pour mettre des exemplaires de cette thèse à la disposition des personnes intéressées.

L'auteur conserve la propriété du droit d'auteur qui protège sa thèse. Ni la thèse ni des extraits substantiels de celle-ci ne doivent être imprimés ou autrement reproduits sans son autorisation.

ISBN 0-315-55440-1

Canada

THE UNIVERSITY OF ALBERTA

ANALYTE SPECIES BEHAVIOUR IN INDUCTIVELY COUPLED PLASMA MASS SPECTROMETRY

by

MARGARET-ANNE VAUGHAN

©

A Thesis

Submitted To The Faculty Of Graduate Studies And Research

In Partial Fulfilment Of The Requirements For The Degree

Of Doctor Of Philosophy

The Department of Chemistry

Edmonton, Alberta

Fall, 1989

Samantha Tan,
Balazs Lab,
2284 Old Middlefield Way,
Mt. View CA. 94043

Dear Sir or Madame,

I give my permission for the material from the journal article:

"Effect of Operating Parameters on Analyte Signals in Inductively Coupled Plasma Mass Spectrometry", Margaret-Anne Vaughan, Gary Horlick and Samantha H. Tan, J. Anal. Atom. Spectroc. **2**, 765-772, (1987).

co-authored by me to appear in the PhD thesis of Margaret-Anne Vaughan.

Sincerely,

Samantha Tan

Samantha H. Tan

THE UNIVERSITY OF ALBERTA

RELEASE FORM

NAME OF AUTHOR: Margaret-Anne Vaughan

TITLE OF THESIS: Analyte Species Behaviour in Inductively Coupled Plasma Mass Spectrometry

DEGREE FOR WHICH THESIS WAS PRESENTED: Ph.D.

YEAR THIS DEGREE GRANTED: 1989

Permission is hereby granted to THE UNIVERSITY OF ALBERTA LIBRARY to reproduce single copies of this thesis and to lend or sell such copies for private, scholarly or scientific research purposes only.

The author reserves other publication rights, and neither the thesis nor extensive extracts from it may be printed or otherwise reproduced without the author's written permission.

Margaret-Anne Vaughan
(signed)

University of Toronto,
Dept. of Clinical Biochemistry
Toronto, Ontario. Canada.
M5G 1L5

Date: June 14, 1989.

THE UNIVERSITY OF ALBERTA

FACULTY OF GRADUATE STUDIES AND RESEARCH

The undersigned certify that they have read, and recommend to the Faculty of Graduate Studies and Research for acceptance, a thesis entitled ANALYTE SPECIES BEHAVIOUR IN INDUCTIVELY COUPLED PLASMA MASS SPECTROMETRY submitted by MARGARET-ANNE VAUGHAN in partial fulfilment of the requirements for the degree of Doctor of Philosophy.

Dr. G. Horlick (supervisor)

Dr. B. Kratochvil

Dr. N. Dovichi

Dr. M. Cowie

Dr. H. Baadgsaard

Dr. J. W. McLaren (external examiner)

Date: June 14, 1989

This thesis is dedicated to the memory

of Maura Margaret Lownds.

Abstract

The technique of inductively coupled plasma mass spectrometry (ICP-MS) has been evaluated with a special emphasis on analyte speciation, namely the formation of oxides, hydroxides and doubly charged ions. The general analyte behaviour in response to changes in instrumental parameters of both the ICP and the MS was determined. Analyte signals are most effected by ICP power and nebulizer flowrate, ion lens settings and by the sampling distance from the load coil. The power, nebulizer flowrate and sampling depth have an interactive effect with one another although a single set of optimized conditions may be achieved for a large mass range. The ion lenses in the vacuum system have an apparent mass discrimination due to the energy differences for ions of different mass caused by the expansion process. This results in the need for different lens settings for various mass ranges if optimum signal intensity is to be attained.

The oxide, hydroxide and doubly charged species respond to changes in instrumental parameters in a similar fashion to the M^+ ion although often optimum conditions differ for each species type. The presence of these species is undesirable because interferences from these species occur in the form of direct spectral overlaps with M^+ species. These overlaps are tabulated for easy reference. Although oxide and hydroxide formation may be minimized by careful adjustment of instrument parameters corrections to the data for their presence is sometimes required and may be accomplished by conventional Gauss elimination methods or by employing factor analysis.

Changes in parameter behaviour and analyte speciation as a function of sample and skimmer orifice size were studied. The resulting information

supports the idea that the majority of oxide species are formed in the boundary layer around the edges of the sampler. There is evidence from the orifice experiments and ion lens studies that the signal from the mass spectrometer is influenced by the instrument settings and interface design. While this poses no problem when the ICP-MS is used for analysis, any fundamental statements about the plasma itself based on ICP-MS data must be made with caution.

Acknowledgements

I would like to thank my supervisor Professor Gary Horlick for his assistance and for his enthusiasm in this project. I would also like to thank Sam Tan and Youbin Shao for the friendship and relaxed atmosphere they provided as we learned the nuances of the ICP-MS. Thank-you goes to Mike Stewart for his help with the abstract factor analysis and to Greg King for his help with the computers from time to time. The staff of the electronics, machine and glass shops deserve honourable mention for all the help and advice they have provided.

I would like to thank Keith Lepla not only for the help with the combined ICP-MS - emission work but for the companionship he provided as we worked through graduate school together.

Mary Albert and her smoking fingers are to be thanked for typing in Chapters 2, 3 and 5 of this thesis. I also want to thank her for taking over the role of my sister Maureen in helping me escape from anything remotely resembling chemistry from time to time.

I would like to thank Steven Pitts for sticking in there with me throughout all of this as I have no doubt taxed his patience from time to time. His love and support have been invaluable.

Finally I would like to thank NSERC and the Department of Chemistry for their financial support.

TABLE OF CONTENTS

CHAPTER		PAGE
1.	Introduction	1
	1. ICP as an Ion Source	3
	2. ICP-MS Interface	6
	3. Ion Optics	22
	4. Quadrupole Mass Spectrometer and Ion Detector	22
	5. Background and Thesis Objective	23
	References	33
2.	Effect of Operating Parameters on Analyte Signals in Inductively Coupled Plasma Mass Spectrometry	39
	Experimental	41
	Results and Discussion	42
	1. Nebulizer Flowrate - Power Parameter Graphs	42
	2. Effect of Sampling Depth	47
	3. Effects of Input Ion-Optic Voltages	49
	Conclusions	60
	References	62
3.	Oxide, Hydroxide and Doubly Charged Analyte Species in Inductively Coupled Plasma Mass Spectrometry	63
	Experimental	66
	Results and Discussion	67
	1. Ba and Sr Species Distribution in ICP-MS	67
	2. Species Distribution of Ti, W and Ce	80

3. Tables of Oxide, Hydroxide and Doubly Charged Ion Interferences in ICP-MS 84

References 100

4. Corrections for the Spectroscopic Overlap of Oxides and Hydroxides on Rare Earth Elements in ICP-MS 101

Experimental 104

Results and Discussion 104

1. Gauss Elimination 108

2. Applying Principal Components Analysis 115

3. Comparison of Gauss Elimination and PCA 125

Conclusions 131

References 132

5. Analysis of Steels using Inductively Coupled Plasma Mass Spectrometry 134

Experimental 134

Results and Discussion 137

1. Qualitative Spectral Scans 137

2. Evaluation of Potential Spectral Interferences 141

3. Instrument Stability and Internal Standardation 146

4. Matrix Effects 147

5. Analytical Results 155

Conclusions 165

References 166

6. ICP-MS Ion Lens Simulations 168

Theory 169

Experimental 173

Results and Discussion 174

1. Basic Lens Behaviour 174

2. Effects of Individual Lens Elements 185

3. Higher Energy Ions 196

4. Signal Intensity as a Function of Lens Potential 198

5. Effect of Photon Stop Voltage on Parameter Plots 211

Conclusions 213

References 215

7. Effect of Sampler and Skimmer Orifice Size on Parameter Behaviour and Oxide Formation 216

Experimental 218

Results and Discussion 219

1. Effect of Sampler Orifice Diameter on Intensity Versus Flowrate Plots 219

2. Orifice Size Effects on Oxide Formation 226

3. The (M^++MO^+) Phenomenon 234

4. Temperature Estimates from Oxide Formation 239

5. Skimmer Orifice Size Effects 243

6. General Discussion 252

Conclusions 256

References 258

8. The Use of Inductively Coupled Plasma Mass Spectrometry Results for Plasma Diagnostics 260

Experimental 261

Results and Discussion 262

1. Simultaneous Emission and Mass Spectral Measurements 262

2. CsI Measurements 267

Conclusions 277

References 278

9. Conclusions and Future Directions 279

References 284

LIST OF TABLES

TABLE		PAGE
1.1	Degree of ionization	7
2.1	Lens voltage setting	42
3.1	Oxide, hydroxide and doubly charged ion interferences in order of increasing mass.	87
3.2	Table of elements most likely to form oxides, hydroxides and doubly charged species, plus elements potentially affected by these interferences	92
4.1	Spectral overlap of rare earth element oxides LaO to DyO on rare earth elements Gd to Lu.	102
4.2	Rare earth isotope list	105
4.3	Rare earth element interferences on isotopes required for gauss elimination	110
4.4	Equations from gauss elimination	113
4.5	Results from gauss elimination	116
4.6	Concentrations for the seven rare earth elements as determined by PCA	120
4.7	Results from principal components analysis	127
4.8	Alternate PCA mass set	129
4.9	PCA results in a 550mg/mL Sm matrix	130
5.1	Ion lens voltage settings	136
5.2	Basic spectral interferences for elements of major interest in ferrous alloys	142
5.3	Spectral interferences due to FeO and FeOH	145

5.4 RSD's for short (11 min) and medium term (30 min) measurement times with and without internal standardization. 149

5.5 A comparison of signal intensities at nebulizer flowrates yielding maximum signal or reduced matrix effects. 153

5.6 Concentration ranges and slopes for aqueous calibration curves 159

5.7 Analysis of 0.01% solutions of the standard reference steels. Results reported as % in steel; precision expressed as the standard deviation (n = 4). Aqueous calibration solutions used with Rh used as an internal standard. 161

5.8 Analysis of 0.1% solutions of the NBS standard reference steels 361 and 363 by the method of standard additions. Results reported as % in steel. Rh used as an internal standard. 162

5.9 Analysis of standard reference steels. results reported as % in steel. Aqueous calibration solutions used with Rh used as an internal standard. 164

6.1 Major Behaviour Trends 192

7.1 Calculated temperature based on oxide ratios (MO^+/M^+) for different sampler orifice sizes. 242

8.1 I^+/Cs^+ Ratios and Temperature Estimates for a 1.3kW Plasma with Different Sampler Orifice Sizes 274

LIST OF FIGURES

FIGURE		PAGE
1.1	Schematic of a P.E. Sciex Elan 250 ICP-MS.	2
1.2	Typical ICP torch.	4
1.3	ICP-MS sampling interface showing sampler and skimmer	11
1.4	Flow field for the expansion of gas through the sampler	13
1.5	Relative positioning of the skimmer with respect to the Mach disc. (a) disc in front of skimmer, (b) disc attached to skimmer, (c) disc behind skimmer.	15
2.1	Nebulizer flowrate - power parameter behaviour graphs for Ti^+, Zr^+, Hf^+, Cr^+, Mo^+, W^+, Ni^+, Pd^+ and Pt^+; power in kW shown on each line.	43
2.2	Nebulizer flowrate - power parameter behaviour graphs for Ga^+, In^+, Tl^+, Ge^+, Sn^+, Pb^+, As^+, Sb^+ and Bi^+; power in kW shown on each line.	45
2.3	Nebulizer flowrate - power parameter behaviour graph for Li^+, B^+, Na^+ and Al^+; power in kW shown on each line	46
2.4	Nebulizer flowrate - power parameter behaviours graphs for Ni^+, Pd^+ and Pt^+ at sampling depths of 10, 15, 20 and 25 mm; power in kW shown on each line	48
2.5	Nebulizer flowrate - power parameter behaviour graphs for Sr^+ and Ba^+ at sampling depths of 10, 15, 20 and 25 mm; power in kW shown on each line	50
2.6	Schematic diagram of the input ion optics of the SCIEX ELAN	51
2.7	Dependence of ion count on einzel-lens voltage for Ti^+, Ni^+, As^+, Zr^+, Pd^+, Sb^+, Hf^+, Pt^+ and Bi^+	53
2.8	Dependence of ion count on bessel box plate voltage for Ti^+, Ni^+, As^+, Zr^+, Pd^+, Sb^+, Hf^+, Pt^+ and Bi^+	54
2.9	Dependence of ion count on bessel box barrel voltage for Ti^+, Ni^+, As^+, Zr^+, Pd^+, Sb^+, Hf^+, Pt^+ and Bi^+	56

2.10 Dependence of ion count on the photon stop voltage for Ti^+, Ni^+, As^+, Zr^+, Pd^+, Sb^+, Hf^+, Pt^+ and Bi^+ 57

2.11 Nebulizer flowrate - power parameter behaviour graphs for Ti^+, Pd^+ and Bi^+ at photon stop voltages -9V, -11V and -13V. Power in kW shown on each line 59

3.1 Dependence of ion count on nebulizer flowrate at various powers for Ba^{2+}, Ba^+, BaO^+, and $BaOH^+$ 68

3.2 Relative (a) and normalized (b) plots of ion count vs. nebulizer flowrate at 1.3 kW for Ba^{2+}, Ba^+, BaO^+, and $BaOH^+$ 70

3.3 Dependence of barium species ion count on nebulizer flowrate at various sampling depths 72

3.4 Dependence of barium species ratios as a function of nebulizer flowrate at 1.3kW 73

3.5 Dependence of barium species ratios as a function of power at 1.2L/min 75

3.6 Spectra of Ba and Sr species distribution at different nebulizer flowrates 77

3.7 Spectra of Ba^+ and $BaO^+/BaOH^+$ species at different nebulizer flowrates 78

3.8 Spectra of BaO^+ and $BaOH^+$ species at different nebulizer flowrates 79

3.9 Ti^+ and TiO^+ spectra at different nebulizer flowrates 81

3.10 W^+ and WO^+ spectra at different nebulizer flowrates 82

3.11 Ce^+ and CeO^+ spectra at different nebulizer flowrates 83

3.12 Effect of "B" lens setting on Ce^{2+}, Ce^+, and CeO^+ signals 85

4.1 Mass spectra for Ce, Gd, Sm and Dy. Some masses are omitted along the mass axis 106

4.2 Mass spectra for Ho, Yb and Er. Some masses are omitted along the mass axis 107

4.3 Mass spectrum for a mixture of rare earths,Yb, Er, Ho, Gd, Sm and Ce (a). Synthesized mass spectrum for the same mixture built up from the mass spectra of each of its components (b) 109

4.4 Data matrix for factor analysis 118

4.5 Typical eigenratio plot (a) and IND plot (b) obtained from abstract factor analysis 122

4.6 Typical SPOIL plot for target transformation analysis. Plot (a) corresponds to seven applicable target vectors. Plot (b) includes two inappropriate target vectors, 8 and 9 124

5.1. Spectrum of 0.01% stainless steel solution (Standard Reference Material NBS 160b) 138

5.2. Spectra of 0.1% stainless steel solution (Standard Reference Material NBS 160b) 139

5.3. Spectrum of 1% steel solution showing rare earths and the associated oxides (Standard Reference Material NBS 361) 140

5.4. Spectrum of FeO and FeOH for a 0.2% Fe solution 144

5.5. Signal intensity changes as a function of time for Cu, Mo and W in a 0.01% steel solution with and without the use of the Rh internal standard 148

5.6. Ion count as a function of nebulizer flowrate for Zr, Ce and Ta in 5% HNO_3 and in a matrix of 1000 μg/mL Fe 150

5.7. Effect of increasing Fe concentration on the Zr signal at the nebulizer flowrate yielding maximum signal intensity and at a reduced nebulizer flow rate 152

5.8. Effect of increasing Fe concentration on Rh, Nd and Ce signals plotted as percent matrix effect 154

5.9. Effect of increasing Fe concentration on the Ce signal with and without the use of Rh as an internal standard 156

5.10. Effect of increasing Fe concentration on the Ta signal with and without the use of Rh as an internal standard. 157

5.11. Aqueous calibration curve for Mo. Two calibrations acquired 0.5h apart. Rh used as an internal standard 158

5.12. Standard Addition Calibration for W. Rh used as an internal standard 163

6.1 Equipotential lines for the einzel lens (a) and ion trajectories through the einzel lens (b). Ion energy, 7.5eV. Entry angles, 9° and -9°. E1 = -30V, central einzel element, -130V 171

6.2 Schematic of a P.E. Sciex Elan 250 ICP-MS 175

6.3 Schematic of the ion lenses as drawn in MacSimion 176

6.4 Equipotential lines generated for the ion lenses with E1 = -30V, P = -18V, B = 4V and S2 = -9V 177

6.5 Typical ion trajectory. Ion energy is 3.3eV, entry angle is 9°. Lens settings: E1 = -30V, P = -18V, B = 4V and S2 = -9V 179

6.6 Trajectories for ions of varying kinetic energies. (A) small energy range: (a) 3.3eV, (b) 4.3eV, (c) 5.3eV, (d) 6.3eV and (e) 7.3eV. (B) larger energy range. Lens settings: E1 = -30V, P = -18V, B = 4V and S2 = -9V. Entry angle is 9° 180

6.7 Ion trajectories for Ba^{+} and Ba^{2+} (5.62eV). Lens settings: E1 = -30V, P = -18V, B = 4V and S2 = -9V. Entry angle is 9° 182

6.8 Ion trajectories for a 4.8eV ion with entry angles of 6°, 9°, 12° and 15° 183

6.9 Trajectories for 1, 5 and 9eV ions at varied E1 voltages. Lens settings: P = -18V, B = 4V and S2 = -9V. Entry angle is 9° 186

6.10 Trajectories for 1, 5 and 9eV ions at varied S2 voltages. Lens settings: E1 = -30V, P = -18V and B = 4V. Entry angle is 9° 188

6.11 Trajectories for 1, 5 and 9eV ions at varied B voltages. Lens settings: E1 = -30V, P = -18V and S2 = -9V. Entry angle is 9° 189

6.12 Trajectories for 1, 5 and 9eV ions at varied P voltages. Lens settings: E1 = -30V, B = 4V and S2 = -9V. Entry angle is 9° 190

6.13 Trajectories for 1, 5 and 9eV ions. Lens settings: E1 = -30V, B = 4V, S2 = -9V and P = -21V (a). Lens settings:E1 = -30V, B = 4V, S2 = -15V and P = -21V (b). Lens settings:E1 = -30V, B = 6V, S2 = -9V and P = -21V (c). Entry angle is 9° 195

6.14 Trajectories for 1, 5 and 9eV ions. Lens settings: E1 = -35V, B = 4V, S2 = -9V and P = -18V (a). Lens settings: E1 = -35V, B = 2V, S2 = -9V and P = -18V (b). Lens settings: E1 = -35V, B = 2V, S2 = -12V and P = -18V (c). Entry angle is 9° 197

6.15 Trajectories for 14, 15, 16 and 17eV ions at varied E1 voltages. Lens settings: P = -18V, B = 4V and S2 = -9V. Entry angle is 9° 199

6.16 Trajectories for 14, 15, 16 and 17eV ions at varied S2 voltages. Lens settings: E1 = -16V, P = -18V and B = 4V. Entry angle is 9° 200

6.17 Trajectories for 14, 15, 16 and 17eV ions at varied B voltages. Lens settings: E1 = -16V, P = -18V and S2 = -9V. Entry angle is 9° 201

6.18 Trajectories for 14, 15, 16 and 17eV ions at varied P voltages. Lens settings: E1 = -16V, B = 4V and S2 = -9V. Entry angle is 9° 202

6.19 Estimated ion throughput (arbitrary units) as a function of photon stop voltage. Lens settings: E1 = -30V, P = -18V and B = 4V (a). Lens settings: E1 = -25V, P = -18V and B = 4V (b). Entry angle is 9° 204

6.20 Estimated ion throughput (arbitrary units) as a function of photon stop voltage (a), plate voltage (b) and barrel voltage (c). E1 = -30V 206

6.21 Estimated ion throughput (arbitrary units) as a function of photon stop voltage (a), plate voltage (b) and barrel voltage (c). E1 = -16V 207

6.22 Estimated ion throughput (arbitrary units, normalized for each element) as a function of barrel voltage (a). Experimental results of intensity as a function of barrel voltage,normalized for each element (b) 208

6.23 Estimated ion throughput (arbitrary units, normalized for each element) as a function of plate voltage (a). Experimental results of intensity as a function of plate voltage, normalized for each element (b) 209

6.24 Estimated ion throughput (arbitrary units, normalized for each element) as a function of photon stop voltage (a). Experimental results of intensity as a function of photon stop voltage, normalized for each element (b) 210

6.25 Nebulizer flowrate power parameter plots for Ni^+ at two photon stop voltages, -9V and -13V. Power in kW shown on each line 212

7.1 Nebulizer flowrate parameter plots for Zn^+, Ge^+, As^+, Sr^+, Y^+, Zr^+, Ru^+, Te^+ and Ba^+. Sampler orifice diameter, 0.51mm 220

7.2 Nebulizer flowrate parameter plots for Zn^+, Ge^+, As^+, Sr^+, Y^+, Zr^+, Ru^+, Te^+ and Ba^+.. Sampler orifice diameter, 0.64mm 221

7.3 Nebulizer flowrate parameter plots for Zn^+, Ge^+, As^+, Sr^+, Y^+, Zr^+, Ru^+, Te^+ and Ba^+. Sampler orifice diameter, 0.76mm 223

7.4 Nebulizer flowrate parameter plots for Zn^+, Ge^+, As^+, Sr^+, Y^+, Zr^+, Ru^+, Te^+ and Ba^+. Sampler orifice diameter, 0.89mm 224

7.5 Nebulizer flowrate parameter plots for Zn^+, Ge^+, As^+, Sr^+, Y^+, Zr^+, Ru^+, Te^+ and Ba^+. Sampler orifice diameter, 0.94mm 225

7.6 Nebulizer flowrate parameter plots for La^+ and LaO^+ . Sampler orifice diameters: 0.51, 0.64, 0.76, 0.89 and 0.94mm 227

7.7 Nebulizer flowrate parameter plots for Ho^+ and HoO^+ . Sampler orifice diameters: 0.51, 0.64, 0.76, 0.89 and 0.94mm 229

7.8 Nebulizer flowrate parameter plots for Lu^+ and LuO^+ . Sampler orifice diameters: 0.51, 0.64, 0.76, 0.89 and 0.94mm 230

7.9 Nebulizer flowrate parameter plots for Yb^+ and YbO^+ . Sampler orifice diameters: 0.51, 0.64, 0.76, 0.89 and 0.94mm 231

7.10 Nebulizer flowrate parameter plots for Bi^+. Sampler orifice diameters: 0.51, 0.64, 0.76, 0.89 and 0.94mm 233

7.11 Nebulizer flowrate parameter plots for the sum of (Lu^++LuO^+) signals. Sampler orifice diameters: 0.51, 0.64, 0.76, 0.89 and 0.94mm 235

7.12 Nebulizer flowrate parameter plots for the sum of (Ho^++HoO^+) signals. Sampler orifice diameters: 0.51, 0.64, 0.76, 0.89 and 0.94mm 236

7.13 Nebulizer flowrate parameter plots for the sum of (La^++LaO^+) signals. Sampler orifice diameters: 0.51, 0.64, 0.76, 0.89 and 0.94mm 237

7.14 Nebulizer flowrate parameter plots for Cs^+. Sampler orifice diameters: 0.51, 0.64, 0.76, 0.89 and 0.94mm 238

7.15 Normalized nebulizer flowrate parameter plots comparing Rh^+ and (Y^+ + YO^+), Cs^+ and (Ce^+ + CeO^+), Cs^+ and (Pr^+ + PrO^+), Bi^+ and (Ho^+ + HoO^+), Bi^+ and (Tm^+ + TmO^+) and Bi^+ and (Th^+ + ThO^+). Sampler orifice diameter, 0.89mm 240

7.16 MO^+/M^+ versus dissociation energy for sampler orifice diameters 0.51, 0.64, 0.76, 0.89 and 0.94mm. Nebulizer flowrate, 1.15L/min 241

7.17 Nebulizer flowrate parameter plots for La^+ and LaO^+ . Sampler orifice diameters: 0.51, 0.64, 0.76, 0.89 and 0.94mm. Skimmer orifice diameters 0.76 and 1.0mm 244

7.18 Nebulizer flowrate parameter plots for (La^+ + LaO^+) . Sampler orifice diameters: 0.51, 0.64, 0.76, 0.89 and 0.94mm. Skimmer orifice diameters 0.76 and 1.0mm 246

7.19 Nebulizer flowrate parameter plots for Cs^+. Sampler orifice diameters: 0.51, 0.64, 0.76, 0.89 and 0.94mm. Skimmer orifice diameters 0.76 and 1.0mm 247

7.20 Nebulizer flowrate parameter plots for (Yb^+ + YbO^+). Sampler orifice diameters: 0.51, 0.64, 0.76, 0.89 and 0.94mm. Skimmer orifice diameters 0.76 and 1.0mm 248

7.21 Nebulizer flowrate parameter plots for Bi^+. Sampler orifice diameters: 0.51, 0.64, 0.76, 0.89 and 0.94mm. Skimmer orifice diameters 0.76 and 1.0mm 249

7.22 Nebulizer flowrate parameter plots for (Lu^+ + LuO^+). Sampler orifice diameters: 0.51, 0.64, 0.76, 0.89 and 0.94mm. Skimmer orifice diameters 0.76 and 1.0mm 250

7.23 Nebulizer flowrate parameter plots for (Ho^+ + HoO^+). Sampler orifice diameters: 0.51, 0.64, 0.76, 0.89 and 0.94mm. Skimmer orifice diameters 0.76 and 1.0mm 251

7.24 Flow field around the sampling cone. (Modified from reference [11]) 253

8.1 Nebulizer flowrate power parameter plot for Sr^+. Power in kW shown on each line 263

8.2 Nebulizer flowrate power parameter plot for SrII emission. Power in kW shown on each line. Intensity in arbitrary units..... 264

8.3 Nebulizer flowrate power parameter plot for Sr^+ (a) and SrII (b). Power in kW shown on each line. Measurements made simultaneously from same ICP..... 265

8.4 Ion count versus distance from the load coil plots for Cs^+ (a) and I^+ (b) plus overlay plots of I^+/Cs^+ versus distance from the load coil. Ion count versus distance from the load coil plots for Cs^+ and I^+ (c)..... 268

8.5 Nebulizer flowrate parameter plots for Cs^+ (a) and I^+ (b) plus I^+/Cs^+ versus nebulizer flowrate overlay plots. Nebulizer flowrate parameter plots for Cs^+ and I^+ (c)..... 270

8.6 Nebulizer flowrate parameter plots for Cs^+ (a and I^+ (b) with photon stop voltages of -9V and -5V. I^+/Cs^+ versus nebulizer flowrate plot (c)..... 271

8.7 I^+/Cs^+ ratio versus nebulizer flowrate for five sampler orifice diameters..... 273

8.8 Nebulizer flowrate parameter plots for Cs^+ (a) and I^+ (b) plus I^+/Cs^+ versus nebulizer flowrate overlay plots. Sampler orifice diameter, 0.51mm..... 275

8.9 Nebulizer flowrate parameter plots for Cs^+ (a) and I^+ (b) plus I^+/Cs^+ versus nebulizer flowrate overlay plots. Sampler orifice diameter, 0.76mm..... 276

Chapter 1

Introduction.

The inductively coupled plasma - mass spectrometer (ICP-MS) has captured the interest of many since it has become commercially available. The high sensitivity of the system is perhaps its most attractive characteristic although the capability for rapid qualitative analysis and isotope ratio information is also appealing. Being a combination of two techniques, the ICP-MS is a complex piece of instrumentation and much work has been done on how to take full advantage of its capabilities. Although the instruments vary somewhat with the manufacturer, they all contain the same basic components. These include an inductively coupled plasma (ICP), an atmospheric pressure sampling interface between the the ICP and the vacuum system of the mass spectrometer, a lens system used to direct ions to the quadrupole, a quadrupole mass analyser, and a detector.

A schematic of the P.E. Sciex Elan 250 ICP-MS is presented in Figure 1.1. The ICP supply has been modified to support a center tapped ground on the load coil. It has also been repositioned from a vertical orientation to a horizontal one. Although Sciex provides an ICP torch with an extended outer tube, a standard emission torch can be employed and was routinely used throughout this work. The atmospheric pressure sampling interface consists of the sampler and skimmer cones and the region between them. The ion optics are located behind the interface in the high vacuum region and consist of an einzel lens and a bessel box. These lenses function to direct the ions into

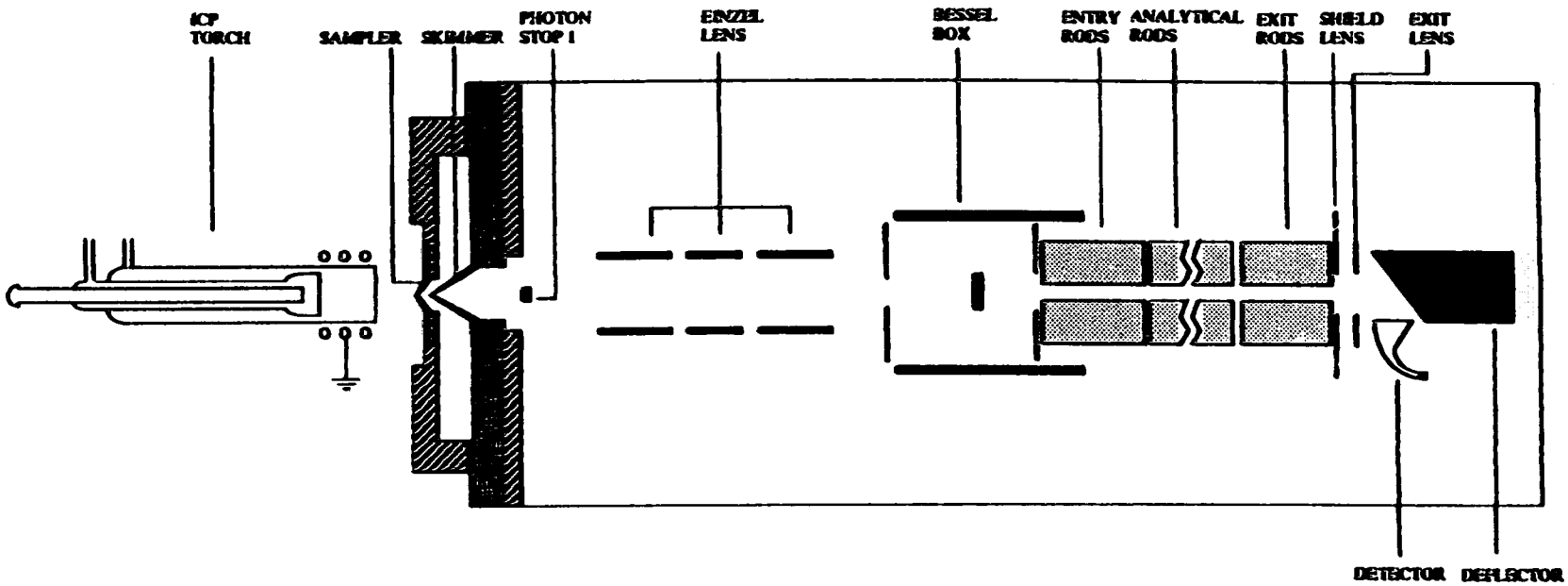

Figure 1.1 Schematic of a P.E. Sciex Elan 250 ICP-MS.

the quadrupole mass analyser where the ions are separated and those with the proper mass to charge ratio enter the ion detection system.

1. ICP as an Ion Source.

The inductively coupled plasma has been recognized as a source of elemental ions from its use as an atomic ion emission source [1-4]. The ICP used in emission and mass spectrometric measurements is formed and sustained at the open end of an assembly of quartz tubes [5]. The end of the tube assembly is positioned inside a load coil which is usually made of copper tubing and is water cooled. Radio frequency (R.F.) power is transferred from the load coil to the plasma. High frequency currents flowing in the induction coil generate oscillating magnetic fields whose lines of force are axially oriented inside the quartz tube and follow elliptical closed paths outside the coil. With Ar flowing through the torch, a tesla coil is used to seed electrons in the gas and the electrons and ions thus formed travel in closed annular paths inside the quartz tube. The induced magnetic fields are time varying and the electrons and ions are accelerated every half cycle. The accelerating electrons and ions meet resistance to their flow and Joule or ohmic heating results which in turn results in additional ionization and a stable plasma.

In a typical ICP torch there are three tubes through which Ar is introduced into the plasma. There is a central gas flow, an intermediate gas flow, and an outer gas flow. (See Figure 1.2.) The outer gas flow is the main Ar source in the plasma with a flowrate typically in the range of 11 - 12L/min. The intermediate gas flow functions to keep the plasma off the central injector tube, it serves to move the plasma up and down slightly and can vary

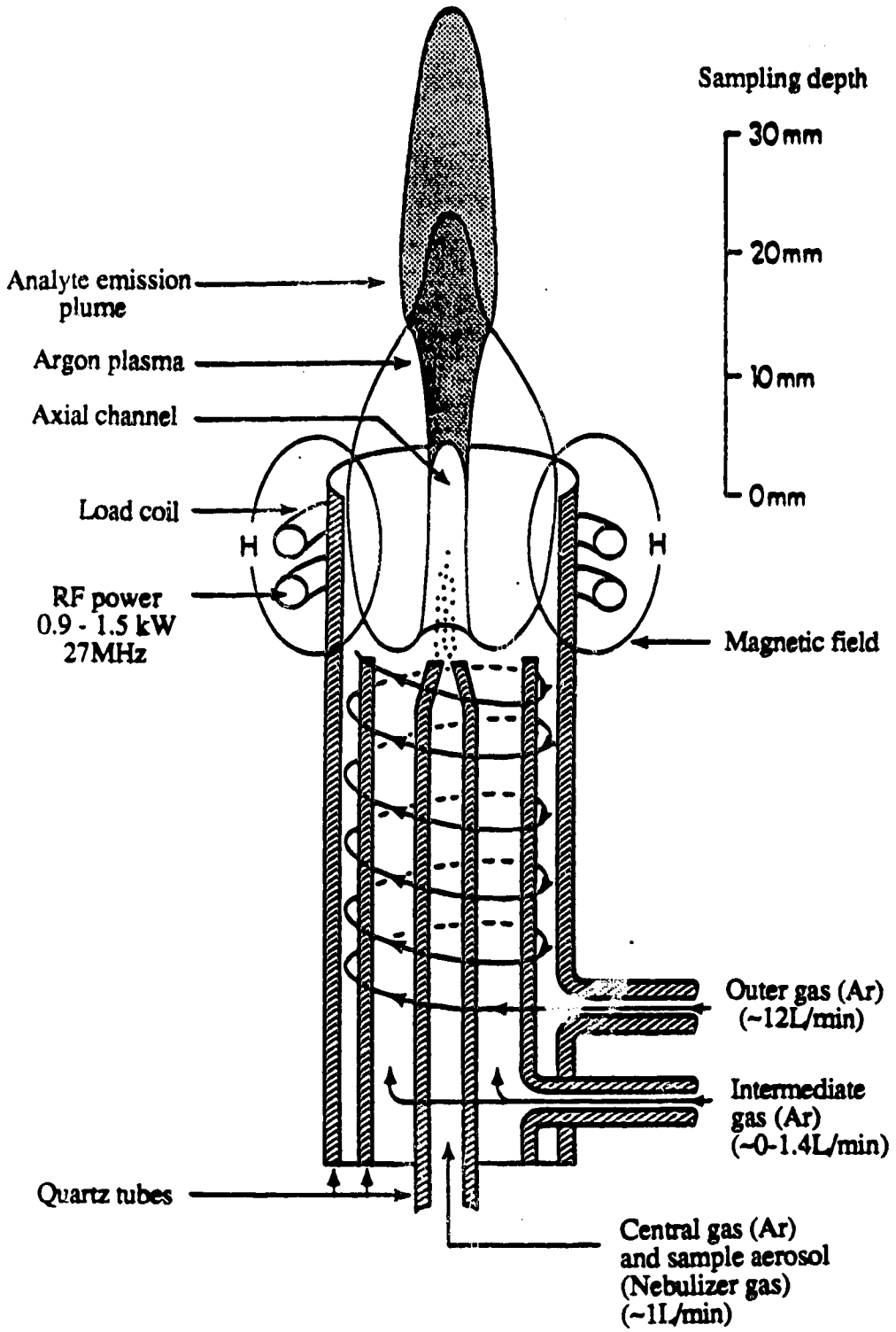

Figure 1.2 Typical ICP torch.

in a range from 0 to 1.4L/min or greater. The central aerosol or nebulizer gas flow is used to introduce the aqueous samples into the ICP. This gas flows through the nebulizer, through the central tube of the torch and forms the central aerosol channel in the plasma. The flowrates used are typically between 0.6 and 1.3L/min, although they vary with the nebulizer used.

Fine droplets of a nebulized aqueous sample are swept along by the central gas and the following processes occur [6]. The sample is desolvated, vapourized, atomized and then excited, ionized or both. The degree of ionization, α, varies from analyte to analyte and α may be calculated as follows [6,7].

$$\alpha = \frac{n_i}{n_a+n_i} = \frac{n_i n_a/n_a}{n_e+n_i n_a/n_a} = \frac{K_m}{n_e+K_m} \qquad 1.1$$

n_a= number density of atoms

n_i = number density of ions

n_e = electron number density

K_m= Saha equilibrium constant

The Saha equilibrium constant in the α relationship is obtained from the Saha equation [8-10] which represents the relationship between the ionization energy, E_i and the temperature, T_{ion}.

$$K_m = \frac{N_i}{N_a} n_e = \frac{(2\pi mkT_{ion})^{3/2}}{h^3} \frac{2Z_i}{Z_a} \exp\left(\frac{-E_i}{kT_{ion}}\right) \qquad 1.2$$

n_e = electron density

m = mass of electron

E_i = ionization energy

T_{ion} = ionization temperature

N_a = number density of atoms

N_i = number density of ions

Z_i = partition function of ion

Z_a = partition function of atom

k = Boltzmann's constant

h = Planck's constant

The degree of ionization for the elements based on T_{ion} (Ar) = 6680K and n_e= 1.475×10^{14} cm^{-3} is listed in Table 1.1. A large number, although not all elements, are strongly ionized in the ICP. Under the conditions described above 40 elements are over 90% ionized.

2. ICP-MS Interface.

The interface between the inductively coupled plasma and the mass spectrometer is of critical importance. It must be capable of sampling the plasma at atmospheric pressure and yet introduce the ions into the quadrupole mass spectrometer at a pressure of 10^{-5} torr. Small sampling orifices (70μm) were tried during the development of the technique but there was trouble with orifice clogging and boundary layer sampling resulted [1,12]. Consequently the interface chosen was a Campargue type [13,14] taken from

TABLE 1.1 Degree of ionization (Based on Furuta [11]).

Element	I.P. (eV)	Degree of Ionization (%)
Cs	3.894	99.98
Rb	4.177	99.98
K	4.341	99.97
Na	5.139	99.91
Ba	5.212	99.96
Ra	5.279	99.95
Li	5.392	99.85
La	5.577	99.91
Sr	5.695	99.92
In	5.786	99.42
Al	5.986	98.92
Ga	5.999	99.00
Tl	6.108	99.38
Ca	6.113	99.86
Y	6.38	98.99
Sc	6.54	99.71
V	6.74	99.23
Cr	6.766	98.89
Ti	6.82	99.49
Zr	6.84	99.31
Nb	6.88	98.94
Hf	7.0	98.89
Mo	7.099	98.54

Element	I.P. (eV)	Degree of Ionization (%)
Tc	7.28	97.50
Bi	7.289	94.14
Sn	7.344	96.72
Ru	7.37	96.99
Pb	7.416	97.93
Mn	7.435	97.10
Rh	7.46	95.87
Ag	7.576	94.45
Ni	7.635	92.55
Mg	7.646	98.25
Cu	7.726	91.59
Co	7.86	94.83
Fe	7.870	96.77
Re	7.88	94.54
Ta	7.89	96.04
Ge	7.899	91.64
W	7.98	94.86
Si	8.151	87.90
B	8.298	62.03
Pd	8.34	94.21
Sb	8.641	81.07
Os	8.7	79.96
Cd	8.993	85.43

Element	I.P. (eV)	Degree of Ionization (%)
Pt	9.0	61.83
Te	9.009	66.74
Au	9.225	48.87
Be	9.322	75.36
Zn	9.394	74.50
Se	9.752	30.53
As	9.81	48.87
S	10.360	11.47
Hg	10.437	32.31
I	10.451	24.65
P	10.486	28.79
Rn	10.748	35.74
Br	11.814	3.183
C	11.260	3.451
Xe	12.130	5.039
Cl	12.967	0.4558
O	13.618	0.04245
Kr	13.999	0.2263
N	14.534	0.04186
Ar	15.759	0.01341
F	17.422	0.0001919
Ne	21.564	0.0000005468
He	24.587	0.000000001007

work done on molecular beams [15]. This interface consists of two cones, a sampler and a skimmer, having orifices typically in the range of 0.9 - 1.4mm. The arrangement of these cones in the ICP-MS is shown in Figure 1.3. These cones may be made from a variety of metals such as nickel, copper or platinum. The region between the two cones is pumped mechanically to a pressure of approximately 1-5 torr. The region behind the skimmer, where the ion lenses, quadrupole and detector are located, is pumped to a running pressure of approximately 10^{-5} torr. During operation of the ICP-MS the sampler is positioned such that the plasma flows around the cone with a portion of the plasma flowing through the sampling orifice. The gas flow through the sampler is dependent on the orifice diameter, plasma pressure and temperature and may be calculated as follows [16,17]:

$$U_o = \frac{\pi f(\gamma) N_a D_o^2 P_o}{4(mRT_o)^{1/2}} \qquad 1.3$$

where $f(\gamma)$ is a constant for a given gas (for Ar $f(\gamma) = 0.73$) and may be calculated by:

$$f(\gamma) = \gamma^{1/2}\left[\frac{2}{\gamma+1}\right]^{\left(\frac{\gamma+1}{2(\gamma-1)}\right)} \qquad 1.4$$

and

m = molar mass

R = gas constant

P_O = initial pressure

T_O = initial temperature

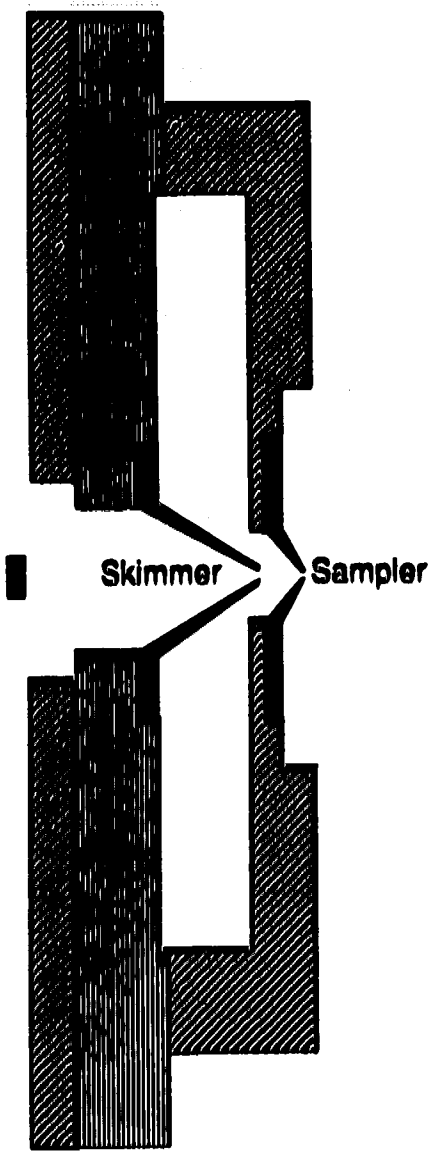

Figure 1.3 ICP-MS sampling interface showing sampler and skimmer.

N_a = Avagadro's Number

γ = ratio of specific heats c_p/c_v (5/3 for Ar)

D_o = orifice diameter

U_o = total flowrate

For the Sciex Elan ICP-MS with a 0.89mm diameter sampler orifice (D_o = 0.89mm), assuming a T_o = 4900K and P_o = 101.3kPa, the gas flow, U_o, through the sampler may be calculated to be $6.9 \times 10^{20}\ s^{-1}$.

Because of the difference in pressure between the plasma and the 5 torr region a supersonic expansion of the plasma gas results. The size of the sampling orifice is large (0.89mm) compared to the mean free path of the gas so the behaviour of the expansion through the sampler falls into the regime of continuum gas dynamics. The resulting flow field from the expansion of the gas through the sampler is shown in Figure 1.4. The plasma gas expands outward until the collisions with the residual gas in the chamber hinder further expansion and shockwaves are formed. In these shockwaves, the barrel shock and the Mach disc, the density increases and the flow stagnates and becomes subsonic. The shockwaves surround an undisturbed region of the expansion referred to as the zone of silence and serve to protect this region from the background gases. What is desired, then, is skimming the beam from within the zone of silence. The gas flow through the skimmer depends on the initial gas flowrate through the sampler, the skimmer orifice diameter, and the sampler to skimmer distance. The flowrate is given by:

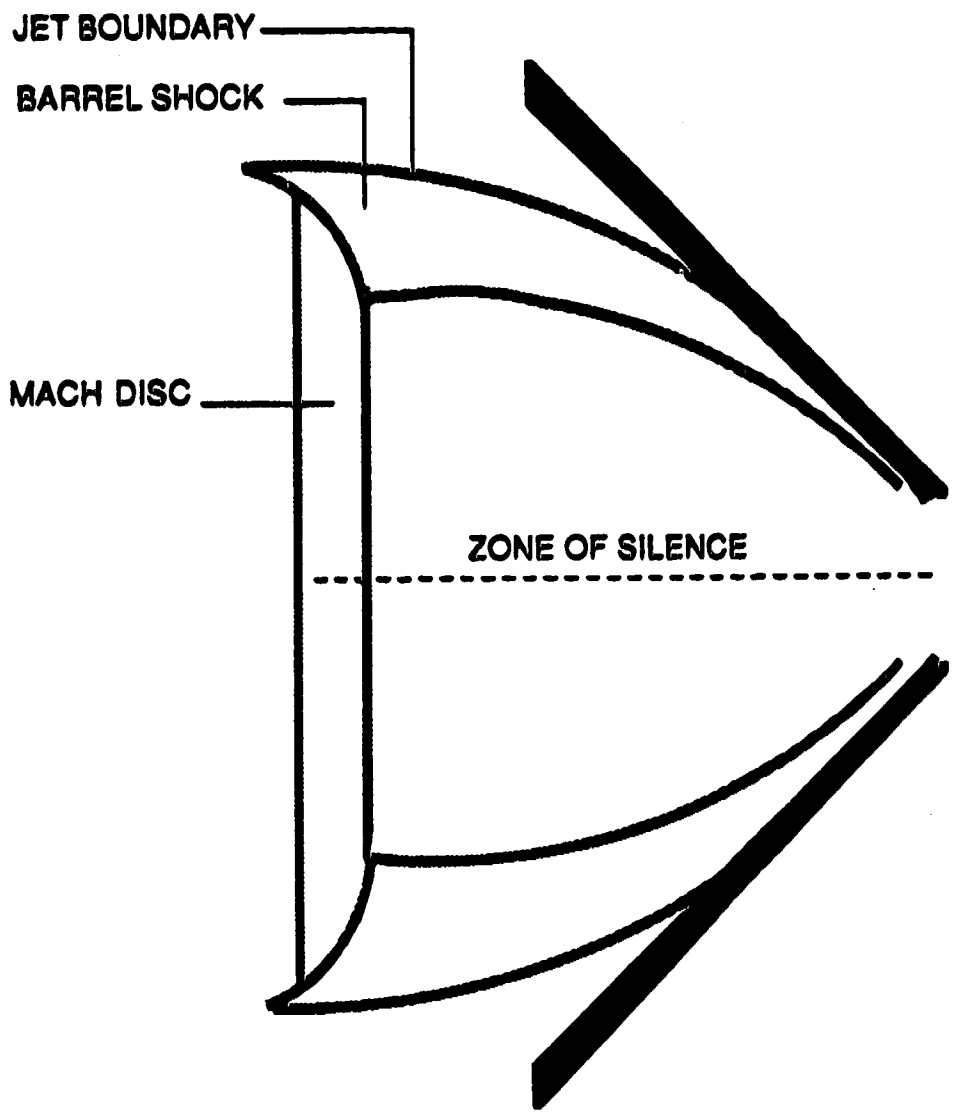

Figure 1.4 Flow field for the expansion of gas through the sampler.

$$U_s = U_o f(\gamma)\left(\frac{D_s}{x_s}\right)^2 \qquad 1.5$$

D_S = skimmer diameter

x_S = skimmer to sampler distance

In the Sciex Elan the sampler-skimmer distance is 6.1mm and assuming a skimmer diameter D_S of 0.89mm, $U_S = 1.1\times10^{19}\ s^{-1}$. The relative positions of the skimmer and the Mach disc are important for effective sampling of the plasma. The position of the Mach disc may be calculated using the well established relationship [16]:

$$X_m = 0.67 D_o\left(\frac{P_o}{P_1}\right)^{1/2} \qquad 1.6$$

X_m = position of the Mach disc

D_O = orifice diameter

P_O = initial pressure

P_1 = pressure in first expansion region

Assuming the pressure in the first expansion region is 5torr, the position of the Mach disc would be 7.4mm behind the sampler. Once the position of the Mach disc is known the skimmer must be properly positioned for effective beam production. Improper insertion of the skimmer into the zone of silence can cause loss in beam intensity. Depending on the position of the skimmer with respect to the sampler, Figure 1.5, the Mach disc can be in front of (Figure

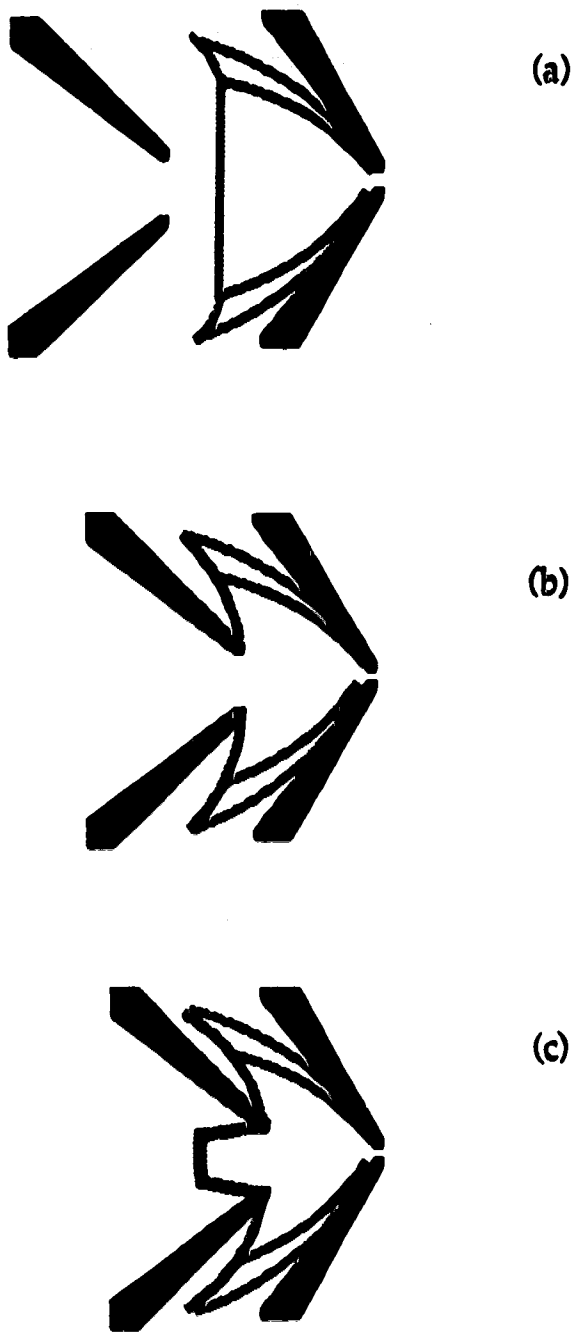

Figure 1.5 Relative positioning of the skimmer with respect to the Mach disc. (a) disc in front of skimmer, (b) disc attached to skimmer, (c) disc behind skimmer.

1.5a), attached to (Figure 1.5c) or penetrating downstream (Figure 1.5c) of the skimmer orifice [18]. The maximum beam intensity is obtained when the skimmer is attached to Mach disc, Figure 1.5b, [19]. Under these conditions there is no shock wave formation in the center of the expansion to scatter the beam. Douglas and French [20] report an equation which may be used to calculate the sampler - skimmer separation yielding the best neutral beam intensity downstream of the skimmer.

$$\frac{X_{s,m}}{D_o} = 0.125\left(K_{n_o}^{-1}\frac{P_o}{P_1}\right)^{1/3} \qquad 1.7$$

$X_{s,m}$ = sampler skimmer distance

D_o = sampler orifice diameter

P_o = initial pressure

P_1 = pressure in first expansion region

K_{no} = Knudsen number at the sampling orifice

K_n, the Knudsen number, is the ratio of the mean free path of the gas to the sampler orifice diameter.

$$K_n = \frac{\lambda}{D_o} \qquad 1.8$$

The mean free path may be calculated using [22]:

$$\lambda = \frac{(16/5)\eta}{nm(2\pi kT/m)^{1/2}} \qquad 1.9$$

η = viscosity coefficient of Ar (0.6mP)

n = number density at skimmer orifice

m = mean atomic weight of Ar

k = Boltzmann's constant

The number density at the skimmer orifice n, may be obtained using the relationship for the number density as a function of distance, x, along the streamline from the sampler [17,20].

$$\frac{n(x)}{n_o} = 0.161\left(\frac{x}{D_o}\right)^{-2} \qquad 1.10$$

For the Sciex Elan, $n_o = 1.5\times10^{24}\ m^{-3}$, $\lambda_o = 7.5\times10^{-7}m$ and $K_{no} = 8.4\times10^{-4}$ m which gives an optimum sampler-skimmer distance, $X_{s,m}$ of 6.3mm. Thus with the proper positioning of the sampler and skimmer, the expansion of the gas through the interface may be assumed to be nearly isentropic and to a first approximation adiabatic. As the expansion proceeds, a sizable fraction of the random thermal motion gets converted into directed translational

motion. The atoms and ions in the jet have the same bulk speed, that of Ar, regardless of mass. This results in a variation of ion kinetic energies for the analyte ions as a function of ion mass. Such variations have been observed [22]. For example ^{48}Ti and ^{208}Bi have ion energies of 3.3eV and 7.5eV respectively.

As the plasma expands through the interface, the kinetic temperature and the density of the gas decrease. As long as the beam can be treated as a freely expanding bulk gas, the Mach number and kinetic temperature may be estimated as a function of distance, x, along the axis of expansion [20,23].

$$M(\frac{x}{D_o}) = 3.26(\frac{x}{D_o})^{2/3} - 0.61(\frac{x}{D_o})^{-2/3} \qquad 1.11$$

and

$$T=T_o\left[1+1/2(\gamma-1)M(\frac{x}{D_o})^2\right]^{-1} \qquad 1.12$$

For example at x = 40mm, M(40/0.89) = 41 and T = 8.7K. Eventually the number of collisions reduces to the point where the flow changes from isentropic to nonisentropic, or collisionless. At this point the gas can no longer achieve equilibrium and the thermodynamic parameters at that time are frozen in and remain unchanged with further flow. The limiting or terminal Mach number is reached at this point. For Ar, the value is given by [23]:

$$M_T=133(P_oD_o)^{0.4} \qquad 1.13$$

where D_O is in cm and P_O in atmospheres. For the Sciex Elan, as described, M_T = 50. As Douglas and French note [20], equilibrium of the plasma is not achieved at the expansion temperature or else the ions of even low ionization potential would not be detected.

Finally, the collision frequency that occurs in the plasma expansion must be considered. Lubman, Rettner and Zare [23], discuss collision rates in molecular beams in detail. Douglas and French [20] use this information to make an estimate of the total number of collisions an ion from the plasma will undergo during the expansion process. They divide the expansion into two sections, before and after the M=1 plane, where $x = 0.5D_O$. Assuming that the plasma starts to cool significantly at M= 0.7 they consider first the region from M= 0.7 to M=1. In this region the flow speed, temperature and density do not change greatly so the region is approximately characterized using M= 0.8. From the relationships:

$$\left(\frac{\mu}{a_o}\right)^2 = \frac{2}{\frac{2}{M^2}+(\gamma-1)} \qquad 1.14$$

$$\frac{n_o}{n} = \left(1+\frac{\gamma-1}{2}M^2\right)^{1/(\gamma-1)} \qquad 1.15$$

$$\frac{T_o}{T} = 1+\left(\frac{\gamma-1}{2}\right)M^2 \qquad 1.16$$

where a_o = speed of sound, μ = flow speed and where $n_o = P_o/kT_o$, $\mu = 0.73a_o$, $n=0.75n_o$ and $T = 0.85\ T_o$ at M = 0.8. Using V_{th}, the thermal velocity, where

$$V_{th} = \left(\frac{8kT}{\pi m}\right)^{1/2} \qquad 1.17$$

and substituting for T from above, the collision frequency may be calculated as:

$$Z = n(x)V_{th}\sigma \qquad 1.18$$

where $\sigma = 50A^2$. The number of collisions may be estimated by multiplying the collision frequency, Z, by the time an ion spends traveling through the region. This time is obtained by calculating the distance between the M = 0.7 and M=1.0 planes and dividing by the flow speed (for M=1.0 $x/D_o = 0.5$ and for M= 0.7 $x/D_o = 0.414$).

For the region M =1 to M = ∞ the following approximations are made:

$$T(x) \cong T_o\left(1/2(\gamma-1)M^2\right)^{-1} \qquad 1.19$$

for Ar

$$T(x) \cong \frac{3T_o}{M^2} \qquad 1.20$$

and

$$M(\frac{x}{D_o}) \cong 3.26(\frac{x}{D_o})^{2/3} \qquad 1.21$$

Using equation 1.18 and approximating the flowspeed as :

$$V = \left(\frac{5kT_o}{m}\right)^{1/2} \qquad 1.22$$

the number of collisions may be estimated as:

$$dN = 0.061\left(\frac{D_o}{x}\right)^{8/3} n_o \sigma dx \qquad 1.23$$

Upon integration, the total number of collisions is obtained as:

$$N_{tot} = 0.116 D_o n_o \sigma \qquad 1.24$$

Combining the total number of collisions for both regions yields an approximation of the total number of collisions an ion would undergo during the expansion. For the Sciex Elan with D_o and D_s both equal to 0.89mm, $N_{tot} = 77$.

3. Ion Optics

The ions sampled from the ICP undergo a rather convoluted path in reaching the quadrupole mass analyser. Due to the photon noise from the ICP emission a photon stop is included in the ion optics. In the Sciex Elan there are two photon stops. The first, a grounded solid disc, is located just downstream from the skimmer and shadows the second photon stop which is located inside the bessel box. The first photon stop protects the second photon stop from being bombarded with too many ions which has a deleterious effect on the stability of the voltage of the second photon stop. In order for ions to reach the quadrupole mass analyzer, they must be traveling at an angle in order to avoid the first photon stop. After that, the voltages on each lens element must be set such that the ions pass through the einzel lens into and through the bessel box. The ion trajectories are dependent on ion energy and are studied in more detail in Chapter 6.

4. Quadrupole Mass Spectrometer and Ion Detector

Ion separation in ICP-MS is usually achieved using a quadrupole mass filter. The quadrupole was chosen for its simplicity, economy, its ability to run at fairly high pressures (10^{-5} torr) and because it is amenable to electronic control over ion transmission and resolution. Spectral scan rates may be varied. Rapid scanning is possible, or when need be, the spectra can be obtained by counting over extended periods of time. Peak hopping, where only selected masses are scanned and large sections of the spectrum are skipped, is also a useful feature of electronically controlled quadrupole

systems. The quadrupole mass filter is a line focussing ion lens which has been studied extensively and has been described in detail elsewhere [24, 25].

The ion detector used in the Sciex Elan 250 ICP-MS is a continuous dynode channel electron multiplier, operated in a pulse counting mode. The detector is located off axis from the quadrupole to reduce noise from the light emitted by the ICP. The instrument is designed to go into a shutdown mode to protect the detector if the ion count becomes too large. Depending on the sensitivity of the element being measured, this can put a ceiling on the concentration levels for aqueous samples in the range of 10μg/mL.

5. Background and Thesis Objective

The combination of an inductively coupled plasma and a mass spectrometer was first reported in the literature in 1980 in a paper by Houk et al. [1]. Four years after the publication of that paper two companies, VG, in Britain and Sciex, in Canada, began selling the instruments. There has been a rapid increase in the number of publications in the field since then. As with any new technique, there has been a lot of effort directed toward understanding the general instrumental behaviour in ICP-MS. A detailed study of the effects of the ICP parameters, power and Ar gas flowrates was made by Horlick et al [26]. They determined that the most important of the ICP parameters affecting ICP-MS signals were power and nebulizer flowrate and they established an ion count versus nebulizer flowrate-power parameter format for displaying the data which proved very useful. Shortly after that study was completed there were changes made by the instrument company (Sciex) to the ion optics and instrument electronics. Consequently, as part of this thesis work the ICP parameter studies in ICP-MS were repeated on the

upgraded instrument and expanded to include the effects of sampling depth on the nebulizer flowrate-power parameter plots and the effects of ion lens voltages on signal intensities.

Zhu and Browner [27] investigated the effects of changing operating conditions on signal intensities for a VG PlasmaQuad ICP-MS. The intensity versus nebulizer flowrate plots they obtained have characteristic mountain shapes which shift to higher flowrates for higher power settings and are similar to those reported by Horlick et al. [26] and those observed in this work. Gray and Williams [28] have also published plots of ion response versus nebulizer flowrate for data taken with a VG PlasmaQuad. Their data revealed that the position of the maxima are insensitive to the element being detected which is what we observed using the Sciex Elan ICP-MS. Although the VG and Sciex instrument designs are different, the basic nebulizer flowrate-power parameter behaviour observed is common to both instrument types.

An important difference in instrument design between the two instruments involves the load coil for the ICP. The Sciex instrument has a center tapped ground on the load coil of the ICP. This modification is described by Douglas and French [29]. Langmuir probe measurements made by Gray et al [30] on a VG type instrument were in the range of 5 to 20V and were dependent on operating conditions. Similar measurements made by Houk et al [31] on a Sciex were lower, 0.5 to -3.5V, and were only moderately dependent on operating conditions. Load coil geometry also effects the ion kinetic energies and those measured by Fulford and Douglas [22] on the Sciex were in the range of 2 to 9V; lower than those measured by Olivares and Houk [32] on a VG type measurement.

The range of kinetic energies for the ions entering the ICP-MS ion lens system affects the settings required for optimum signal intensity. With the Sciex Elan we observed a mass dependence of signal intensity as a function of ion lens voltage. Plots of signal intensity versus ion lens voltage reached their maxima at different voltages depending on the element measured. Schmit and Chtaib [33] also looked at the effect of ion lens voltages on multielement analysis using a Sciex Elan 250. Their results are in agreement with the lens behaviour observed in this work. Gray and Williams [28] discussed the ion lens system in a VG PlasmaQuad. The kinetic energies of the ions are different for this instrument design and they vary with changes in plasma power and nebulizer flowrate. They report that at the usual operating flowrate there is very little difference in ion energy with respect to ion mass. However, at low potentials they observed a similar dependence on mass as is seen with the Sciex. They also report that for flowrates above the usual operating flowrate the ion energies diverge again. Although a narrow energy range for ions entering the ICP-MS ion lens system is desirable it is also desirable that the ICP power and nebulizer flowrate have a minimal effect on ion lens settings.

The first step in this thesis work, then, was to characterize the parameter behaviour of the Sciex Elan ICP-MS. The study is presented in Chapter 2. From this work we understand what is required to reach the desired operating conditions and know the effects of: the ICP parameters, power and nebulizer flowrate; the ion lens settings; and the position of the plasma with respect to the sampler of the ICP-MS interface.

The basic parameter behaviour in ICP-MS is vital in running the instrument most effectively. Once the instrument is optimized for a strong M^+ signal the spectral characteristics of the technique may be studied. Ideally it would be desirable for the spectra to consist only of the M^+ ion for each element. Unfortunately the spectra are more complex than that. There are a number of doubly charged ions and molecular ion species formed resulting in spectroscopic overlaps that complicate both qualitative and quantitative analysis. These species may be formed from the analyte, from matrix components in the sample, from the plasma gas, or from some combination of these sources. Reports of these species began to appear shortly after the technique was announced. These species may be arbitrarily split into two groups: those formed from the matrix materials and those associated with the analyte ions. Ions in the first group include Ar_2^+, ClO^+, and NO^+ to name a few. Tan and Horlick [34] have reported an extensive listing of these species in their tabulation of the background ion species formed for several common acids.

The ions associated with the analyte species that cause spectroscopic interferences are usually the oxides, hydroxides and doubly charged analyte ions. Zhu and Browner [27] discussed the formation of the three species, M^{2+}, MO^+ and MOH^+ and studied their parameter behaviour with a VG PlasmaQuad. A VG PlasmaQuad was also employed by Gray [35] in his study of doubly charged ions and molecular ions. Longerich et al. [36] used a Sciex Elan to investigate the analysis of rare earth elements. They included a study of the oxide ions of the rare earth elements as part of their parameter investigation.

The formation of M^{2+}, MO^+ and MOH^+ ions is an area where the VG and Sciex instruments differ in their behaviour and there has been a great deal of debate in this area. Although the nebulizer flowrate-power parameter plots for these species for the two instruments are similar, as demonstrated by a comparison of Ba data in the work of Zhu and Browner [27] and Chapter 3 of this thesis, the relative amounts of each type of ion differ. With the VG PlasmaQuad the most intense ion of the Ba species other than Ba^+ is Ba^{2+}. In contrast the oxide and hydroxide species, BaO^+ and $BaOH^+$ are the more intense ions with a Sciex ICP-MS. The behaviour of the ion ratios for M^{2+}/M^+ as a function of power and nebulizer flowrate are opposite for the two instrument types. In this thesis work we show that the ratio increases with increasing power and decreases with increasing nebulizer flowrate. Data presented by Gray and Williams [28] for a VG PlasmaQuad and by Olivares and Houk [37] with their VG type instrument show the opposite effect, the ratio decreases with increasing power and increases with increasing nebulizer flowrate. In contrast the behaviour of the MO^+/M^+ ratio as a function of power or nebulizer flowrate is the same for both instrument designs. The ratio increases with nebulizer flowrate and decreases with power.

The problem of spectral overlap caused by these species has been reported in numerous application papers by users of both instrument types. For example the problems of spectral overlap caused by the formation of M^{2+}, MO^+ and MOH^+ have been reported by McLeod et al. [38] in their analysis of nickel based alloys and Doherty and Vander Voet [39] report oxide interferences that complicate their analysis of geological materials. Regardless of the percent formation of these species, which varies with instrument type, if the concentration of the element is large enough there is potential for

spectral interferences. Interferences from oxide, hydroxide and doubly charged ion species in ICP-MS have been tabulated in Chapter 3 of this thesis.

The second section of this thesis work deals with the problems of oxide, hydroxide and doubly charged ion species formation in ICP-MS. The parameter behaviour of these species must be known in order for us to understand whether we can reduce the problem instrumentally and if so, how and to what extent. It is also vital to know where interferences will occur, which prompted the compilation of the interference tables. These topics are addressed in Chapter 3 of this thesis. It is also important to be aware that reducing the levels of these species, especially the oxides and hydroxides, to negligible amounts is not always possible. When this situation exists, the data must be corrected for the presence of the undesired species. This may be done by the traditional algebraic method of Gauss elimination or by employing principal components analysis. These methods are demonstrated in an analysis of the rare earth elements in Chapter 4.

As well as spectral interferences, non-spectral matrix effects are observed in ICP-MS and are of extreme importance because of the severity of the signal suppression under certain conditions. Olivares and Houk [40] studied the effects of various concomitant salts and they report that ICP-MS is more susceptible to ionization suppression effects than is ICP-atomic emission spectrometry (ICP-AES) and that total solutes above 1% are complicated by orifice plugging problems. Tan and Horlick [41] carried out a major study on matrix induced intensity changes in ICP-MS. They observed that high concentrations of any element caused signal suppression, heavier matrix elements cause more severe suppression, and the lighter analyte elements are suppressed more than the heavier ones. These results are

supported by Kawaguchi et al [42] who propose an ion scattering mechanism as the source of the effect. Gregoire [43] studied the effects of easily ionizable concomitant elements on ICP-MS and observed the same behaviour as others. He has speculated that ambipolar diffusion effects may be responsible for the non-spectroscopic interferences. A comparison of ICP-MS and ICP-AES was carried out by Pickford and Brown [44] and they reported the potential for considerable matrix suppression in ICP-MS compared to ICP-AES.

The existence of the non-spectroscopic matrix effects in ICP-MS is well documented and there has been some attempt at understanding why such effects are observed. Toward that end, Gillson et al. [45] have investigated space charge effects in the einzel lens of the Sciex Elan instrument and Crain et al. [46] have investigated some effects of skimmer orifice diameter and ion lens voltages. The actual cause or causes of the non-spectroscopic matrix effects observed in ICP-MS is not yet known, however, there are ways to reduce the effects. Careful selection of operating parameters can help reduce problems, as reported by Tan and Horlick [41] and, where feasible, sample dilution can help.

Hutton and Eaton [47] report the analysis of solutions containing high levels of dissolved solids by using a flow injection sample introduction method. With the flow injection method solutions with high levels of total dissolved solids can be analysed with minimum problems of orifice blockage. This approach reduces the physical effects of large amounts of dissolved solids being deposited on the sampler thereby reducing the orifice size and lowering the signal intensity. It does not reduce the matrix suppression from other sources.

Although the topic of non- spectroscopic matrix effects was not the focus of this thesis it is of vital importance in ICP-MS when methods development is undertaken. A number of groups have used the instrument for the elemental analysis of geological materials [48-53] with a fair bit of attention on the rare earth elements [48-50]. There is an interest in Os isotopic ratios [54,55] for the dating of geological samples as well as studying the trace components in silver artifacts [56], steels [57], and iron ores [58]. There has been a lot of work done on water analysis: ocean waters [59,60], river water [61], and acid precipitation samples [62]. Stable isotope dilution analysis [63] has been done on hydrologic samples, primarily surface waters. Sea sediments have also received attention [64] including analysis done with stable isotope dilution [65]. Organic materials such as a reference material lobster hepatopancreas [67] have been analysed and the ICP-MS has been used for trace elemental analysis of foods [68]. The ICP-MS is also being employed in clinical chemistry for multielement analysis [69] and for Pb and Pb isotope ratio measurements [70,71] and for stable isotope measurements of Mg [72] and K [73]. For all of these analyses consideration of the relevant spectroscopic and non-spectroscopic interferences had to be made during method refinement.

In Chapter 5 of this thesis, the method development for the analysis of steel is described. The information obtained in the earlier studies is used as a guide to the stepwise approach to the problem. Qualitative spectral scans aid in identifying potential spectral interferences, instrument stability and non-spectroscopic interferences are addressed and the function of the internal standard is discussed.

The remainder of the thesis deals with understanding why we observe some of the things we see in ICP-MS and whether the results of ICP-MS are useful as indicators of what is occurring in the undisturbed plasma. The ion lenses play an important role in the ICP-MS. They are required to direct the ions into the quadrupole for mass analysis and are usually designed to block light from the plasma, thus reducing photon noise at the ion detector. Consequently the paths of the ions can be rather convoluted, having to travel around some sort of photon stop. The ion lens system for the Sciex Elan was modeled and the ion trajectories were studied under varied conditions. The modeling helps in the understanding of the lens data collected with the ICP-MS.

Another question that arises from the study of the ICP-MS is that of where the oxide species are formed. This is an interesting question, due in part to the similarities in oxide behaviour as a function of power and nebulizer flowrate between the two instrument designs (even though users of the VG PlasmaQuad report lower levels of oxide). The question of oxide formation is addressed in detail in a parameter study involving the orifice sizes of the sampler and skimmer cones. The changes in parameter behaviour and in oxide formation with orifice size indicate that the oxides are formed in a boundary layer around the sampler.

Finally the question of how useful are the results of ICP-MS as an indicator of what is occurring in the undisturbed plasma is addressed. The comparison of mass spectrometric and atomic emission data is difficult due in part to the complexity of the ICP-MS. There has been some attempt at using ICP-MS results to give an indication of plasma conditions such as

temperature [74]. We have observed the method to be insensitive to significant changes in ICP-MS conditions which limits its usefulness for this purpose.

Thus this thesis addresses three general areas in ICP-MS. The first area is the behaviour of parameters which influence signal intensity, including those parameters which have an effect on the basic nebulizer flowrate parameter plots such as power, sampling depth, photon stop lens voltages and the orifice sizes of the sampler and skimmer. Analyte ion species formation is the second area of study. This section addresses the types of ions formed and the parameter behaviour they exhibit, the resulting problems from these species and correction schemes to handle the resulting interferences. The third area is the qualitative and quantitative capabilities of ICP-MS. The importance of parameter behaviour and ion species formation in the development of an analytical method for this instrument is stressed.

References

1. R. S. Houk, V. A. Fassel, G. D. Flesch, H. J. Svec, A. L. Gray and C. E. Taylor, Anal. Chem. **52**, 2283-2289, (1980).

2. R. S. Houk, V. A. Fassel and H. J. Svec, Dyn. Mass Spectrometry, **6**, 234-251, (1981).

3. D.J. Douglas, E. S. K. Quan and R. G. Smith, Spectrochim. Acta,**38B**, 39-48, (1983).

4. A. L. Gray, Spectrochim. Acta, **40B**, 1525-1537, (1985).

5. V. A. Fassel, R. N. Kiniseley, Anal. Chem. **46**, 1155A-1164A, (1974).

6. M. W. Blades, B. L. Caughlin, Z. H. Walker and L.L. Burton, Prog. Analyt. Spectrosc. **10**, 57-109, (1987).

7. B. L. Caughlin and M. W. Blades, Spectrochim. Acta, **40B**, 1539-1554, (1985).

8. N. Furuta, Spectrochim. Acta, **40B**, 1013-1022, (1985).

9. N. Furuta and G. Horlick, Spectrochim. Acta, **37B**, 53-64, (1982).

10. D.J. Douglas and R.S. Houk, Prog. Analyt. Atom. Spectrosc. **8**, 1-18, (1985).

11. N. Furuta, Spectrochim. Acta, **41B**, 1115-1129, (1986).

12. A. R. Date and A. L. Gray, Analyst, **106**, 1255-1267, (1981).

13. D.J. Douglas and J. B. French, Anal. Chem. **53**, 37-41, (1981).

14. A. L. Gray and A. R. Date, Analyst, **108**, 1033-1050, (1983).

15. R. Campargue, J. Chem. Phys. **52**, 1795-1802, (1970).

16. A. Hoglund and L-G. Rosengren Int. J. Mass. Spec. Ion Process. **60**, 173-187, (1984).

17. H. C. W. Beijerinck, R. J. F. Van Gerwen, E. R. T. Kerstel, J. F. M. Martens, E. J. W. Van Vliembergen, M. R. Th. Smits and G. H. Kaashock, Chem. Phys. **96**, 153-173, (1985).

18. R. Pertel, Int. J. Mass Spec. Ion Phys. **16**, 39-52, (1975).

19. R. Campargue, Proceedings of the IV Symposium on Rarefied Gas Dynamics, ed. J. H. de Leeuw, Academic Press N.Y.(1966) pp279-298 .

20. D. J. Douglas and J. B. French, J. Anal. Atom. Spectrosc. **3**, 743-747 (1988).

21. J. A. Olivares and R. S. Houk, Anal. Chem. **57**, 2674-2679,(1985).

22. J. E. Fulford and D. J. Douglas, Applied Spectrosc. **40**, 971-974, (1986).

23. D.M. Lubman, C.T. Rettner and R. N. Zare, J. Phys. Chem. **86**, 1129-1135, (1982).

24. J. E. Campana, Int, J. Mass Spec. Ion Phys. **33**, 101-117, (1980).

25. P.H. Dawson, Quadrupole Mass Spectrometry and its Applications, Elsevier Scientific Publishing Co. 1976, Chapter 2.

26. G. Horlick, S. H. Tan, M. A. Vaughan and C.A. Rose, Spectrochim. Acta **40B**, 1555-1572, (1985).

27. G. Zhu and R. F. Browner, Applied Spectrosc. **41**, 349-359, (1987).

28. A. L. Gray and J.G. Williams, J. Anal. Atom. Spectrom. **2**, 599-606, (1987).

29. D. J. Douglas and J. B. French, Spectrochim. Acta, **41B**, 197-204, (1986).

30. A. L. Gray, R. S. Houk and J. G. Williams, J. Anal. Atom. Spectrom. **2**, 13-20, (1987).

31. R. S. Houk, J. K. Schoer and J. S. Crain, J. Anal. Atom. Spectrom. **2**, 283-286, (1987).

32. J. A. Olivares and R. S. Houk, Applied Spectrosc. **39**, 1070-1077, (1985).

33. J. P. Schmit and M. Chtaib, Can. J. Spectrosc. **32**, 56-60, (1987).

34. S. H. Tan and G. Horlick, Applied Spectrosc. **40**, 445-460, (1986).

35. A. L. Gray, Spectrochim. Acta, **41B**, 151-167, (1986).

36. H. P. Longerich, B. J. Fryer, D. F. Strong and C.J. Kantipuly, Spectrochim. Acta, **42B**, 79-92, (1987).

37. J. A. Olivares and R. S. Houk, Anal. Chem., **57**, 2674-2679, (1985).

38. C. W. McLeod, A. R. Date and Y. Y. Cheung, Spectrochim. Acta **41B**, 169-174, (1986).

39. W. Doherty and A. Vander Voet, Can. J. Spectrosc., **30**, 135-141, (1985).

40. J. A. Olivares and R. S. Houk, Anal. Chem. **58**, 20-25, (1986).

41. S. H. Tan and G. Horlick, J. Anal. Atom. Spectrom. **2**, 745-763, (1987).

42. H. Kawaguchi, T. Tanaka, T. Nakamura, M. Morishita and A. Mizuike, Analytical Sci. **3**, 305-308, (1987).

43. D. C. Gregoire, Spectrochim. Acta **42B**, 895-907, (1987).

44. C. J. Pickford and R. M. Brown, Spectrochim. Acta, **41B**, 183-187, (1986).

45. G. R. Gillson, D. J. Douglas, J. E. Fulford, K. W. Halligan and S. Tanner, Anal. Chem. **60**, 1472-1474, (1988).

46. J. S. Crain, R. S .Houk and F. G. Smith, Spectrochim. Acta, **43B**, 1355-1364, (1988).

47. R. C. Hutton and A. N. Eaton, J. Anal. Atom. Spectrom. **3**, 547-550, (1988).

48. W. Doherty and A. Vander Voet, Can. J. Spectrosc. **30**, 135-141, (1985).

49. F. E. Lichte, A. L. Meier and J. G. Crock, Anal. Chem. **59**, 1150-1157, (1987).

50. A.R. Date and D. Hutchison, J. Anal. Atom. Spectrom. **2**, 269-276, (1987).

51. G. E. M. Hall, C. J. Park and J. C. Pelchat, J. Anal. Atom. Spectrom. **2**, 189-196, (1987).

52. A. R. Date and A. L. Gray, Spectrochim. Acta **40B**, 115-122, (1985).

53. A. R. Date and D. Hutchison, Spectrochim. Acta, **41B**, 175-181, (1986).

54. A. P. Dickin, R. H. McNutt and J.I. McAndrew, J. Anal. Atom. Spectrom. **3**, 337-342, (1988).

55. G. P. Russ III, J. M. Bazan and A. R. Date, Anal. Chem. **59**, 984-989, (1987).

56. H. P. Longerich, J. B. Fryer and D. F. Strong, Spectrochim. Acta, **42B**, 101-109, (1987).

57. J. Luck and U. Siewers, Fresenius Z. Anal. Chem. **331**, 129-132, (1988).

58. A. R. Date, Y. Y. Cheung, M. E. Stuart and X.-H. Jin, J. Anal. Atom. Spectrom. **3**, 653-658, (1988).

59. D. Beauchemin, J. W. McLaren, A. P. Mykytiuk and S. S. Berman, J. Anal. Atom. Spectrom. **3**, 305-308, (1988).

60. J. W. McLaren, A. P. Mykytiuk, S. N. Willie and S. S. Berman, Anal. Chem. **57**, 2907-2911, (1985).

61. D. Beauchemin, J. W. McLaren, A. P. Mykytiuk and S. S. Berman, Anal. Chem. **59**, 778-783, (1987).

62. D. W. Boomer and M. J. Powell, Can. J. Spectrosc. **31**, 104-109, (1986).

63. J. R. Garbarino and H. E. Taylor, Anal. Chem. **59**, 1568-1575, (1987).

64. J. W. McLaren, D. Beauchemin and S. S. Berman, J. Anal. Atom. Spectrom. **2**, 277-281, (1987).

65. J. W. McLaren, D. Beauchemin and S. S. Berman, Anal.Chem. **59**, 610-613, (1987).

66. R. S. Houk, V. A. Fassel and H. J. Svec, Org. Mass Spec. **17**, 240-244, (1982).

67. P. S. Rideout, H. R. Jones and J. G. Williams, Analyst **113**,1383-1386, (1988).

68. R. D. Satzger, Anal. Chem. **60**, 2500-2504, (1988).

69. T. D. B. Lyon, G. S. Fell, R. C. Hutton and A. N. Eaton, J. Anal. Atom. Spectrom. **3**, 265-271, (1988).

70. H. T. Delves and M. J. Campbell,J. Anal. Atom. Spectrom. **3**, 343-348, (1988).

71. B. T. G. Ting and M. Janghorbani, Anal. Chem. **58**, 1334-1340, (1986).

72. S. Schuette, D. Vereault, B. T. G. Ting and M. Janghorbani, Analyst, **113**, 1837-1842, (1988).

73. S. J. Jiang, R. S. Houk and M. A. Stevens Anal. Chem. **60**, 1217-1221, (1988).

74. D. A. Wilson, H. G. Vickers and G. M. Hieftje, Applied Spectrosc. **41**, 875-880, (1987).

Chapter 2

Effect of Operating Parameters on Analyte Signals in Inductively Coupled Plasma Mass Spectrometry *

Inductively coupled plasma mass spectrometry (ICP-MS) is a fairly new technique for trace element analysis. In order to utilize a technique efficiently and to take full advantage of its capability, it is necessary to know the effect of instrument operating parameters on the analytical signal. Being the combination of an inductively coupled plasma and an atmospheric pressure sampling quadrupole mass spectrometer the instrumentation involved in ICP-MS is complex and a large number of variables affect the analytical signal. The majority of studies to date have focused on the basic analytical capability at one set of operating parameters.

In an initial investigation on a commercial instrument (SCIEX ELAN) Horlick et al. [1] carried out a study of the effect of plasma operating parameters on analyte signals in ICP-MS. The key ICP variables were found to be nebulizer flowrate and power and it was particularly informative to plot the analyte ion signal as a function of nebulizer flowrate for a set of power levels. Such graphs, for a wide range of elements, are useful for selecting compromise operating conditions because they clearly illustrate signal trends and clarify single parameter observations.

---

* A version of this chapter has been published. M. A. Vaughan, G. Horlick and S. H. Tan, J. Anal. Atom. Spectrom. **2**, 765-772,(1987).

During this initial study some instrumental variables and components were undergoing modification. In particular, the SCIEX instrument was delivered with a so-called long torch, which was 2 cm longer than that normally used for atomic emission work. As such, most of our first observations were made at a sampling depth (distance from the load coil to the sampling cone) of about 30 mm. Since that time we have standardized on using a normal ICP torch identical with that used in atomic emission work which we typically run at a sampling depth of about 15 mm from the load coil. As will be seen from the data presented in this chapter, an important consequence of this change is that the nebulizer flowrate - power parameter plots are more consistent over a wide range of elements and that there is less variability in the optimum settings. Data are presented for a wide range of elements, studied not only as functions of nebulizer flowrate and power, but also as a function of the sampling depth. The elements studied include the transition metals from groups 4B (Ti, Zr and Hf), 6B (Cr, Mo and W) and 8B (Ni, Pd and Pt), a set of light elements (Li, B, Na and Al), and main group elements from 2A (Sr and Ba), 3A (Ga, In and Tl), 4A (Ge, Sn and Pb) and 5A (As, Sb and Bi).

A second key set of variables in ICP-MS, in addition to the ICP parameters, are the settings of the mass spectrometer input ion-optic voltages. The effect of these lens voltages on the analytical signals was not presented in our initial investigation because the manufacturer was in the process of developing major modifications to the input ion optics. The design of these optics has been stable since then and results are presented in this chapter on the effect of ion-optic voltage settings on analyte signals.

Experimental

A SCIEX ELAN Model 250 ICP-MS was used for all data acquisition. A standard length MAK torch was used with a Meinhard nebulizer and a Scott spray chamber. The Ar coolant flowrate was 11L/min and the auxiliary flowrate was 1.4L/min. The flowrate of the nebulizer gas, which was also Ar, was varied. Both the nebulizer and auxiliary gas flowrates were controlled by Matheson Model 8240-0423 mass-flow controllers. The plasma power was varied from 0.9 to 1.5kW. Sampling of the plasma into the mass spectrometer was carried out using a copper sampler with a 0.94mm diameter orifice. The skimmer was made of nickel and had a 0.89mm diameter orifice.

All solutions were prepared from Spex Industries standard solutions and were diluted to volume with deionized water. The solutions were 0.1μg/mL in each element. The data acquisition was carried out in low resolution (1amu at the base of the peak) in sequential mode. An integration time of 0.1s per point for ten points across the peak was used for all elements except the power - flowrate study of the light elements. For these elements seven points across the peak were used. The number of points across the peak was reduced for these elements because of the structured background in the low mass region. In all instances six replicate determinations were carried out. All data were uncorrected for isobaric interferences, except for Hf and In which were corrected for W and Sn respectively. The background count was low and was not subtracted. All data were taken at a sampling depth of 15mm from the load coil unless otherwise stated.

The data for the lens study were taken at 1.3kW plasma forward power and a nebulizer flowrate of 1.18L/min. The ion-lens voltages for each of the types of experiments are given in Table 2.1. For the ion-lens experiments the voltage on one lens was varied while the remaining three lenses were kept at the voltages listed under Lens study in column two of Table 2.1. The lens voltages for the power-flowrate studies that yielded Figures 2.1 and 2.2 are listed in the third column of Table 2.1 under Power -flowrate. For the power-flowrate study of the light elements the lens settings are listed under Light elements in the fourth column of Table 2.1. Finally, the lens voltages for the data acquired at a series of depths are listed in the fifth column of Table 2.1 under Depth study.

Table 2.1 Lens voltage settings (V).

Lens	Lens study	Power-flowrate	Light elem.	Depth study
Bessel box barrel (B)	4	5	5	5
Photon stop (S2)	-9	-10	-6	-11
Bessel box plates (P)	-18	-18	-18	-18
Einzel lens (E1)	-16	-16	-16	-16

Results and Discussion

1. Nebulizer Flowrate - Power Parameter Graphs.

The effects of nebulizer flowrate and power on the analyte ion signals for Ti^+, Zr^+, Hf^+, Cr^+, Mo^+, W^+, Ni^+, Pd^+ and Pt^+ are shown in Figure 2.1. Clearly all these elements exhibit similar behaviour. At any one power, the

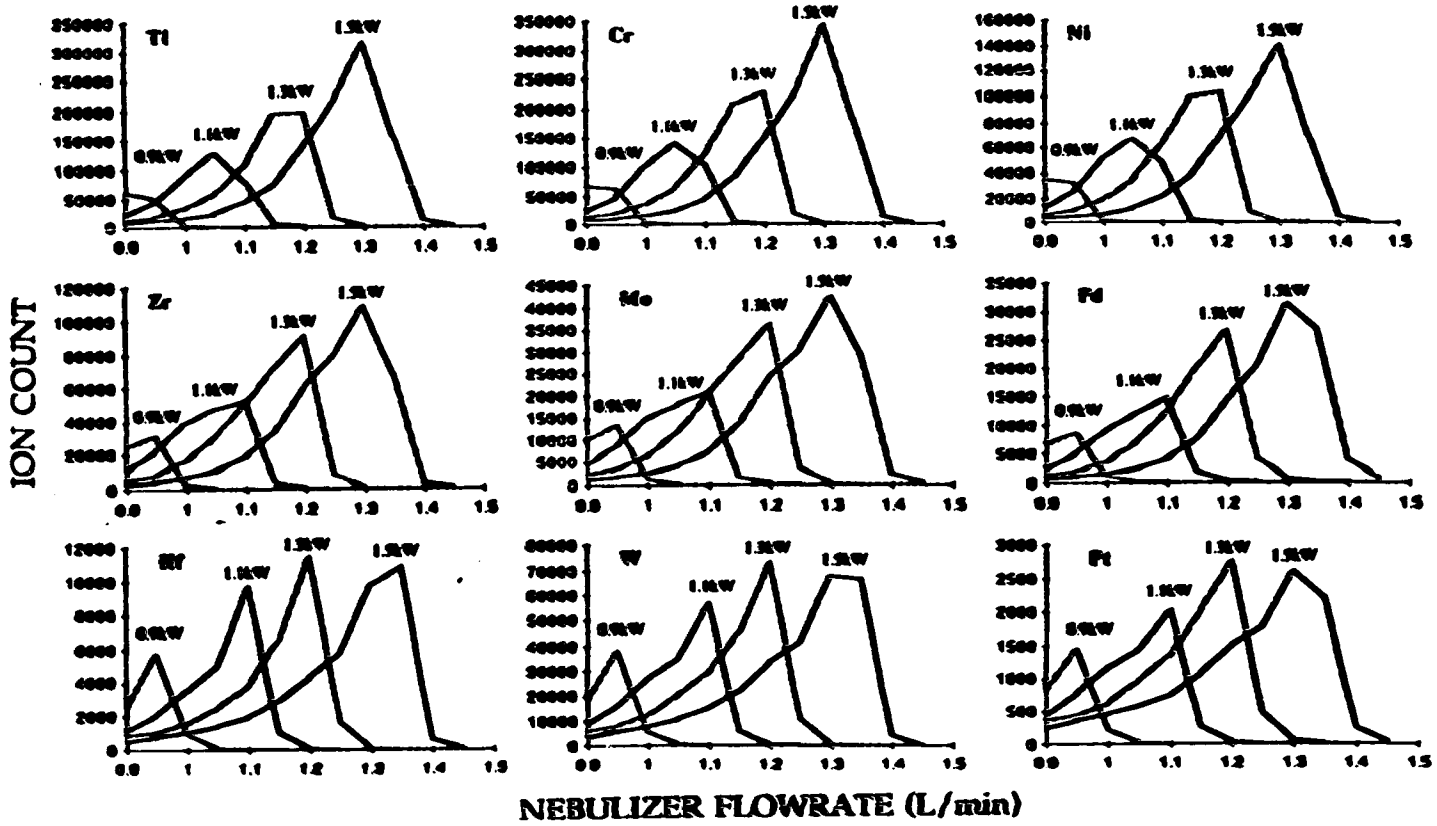

Figure 2.1 Nebulizer flowrate - power parameter behaviour graphs for Ti^+, Zr^+, Hf^+, Cr^+, Mo^+, W^+, Ni^+, Pd^+ and Pt^+; power in kW shown on each line.

signal has a relatively sharp maximum value at a particular nebulizer flowrate. Note that at one power setting, all of these elements have their maximum signal value at essentially the same nebulizer flowrate and thus a single nebulizer flowrate and power setting is optimum for all these elements with little compromise. It is also clear that if either parameter is altered, the other parameter must also be adjusted in order to re-maximize the signal. Thus changing power from 1.3 to 1.5 kW does not increase the signal level unless the nebulizer flowrate is also increased from 1.2 to 1.3 1 L/min.

It should be noted that the absolute position of these maxima along the flowrate axis can vary from day to day. The exact position of maximum response depends on the exact torch dimensions, sampling depth and lens settings. However, the over-all relative patterns are consistent.

A similar set of data is show in Figure 2.2 for Ga^+, In^+, Tl^+, Ge^+, Sn^+, Pb^+, As^+, Sb^+ and Bi^+ and it is remarkably similar to the set of data shown in Figure 2.1. Although ion counts are not normalized for natural abundances, there is a general trend, which can be noted from the data shown in Figures 2.1 and 2.2, for the ion counts to decrease steadily in going from left to right and in particular from top to bottom within each figure. This trend is caused by the facts that in general the ionization potential of the elements increases from left to right, the solutions are not equimolar (i.e., all 0.1 μg/mL), thus there are fewer moles of the heavier elements, and finally the ion-optic voltage settings were closer to being optimum for the first row elements.

The nebulizer flowrate - power parameter graphs for the light elements Li^+, B^+, Na^+ and Al^+ are shown in Figure 2.3. The basic parameter behaviour of these elements is similar to those already illustrated although for a given

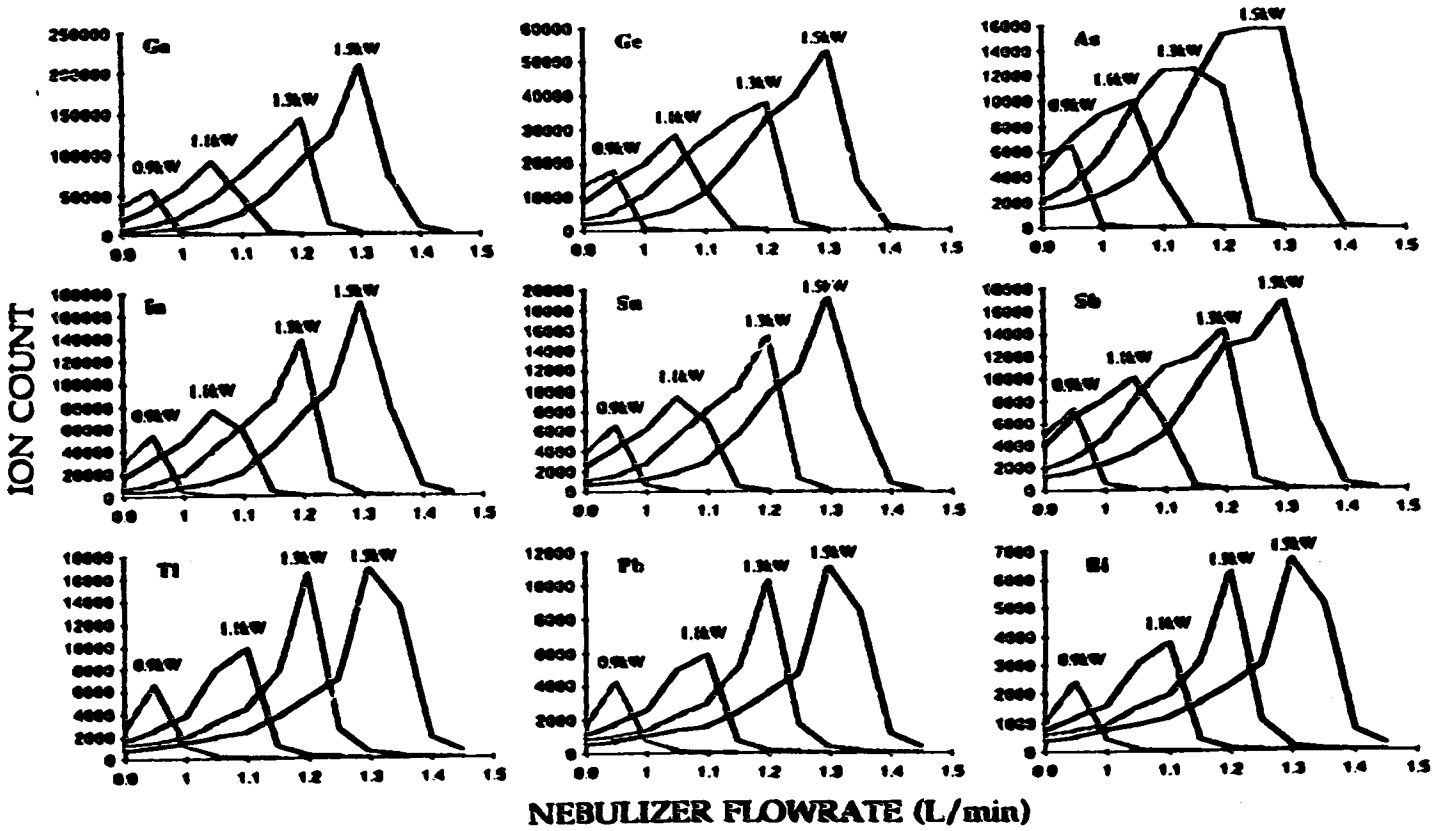

Figure 2.2 Nebulizer flowrate - power parameter behaviour graphs for Ga^+, In^+, Tl^+, Ge^+, Sn^+, Pb^+, As^+, Sb^+ and Bi^+; power in kW shown on each line.

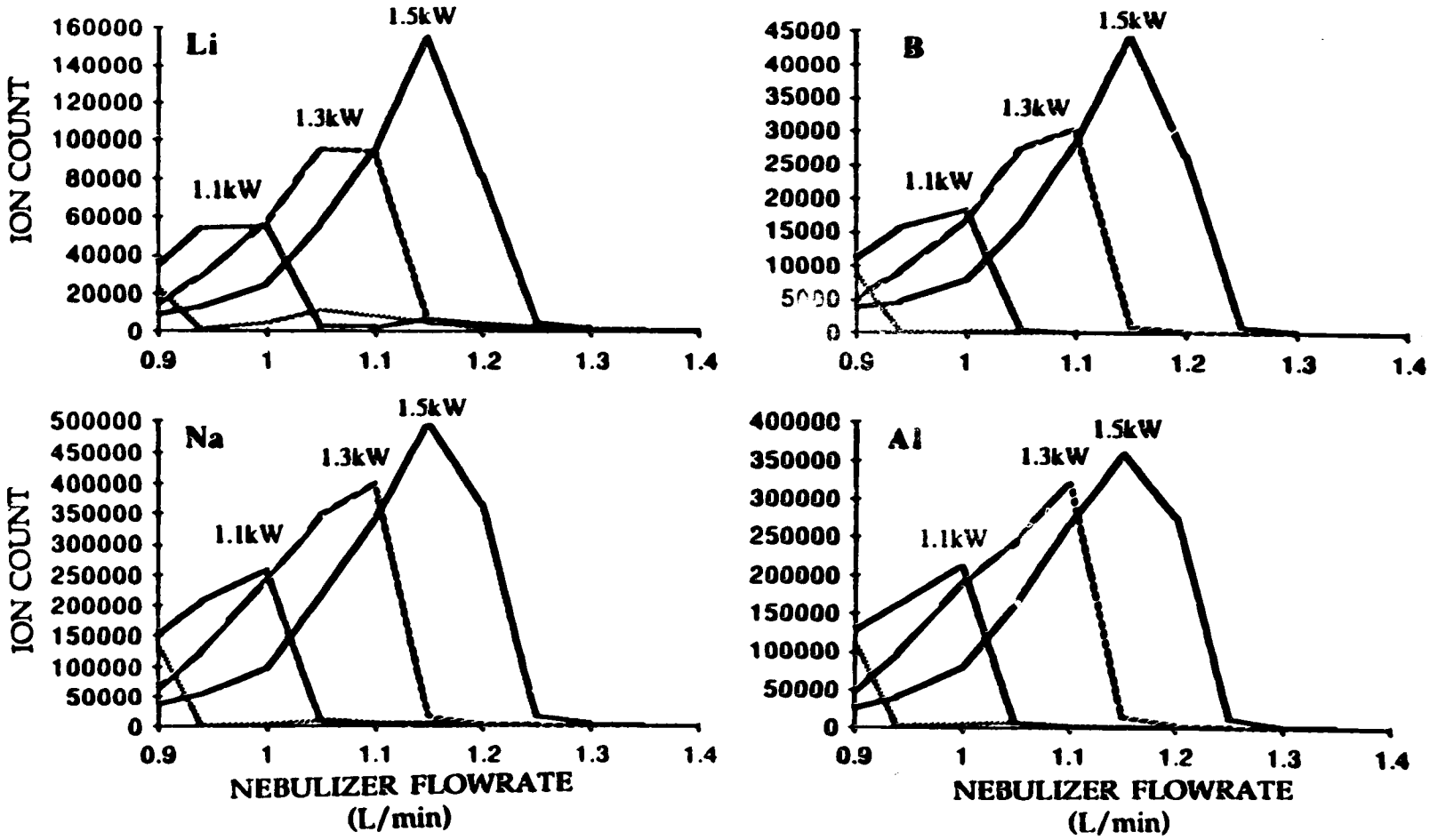

Figure 2.3 Nebulizer flowrate - power parameter behaviour graph for Li^+, B^+, Na^+ and Al^+; power in kW shown on each line.

power level, their signals are maximized at a lower nebulizer flowrate. This means that the same set of compromise operating conditions cannot be used for these elements and for those presented in Figures 2.1 and 2.2. These lighter elements when present together can, however, be determined individually under a single set of conditions.

2. Effect of Sampling Depth.

Nebulizer flowrate - power parameter graphs are shown in Figure 2.4 for Ni^+, Pd^+ and Pt^+ at sampling depths of 10, 15, 20 and 25 mm. The sampling depth is the distance from the tip of the sampling cone to the load coil of the ICP torch. The data were not collected on the same day as those shown in Figure 2.1 and shifts in sensitivity and absolute positions of the maximum signal response can be noted.

The nebulizer flowrate - power parameter graphs are basically similar at the various sampling depths except for a shift along the nebulizer flowrate axis. For a given power, as sampling depth is increased, the nebulizer flowrate must also be increased in order to maintain a maximum ion count. It is as if a zone of maximum ion density in the ICP is being adjusted to correspond to the sampling cone distance. For atomic emission reference, Koirtyohann et al. [2] have designated two major zones in the ICP, the initial radiation zone (IRZ) and the normal analytical zone (NAZ). It is known that the nebulizer flowrate has a major effect on the position of these zones relative to the load coil. The NAZ is generally associated with the position at which the best ion line emission is observed in the ICP-AES while the IRZ is that where neutral

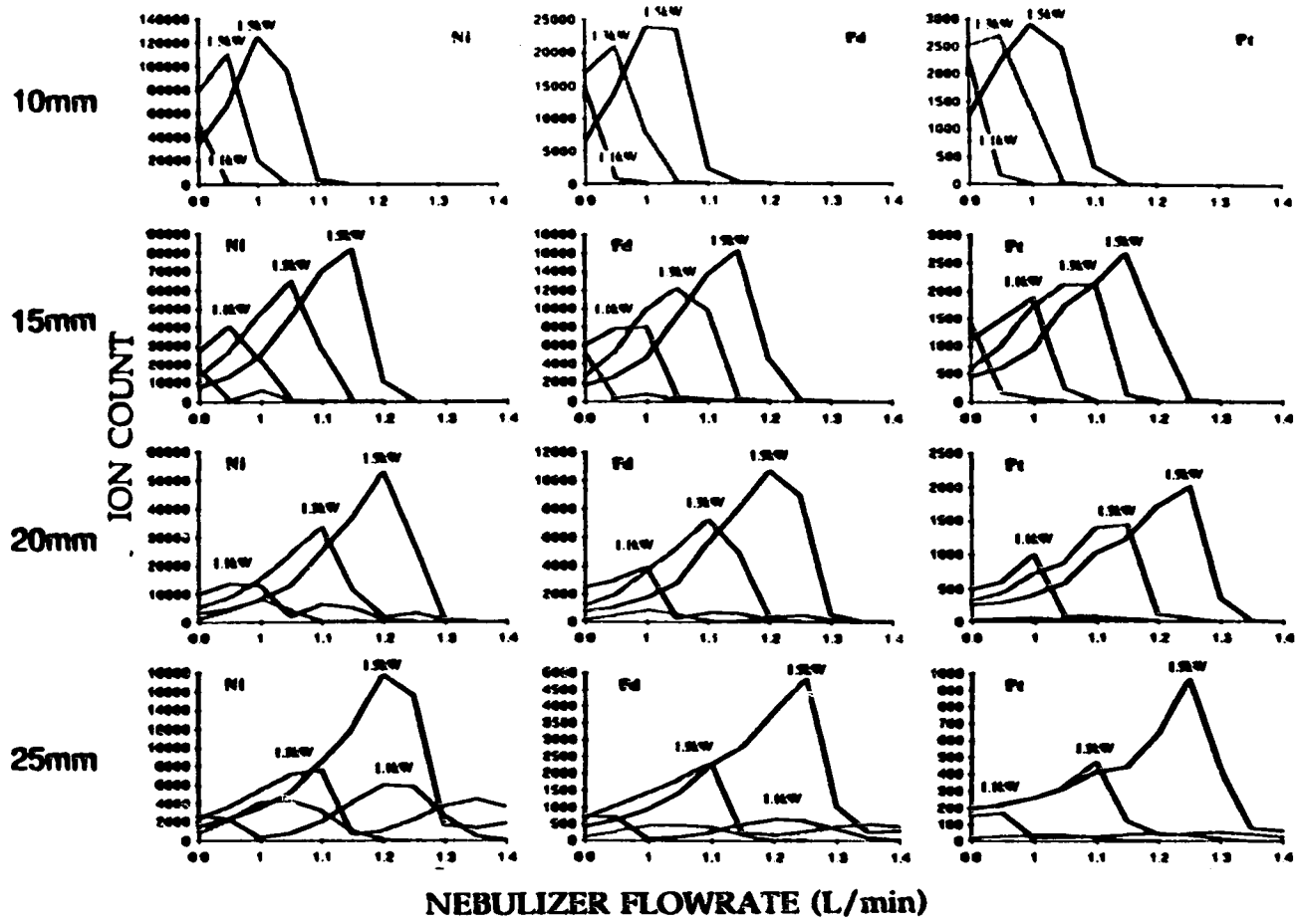

Figure 2.4 Nebulizer flowrate - power parameter behaviours graphs for Ni^+, Pd^+ and Pt^+ at sampling depths of 10, 15, 20 and 25 mm; power in kW shown on each line.

atom line emission is observed. With reference to ICP-MS, it appears that the best observation zone is somewhere in between the IRZ and the NAZ at a position 2-5 mm above the IRZ as visualized by aspirating Y. Other workers have come to this same conclusion for ICP-MS and ion fluorescence data published by Gillson and Horlick [4] have confirmed that ground-state ions have a maximum density that occurs below the NAZ. In addition, Gillson and Horlick [4] noted the similarity between nebulizer flowrate - power parameter graphs for the ionic fluorescence of Sr in ICP-AES and the ion count of Sr in ICP- MS.

Nebulizer flowrate - power parameter graphs are shown in Figure 2.5 for Sr^+ and Ba^+ as a function of sampling depth. In our initial investigation [1] of parameter behaviour, Sr and Ba seemed to be different in that their parameter graphs did not conform to those of most of the other elements (see Figure 12 in reference 1). However, based on the data presented here in Figure 2.5, their parameter behaviour is seen to correspond basically to that of the other elements. In general, our data have been far less element specific when the switch was made to a normal ICP-AES torch along with sampling depths in the range of 10-15 mm, a fact that is clearly seen in the data presented in this study.

3. Effects of Input Ion-optic Voltages.

A schematic diagram of the current input ion optics of the SCIEX ELAN is shown in Figure 2.6. These lenses are located after the skimmer and before the quadrupole. There are four pushbutton indexing switches, labeled B, S2, P and E1, accessible to the user. These correspond to the bessel box barrel (0 to +10 V), the photon stop (0 to -20 V), the bessel box plates (0 to -60V) and

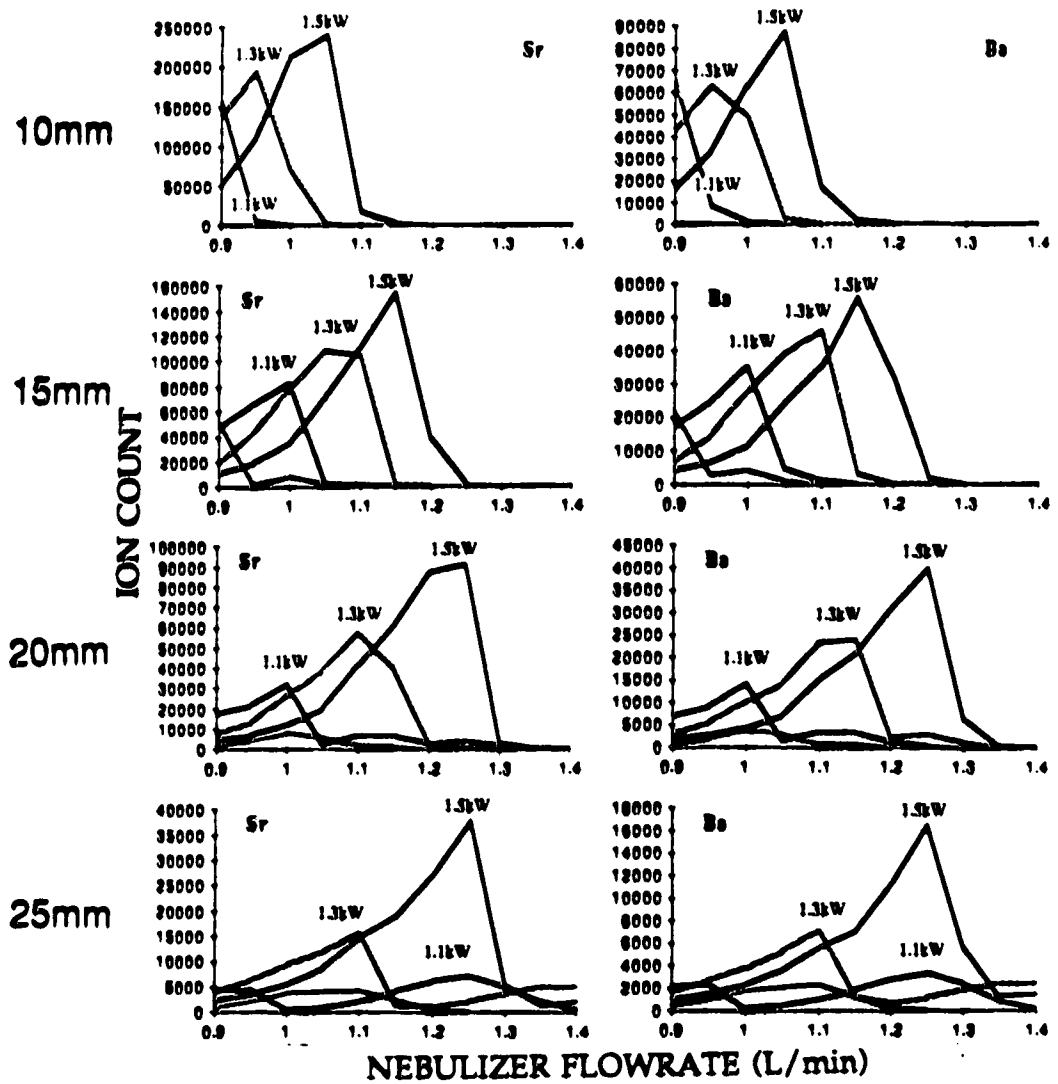

Figure 2.5 Nebulizer flowrate - power parameter behaviour graphs for Sr^+ and Ba^+ at sampling depths of 10, 15, 20 and 25 mm; power in kW shown on each line

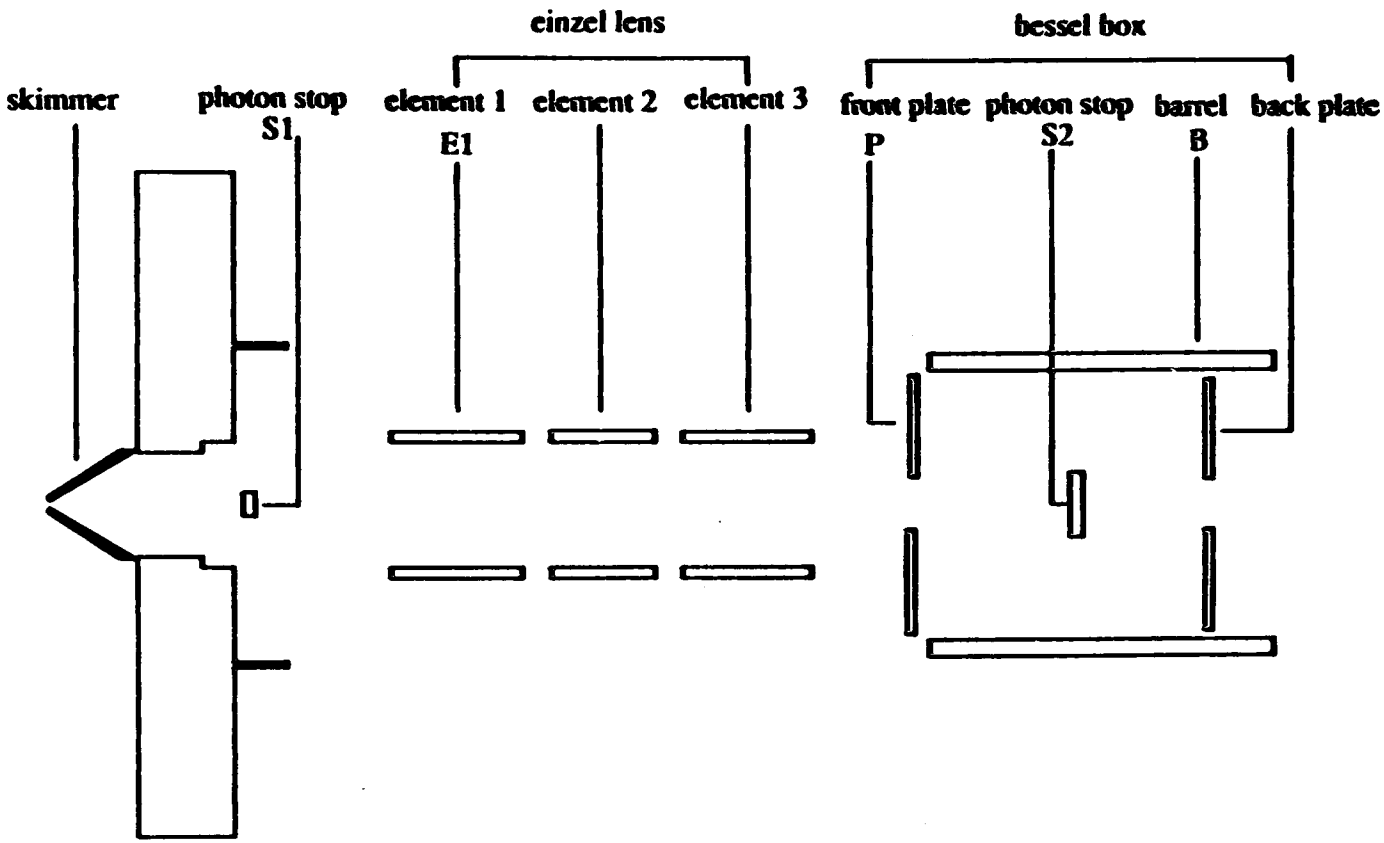

Figure 2.6 Schematic diagram of the input ion optics of the SCIEX ELAN.

cylinders 1 and 3 of the einzel lens (0 to -20 V), respectively. E2, the supply for the center cylinder of the einzel lens is not accessible to the user with an indexing switch but is set by the manufacturer at -130 V.

The change in analyte signal upon changing the voltage of each of the four accessible ion lenses was measured for a set of nine elements covering a range of atomic masses. The elements chosen were Ti, Ni, As, Zr, Pd, Sb, Hf, Pt and Bi, ranging in atomic mass from 48 to 209 amu. Plots of ion count versus einzel-lens potential for these nine elements are shown in Figure 2.7. The einzel lens potential is the voltage on cylinders 1 and 3 of the einzel lens. For the elements Ti to Sb, in the voltage range available, the more negative the potential applied to the lens, the larger the resultant ion count. The plots for the heavier elements, Hf, Pt and Bi have more curvature. The signal increases with increasingly negative voltages to a particular point and then starts to decrease. The discriminating effect of this lens to ions of different masses is not too severe and, in general, a compromise setting of -16 V on the einzel lens has been used.

A set of graphs of ion count versus bessel box plate voltage is shown in Figure 2.8. All of these graphs have a distinct peak shape with the peak maxima occurring at less negative voltages for the singly charged ions of higher mass. Titanium, for example, has a maximum ion count at -21 V while Hf has a maximum at -15 V and Bi at -12 V. For work where the sensitivity of the instrument does not have to be pushed to the limit and a group of elements covering a wide range of masses are of interest, a compromise voltage such as -18 V is satisfactory on the plate voltage.

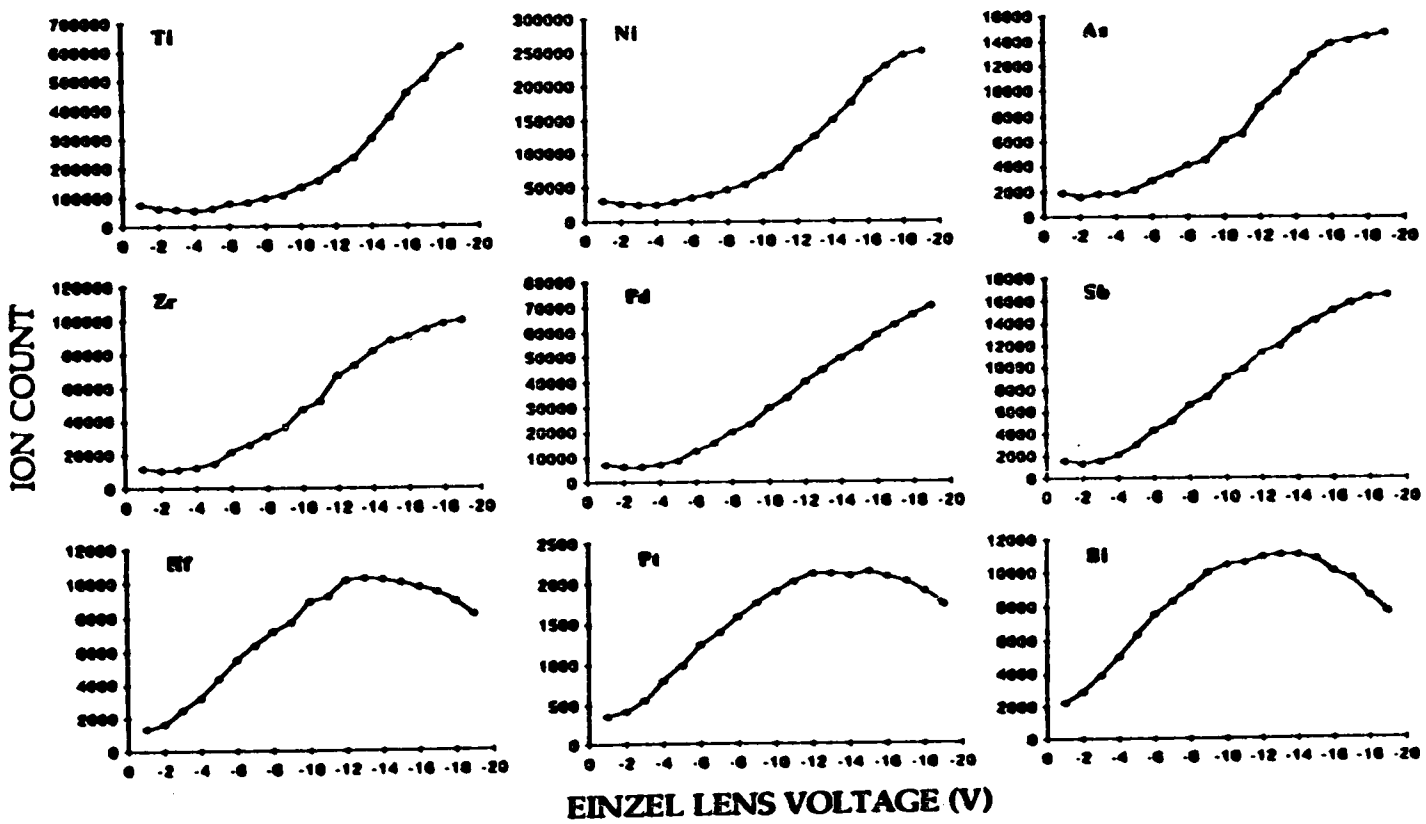

Figure 2.7 Dependence of ion count on einzel-lens voltage for Ti^+, Ni^+, As^+, Zr^+, Pd^+, Sb^+, Hf^+, Pt^+ and Bi^+.

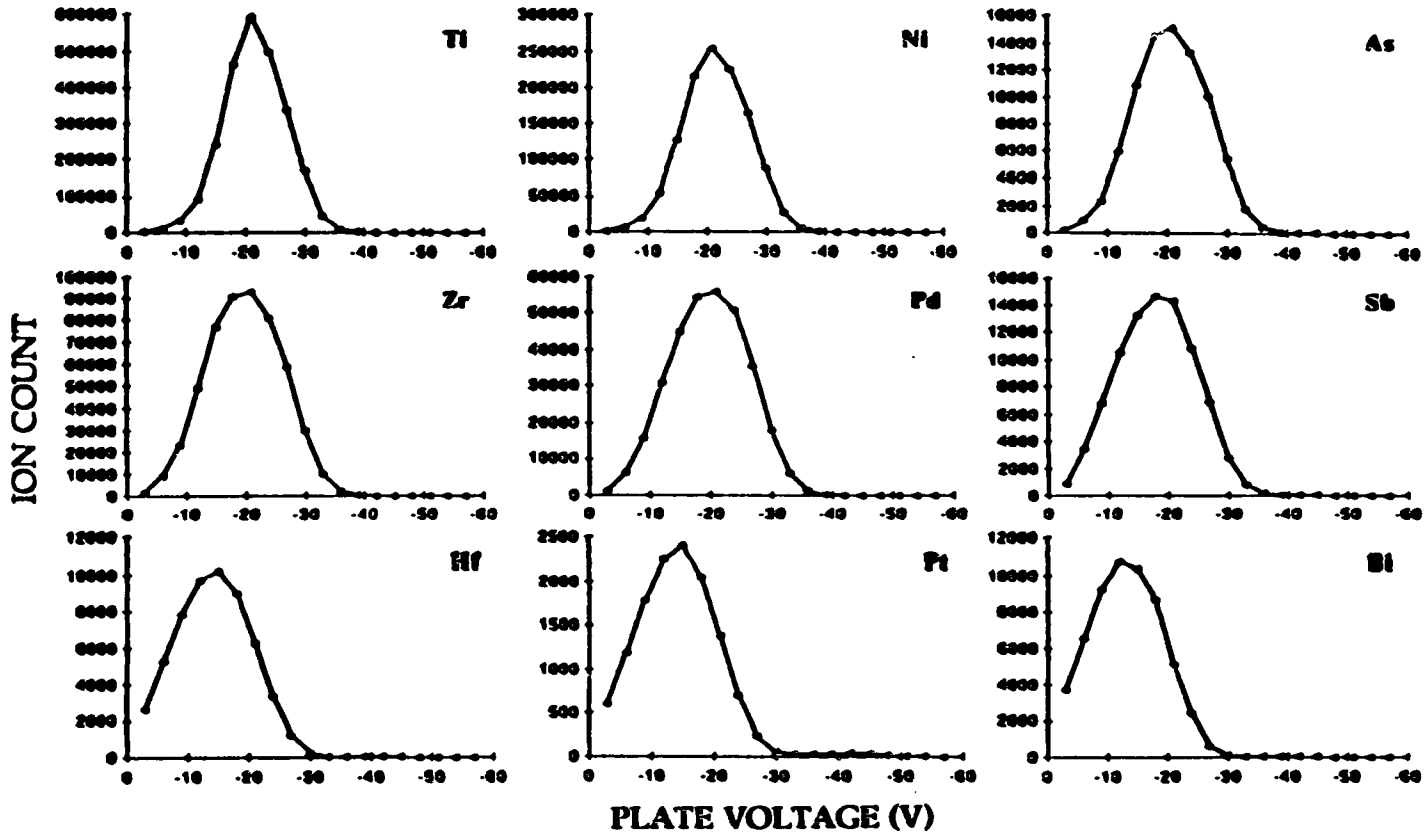

Figure 2.8 Dependence of ion count on bessel box plate voltage for Ti^+, Ni^+, As^+, Zr^+, Pd^+, Sb^+, Hf^+, Pt^+ and Bi^+.

The effect of the bessel box barrel voltage on the ion signal is presented in Figure 2.9. The curves are broader than the peaks obtained for the bessel box plate voltage. The maxima for this group of elements occur over a voltage range from 3 to 5.5 V. The peaks are fairly broad at the top with only small changes in ion count at ±0.5V of the maximum. The peaks appear broader for the higher relative atomic mass elements such as Bi or even Sb, compared with the peaks for Ti and Ni. A compromise condition for this lens over a wide range of masses is more difficult. It may be desirable to deal with two sets of lens settings in a particular analysis, one for the lower masses and one for the higher masses. For most of this work a compromise setting of 5 V was chosen which favoured the heavier elements at the expense of only the light elements such as Ti and Ni. This seemed the best choice as our ICP mass spectrometer displays a high sensitivity for elements such as Ti, Cr and Ni and therefore some sacrifice in the ion count for these elements was acceptable in this work.

The final lens to be dealt with, and perhaps the one most sensitive to mass, is the photon stop inside the bessel box. The graphs of ion count versus photon stop voltage are shown in Figure 2.10. As with the bessel box barrel, the curves in this figure are peak shaped with narrower peaks for elements of lower atomic mass. Maximum signals are obtained at a lens voltage of -8 V for the elements in the first row in the figure. This voltage is an adequate choice for the elements in the second row as well. The third row elements, Hf, Pt and Bi require a voltage of 11 V on the photon stop to reach maximum signal. If these elements are determined at a photon stop voltage of -8 V, the signal for Hf is down to 62% of the maximum signal while Bi is down to 45%. Power - flowrate experiments of the type shown in Figures 2.1 and 2.2 were

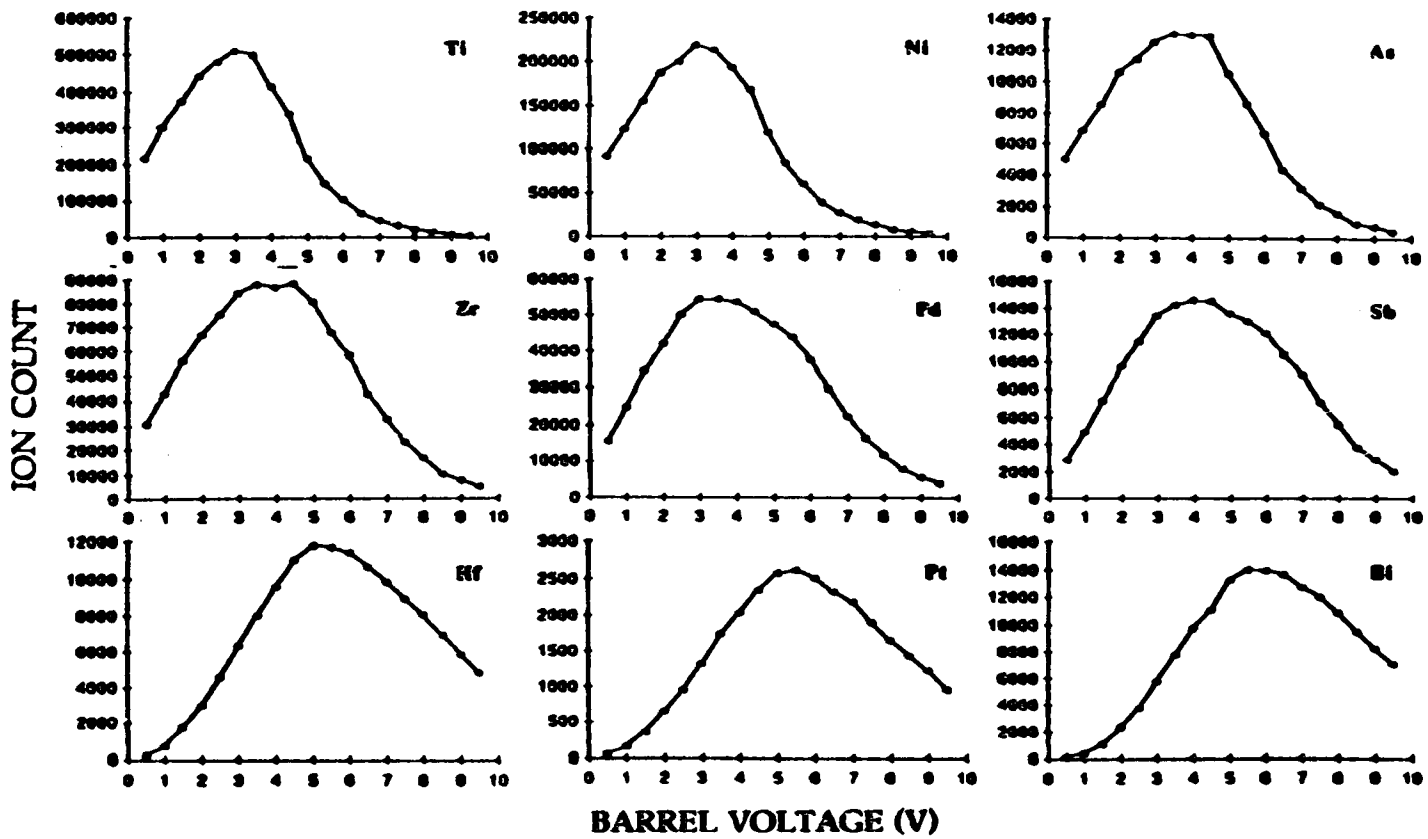

Figure 2.9 Dependence of ion count on bessel box barrel voltage for Ti^+, Ni^+, As^+, Zr^+, Pd^+, Sb^+, Hf^+, Pt^+ and Bi^+.

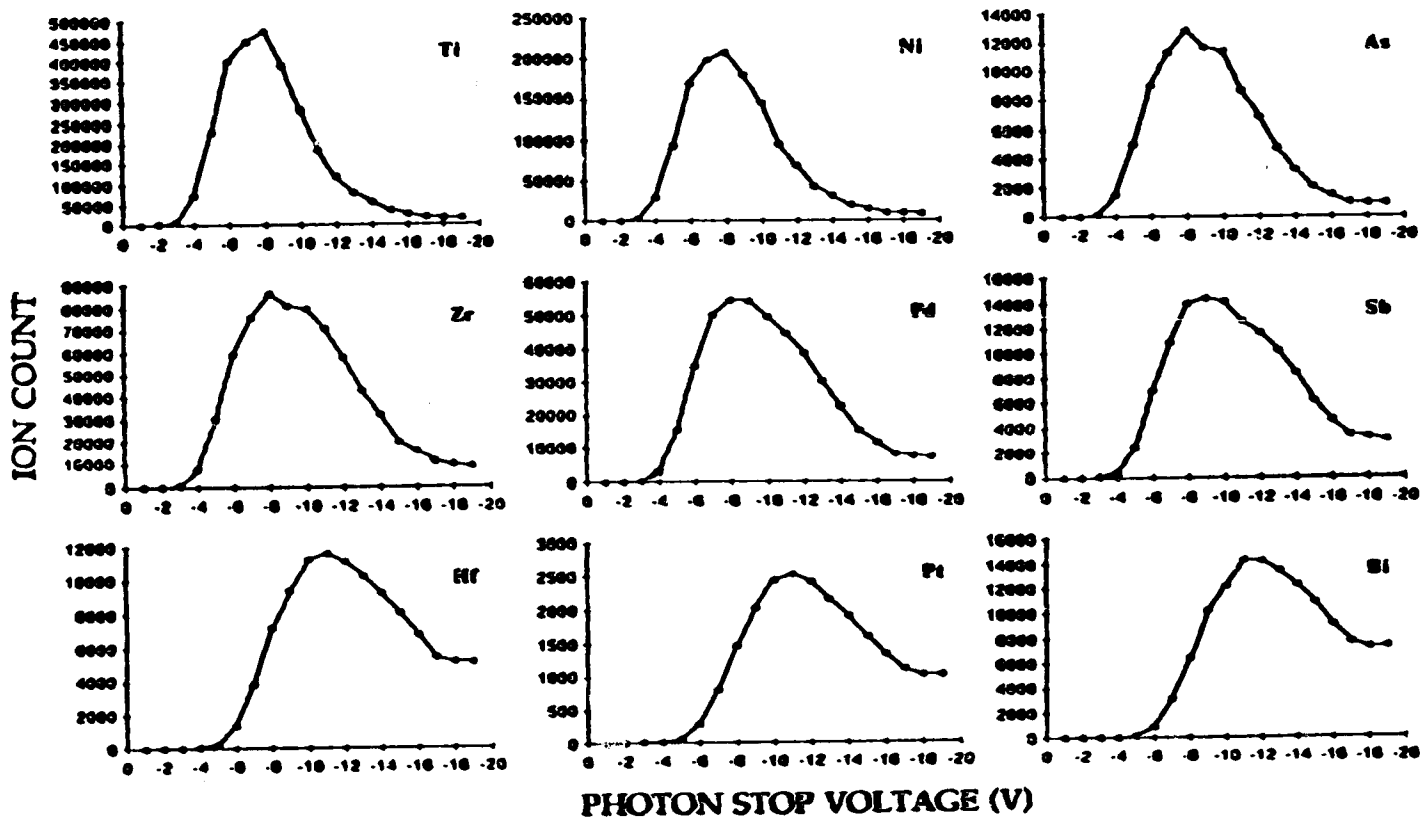

Figure 2.10 Dependence of ion count on the photon stop voltage for Ti^+, Ni^+, As^+, Zr^+, Pd^+, Sb^+, Hf^+, Pt^+ and Bi^+.

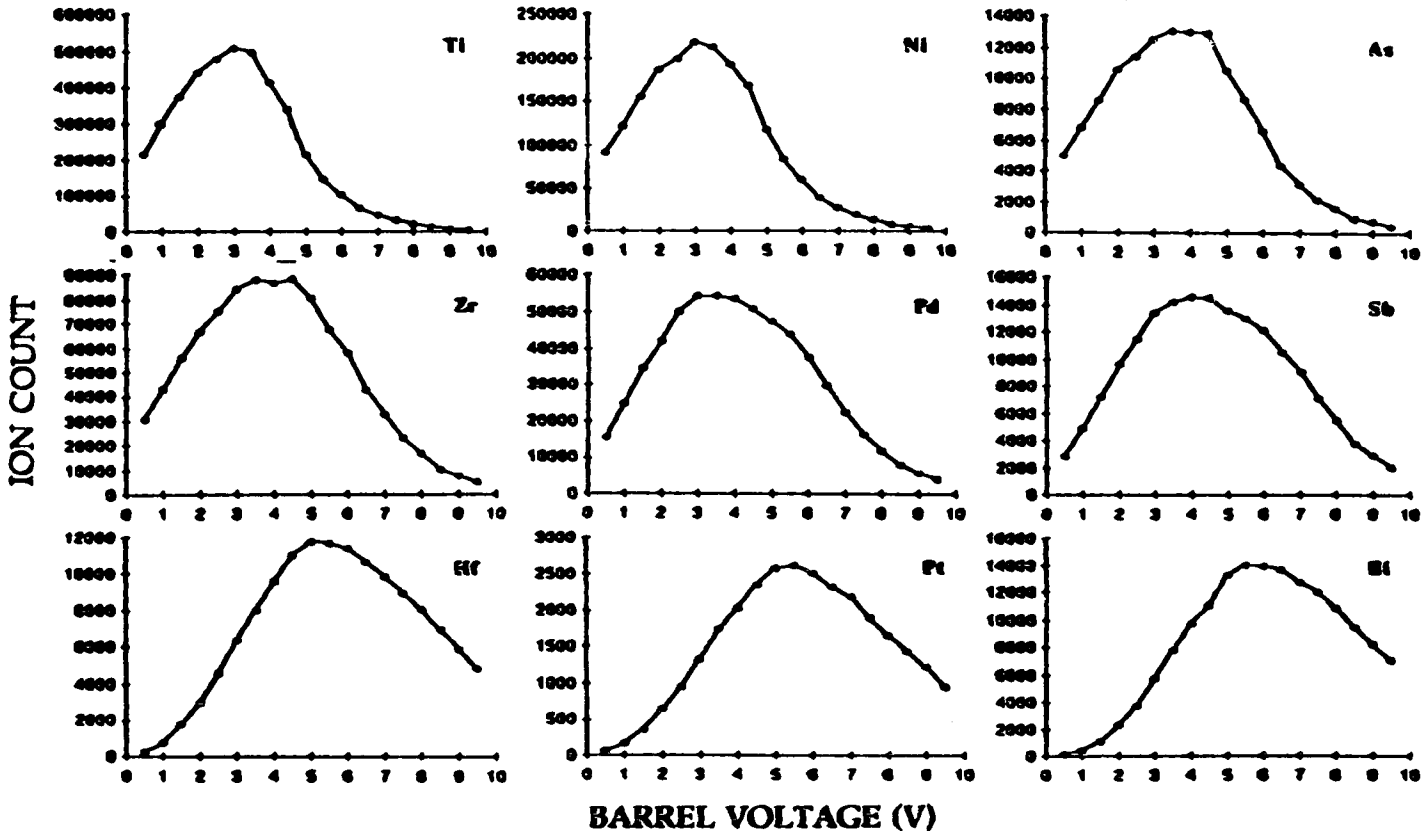

Figure 2.9 Dependence of ion count on bessel box barrel voltage for Ti^+, Ni^+, As^+, Zr^+, Pd^+, Sb^+, Hf^+, Pt^+ and Bi^+.

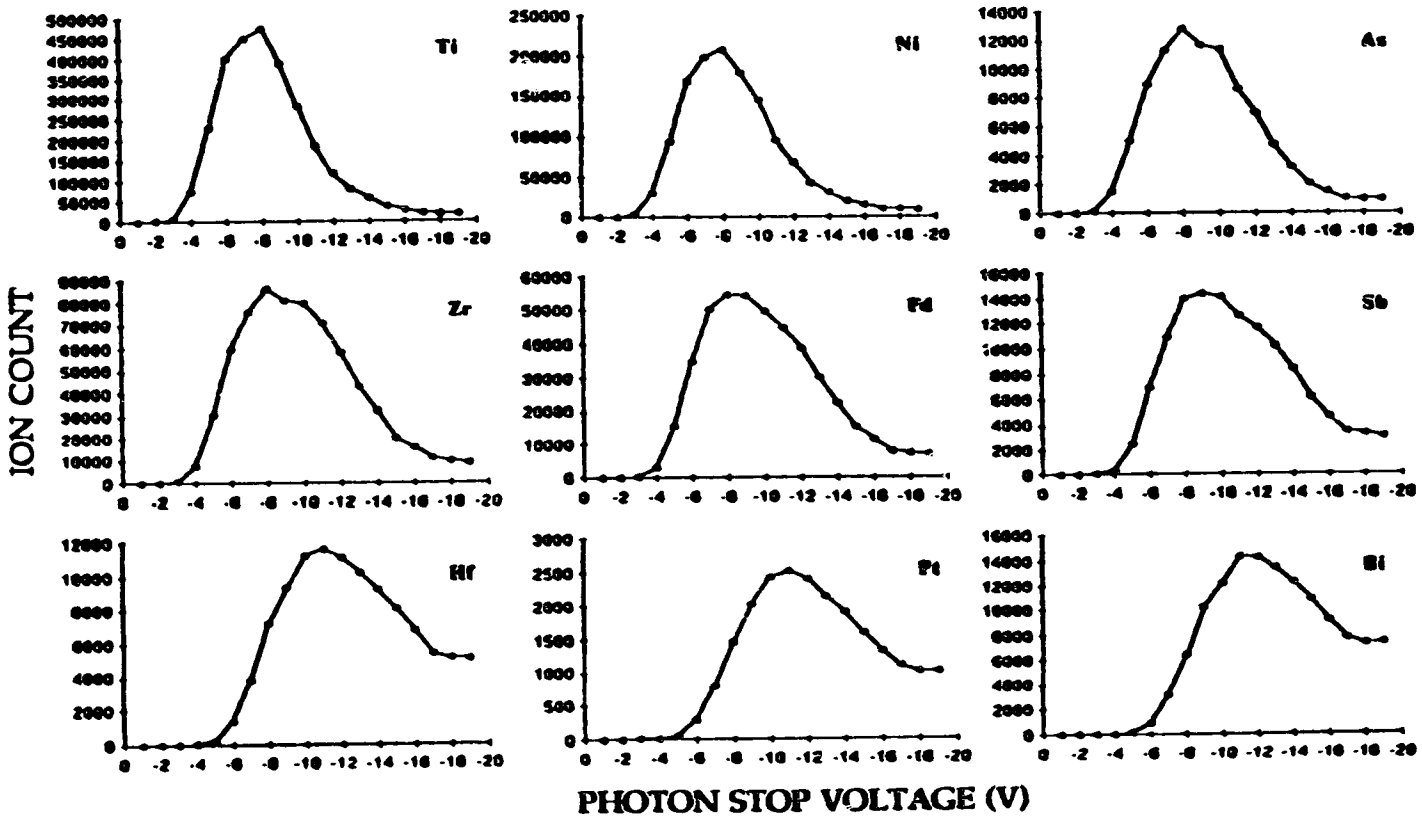

Figure 2.10 Dependence of ion count on the photon stop voltage for Ti^+, Ni^+, As^+, Zr^+, Pd^+, Sb^+, Hf^+, Pt^+ and Bi^+.

carried out at different photon stop voltages. The results for Ti, Pd and Bi at photon stop voltages of -9, -11 and -13 V are presented in Figure 2.11. The absolute ion count obtained for a given element changed depending on the voltage setting, and the position of the peak shifted along the flowrate axis, but the over-all shape of the parameter behaviour graph remained much the same as shown in Figures 2.1 and 2.2. Similar data for the effect of lens voltages on analyte signals have recently been published by Schmit and Chtaib [6].

The evidence suggests that the bessel box barrel voltage and the photon stop voltage are the two voltages that cause the greatest mass discrimination. For ultra-trace analysis, where the maximum sensitivity of the ICP mass spectrometer must be exploited, there is probably no good compromise setting on the lenses for analysis over a wide mass range. It is quite possible, however, to set up two or possibly three sets of conditions and to carry out the analyses over a more limited mass range.

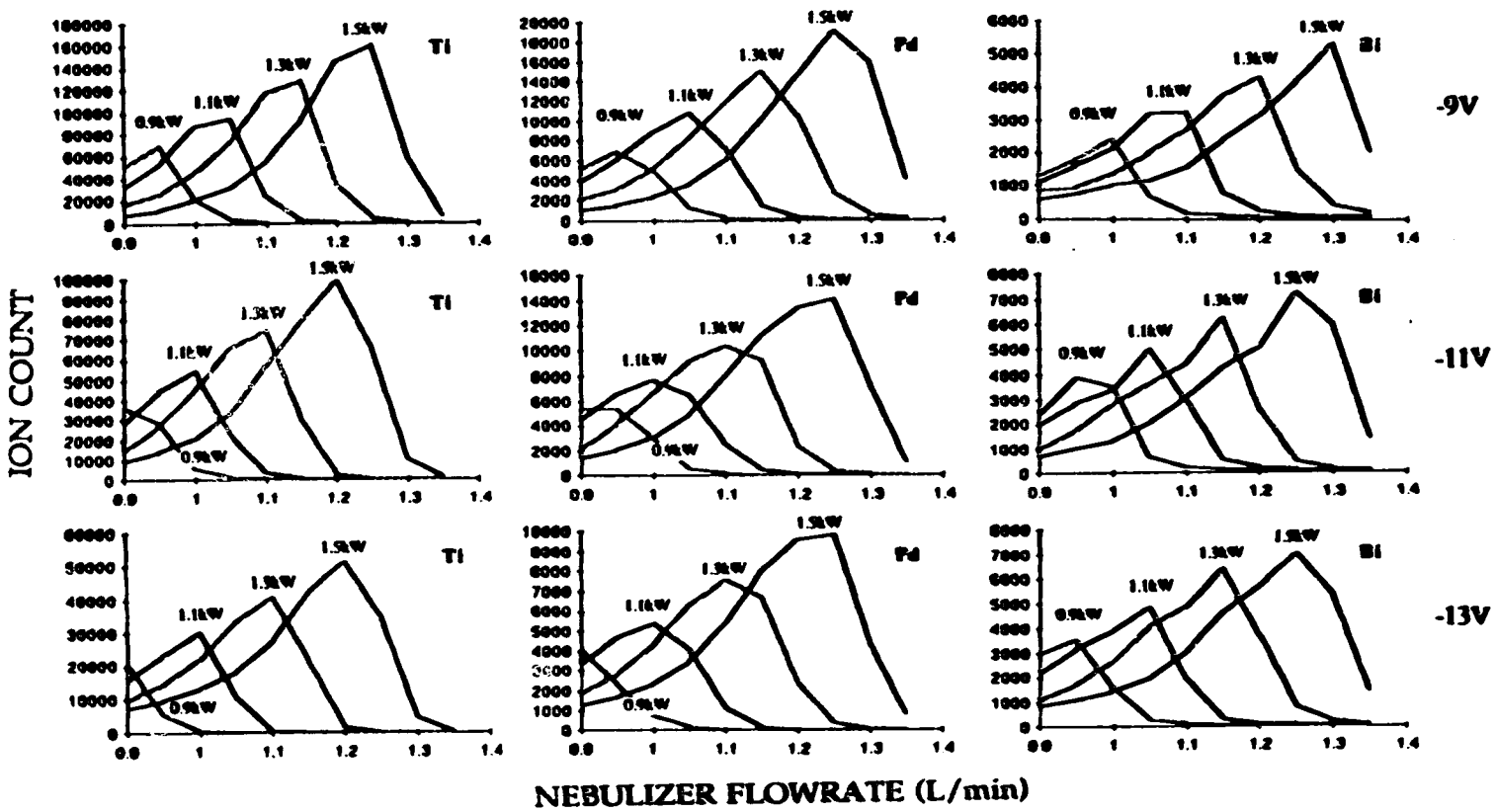

Figure 2.11 Nebulizer flowrate - power parameter behaviour graphs for Ti^+, Pd^+ and Bi^+ at photon stop voltages -9V, -11V and -13V. Power in kW shown on each line.

Conclusions

Considering the results presented here, some conclusions can be drawn about choosing appropriate operating conditions for a particular analysis. A sampling depth of 15 mm from the load coil is a good choice. Sampling further out, 20 or 25 mm, does not provide any advantage and signal intensity is sacrificed. Sampling closer to the load coil, at 10 mm for example, while increasing the signal intensity, is likely to shorten the sampler lifetime. Indeed in some instances there is no gain in sensitivity in going to a 10 mm sampling depth. Platinum, for example, yields comparable signal intensities when measured at 1.5 kW and 10 or 15 mm; see Figure 2.4. Higher plasma powers, 1.3 or 1.5 kW, give stronger ion counts; however, in some instances there is no advantage in increasing the power above a certain level. For example, the ion counts for Hf, W and Pt, see Figure 2.1, are no larger at 1.5 kW than those at 1.3 kW. For Ti, Cr and Ni on the other hand, the counts at 1.5 kW are definitely larger. When a forward power for the ICP has been chosen, the flowrate can be adjusted for maximum signal intensity. Whether the flowrate that provides the maximum signals is the best choice for analysis is not known. It is known [5] that working at lower flowrates can reduce oxide formation but how this choice of flowrates affects precision and signal to noise ratios has not yet been determined.

A compromise condition involving the lens voltages is more difficult to achieve. The mass discrimination displayed by the bessel box barrel and the photon stop limits the mass range over which the analyses can be performed

if maximum sensitivity is required. The best choice for the voltages on the ion lenses will depend on the analysis to be carried out.

Finally, while this study has focused on the SCIEX ELAN ICP-MS instrument it should be noted that similar studies have been carried out on the VG PlasmaQuad. In particular, the studies by Zhu and Browner [7] and by Gray and Williams [8] indicate that the nebulizer flowrate - power parameter behaviour of the two instruments is relatively similar for analyte ion signals.

References

1. G. Horlick, S.H. Tan, M.A.Vaughan and C.A. Rose, Spectrochim. Acta, **40B**, 1555-1572, (1985).

2. S.R. Koirtyohann, J.S. Jones, C.P. Jester and D. A. Yates, Spectrochim. Acta, **36B**, 49-59, (1981).

3. D.W. Boomer and M.J. Powell, Can. J. Spectrosc., **31**, 104-109, (1986).

4. G. Gillson and G. Horlick, Spectrochim. Acta, **41B**, 1323-1346, (1986).

5. M.A. Vaughan and G. Horlick, Appl. Spectrosc., **40**, 434-445, (1986).

6. J. P. Schmit, and M. Chtaib, Can. J. Spectrosc., **32**, 56-60, (1987).

7. G. Zhu and R.F. Browner, Appl. Spectrosc., **41**, 349-359, (1987).

8. A. L. Gray and J.G. Williams, J. Anal. Atom. Spectrom., **2**, 599-606,(1987).

Chapter 3

Oxide, Hydroxide, and Doubly Charged Analyte Species in Inductively Coupled Plasma Mass Spectrometry *

Inductively coupled plasma/mass spectrometry (ICP-MS) is a sensitive technique for trace and ultra-trace elemental analysis. In this technique, singly charged elemental analyte ions generated in an ICP are extracted into and measured with a quadrupole mass spectrometer. For a large number of elements, the singly charged elemental analyte ion (M^+) is by no means the only analyte species that is observed. Many elements form mono-oxides (MO^+), some form doubly charged ions (M^{2+}), and some form hydroxide species (MOH^+).

The presence of these species has been noted in a number of papers. Date and Gray [1] reported observing $^{138}Ba^{2+}$ and show spectra for Ba^+, BaO^+, $BaOH^+$, Ba^{2+}, AsO^+, $AsOH^+$, UO^+, and UO_2^+ [2]. They also reported the presence of ThO^+ [3]. Houk and Thompson [4] reported seeing Sr^{2+}, $SrOH^+$, and PrO^+, UO^+, and UO_2^+. They also discussed the formation of MO^+ and MOH^+ species in general. Gray and Date [5] reported the formation of rare earth oxides, in particular HoO^+, TmO^+, and LuO^+. The behaviour of Sr^{2+}, Ba^{2+}, MoO^+, WO^+, and CeO^+ with power and nebulizer flowrate was discussed by Horlick et al. [6]. Douglas and Houk measured ThO^+/Th^+, Ba^{2+}/Ba^+, and UO^+/U^+ ratios and discussed the potential of MO^+

---

* A version of this chapter has been published. M. A. Vaughan and G. Horlick, Applied Spectrosc. 40, 434-445, (1986).

interferences in ICP-MS [7]. They suggested CeO^+ as one of the worst-case ions for oxide formation. Houk et al. [8] used M^{2+}/M^+ ratios of Sr and Ba in Saha-type calculations for the ICP. They included spectra of Sr^{2+}, $SrOH^+$, Ba^{2+}, and $BaOH^+$ in their work. In addition, analogous species have been reported in the spark source mass spectrometer literature by Bacon and Ure [9]. This is a particularly interesting paper dealing with interelement oxide corrections in the determination of the rare earth elements.

In ICP-MS these species are important from several points of view. Perhaps the most important aspect is that analyte oxide species may result in serious spectral interferences at other analyte ion masses. For example, Ti has five naturally occurring isotopes: ^{46}Ti (7.99%), ^{47}Ti (7.32%), ^{48}Ti (73.98%), ^{49}Ti (5.46%), and ^{50}Ti (5.25%). The corresponding oxide species (^{16}O) at masses 62, 63, 65, 65, and 66 result in spectral interference problems for ^{62}Ni, ^{63}Cu, ^{64}Zn, ^{65}Cu, and ^{66}Zn, respectively. This is but one of literally hundreds of potential spectral interference problems involving oxide species. As well as this obvious interference, which results in falsely high values for the element that is overlapped by an oxide species, there can be another problem. Isobaric corrections are frequently required in ICP-MS when the chosen mass of a sought-for element suffers a spectral overlap caused by a naturally occurring isotope of another element. Normally, an interference-free isotope of the interfering element is measured and, based on its signal level and the natural-abundance information of the interfering element, a correction can be calculated to be applied at the mass of the sought-for element. However, the presence of oxide species from a third element could cause non-applicable and inappropriate isobaric corrections to be implemented.

The species distribution of an analyte among several forms is also important from a pragmatic point of view. For best sensitivity it is desirable to set conditions so that the analyte is all in one form, the singly charged elemental ion, M^+. To the extent that other species are formed, analyte sensitivity is reduced.

Finally, investigation of analyte species distribution is important with respect to fundamental studies of the plasma discharge. Are the M^{2+}/M^+ and MO^+/M^+ ratios that can be measured by ICP-MS accurately representative of the plasma discharge and thus usable for theoretical calculations? Or, are these ratios altered in the sampling process and, hence, misleading about the unperturbed conditions in the ICP? These are not easy questions to answer, but characterization of analyte ion species distribution in the ICP by ICP-MS may provide some answers.

In this study the distribution of analyte among singly charged element ions (M^+), mono-oxide ions (MO^+), hydroxide ions (MOH^+), and doubly charged ions (M^{2+}) is reported as a function of ICP-MS operating conditions. The key parameters varied include ICP power, nebulizer flowrate, and sampling depth. The elements Sr and Ba are used to illustrate the basic behaviour of these analyte species. Although they are not particularly strong oxide-forming elements in ICP-MS, they do form, to some extent, all of the listed species (M^+, M^{2+}, MO^+, and MOH^+) and are generally illustrative of the dependence of species distribution on ICP-MS measurement conditions. However, data are also presented for Ti, W, and Ce, as oxide formation is a greater problem with these elements than it is with Sr and Ba.

In addition, a major component of this chapter is the presentation of extensive tables documenting the potential spectral interference problems that could arise from MO^+, MOH^+, and M^{2+} species in ICP-MS. Two table formats are presented. One table is presented in terms of increasing mass of the sought-for element, with the MO^+, MOH^+, and M^{2+} interferences listed adjacent to each mass. This allows identification of a potential interference at a given mass. The second table is grouped in terms of the interfering element. This format allows identification of the elements which could suffer interference from the species of a particular matrix element.

Experimental

A SCIEX ELAN Model 250 ICP-MS was used for all data acquisition. It was run in sequential mode, at low resolution (1 amu width at base of peak), peak hopping to masses of interest except during the acquisition of spectra. A Meinhard nebulizer and a Scott spray chamber were used. The extended torch supplied with the instrument was replaced with a standard-length torch to allow sampling of the plasma closer to the load coil. Sampling distances used were 15 mm, 20 mm, and 25 mm between sampler tip and load coil. All data were taken at 15 mm unless otherwise stated. The coolant flow rate was 11 L/min of Ar for all work. The nebulizer and auxiliary gas flow rates were controlled by Matheson Model 8240-0423 mass flow controllers. The Ar flowrate for the auxiliary gas was 1.4L/min, while the flowrate for the nebulizer gas, also Ar, was varied from 0.9 L/min to 1.45 L/min. A copper sampler was used, fashioned after the nickel sampler supplied by SCIEX, and had a 0.94mm orifice. The solutions used were prepared from SPEX

Industries, Inc. standard solutions and were diluted with deionized water to the desired concentrations.

Results and Discussion

1. Ba and Sr Species Distribution in ICP-MS.

Previous work in ICP-MS [6] on the dependence of analyte ion signals on plasma operating conditions has indicated that plasma power, nebulizer flowrate, and sampling depth are the major parameters to consider. In particular, plots of signal (ion count) as a function of nebulizer flowrate at a family of different powers clearly illustrate trends in behaviour. Four such plots are shown in Figure 3.1 for Ba^{2+}, Ba^{+}, BaO^{+}, and $BaOH^{+}$. The data shown for Ba^{+} are typical of that for most analyte ions; at one particular power, the signal peaks as a function of aerosol flowrate. As power increases, the flowrate value at which the signal is maximized also increases. Interestingly, the associated analyte species have essentially the same basic behaviour. The nebulizer flowrate - power parameter plots for BaO^{+} and $BaOH^{+}$ are very similar to that of Ba^{+} except that the signals peak at successively higher nebulizer flowrates when compared at the same power. On the other hand, the Ba^{2+} plots are shifted to lower nebulizer flowrates.

The ion count for the Ba species as a function of nebulizer flowrate is shown in Figure 3.2 for one power setting (1.3 kW). The correct relative ion counts are plotted in the upper figure, and in the lower figure they have been normalized. It is clear from the data presented in Figure 3.2 (a) that under most conditions the singly charged ion, Ba^{+}, is the major analyte species. Only at high nebulizer flowrates do the oxide and hydroxide species dominate. The

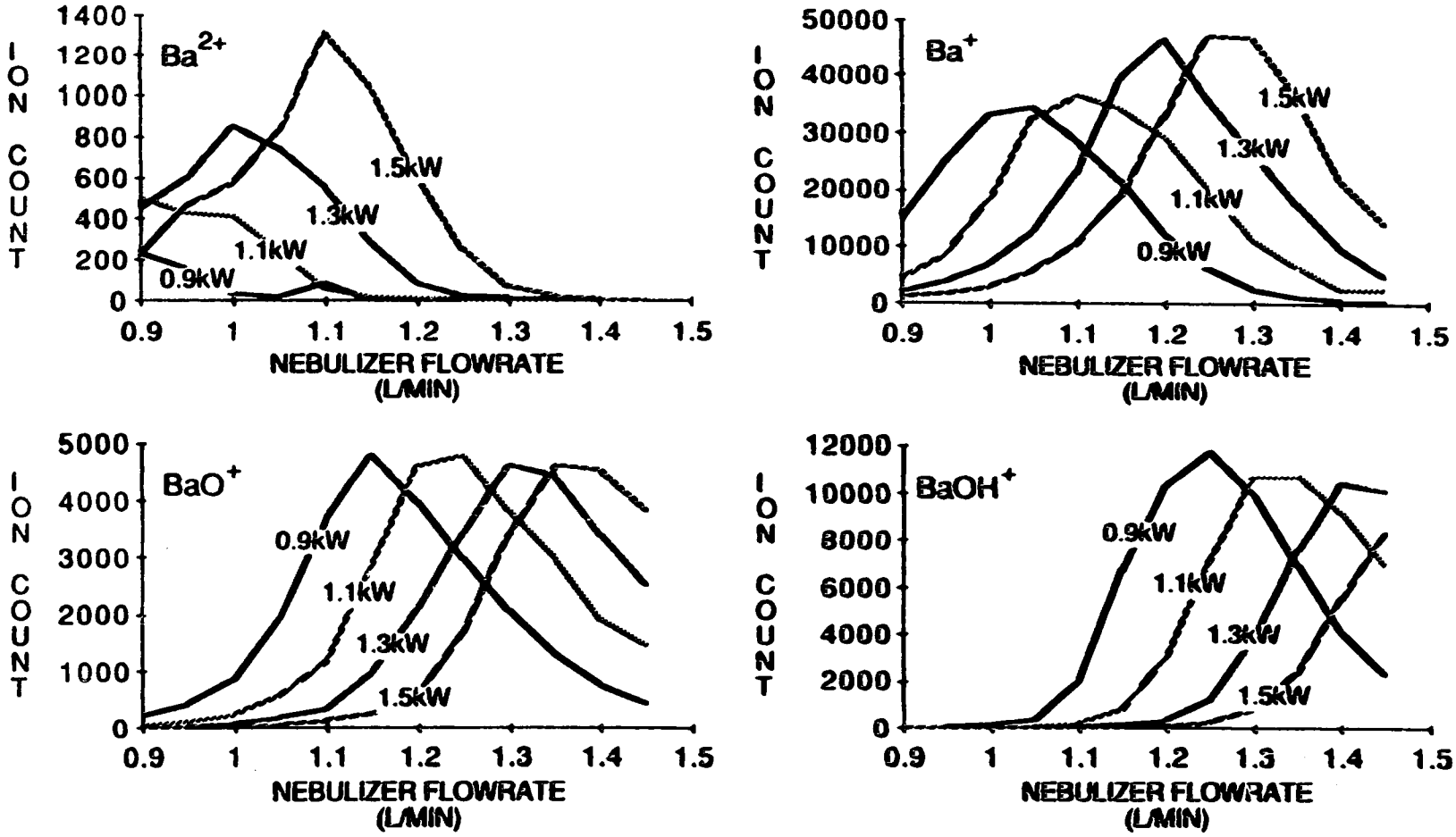

Figure 3.1 Dependence of ion count on nebulizer flowrate at various powers for Ba^{2+}, Ba^{+}, BaO^{+}, and $BaOH^{+}$.

crucial role of nebulizer flowrate in controlling the relative distribution of the analyte species is emphasized by the normalized plot shown in Figure 3.2 (b). With this representation, it is easy to see how the population changes as the nebulizer flow rate is increased. At low flowrates, around 1.0 L/min, the doubly charged species reaches a maximum. Increasing the flowrate, the condition for the Ba^+ maximum signal is reached at around 1.2 L/min for this particular power, 1.3 kW. Similarly BaO^+ and $BaOH^+$ reach their maxima at even higher flowrates, around 1.3 L/min and 1.4L/min, respectively. From this it can be seen that it may be impossible or at least very difficult to get minimum oxide counts and a maximum signal for the singly charged ion. It is clear that in order to reduce oxide and hydroxide problems the plasma must be detuned to lower flow rates (i.e., conditions that give sub-optimal M^+ counts). Of course, that may lead to the conditions where the doubly charged ions are formed, but these are not formed to as great an extent, and, in general, fewer elements form detectable doubly charged ions in the plasma than form oxides.

Data similar to that shown in Figures 3.1 and 3.2 have been measured for Sr species distribution, and the results are identical. It should be noted that care must be exercised in measuring the parameter behaviour of low abundance species such as Ba^{2+} and Sr^{2+} in order that they are not confused with background species. If Cl is present, a background peak attributable to $^{37}Cl^{16}O^{16}O^+$ appears at mass 69, interfering with the measurement of Ba^{2+}. The background species $^{12}C^{16}O^{16}O^+$ can cause similar problems when one is attempting to measure Sr^{2+} at mass 44. These and other background species have been documented by Tan and Horlick [10].

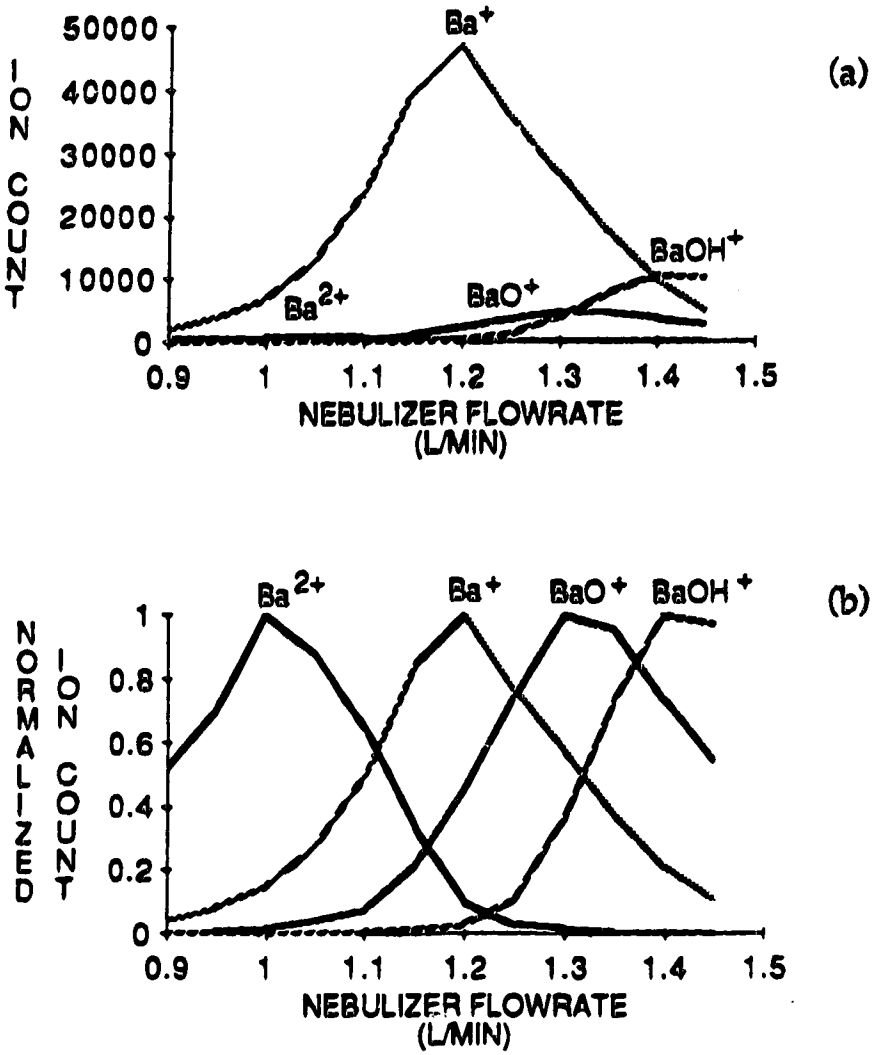

Figure 3.2 Relative (a) and normalized (b) plots of ion count vs. nebulizer flowrate at 1.3 kW for Ba^{2+}, Ba^{+}, BaO^{+}, and $BaOH^{+}$.

As indicated at the beginning of this section, sampling depth (distance of mass spectrometer sampling cone from the load coil) is also an important experimental parameter. Some depth data are shown in Figure 3.3 for the Ba species. These plots show signal level as a function of nebulizer flowrate at three different depths: 15 mm, 20 mm, and 25 mm from the load coil. At a sampling depth of 15 mm, the signal shows a peak response at a particular flowrate; and, at greater sampling depths, the flowrate must be increased to again maximize the signal count, not unlike a power family plot. At greater sampling depths, the peak signal response for all species but Ba^{2+} appears to be shifted off scale to a larger nebulizer flowrate than that tested in this work. The basic trend that can be perceived for the behaviour at 20 mm and 25 mm is, however, similar to that observed at 15 mm.

A performance rating often reported in the ICP-MS literature is the ratio of an oxide count to that of the singly ionized species (MO^+/M^+), from the viewpoint that the smaller the ratio the less that oxide species will present a spectral interference problem. Depending on the element, ratios range from about 0.2% to 3%. However, it is clear from the data presented in Figures 3.1-3.3 that such a ratio for one element is very dependent on measurement conditions. The results for the effect on nebulizer flowrate on the x/Ba^+ ratio where $x = Ba^{2+}$, or BaO^+, or $BaOH^+$ are shown in Figure 3.4. These experiments were done at one power, 1.3 kW.

The two ratios BaO^+/Ba^+ and $BaOH^+/Ba^+$ show similar behaviour. The ratios increase nonlinearly as flowrates increase. The BaO^+/Ba^+ starts its rapid increase at a lower flowrate than does $BaOH^+/Ba^+$. This is not surprising; it could be predicted from the combined species plot shown in Figure 3.2. The behaviour of the Ba^{2+}/Ba^+ ratio is opposite to the oxide and

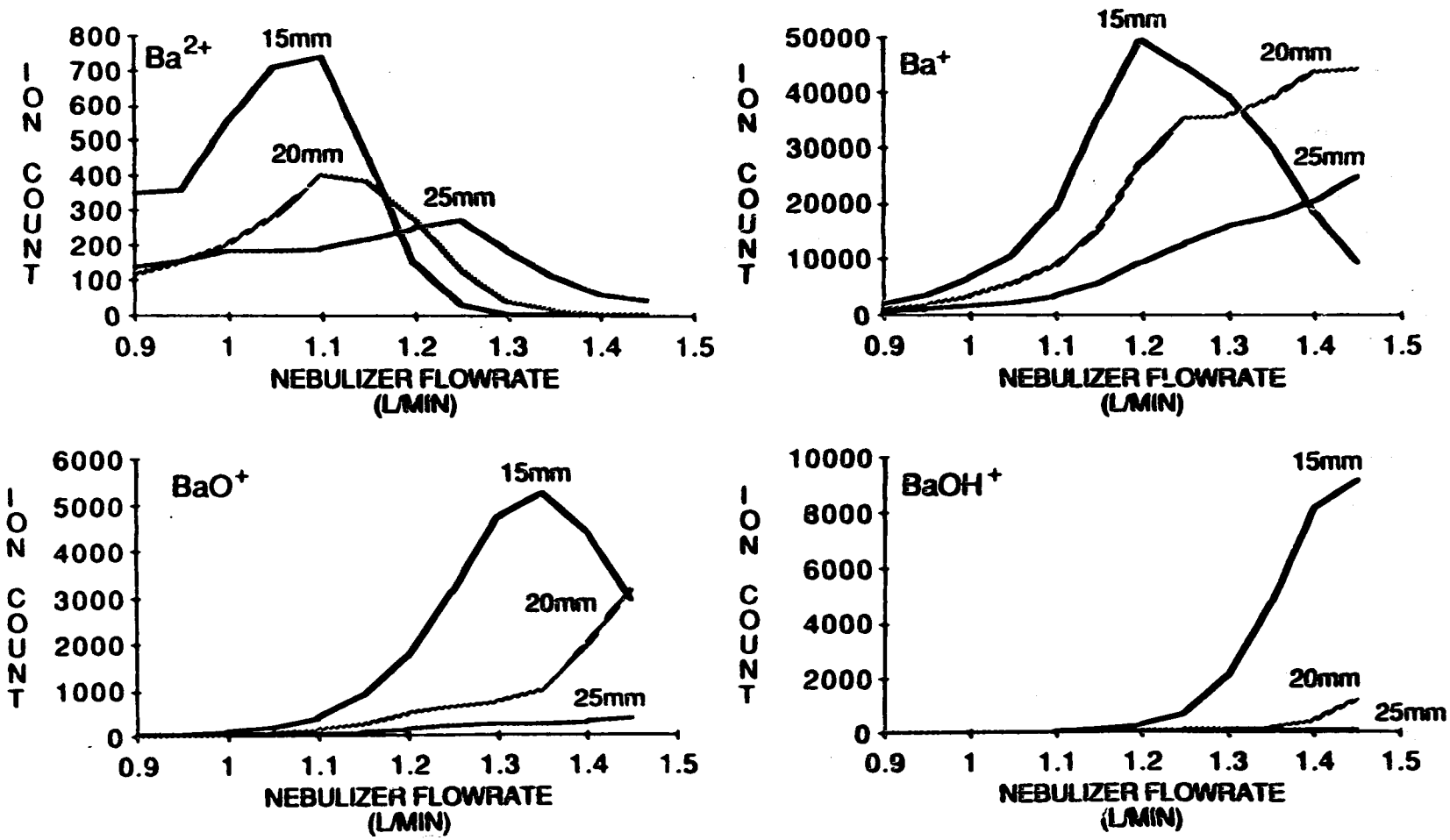

Figure 3.3 Dependence of barium species ion count on nebulizer flowrate at various sampling depths.

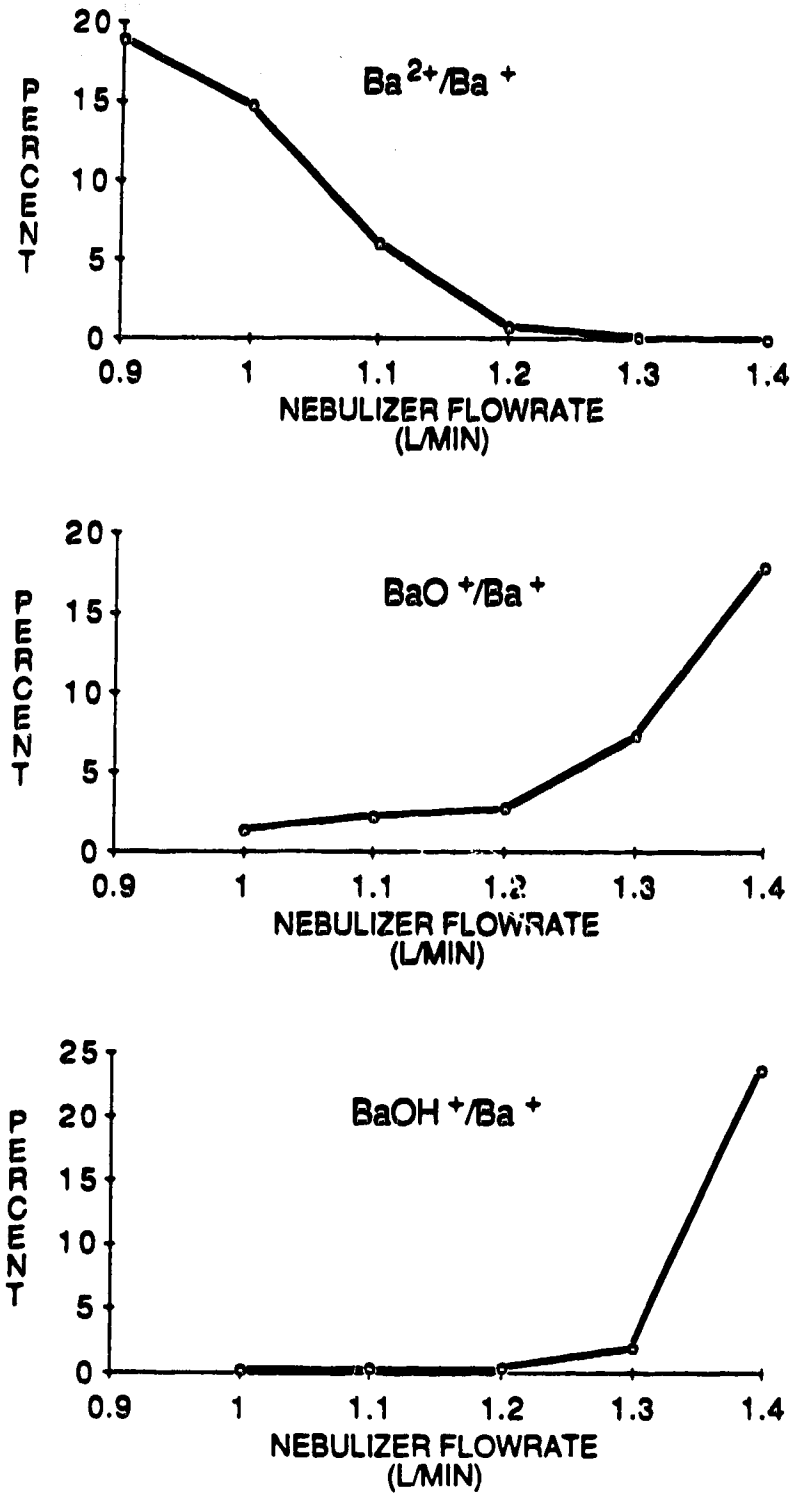

Figure 3.4 Dependence of barium species ratios as a function of nebulizer flowrate at 1.3kW.

hydroxide ratios. The ratio drops off with increasing flowrate, also in a nonlinear fashion.

Perhaps the effect of nebulizer flowrate on these ratios can be explained to some extent by the cooling effect the nebulizer gas has on the plasma. At low flowrates that plasma is hotter and the doubly charged ions are favoured, but not the oxides or hydroxides. As the nebulizer flow is increased, the plasma cools a little, favouring first the oxides and then, finally, the hydroxides.

The second set of ratio graphs, shown in Figure 3.5, consists of x/Ba^+ vs. power at a flowrate of 1.2 L/min. Again, BaO^+/Ba^+ and $BaOH^+/Ba^+$ show similar behaviour, the highest values being at lowest powers and decreasing as the power is increased. Ba^{2+}/Ba^+ vs. power has the opposite sort of trend. The Ba^{2+}/Ba^+ ratio increases with increasing power. This makes sense; the Ba^{2+}/Ba^+ ratio is larger in the higher energy conditions of higher power. Likewise, the oxides and hydroxides prefer the lower powers and less energy, and the BaO^+/Ba^+ and $BaOH^+/Ba^+$ ratios are higher at these lower power settings.

The signals corresponding to Sr and Ba singly charged ions, plus all the associated ions have interesting responses to changes in power, nebulizer flowrate, and sampling depth. The power flowrate plots and ratio graphs are effective summaries of the data, but it is always informative to see spectra of the species being studied. In order to show pictorially just how the ion population changes with power and flowrate, a series of spectra was recorded. From the power and flowrate plots it is obvious that similar things happen at the various power settings if the flow rate is adjusted to the appropriate

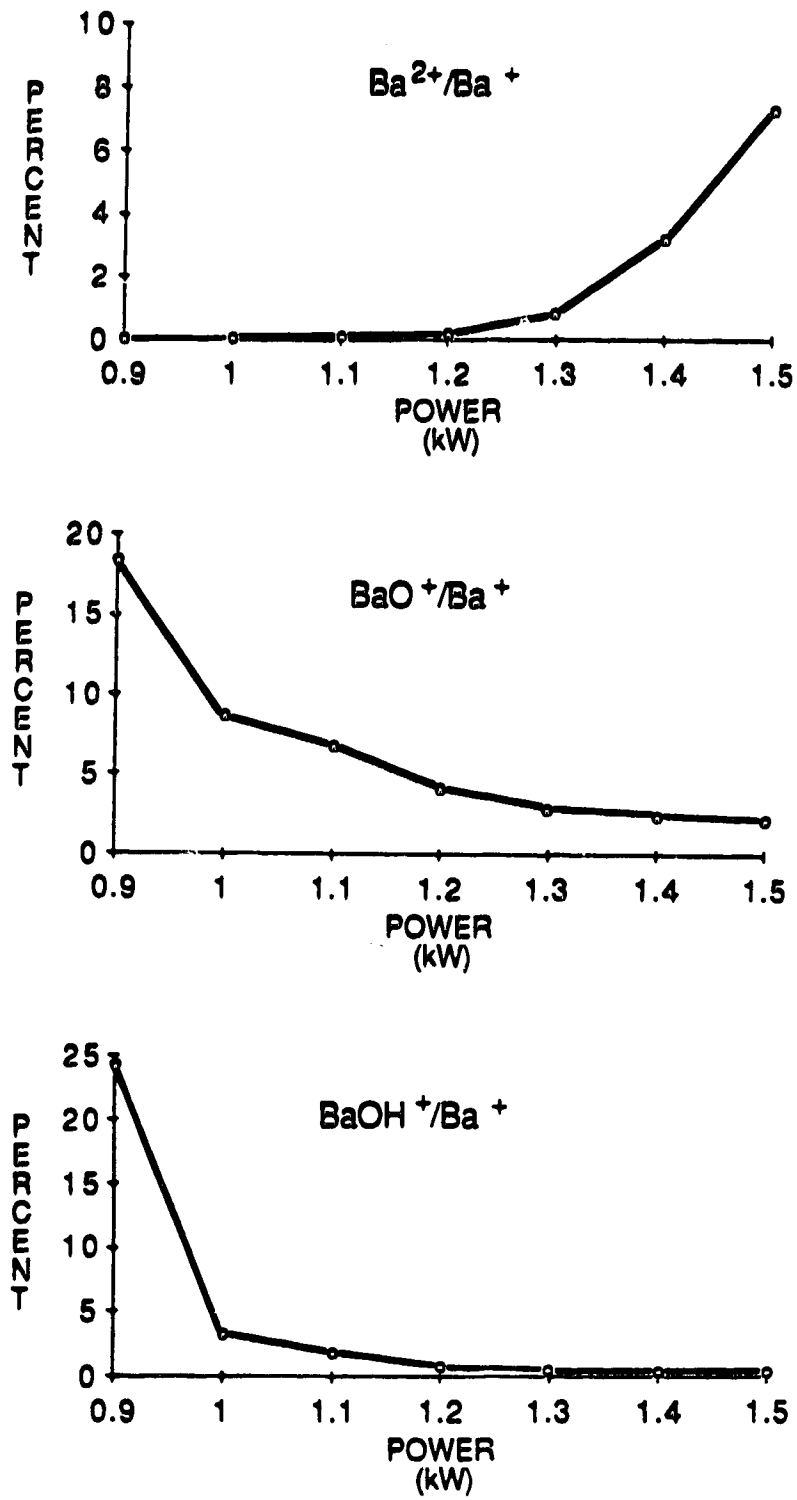

Figure 3.5 Dependence of barium species ratios as a function of power at 1.2L/min.

value. Therefore, spectra were recorded at a variety of flowrates but at only one power, 1.3kW, and sampling depth, 15 mm. Four spectra scanned from m/z 45 to 160 at flowrates of 1.1L/min, 1.2 L/min, 1.3 L/min, and 1.4L/min are shown in Figure 3.6. A 1-μM solution was used for all the spectra. The ion count scale is the same for all four spectra in this figure. At 1.1 L/min the largest peak is the argon dimer, Ar_2^+; Sr^+ and Ba^+ are prominent features in the spectrum; and no peaks for oxides, hydroxides, or doubly charged ions are seen at this scale. Looking at 1.2 L/min, it is easily seen that this is the best flowrate of the four for Sr^+ and Ba^+ signals. The largest ion count is for Sr^+, followed by Ba^+, and the Ar_2^+ peak is significantly lower at this nebulizer flowrate. The oxide peaks are just visible above baseline on this scale. Increasing the flowrate to 1.3L/min or 1.4L/min introduces the hydroxide peaks along with the oxides of Sr and Ba.

The spectra shown in Figure 3.7 focus on Ba^+ and the oxides and hydroxides as they vary with nebulizer flowrate from 1.0 L/min to 1.4L/min at 1.3kW. Once again it is clear that 1.2 L/min is the best flowrate for the Ba^+ signal, with the signal dropping at flowrates higher or lower than 1.2 L/min. As with Ba^+ it can be seen at a glance how the oxide and hydroxide values change with flowrate. This makes it clear that a single value of an oxide ratio is not all that meaningful.

The next set of spectra (Figure 3.8) is an enlargement of the BaO^+ and $BaOH^+$ peaks in Figure 3.7. The overlapping of the oxide and hydroxide peaks is the reason the isotope pattern does not look exactly like that for Ba^+ and why it changes with flowrate. The peak at 1.1 L/min is mainly BaO^+ (m/z = 154), but at higher flowrates all the peaks are BaO^+ plus $BaOH^+$ except for m/z = 155, which is $BaOH^+$. This overlap of associated species can seriously

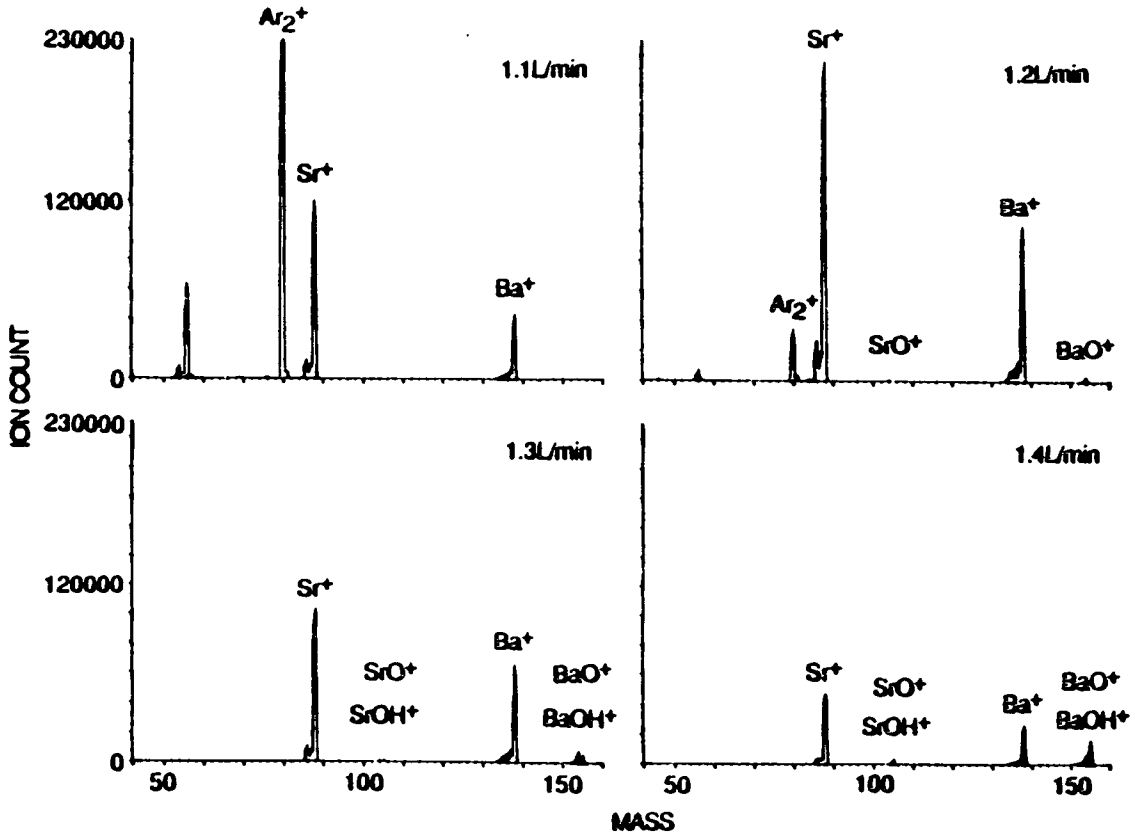

Figure 3.6 Spectra of Ba and Sr species distribution at different nebulizer flowrates.

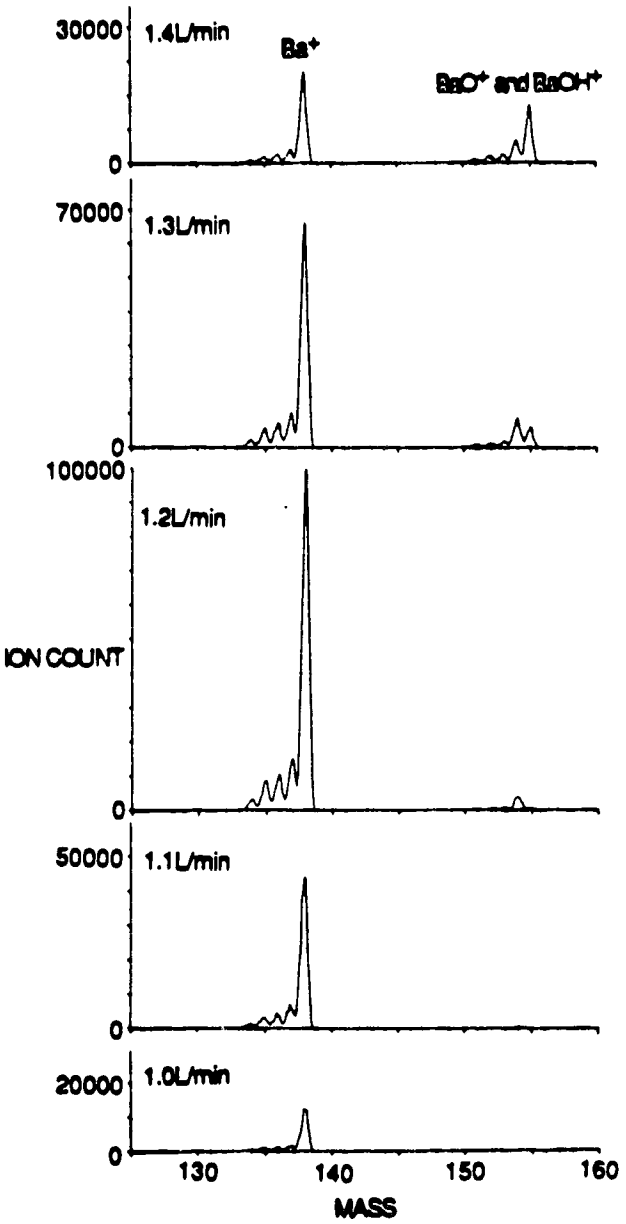

Figure 3.7 Spectra of Ba^+ and $BaO^+/BaOH^+$ species at different nebulizer flowrates.

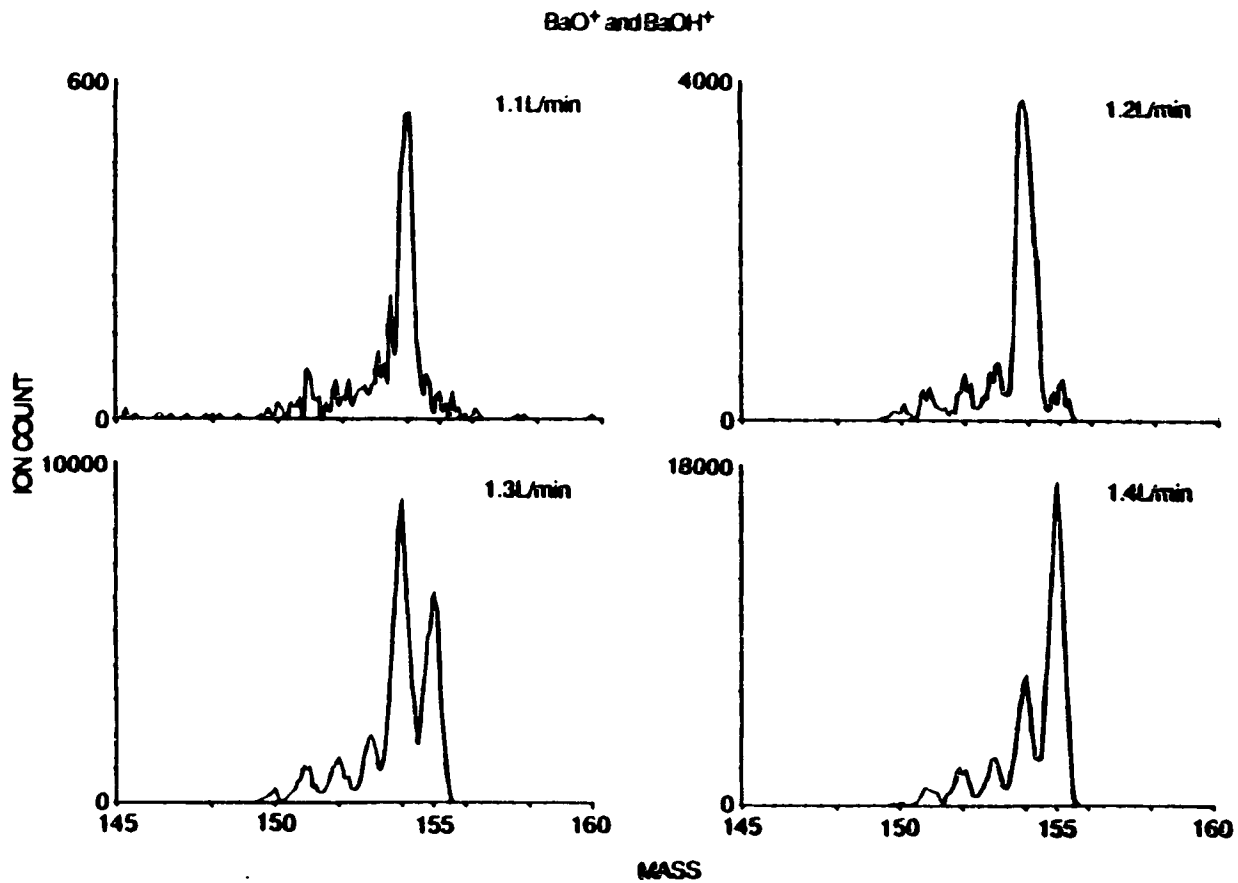

Figure 3.8 Spectra of BaO^+ and $BaOH^+$ species at different nebulizer flowrates.

complicate the calculations needed to correct for these interferences and the measurement of isotope ratios.

2. Species Distribution of Ti, W, and Ce.

A few spectra are presented in this section for Ti, W, and Ce to indicate that the same basic species distribution behaviour exists for most elements, although the degree of formation of specific species varies considerably. The three elements were chosen to represent different sections of the periodic table.

Ti was chosen as an oxide-forming, first-row transition element, and W as an oxide-forming, third-row transition element. Ce was chosen to represent the rare earths, some of which form both doubly charged ions and oxides. These spectra were taken in an argon plasma, 15 mm from the load coil. The power was 1.3kW, the coolant flowrate was 11 L/min, and the auxiliary gas flowrate was 1.4 L/min. A MAK torch was used in a SCIEX ELAN 250 ICP-MS. Appropriate B lens settings for each element were used. B lens settings for Ti and W were 5V and 9V, respectively. For Ce, B lens settings of 7V and 5V were used. All solutions were 1 μg/mL.

The isotope patterns of the M^+ ions are seen for the MO^+, MOH^+, and M^{2+} spectra if the ion counts are high enough. This helps in identifying the associated species. The Ti (Figure 3.9) and W (Figure 3.10) spectra show the oxide peaks becoming larger as the nebulizer flowrate increases from 0.95 L/min to 1.25 L/min. Ce and CeO also behave in this manner. On the scale chosen for the Ce spectra (Figure 3.11), with the B lens set at 7V, the Ce^{2+} peaks are not seen above baseline. Ce^{2+} is present, however, at 1.05 L/min, as

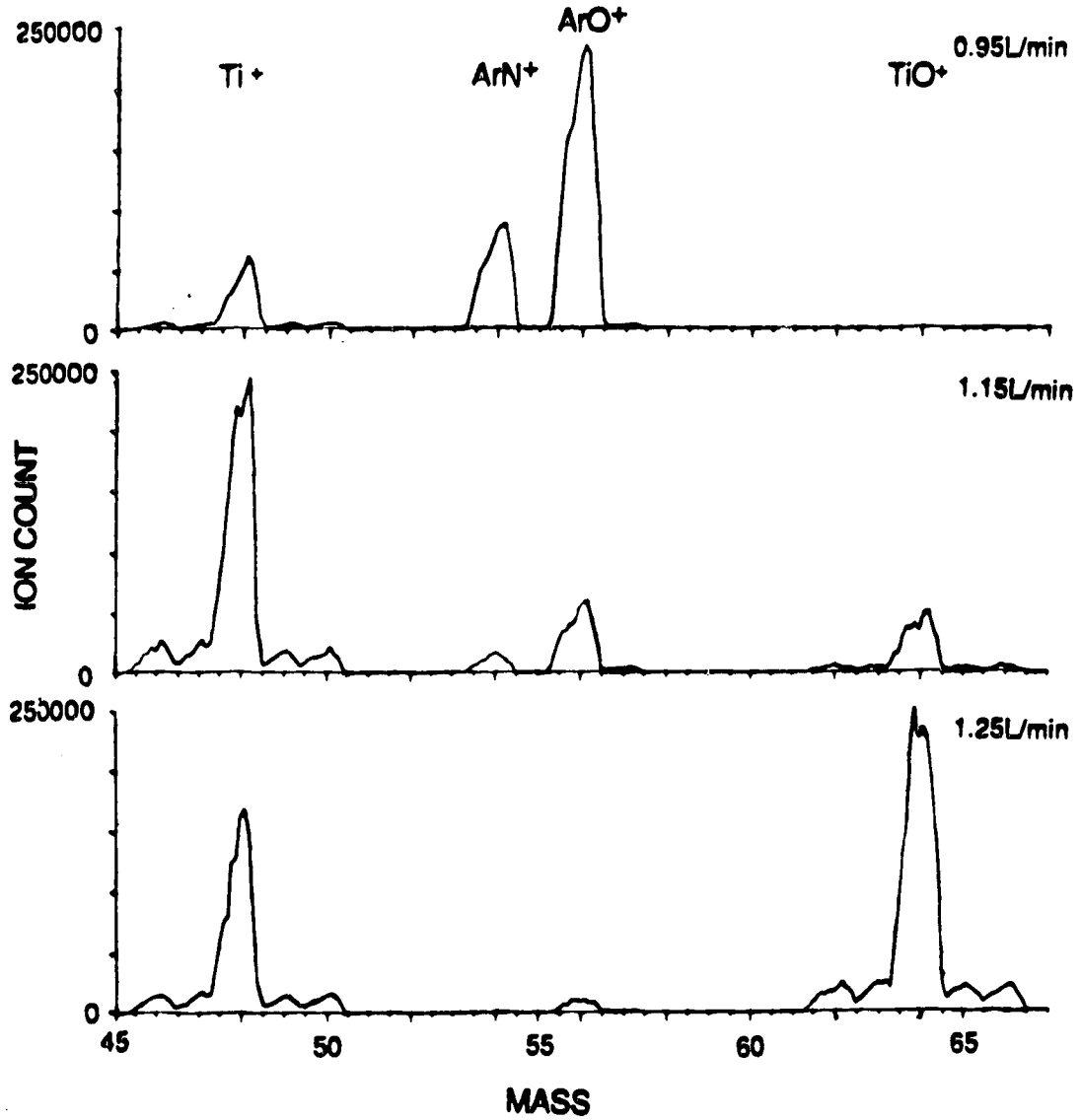

Figure 3.9 Ti^+ and TiO^+ spectra at different nebulizer flowrates.

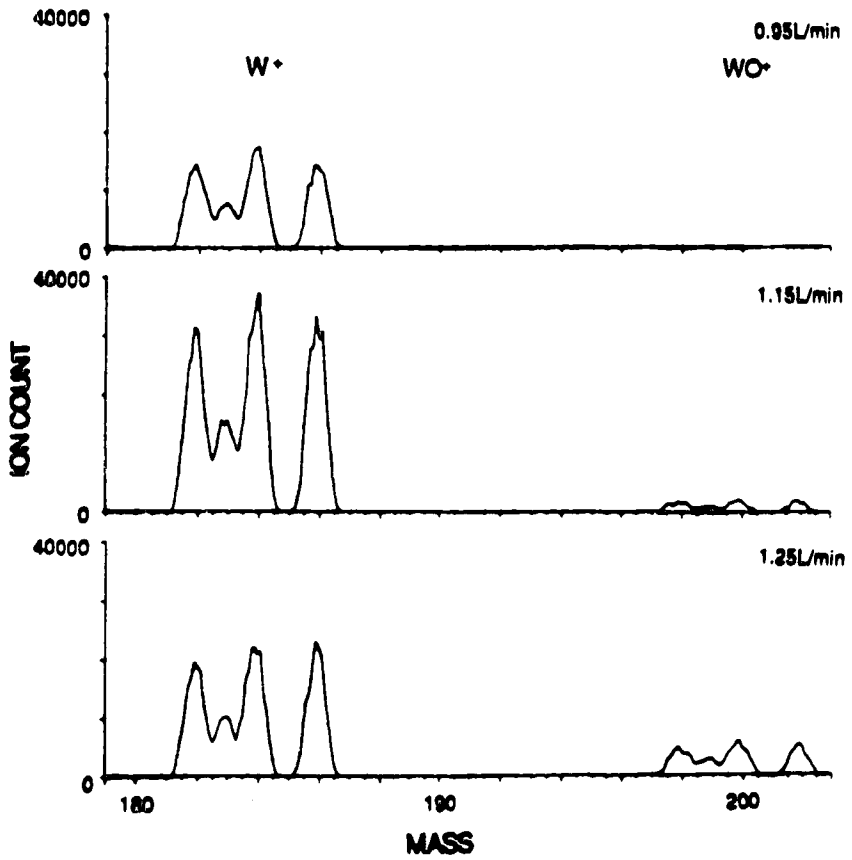

Figure 3.10 W^+ and WO^+ spectra at different nebulizer flowrates.

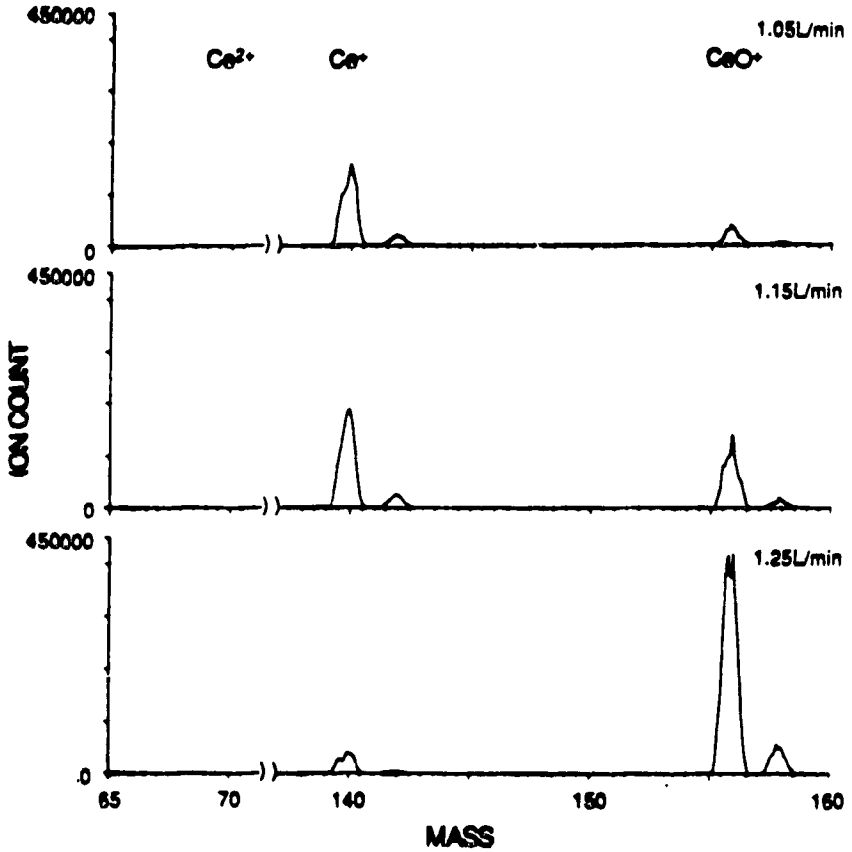

Figure 3.11 Ce^+ and CeO^+ spectra at different nebulizer flowrates.

can be seen in the insert in the lower spectrum in Figure 3.12. Figure 3.12 also shows the effect of changing the B lens from 7V, appropriate for Ce^+, to 5V, appropriate for the lower m/z of Ce^{2+}. The Ce^{2+} signal increases by over a factor of 10 and a drop in both the Ce^+ and CeO^+ signal results. Lower B lens settings are more optimal for lower m/z species.

From these spectra the importance of choosing the proper ICP-MS operating conditions can be seen. We must also be aware of the possibility of oxide, hydroxide, and doubly charged ion interferences. It is possible to detune the instrument to reduce these interferences, although mathematical corrections are likely needed in some cases, especially if the concentration of the interfering element is high.

3. Tables of Oxide, Hydroxide, and Doubly Charged Ion Interferences in ICP-MS.

From the foregoing data and discussion, it is clear that complex interelement spectral interferences can result in ICP-MS when one is analyzing multielement solutions. Depending on operating conditions, several element species can coexist (M^+, MO^+, MOH^+, and M^{2+}) and serious spectral interferences are possible, particularly from a matrix element present at a much higher concentration than a trace or ultra-trace sought-for constituent. Two tables have been prepared to assist other workers in recognizing the potential for such spectral interference problems. In the first table (Table 3.1) the elements are listed in order of increasing mass. At each mass, potential mono-oxide, hydroxide, and doubly charged species interferences are also listed. In the second table format (Table 3.2), the elements that are most likely to form mono-oxide, hydroxide, and doubly

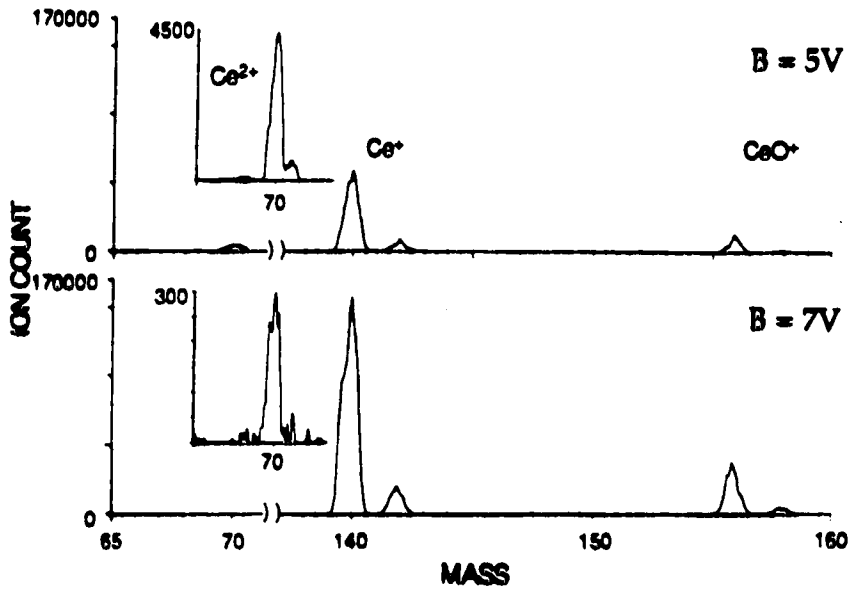

Figure 3.12 Effect of "B" lens setting on Ce^{2+}, Ce^{+}, and CeO^{+} signals.

charged species are listed, along with the elements they are most likely to interfere with. Thus, if a particular sample matrix has a high concentration of one of these elements, potential spectral interference problems can be anticipated by referring to this table.

It should be cautioned that, if anything, these tables are conservative. Only strong oxide-forming elements have been included. At high concentrations (> 1000 μg/mL), almost any element will show oxide species in its ICP-MS spectrum. At the 1000 μg/mL level, mono-oxides have been observed for Se, Ge, Ru, and Cd. In addition, such species are only one source of spectral interference. In a companion study, tables of background species observed in ICP-MS are presented [10]. The reader should consult those tables in conjunction with the tables presented here in order to be more thoroughly aware of potential problems.

Table 3.1 Oxide, hydroxide and doubly charged ion interferences in order of increasing mass. (Expressions in boldface refer to the most abundant isotope; expressions in parentheses refer to the percentage natural abundance.)

Mass	Elements	Interferences
20	**Ne(90.9)**	$^{40}Ca^{2+}$
21	Ne(0.26)	$^{42}Ca^{2+}$, $^{43}Ca^{2+}$
22	Ne(8.82)	$^{43}Ca^{2+}$, $^{44}Ca^{2+}$, $^{45}Sc^{2+}$
23	**Na(100)**	$^{45}Sc^{2+}$, $^{46}Ca^{2+}$
24	**Mg(78.8)**	$^{48}Ca^{2+}$
40	**Ar(99.6)**, **Ca(97.0)**, K(0.01)	$^{24}Mg^{16}O$
41	K(6.91)	$^{25}Mg^{16}O$
42	Ca(0.64)	$^{26}Mg^{16}O$, $^{84}Sr^{2+}$
43	Ca(0.14)	$^{86}Sr^{2+}$, $^{87}Sr^{2+}$
44	Ca(2.06)	$^{87}Sr^{2+}$, $^{88}Sr^{2+}$
56	**Fe(91.7)**	$^{40}Ca^{16}O$
58	**Ni(67.7)**, Fe(0.33)	$^{42}Ca^{16}O$
59	**Co(100)**	$^{43}Ca^{16}O$
60	Ni(26.2)	$^{44}Ca^{16}O$
61	Ni(1.25)	$^{45}Sc^{16}O$
62	Ni(3.66)	$^{46}Ca^{16}O$, $^{46}Ti^{16}O$
63	**Cu(69.1)**	$^{47}Ti^{16}O$
64	**Zn(48.9)**, Ni(1.16)	$^{48}Ca^{16}O$, $^{48}Ti^{16}O$
65	Cu(30.9)	$^{49}Ti^{16}O$, $^{130}Ba^{2+}$
66	Zn(27.8)	$^{50}Ti^{16}O$, $^{50}V^{16}O$, $^{50}Cr^{16}O$, $^{132}Ba^{2+}$
67	Zn(4.11)	$^{51}V^{16}O$, $^{134}Ba^{2+}$, $^{135}Ba^{2+}$

Mass	Elements	Interferences
68	Zn(18.6)	$^{52}Cr^{16}O$, $^{135}Ba^{2+}$, $^{136}Ba^{2+}$, $^{137}Ba^{2+}$, $^{136}Ce^{2+}$
69	Ga(60.2)	$^{53}Cr^{16}O$, $^{137}Ba^{2+}$, $^{138}Ba^{2+}$, $^{138}Ce^{2+}$ $^{138}La^{2+}$, $^{139}La^{2+}$
70	Ge(20.5), Zn(0.62)	$^{54}Cr^{16}O$,$^{139}La^{2+}$, $^{140}Ce^{2+}$, $^{141}Pr^{2+}$
71	Ga(39.8)	$^{141}Pr^{2+}$, $^{142}Ce^{2+}$, $^{142}Nd^{2+}$, $^{143}Nd^{2+}$
72	Ge(27.4)	$^{143}Nd^{2+}$, $^{144}Nd^{2+}$, $^{144}Sm^{2+}$, $^{145}Nd^{2+}$
73	Ge(7.76)	$^{145}Nd^{2+}$, $^{146}Nd^{2+}$, $^{147}Sm^{2+}$
74	Ge(36.6), Se(0.87)	$^{147}Sm^{2+}$, $^{148}Nd^{2+}$, $^{148}Sm^{2+}$, $^{149}Sm^{2+}$
75	As(100)	$^{149}Sm^{2+}$,$^{150}Sm^{2+}$, $^{150}Nd^{2+}$, $^{151}Eu^{2+}$
76	Se(9.02), Ge(7.77)	$^{151}Eu^{2+}$, $^{152}Sm^{2+}$, $^{152}Gd^{2+}$, $^{153}Eu^{2+}$
77	Se(7.58)	$^{153}Eu^{2+}$, $^{154}Sm^{2+}$, $^{154}Gd^{2+}$, $^{155}Gd^{2+}$
78	Se(23.5), Kr(0.35)	$^{155}Gd^{2+}$, $^{156}Gd^{2+}$, $^{156}Dy^{2+}$, $^{157}Gd^{2+}$
79	Br(50.5)	$^{157}Gd^{2+}$, $^{158}Gd^{2+}$, $^{158}Dy^{2+}$, $^{159}Tb^{2+}$
80	Se(49.8), Kr(2.27)	$^{159}Tb^{2+}$, $^{160}Gd^{2+}$, $^{160}Dy^{2+}$, $^{161}Dy^{2+}$
81	Br(49.5)	$^{161}Dy^{2+}$, $^{162}Dy^{2+}$, $^{162}Er^{2+}$, $^{163}Dy^{2+}$
82	Kr(11.6), Se(9.19)	$^{163}Dy^{2+}$, $^{164}Dy^{2+}$, $^{164}Er^{2+}$, $^{165}Ho^{2+}$
83	Kr(11.6)	$^{165}Ho^{2+}$, $^{166}Er^{2+}$, $^{167}Er^{2+}$
84	Kr(56.9), Sr(0.56)	$^{167}Er^{2+}$, $^{168}Er^{2+}$, $^{168}Yb^{2+}$, $^{169}Tm^{2+}$
85	Rb(72.2)	$^{169}Tm^{2+}$, $^{170}Er^{2+}$, $^{170}Yb^{2+}$, $^{171}Yb^{2+}$
86	Kr(17.4), Sr(9.87)	$^{171}Yb^{2+}$, $^{172}Yb^{2+}$, $^{173}Yb^{2+}$
87	Rb(27.8), Sr(7.04)	$^{173}Yb^{2+}$, $^{174}Yb^{2+}$, $^{175}Lu^{2+}$
88	Sr(82.5)	$^{175}Lu^{2+}$, $^{176}Lu^{2+}$, $^{176}Yb^{2+}$
100	Ru(12.6), Mo(9.62)	$^{84}Sr^{16}O$
101	Ru(17.1)	$^{84}Sr^{16}O^{1}H$

Mass	Elements	Interferences
102	**Ru(31.6)**, Pd(0.96)	$^{86}Sr^{16}O$
103	**Rh(100)**	$^{86}Sr^{16}O^{1}H$, $^{87}Sr^{16}O$
104	Ru(18.6), Pd(11.0)	$^{87}Sr^{16}O^{1}H$, $^{88}Sr^{16}O$
105	Pd(22.2)	$^{88}Sr^{16}O^{1}H$, $^{89}Y^{16}O$
106	**Pd(27.3)**, Cd(1.21)	$^{90}Zr^{16}O$
107	**Ag(51.8)**	$^{91}Zr^{16}O$
108	Pd(26.7), Cd(0.88)	$^{92}Zr^{16}O$, $^{92}Mo^{16}O$
109	Ag(48.2)	$^{93}Nb^{16}O$
110	Cd(12.4), Pd(11.8)	$^{94}Zr^{16}O$, $^{94}Mo^{16}O$
111	Cd(12.8)	$^{95}Mo^{16}O$
112	Cd(24.1), Sn(0.95)	$^{96}Zr^{16}O$, $^{96}Mo^{16}O$
113	Cd(12.3), In(4.28)	$^{97}Mo^{16}O$
114	**Cd(28.9)**, Sn(0.65)	$^{98}Mo^{16}O$
116	Sn(14.2), Cd(7.58)	$^{100}Mo^{16}O$, $^{232}Th^{2+}$
117	Sn(7.57)	$^{234}U^{2+}$, $^{235}U^{2+}$
118	Sn(24.0)	$^{235}U^{2+}$
119	Sn(8.58)	$^{238}U^{2+}$
146	Nd(17.2)	$^{130}Ba^{16}O$
147	Sm(15.1)	$^{130}Ba^{16}O^{1}H$
148	Sm(11.4), Nd(5.73)	$^{132}Ba^{16}O$
149	Sm(14.0)	$^{132}Ba^{16}O^{1}H$
150	Sm(7.47), Nd(5.62)	$^{134}Ba^{16}O$
151	Eu(47.8)	$^{134}Ba^{16}O^{1}H$, $^{135}Ba^{16}O$
152	Sm(26.6), Gd(0.21)	$^{135}Ba^{16}O^{1}H$, $^{136}Ba^{16}O$, $^{136}Ce^{16}O$
153	**Eu(52.2)**	$^{136}Ba^{16}O^{1}H$, $^{137}Ba^{16}O$
154	Sm(22.4), Gd(2.23)	$^{137}Ba^{16}O^{1}H$, $^{138}Ba^{16}O$, $^{138}Ce^{16}O$, $^{138}La^{16}O$

Mass	Elements	Interferences
155	Gd(15.1)	$^{138}Ba^{16}O^{1}H$, $^{139}La^{16}O$
156	Gd(20.6), Dy(0.05)	$^{140}Ce^{16}O$
157	Gd(15.7)	$^{141}Pr^{16}O$
158	Gd(24.5), Dy(0.09)	$^{142}Ce^{16}O$, $^{142}Nd^{16}O$
159	Tb(100)	$^{143}Nd^{16}O$
160	Gd(21.6), Dy(2.29)	$^{144}Nd^{16}O$, $^{144}Sm^{16}O$
161	Dy(18.9)	$^{145}Nd^{16}O$
162	Dy(25.5), Er(0.14)	$^{146}Nd^{16}O$
163	Dy(25.0)	$^{147}Sm^{16}O$
164	Dy(28.2), Er(1.56)	$^{148}Nd^{16}O$, $^{148}Sm^{16}O$
165	Ho(100)	$^{149}Sm^{16}O$
166	Er(33.4)	$^{150}Nd^{16}O$, $^{150}Sm^{16}O$
167	Er(22.9)	$^{151}Eu^{16}O$
168	Er(27.1), Yb(0.14)	$^{152}Sm^{16}O$, $^{152}Gd^{16}O$
169	Tm(100)	$^{153}Eu^{16}O$
170	Er(14.9), Yb(3.03)	$^{154}Sm^{16}O$, $^{154}Gd^{16}O$
171	Yb(14.3)	$^{155}Gd^{16}O$
172	Yb(21.8)	$^{156}Gd^{16}O$, $^{156}Dy^{16}O$
173	Yb(16.1)	$^{157}Gd^{16}O$
174	Yb(31.8), Hf(0.18)	$^{158}Gd^{16}O$, $^{158}Dy^{16}O$
175	Lu(97.4)	$^{159}Tb^{16}O$
176	Yb(12.7),Hf(5.2), Lu(2.59)	$^{160}Gd^{16}O$, $^{160}Dy^{16}O$
177	Hf(18.5)	$^{161}Dy^{16}O$
178	Hf(27.1)	$^{162}Dy^{16}O$, $^{162}Er^{16}O$
179	Hf(13.8)	$^{163}Dy^{16}O$

Mass	Elements	Interferences
180	**Hf(35.2)**, W(0.14), Ta(0.01)	$^{164}Dy^{16}O$, $^{164}Er^{16}O$
181	**Ta(99.9)**	$^{165}Ho^{16}O$
182	W(26.3)	$^{166}Er^{16}O$
183	W(14.3)	$^{167}Er^{16}O$
184	W(30.7), Os(0.02)	$^{168}Er^{16}O$, $^{168}Yb^{16}O$
185	Re(37.1)	$^{169}Tm^{16}O$
186	W(28.6), Os(1.59)	$^{170}Er^{16}O$, $^{170}Yb^{16}O$
187	**Re(62.9)**, Os(1.64)	$^{171}Yb^{16}O$
188	Os(13.3)	$^{172}Yb^{16}O$
189	Os(16.1)	$^{173}Yb^{16}O$
190	Os(26.4), Pt(0.01)	$^{174}Yb^{16}O$, $^{174}Hf^{16}O$
191	Ir(38.5)	$^{175}Lu^{16}O$
192	**Os(41)**, Pt(0.78)	$^{176}Yb^{16}O$, $^{176}Hf^{16}O$, $^{176}Lu^{16}O$
193	**Ir(61.5)**	$^{177}Hf^{16}O$
194	Pt(32.9)	$^{178}Hf^{16}O$
195	**Pt(33.8)**	$^{179}Hf^{16}O$
196	Pt(25.2), Hg(0.15)	$^{180}Hf^{16}O$, $^{180}W^{16}O$, $^{180}Ta^{16}O$
197	**Au(100)**	$^{181}Ta^{16}O$
198	Hg(10.0), Pt(7.19)	$^{182}W^{16}O$
199	**Hg(16.8)**	$^{183}W^{16}O$
200	Hg(23.1)	$^{184}W^{16}O$
202	**Hg(29.8)**	$^{186}W^{16}O$
248		$^{232}Th^{16}O$
250		$^{234}U^{16}O$
251		$^{235}U^{16}O$
254		$^{238}U^{16}O$

Table 3.2 Table of elements most likely to form oxides, hydroxides and doubly charged species, plus elements potentially affected by these interferences. (Expressions in boldface refer to the most abundant isotope; expressions in parentheses refer to the percentage natural abundance.)

Elem.	Mass	%Ab.	Assoc. Spec.	Mass	Affected Elements		
Mg	24	78.8	MgO	40	**Ar(99.6)**	**Ca(97.0)**	K(0.01)
Mg	25	10.15	MgO	41	K(6.91)		
Mg	26	11.05	MgO	42	Ca(0.64)		
Ca	40	96.97	Ca^{2+}	20	**Ne(90.9)**		
Ca	42	0.64	Ca^{2+}	21	Ne(0.26)		
Ca	43	0.145	Ca^{2+}	21.5	^{22}Ne(8.82)	^{21}Ne(0.26)	
Ca	44	2.06	Ca^{2+}	22	Ne(8.82)		
Ca	46	0.003	Ca^{2+}	23	**Na(100)**		
Ca	48	0.185	Ca^{2+}	24	**Mg(78.8)**		
Ca	40	96.97	CaO	56	**Fe(91.7)**		
Ca	42	0.64	CaO	58	**Ni(67.7)**	Fe(0.33)	
Ca	43	0.145	CaO	59	**Co(100)**		
Ca	44	2.06	CaO	60	Ni(26.2)		
Ca	46	0.003	CaO	62	Ni(3.66)		
Ca	48	0.185	CaO	64	**Zn(48.9)**	Ni(1.16)	
Sc	45	100	Sc^{2+}	22.5	^{23}**Na(100)**	^{22}Ne(8.82)	
Sc	45	100.	ScO	61	Ni(1.25)		
Ti	46	7.99	TiO	62	Ni(3.66)		
Ti	47	7.32	TiO	63	**Cu(69.1)**		
Ti	48	73.98	TiO	64	**Zn(48.9)**	Ni(1.16)	
Ti	49	5.46	TiO	65	Cu(30.9)		
Ti	50	5.25	TiO	66	Zn(27.8)		

Elem.	Mass	%Ab.	Assoc. Spec.	Mass	Affected Elements	
V	50	0.24	VO	66	Zn(27.8)	
V	51	99.76	VO	67	Zn(4.11)	
Cr	50	4.352	CrO	66	Zn(27.8)	
Cr	52	83.764	CrO	68	Zn(18.6)	
Cr	53	9.509	CrO	69	Ga(60.2)	
Cr	54	2.375	CrO	70	Ge(20.5)	Zn(0.62)
Sr	84	0.56	Sr^{+2}	42	Ca(0.64)	
Sr	86	9.87	Sr^{+2}	43	Ca(0.14)	
Sr	87	7.035	Sr^{+2}	43.5	^{44}Ca(2.06)	^{43}Ca(0.14)
Sr	88	82.535	Sr^{+2}	44	Ca(2.06)	
Sr	84	0.56	SrO	100	Ru(12.6)	Mo(9.62)
Sr	86	9.87	SrO	102	Ru(31.6)	Pd(0.96)
Sr	87	7.035	SrO	103	Rh(100)	
Sr	88	82.535	SrO	104	Ru(18.6)	Pd(11.0)
Sr	84	0.56	SrOH	101	Ru(17.1)	
Sr	86	9.87	SrOH	103	Rh(100)	
Sr	87	7.035	SrOH	104	Ru(18.6)	Pd(11.0)
Sr	88	82.535	SrOH	105	Pd(22.2)	
Y	89	100.	YO	105	Pd(22.2)	
Zr	90	51.46	ZrO	106	Pd(27.3)	Cd(1.21)
Zr	91	11.23	ZrO	107	Ag(51.8)	
Zr	92	17.11	ZrO	108	Pd(26.7)	Cd(0.88)
Zr	94	17.4	ZrO	110	Cd(12.4)	Pd(11.8)
Zr	96	2.8	ZrO	112	Cd(24.1)	Sn(0.95)
Mo	92	15.86	MoO	108	Pd(26.7)	Cd(0.88)
Mo	94	9.12	MoO	110	Cd(12.4)	Pd(11.8)
Mo	95	15.7	MoO	111	Cd(12.8)	

Elem.	Mass	%Ab.	Assoc. Spec.	Mass	Affected Elements	
Mo	96	16.5	MoO	112	Cd(24.1)	Sn(0.95)
Mo	97	9.45	MoO	113	Cd(12.3)	In(4.28)
Mo	98	23.75	MoO	114	Cd(28.9)	Sn(0.65)
Mo	100	9.62	MoO	116	Sn(14.2)	Cd(7.58)
Nb	93	100.	NbO	109	Ag(48.2)	
Ba	130	0.101	Ba^{+2}	65	Cu(30.9)	
Ba	132	0.097	Ba^{+2}	66	Zn(27.8)	
Ba	134	2.42	Ba^{+2}	67	Zn(4.11)	
Ba	135	6.59	Ba^{+2}	67.5	^{68}Zn(18.6)	^{67}Zn(4.11)
Ba	136	7.81	Ba^{+2}	68	Zn(18.6)	
Ba	137	11.32	Ba^{+2}	68.5	^{69}Ga(60.2)	^{68}Zn(18.6)
Ba	138	71.66	Ba^{+2}	69	Ga(60.2)	
Ba	130	0.101	BaO	146	Nd(17.2)	
Ba	132	0.097	BaO	148	Sm(11.4)	Nd(5.73)
Ba	134	2.42	BaO	150	Sm(7.47)	Nd(5.62)
Ba	135	6.59	BaO	151	Eu(47.8)	
Ba	136	7.81	BaO	152	Sm(26.6)	Gd(0.21)
Ba	137	11.32	BaO	153	Eu(52.2)	
Ba	138	71.66	BaO	154	Sm(22.4)	Gd(2.23)
Ba	130	0.101	BaOH	147	Sm(15.1)	
Ba	132	0.097	BaOH	149	Sm(14.0)	
Ba	134	2.42	BaOH	151	Eu(47.8)	
Ba	135	6.59	BaOH	152	Sm(26.6)	Gd(0.21)
Ba	136	7.81	BaOH	153	Eu(52.2)	
Ba	137	11.32	BaOH	154	Sm(22.4)	Gd(2.23)
Ba	138	71.66	BaOH	155	Gd(15.1)	
Ce	136	0.193	Ce^{+2}	68	Zn(18.6)	
Ce	138	0.25	Ce^{+2}	69	Ga(60.2)	
Ce	140	88.48	Ce^{+2}	70	Ge(20.5)	Zn(0.62)
Ce	142	11.07	Ce^{+2}	71	Ga(39.8)	

Elem.	Mass	%Ab.	Assoc. Spec.	Mass	Affected Elements		
Ce	136	0.193	CeO	152	Sm(26.6)	Gd(0.21)	
Ce	138	0.25	CeO	154	Sm(22.4)	Gd(2.23)	
Ce	140	88.48	CeO	156	Gd(20.6)	Dy(0.05)	
Ce	142	11.07	CeO	158	Gd(24.5)	Dy(0.09)	
La	138	0.089	La^{+2}	69	Ga(60.2)		
La	139	99.911	La^{+2}	69.5	^{69}Ga(60.2)	^{70}Ge(20.5)	^{70}Zn(0.62)
La	138	0.089	LaO	154	Sm(22.4)	Gd(2.23)	
La	139	99.911	LaO	155	Gd(15.1)		
Pr	141	100.	Pr^{+2}	70.5	^{71}Ga(39.8)	^{70}Ge(20.5)	^{70}Zn(0.62)
Pr	141	100.	PrO	157	Gd(15.7)		
Nd	142	27.11	Nd^{+2}	71	Ga(39.8)		
Nd	143	12.17	Nd^{+2}	71.5	^{71}Ga(39.8)	^{72}Ge(27.4)	
Nd	144	23.85	Nd^{+2}	72	Ge(27.4)		
Nd	145	8.3	Nd^{+2}	72.5	^{72}Ge(27.4)	^{73}Ge(7.76)	
Nd	146	17.22	Nd^{+2}	73	Ge(7.76)		
Nd	148	5.73	Nd^{+2}	74	Ge(36.6)	Se(0.87)	
Nd	150	5.62	Nd^{+2}	75	As(100)		
Nd	142	27.11	NdO	158	Gd(24.5)	Dy(0.09)	
Nd	143	12.17	NdO	159	Tb(100)		
Nd	144	23.85	NdO	160	Gd(21.6)	Dy(2.29)	
Nd	145	8.3	NdO	161	Dy(18.9)		
Nd	146	17.22	NdO	162	Dy(25.5)	Er(0.14)	
Nd	148	5.73	NdO	164	Dy(28.2)	Er(1.56)	
Nd	150	5.62	NdO	166	Er(33.4)		
Sm	144	3.15	Sm^{+2}	72	Ge(27.4)		
Sm	147	15.09	Sm^{+2}	73.5	^{74}Ge(36.6)	^{73}Ge(7.76)	^{74}Se(0.87)
Sm	148	11.35	Sm^{+2}	74	Ge(36.6)	Se(0.87)	

Elem.	Mass	%Ab.	Assoc. Spec.	Mass	Affected Elements		
Sm	149	13.96	Sm^{+2}	74.5	^{75}As(100)	^{74}Ge(36.6)	^{74}Se(0.87)
Sm	150	7.47	Sm^{+2}	75	As(100)		
Sm	152	26.55	Sm^{+2}	76	Se(9.02)	Ge(7.77)	
Sm	154	22.43	Sm^{+2}	77	Se(7.58)		
Sm	144	3.15	SmO	160	Gd(21.6)	Dy(2.29)	
Sm	147	15.09	SmO	163	Dy(25.0)		
Sm	148	11.35	SmO	164	Dy(28.2)	Er(1.56)	
Sm	149	13.96	SmO	165	Ho(100)		
Sm	150	7.47	SmO	166	Er(33.4)		
Sm	152	26.55	SmO	168	Er(27.1)	Yb(0.14)	
Sm	154	22.43	SmO	170	Er(14.9)	Yb(3.03)	
Eu	151	47.82	Eu^{+2}	75.5	^{75}As(100)	^{76}Se(9.02)	^{76}Ge(7.77)
Eu	153	52.18	Eu^{+2}	76.5	^{76}Se(9.02)	^{76}Ge(7.77)	^{77}Se(7.58)
Eu	151	47.82	EuO	167	Er(22.9)		
Eu	153	52.18	EuO	169	Tm(100)		
Gd	152	0.205	Gd^{+2}	76	Se(9.02)	Ge(7.77)	
Gd	154	2.23	Gd^{+2}	77	Se(7.58)		
Gd	155	15.1	Gd^{+2}	77.5	^{78}Se(23.5)	^{77}Se(7.58)	^{78}Kr(0.35)
Gd	156	20.6	Gd^{+2}	78	Se(23.5)	Kr(0.35)	
Gd	157	15.7	Gd^{+2}	78.5	^{79}Br(50.5)	^{78}Se(23.5)	^{78}Kr(0.35)
Gd	158	24.5	Gd^{+2}	79	Br(50.5)		
Gd	160	21.6	Gd^{+2}	80	Se(49.8)	Kr(2.27)	
Gd	152	0.205	GdO	168	Er(27.1)	Yb(0.14)	
Gd	154	2.23	GdO	170	Er(14.9)	Yb(3.03)	
Gd	155	15.1	GdO	171	Yb(14.3)		
Gd	156	20.6	GdO	172	Yb(21.8)		
Gd	157	15.7	GdO	173	Yb(16.1)		
Gd	158	24.5	GdO	174	Yb(31.8)	Hf(0.18)	
Gd	160	21.6	GdO	176	Yb(12.7)	Hf(5.2)	Lu(2.59)

Elem.	Mass	%Ab.	Assoc. Spec.	Mass	Affected Elements		
Dy	156	0.052	Dy^{+2}	78	Se(23.5)	Kr(0.35)	
Dy	158	0.09	Dy^{+2}	79	Br(50.5)		
Dy	160	2.284	Dy^{+2}	80	Se(49.8)	Kr(2.27)	
Dy	161	18.88	Dy^{+2}	80.5	^{80}Se(49.8)	^{81}Br(49.5)	^{80}Kr(2.27)
Dy	162	25.53	Dy^{+2}	81	Br(49.5)		
Dy	163	24.97	Dy^{+2}	81.5	^{81}Br(49.5)	^{82}Kr(11.6)	^{82}Se(9.19)
Dy	164	28.18	Dy^{+2}	82	Kr(11.6)	Se(9.19)	
Dy	156	0.052	DyO	172	Yb(21.8)		
Dy	158	0.09	DyO	174	Yb(31.8)	Hf(0.18)	
Dy	160	2.284	DyO	176	Yb(12.7)	Hf(5.2)	Lu(2.59)
Dy	161	18.88	DyO	177	Hf(18.5)		
Dy	162	25.53	DyO	178	Hf(27.1)		
Dy	163	24.97	DyO	179	Hf(13.8)		
Dy	164	28.18	DyO	180	Hf(35.2)	W(0.14)	Ta(0.01)
Tb	159	100.	Tb^{+2}	79.5	^{79}Br(50.5)	^{80}Se(49.8)	^{80}Kr(2.27)
Tb	159	100.	TbO	175	Lu(97.4)		
Er	162	0.136	Er^{+2}	81	Br(49.5)		
Er	164	1.56	Er^{+2}	82	Kr(11.6)	Se(9.19)	
Er	166	33.41	Er^{+2}	83	Kr(11.6)		
Er	167	22.94	Er^{+2}	83.5	^{84}Kr(56.9)	^{83}Kr(11.6)	^{84}Sr(0.56)
Er	168	27.07	Er^{+2}	84	Kr(56.9)	Sr(0.56)	
Er	170	14.88	Er^{+2}	85	Rb(72.2)		
Er	162	0.136	ErO	178	Hf(27.1)		
Er	164	1.56	ErO	180	Hf(35.2)	W(0.14)	Ta(0.01)
Er	166	33.41	ErO	182	W(26.3)		
Er	167	22.94	ErO	183	W(14.3)		
Er	168	27.07	ErO	184	W(30.7)	Os(0.02)	
Er	170	14.88	ErO	186	W(28.6)	Os(1.59)	

Elem.	Mass	%Ab.	Assoc. Spec.	Mass	Affected Elements		
Ho	165	100.	Ho^{+2}	82.5	^{82}Kr(11.6)	^{83}Kr(11.6)	^{82}Se(9.19)
Ho	165	100.	HoO	181	Ta(99.9)		
Yb	168	0.135	Yb^{+2}	84	Kr(56.9)	Sr(0.56)	
Yb	170	3.03	Yb^{+2}	85	Rb(72.2)		
Yb	171	14.31	Yb^{+2}	85.5	^{85}Rb(72.2)	^{86}Kr(17.4)	^{86}Sr(9.87)
Yb	172	21.82	Yb^{+2}	86	Kr(17.4)	Sr(9.87)	
Yb	173	16.135	Yb^{+2}	86.5	^{87}Rb(27.8)	^{86}Kr(17.4)	^{86}Sr(9.87)
					^{87}Sr(7.04)		
Yb	174	31.84	Yb^{+2}	87	Rb(27.8)	Sr(7.04)	
Yb	176	12.73	Yb^{+2}	88	Sr(82.5)		
Yb	168	0.135	YbO	184	W(30.7)	Os(0.02)	
Yb	170	3.03	YbO	186	W(28.6)	Os(1.59)	
Yb	171	14.31	YbO	187	Re(62.9)	Os(1.64)	
Yb	172	21.82	YbO	188	Os(13.3)		
Yb	173	16.135	YbO	189	Os(16.1)		
Yb	174	31.84	YbO	190	Os(26.4)	Pt(0.01)	
Yb	176	12.73	YbO	192	Os(41)	Pt(0.78)	
Tm	169	100.	Tm^{+2}	84.5	^{85}Rb(72.2)	^{84}Kr(56.9)	^{84}Sr(0.56)
Tm	169	100.	TmO	185	Re(37.1)		
Hf	174	0.18	HfO	190	Os(26.4)	Pt(0.01)	
Hf	176	5.2	HfO	192	Os(41)	Pt(0.78)	
Hf	177	18.5	HfO	193	Ir(61.5)		
Hf	178	27.13	HfO	194	Pt(32.9)		
Hf	179	13.75	HfO	195	Pt(33.8)		
Hf	180	35.24	HfO	196	Pt(25.2)	Hg(0.15)	
Lu	175	97.41	Lu^{+2}	87.5	^{88}Sr(82.5)	^{87}Rb(27.8)	^{87}Sr(7.04)
Lu	176	2.59	Lu^{+2}	88	Sr(82.5)		

Elem.	Mass	%Ab.	Assoc. Spec.	Mass	Affected Elements	
Lu	175	97.41	LuO	191	Ir(38.5)	
Lu	176	2.59	LuO	192	Os(41)	Pt(0.78)
Ta	180	0.012	TaO	196	Pt(25.2)	Hg(0.15)
Ta	181	99.988	TaO	197	Au(100)	
W	180	0.14	WO	196	Pt(25.2)	Hg(0.15)
W	182	26.29	WO	198	Hg(10.0)	Pt(7.19)
W	183	14.31	WO	199	Hg(16.8)	
W	184	30.66	WO	200	Hg(23.1)	
W	186	28.6	WO	202	Hg(29.8)	
Th	232	100.	Th^{+2}	116	Sn(14.2)	Cd(7.58)
Th	232	100.	ThO	248		
U	234	0.0056	U^{+2}	117	Sn(7.57)	
U	235	0.7205	U^{+2}	117.5	^{118}Sn(24.0)	^{117}Sn(7.57)
U	238	99.274	U^{+2}	119	Sn(8.58)	
U	234	0.0056	UO	250		
U	235	0.7205	UO	251		
U	238	99.274	UO	254		

References.

1. A.R. Date and A.L. Gray, Spectrochim. Acta 40B, 115-122, (1985).

2. A.R. Date and A.L. Gray, Spectrochim. Acta 38B, 29-37, (1983).

3. A.R. Date and A.L. Gray, Analyst 108, 159-165, (1983).

4. R.S. Houk and J.J. Thompson, American Mineralogist 67, 238-243, (1982).

5. A.L. Gray and A.R. Date, Analyst 108, 1033-1050, (1983).

6. G. Horlick, S.H. Tan, M.A. Vaughan, and C.A. Rose, Spectrochim, Acta 40B, 1555-1572, (1985).

7. D.J. Douglas and R.S. Houk, Prog. Analyt. Atom. Spectrosc. 8, 1-18, (1985).

8. R.S. Houk, H.J. Svec, and V.A. Fassel, Appl. Spectrosc. 35, 380-384, (1981).

9. J.R. Bacon and A.M. Ure, Anal. Chim. Acta 105, 163-176, (1979).

10. S.H. Tan and G. Horlick, Appl. Spectrosc. 40, 445-460, (1986).

Chapter 4

Corrections for the Spectroscopic Overlap of Oxides and Hydroxides on Rare Earth Elements in ICP-MS

The analyte ion of interest in routine analysis in ICP-MS is the singly charged ion, M^+. In a number of cases, however, the element M is distributed among several species: M^+, M^{2+}, MO^+, or MOH^+. Although the formation of these oxides, hydroxides and doubly charged ions reduces the sensitivity at M^+, the larger problem is the overlap of these associated species on the singly charged species of other elements. The formation of these species and the effects of instrumental parameters on their intensities have been discussed in the previous chapter. Although the amounts of these species can be minimized by instrumental settings, it is not always possible to eliminate them completely and still have an adequate M^+ signal. The rare earth elements (REE's) are a group of elements which include some of the strongest oxide formers in ICP-MS. The problem of spectral overlap is clearly demonstrated with these elements since the strong oxide formers are mostly at the lower mass end of the rare earth elements and their oxides overlap the rare earth elements at the upper mass end as shown in Table 4.1.

Traditionally, spark source mass spectrometry has been used for rare earth element analyses [2,3], although inductively coupled plasma atomic emission spectroscopy [4] and fluorescence [5] have also been employed. Recently, a number of people have used ICP-MS in rare earth element analysis. Date and Hutchison [6] and Hirata et al. [7] reported low levels of oxides and no correction scheme was employed by either group. Longerich et

Table 4.1 Spectral overlap of rare earth element oxides LaO to DyO on rare earth elements Gd to Lu.

Mass	Elements	Interferences
155	Gd(15.1)	$^{138}Ba^{16}O^{1}H$, $^{139}La^{16}O$
156	Gd(20.6), Dy(0.05)	$^{140}Ce^{16}O$
157	Gd(15.7)	$^{141}Pr^{16}O$
158	Gd(24.5), Dy(0.09)	$^{142}Ce^{16}O$, $^{142}Nd^{16}O$
159	Tb(100)	$^{143}Nd^{16}O$
160	Gd(21.6), Dy(2.29)	$^{144}Nd^{16}O$, $^{144}Sm^{16}O$
161	Dy(18.9)	$^{145}Nd^{16}O$
162	Dy(25.5), Er(0.14)	$^{146}Nd^{16}O$
163	Dy(25.0)	$^{147}Sm^{16}O$
164	Dy(28.2), Er(1.56)	$^{148}Nd^{16}O$, $^{148}Sm^{16}O$
165	Ho(100)	$^{149}Sm^{16}O$
166	Er(33.4)	$^{150}Nd^{16}O$, $^{150}Sm^{16}O$
167	Er(22.9)	$^{151}Eu^{16}O$
168	Er(27.1), Yb(0.14)	$^{152}Sm^{16}O$, $^{152}Gd^{16}O$
169	Tm(100)	$^{153}Eu^{16}O$
170	Er(14.9), Yb(3.03)	$^{154}Sm^{16}O$, $^{154}Gd^{16}O$
171	Yb(14.3)	$^{155}Gd^{16}O$
172	Yb(21.8)	$^{156}Gd^{16}O$, $^{156}Dy^{16}O$
173	Yb(16.1)	$^{157}Gd^{16}O$
174	Yb(31.8), Hf(0.18)	$^{158}Gd^{16}O$, $^{158}Dy^{16}O$
175	Lu(97.4)	$^{159}Tb^{16}O$
176	Yb(12.7),Hf(5.2), Lu(2.59)	$^{160}Gd^{16}O$, $^{160}Dy^{16}O$

al. [8] provided a detailed discussion of oxide formation with the rare earth elements and the interferences that they observed. Lichte et al. [9] used instrumental settings to minimize oxide formation and they employed an algebraic correction scheme in their data processing step. Algebraic correction schemes are one approach to take to correct for the oxide and hydroxide overlap problem. This approach has been used in spark source mass spectrometry [3] as well as in ICP-MS. An alternate approach is to employ a principal components analysis method to the system.

Principal components analysis (PCA), is a method of data analysis used extensively in the social sciences and is being successfully employed in a number of areas in chemistry [10-15]. Principal components analysis can be applied whenever a measurement can be expressed as a linear sum of product terms and has been found to be useful in areas of chemistry such as spectrophotometry and mass spectrometry. By employing PCA, a measurement composed of the sum of the signals from a number of components may be separated into each of the independent components. The technique has been described in detail by Malinowski and Howery [16]. In this application, each component is an element and the spectra including the M^+, MO^+ and MOH^+ signals for each element should appear in a distinct region of hyperspace, thus allowing the separation of overlapping oxides and singly charged species. A comparison of rare earth analysis using a traditional algebraic correction scheme and a principal component analysis approach is discussed in this work.

Experimental.

Solutions for the rare earth analysis were prepared from SPEX Industries Inc. standard 1000μg/mL stock solutions. Single element standards were prepared for each of the seven REE's, Ce, Sm, Gd, Dy, Ho, Er and Yb and various mixtures were prepared as samples. Cs was used as an internal standard. The ICP-MS was run in the usual manner. The power was set at 1.3kW and the nebulizer flowrate was adjusted typically between 0.95 and 1.0 L/min to yield maximum ion count. The torch was positioned 15mm from the load coil to the sampler tip and the ion lenses were adjusted for the mass range of the rare earth elements (140-174m/z). The system was well overdetermined by measuring ion counts, uncorrected, at the masses listed in Table 4.2. The measurements were made in low resolution using 3 points /peak, multichannel mode with with a measurement time of 0.1s, 6 repeats/ integration and a 50 ms dwell time.

Results and Discussion.

The problems resulting from isobaric overlaps, oxide formation and hydroxide formation are demonstrated in this group of seven rare earth elements, Ce, Sm, Gd, Dy, Ho, Er and Yb. The severity of the interference that results from each depends on the relative intensities of the signal from the element of interest and from the interferent. Data were collected for each single element standard and for the mixtures at 22 masses in order to have the system well overdetermined. The spectra for each element at the 22 masses measured are presented in Figures 4.1 and 4.2. Note that the mass axis is a category axis only, not a linear scale, since only the masses used in this

Table 4.2. Rare Earth Isotope List.

^{140}Ce	^{163}Dy
^{142}Ce	^{164}Dy
^{147}Sm	^{165}Ho
^{149}Sm	^{166}Er
^{152}Sm	^{167}Er
^{156}Gd	^{168}Er
^{157}Gd	^{170}Er
^{158}Gd	^{171}Yb
^{160}Gd	^{172}Yb
^{161}Dy	^{173}Yb
^{162}Dy	^{174}Yb

^{133}Cs (internal standard)

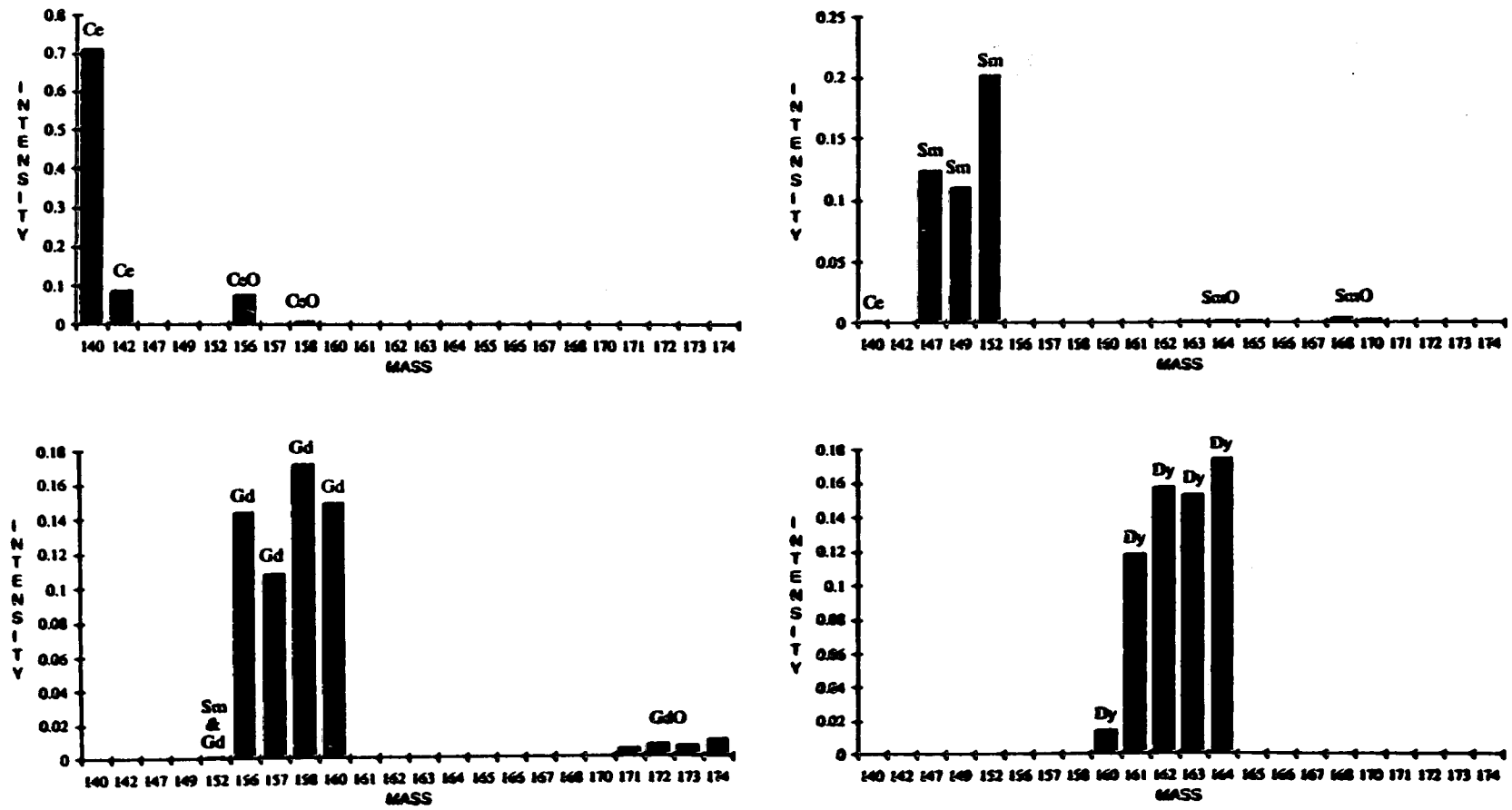

Figure 4.1 Mass spectra for Ce, Gd, Sm and Dy. Some masses are omitted along the mass axis.

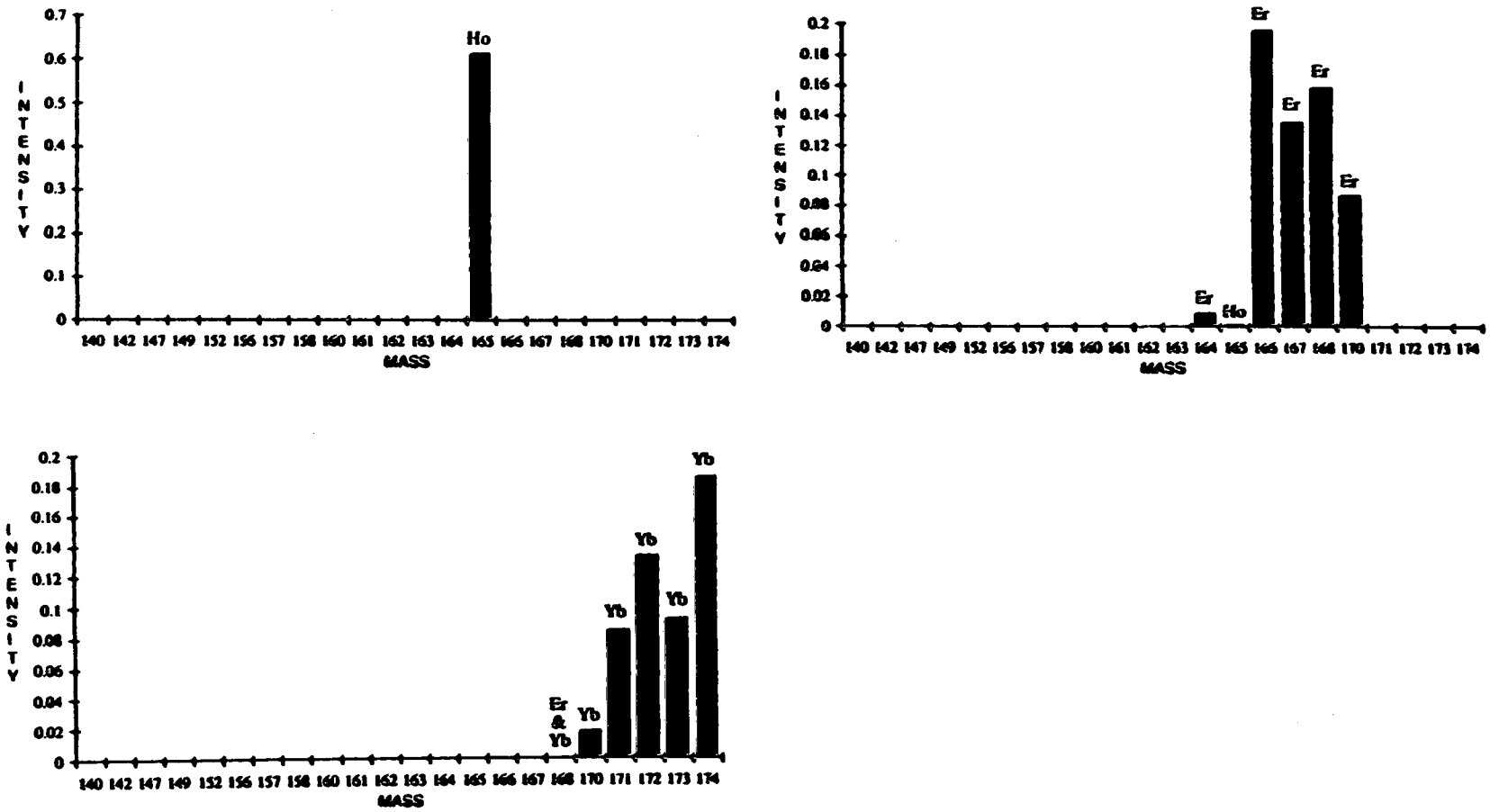

Figure 4.2 Mass spectra for Ho, Yb and Er. Some masses are omitted along the mass axis.

study are included. Because of this, the isotope pattern may not appear as one is used to seeing on a linear mass scale. From the data presented in these bar graphs the necessary oxide ratios and abundance ratios for Gauss elimination may be obtained. It is the characteristic pattern for each element, easily seen in these plots that results in each element ending up in a distinct region of hyperspace, critical for principal components analysis.

The signal intensities obtained for a mixture of 6 rare earth elements are plotted in Figure 4.3a. Below, in Figure 4.3b, is a plot of the components of the sample built up from weighting the measured signals from the appropriate standards. The intensities are in arbitrary units. From the pattern of Figure 4.3b, it is easy to see how complicated the spectra can become even within this limited system and why a reliable correction scheme is valuable.

1. Gauss Elimination.

Gauss elimination is the method of solving n equations in n unknowns algebraically. This method can be used to provide a correction scheme for spectral overlap problems involving the rare earth element oxides. As an example, consider the system of seven rare earth elements: Ce, Sm, Gd, Dy, Ho, Er and Tb and their oxides and hydroxides. A partial list of the interferences within this set is shown in Table 4.3.

The method of Gauss elimination has been used to determine the concentrations of these seven rare earth elements assuming that Nd, Pr and Hf are not present in the standards or the samples. The following terms are used in the Gauss elimination method of oxide correction and rare earth element

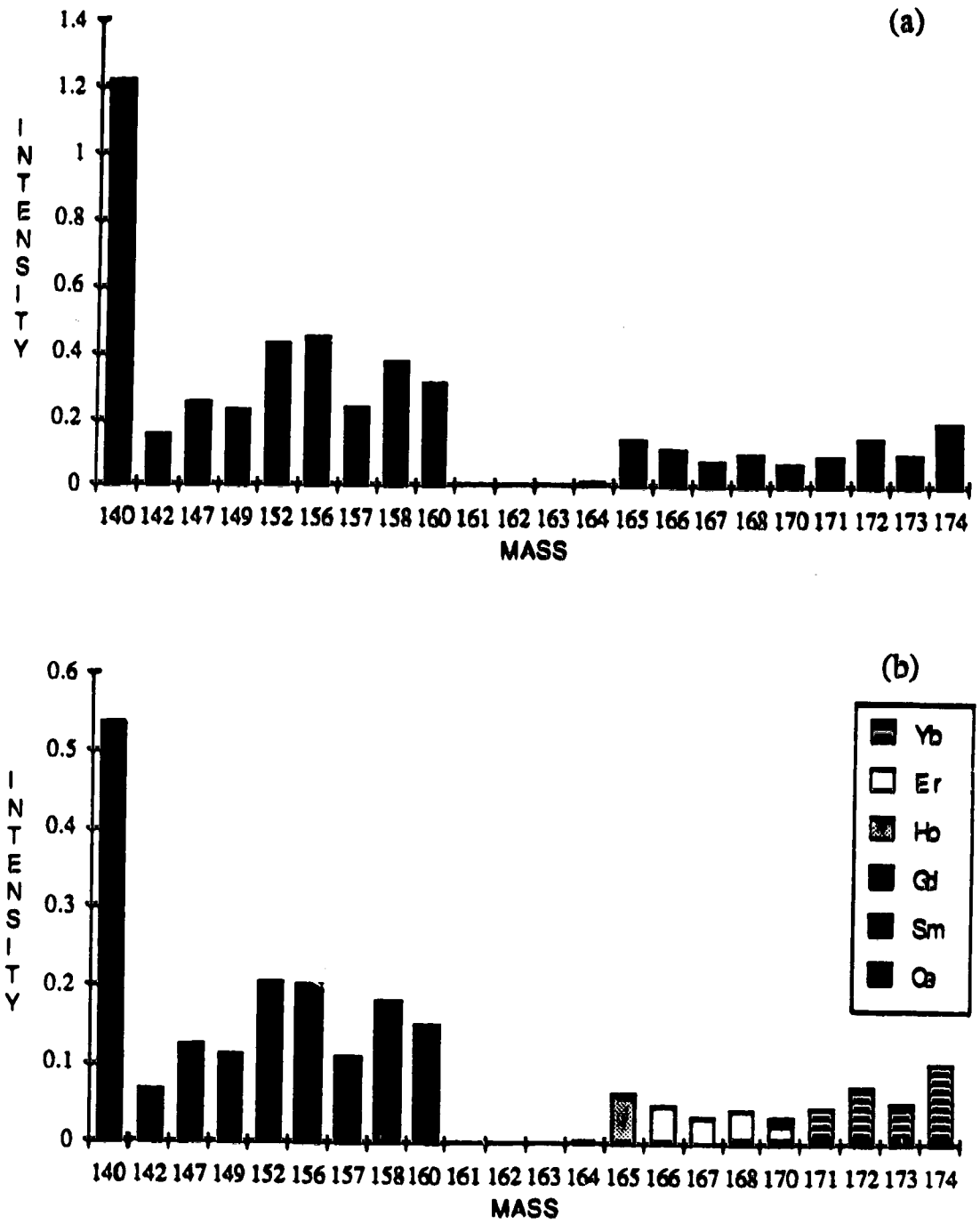

Figure 4.3 Mass spectrum for a mixture of rare earths,Yb, Er, Ho, Gd, Sm and Ce (a). Synthesized mass spectrum for the same mixture built up from the mass spectra of each of its components (b).

Table 4.3 Rare Earth Element Interferences on Isotopes Required for Gauss Elimination.

Isotope	Isobaric	Oxide/Hydroxide
^{140}Ce		
^{152}Sm	^{152}Gd	^{136}CeO
^{149}Sm		
^{157}Gd		$^{140}CeOH$
^{158}Gd	^{158}Dy	^{142}CeO
^{164}Dy	^{164}Er	^{148}SmO
^{163}Dy		^{147}SmO
^{165}Ho		^{149}SmO
^{166}Er		^{150}SmO
^{174}Yb	^{174}Hf	^{158}GdO, ^{158}DyO

determination: I_n, the ion count at mass n; M(x)/M(y), the abundance ratio of isotopes at masses x and y of element M; M(x)O/M(y), the oxide ratio of MO/M where the isotope of M is not necessarily the same; and C, the concentration.

The equations yielding the concentration of each element are derived in the following manner. As an example consider Sm. The concentration of Sm is given by:

$$C_{Sm,unk} = \frac{I_{Sm(152),unk}}{I_{Sm(152),std}} C_{Sm,std} \qquad 4.1$$

In order to solve this equation the term $I_{Sm(152),unk}$ must be found. From the list of interferences (Table 4.3) we can see that:

$$I_{152,unk} = I_{Sm(152)} + I_{Gd(152)} + I_{Ce(136)O} \qquad 4.2$$

This equation introduces the new variables $I_{Gd(152)}$ and $I_{Ce(136)O}$ .We can write an equation for $I_{Ce(136)O}$:

$$I_{Ce(136)O} = \left(\frac{Ce(136)O}{Ce(140)}\right) I_{Ce(140),unk} \qquad 4.3$$

and an equation for $I_{Gd(152)}$:

$$I_{Gd(152)} = \left(\frac{Gd(152)}{Gd(157)}\right) I_{Gd(157)} \qquad 4.4$$

Another new variable has been introduced, $I_{Gd(157)}$, which may be determined by:

$$I_{157,unk} = I_{Gd(157)} + I_{Ce(140)OH} \qquad 4.5$$

which introduces a sixth variable, $I_{Ce(140)OH}$. This variable may be determined by the following equation.

$$I_{Ce(140)OH} = \left(\frac{Ce(140)OH}{Ce(140)}\right) I_{140,unk} \qquad 4.6$$

At this point we have six equations in six unknowns, $C_{Sm,unk}$, $I_{Sm(152)}$, $I_{Gd(152)}$, $I_{Ce(136)O}$, $I_{Gd(157)}$ and $I_{Ce(140)OH}$ and can solve for $C_{Sm,unk}$ (see equation 4.8, Table 4.4). The same procedure was followed for the remaining elements and the resulting equations are presented in Table 4.4. This method may be easily extended to include Nd, Pr and Hf or all the rare earths but in order to keep the correction equations from becoming too cumbersome it was decided to keep the system relatively small.

In order to use these equations ion counts must be measured at each of the masses for the isotopes listed in Table 4.3. Measurements for single element standards for each of the rare earth elements will provide the needed oxide ratios and abundance ratios. The abundance ratios may also be taken from tables of natural abundances of stable isotopes. The measurements for a set of standards and samples at each of the 10 masses listed in Table 4.3 were used for this section of the study. The standards were 10μg/mL as was the Cs internal standard. The concentrations of the elements were calculated by Gauss elimination according to the equations in Table 4.4. The results are

Table 4.4 Equations from Gauss Elimination.

Equation 4.7, Ce at mass 140:

$$C_{Ce} = \frac{I_{140,unk}}{I_{140,std}} C_{Ce,std}$$

Equation 4.8, Sm at mass 152:

$$C_{Sm} = \left\{ \frac{I_{152,unk} - I_{140,unk}\left(\frac{Ce(136)O}{Ce(140)}\right) - \left[I_{157,unk} - I_{140,unk}\left(\frac{Ce(140)OH}{Ce(140)}\right)\right]\left(\frac{Gd(152)}{Gd(157)}\right)}{I_{152,std}} \right\} C_{Sm,std}$$

Equation 4.9, Sm at mass 149:

$$C_{Sm} = \frac{I_{149,unk}}{I_{149,std}} C_{Sm,std}$$

Equation 4.10, Gd at mass 158:

$$C_{Gd} = \left\{ \frac{I_{158,unk} - \left[I_{163,unk} - I_{149,unk}\left(\frac{Sm(147)O}{Sm(149)}\right)\right]\left(\frac{Dy(158)}{Dy(163)}\right) - I_{140,unk}\left(\frac{Ce(142)O}{Ce(140)}\right)}{I_{158,std}} \right\} C_{Gd,std}$$

Equation 4.11, Gd at mass 157:

$$C_{Gd} = \left\{ \frac{I_{157,unk} - I_{140,unk}\left(\frac{Ce(140)OH}{Ce(140)}\right)}{I_{157,std}} \right\} C_{Gd,std}$$

Equation 4.12, Dy at mass 164:

$$C_{Dy}=\left\{\frac{I_{164,unk}-\left[I_{166,unk}-I_{149,unk}\left(\frac{Sm(150)O}{Sm(149)}\right)\right]\frac{Er(164)}{Er(166)}-I_{149,unk}\left(\frac{Sm(148)O}{Sm(149)}\right)}{I_{164,std}}\right\}C_{Dy,std}$$

Equation 4.13, Dy at mass 163:

$$C_{Dy}=\left\{\frac{I_{163,unk}-I_{149,unk}\left(\frac{Sm(147)O}{Sm(149)}\right)}{I_{163,std}}\right\}C_{Dy,std}$$

Equation 4.14, Ho at mass 165:

$$C_{Ho}=\left\{\frac{I_{165,unk}-I_{149,unk}\left(\frac{Sm(149)O}{Sm(149)}\right)}{I_{165,std}}\right\}C_{Ho,std}$$

Equation 4.15, Er at mass 166:

$$C_{Er}=\left\{\frac{I_{166,unk}-I_{149,unk}\left(\frac{Sm(150)O}{Sm(149)}\right)}{I_{166,std}}\right\}C_{Er,std}$$

Equation 4.16, Yb at mass 174:

$$C_{Yb}=\left\{\frac{I_{174,unk}-\left[I_{157,unk}-I_{140,unk}\left(\frac{Ce(140)OH}{Ce(140)}\right)\right]\left(\frac{Gd(158)O}{Gd(157)}\right)\left[I_{163,unk}-I_{149,unk}\left(\frac{Sm(147)O}{Sm(149)}\right)\left(\frac{Dy(158)O}{Dy(163)}\right)\right]}{I_{174,std}}\right\}C_{Yb,std}$$

presented in Table 4.5. There are two equations that may be used to calculate the concentrations of Sm, Gd and Dy in this system and the results for both are included. In general, the concentrations determined in the analysis match the prepared concentrations. In sample 1 the concentration of Ce was found to be lower than expected being only 9.5μg/mL instead of 10.0μg/mL. The determination of Sm in sample 4 was also low but the 100μg/mL concentration in that sample is beyond the linear range of the calibration curve. Sample 5 was prepared with 550μg/mL of Sm and since the signal intensity corresponding to that much Sm exceeds the capabilities of the detection system the ICP-MS was forced into its shutdown mode for the Sm measurements for that sample. Because the Sm intensities could not be determined for this sample the concentrations of Gd, Dy, Er, Ho and Yb could not be calculated. This is a limitation to the Gauss approach for determining element concentrations.

2. Applying Principal Components Analysis.

The limitations in the Gauss elimination approach to correcting for the spectroscopic overlaps caused by oxides in ICP-MS lead us to investigate the applicability of principal components analysis to the problem. Data corresponding to the standards and mixtures of the rare earth elements are placed in a data matrix, [D], as set up in Figure 4.4. A covariance matrix, $[Z] = [D]^T[D]$, is obtained from this data matrix and principal components analysis is done using the NIPALs method [17]. The principal components analysis yields two matrices, one of which (the scores matrix) contains a series of eigenvalues and one of which (the loading matrix) contains the associated eigenvectors. The eigenvector associated with the largest eigenvalue spans

Table 4.5 Results from Gauss Elimination. (Concentration in μg/mL)

Elem.	Sam.	Prep.	GE1	GE2
Ce	1	10.0	9.5	
	2	0	0.0013	
	3	10.0	9.8	
	4	0	0.0019	
	5	0	0.0028	
Sm	1	8.0	8.2	8.0
	2	10.0	9.8	9.1
	3	10.0	9.6	9.4
	4	100	90	89
	5	550	-	-
Gd	1	6	5.9	5.8
	2	0.0	0.006	0.005
	3	0.0	0.045	0.026
	4	0.0	0.005	0.0007
	5	0.0	-	0.0011
Dy	1	4.0	4.2	3.9
	2	0.0	0.047	0.020
	3	5.0	5.0	5.0
	4	5.0	4.2	5.0
	5	2.5	-	-
Er	1	0.0	0.002	
	2	6.0	6.2	
	3	1.0	1.1	
	4	5.0	5.0	
	5	2.5	-	

Elem.	Sam.	Prep.	GE1	GE2
Ho	1	0.0	0.001	
	2	8.0	8.1	
	3	1.0	1.1	
	4	5.0	4.9	
	5	2.5	-	
Yb	1	0.0	0	
	2	4.0	3.8	
	3	1.0	0.98	
	4	0.0	0.003	
	5	0.0	-	

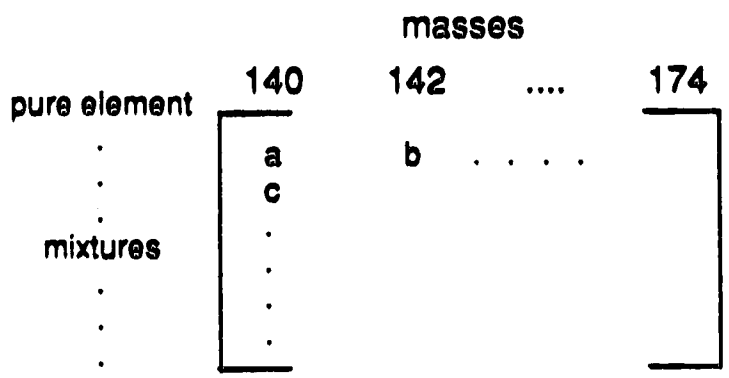

Figure 4.4 Data matrix for factor analysis.

the maximum variance in the data in one direction. The eigenvector associated with the second largest eigenvalue spans the maximum remaining variance in a direction orthogonal to the first eigenvector. This continues until all the variance in the data is accounted for and the factor space is defined. In this study each factor represents an element.

All raw data consists of two terms, pure data and experimental error. Because of this the PCA results yield more eigenvalues and eigenvectors than elements in the system. The eigenvectors associated with the larger eigenvalues are associated primarily with the data and the eigenvectors associated with the smaller eigenvalues are associated primarily with the error. An indicator is required to enable us to decide where the cutoff is between the eigenvectors representing data and those associated with error. Two such indicators are the IND function, an empirical relationship described by Malinowski and Howery [16] and the eigenratio used by Wirsz and Blades [10]. The IND function reaches a minimum and the eigenratio reaches a maximum at the number of factors required to span the data space. The eigenratios and IND function results for the data presented in Table 4.6 are displayed in Figure 4.5. Seven factors are recommended from these indicators which equals the number of elements in the sample. Extracting the proper number of factors tells us that we have chosen a good selection of masses to represent our system. Obtaining an unexpected number of factors may give an indication that we may have missed an element or that another set of masses may be better. The qualitative capabilities of the ICP-MS are excellent and can be employed to help sort out a problem in this area if one occurs.

Upon completion of this first step, we have determined the number of factors required to span the factor space, ie. the number of elements in our

Table 4.6 Concentrations of the seven rare earth elements as determined by PCA. (Concentration in μg/mL)

	Ce		Sm	
Sam.	Prep.	Meas.	Prep.	Meas.
1.	0.10	.097	0.25	0.26
2.	0	0	0.10	0.089
3.	0	0	0.50	0.51
4.	1.0	1.03	0.75	0.77
5.	0.75	0.85	1.0	1.03

	Gd		Dy	
Sam.	Prep.	Meas.	Prep.	Meas.
1.	0.50	0.51	0.75	0.79
2.	0.25	0.25	0.50	0.51
3.	0.10	0.095	0.25	0.27
4.	0	0.014	0.10	0.106
5.	1.0	1.05	0	0.0003

	Ho		Er	
Sam.	Prep.	Meas.	Prep.	Meas.
1.	1.0	1.01	0	0.0001
2.	0.75	0.71	1.0	0.96
3.	0.50	0.53	0.75	0.79
4.	0.25	0.24	0.50	0.52
5.	0.10	0.107	0.25	0.26

	Yb	
Sam.	Prep.	Meas.
1.	0	0.0011
2.	0	0
3.	1.0	0.99
4.	0.75	0.74
5.	0.50	0.46

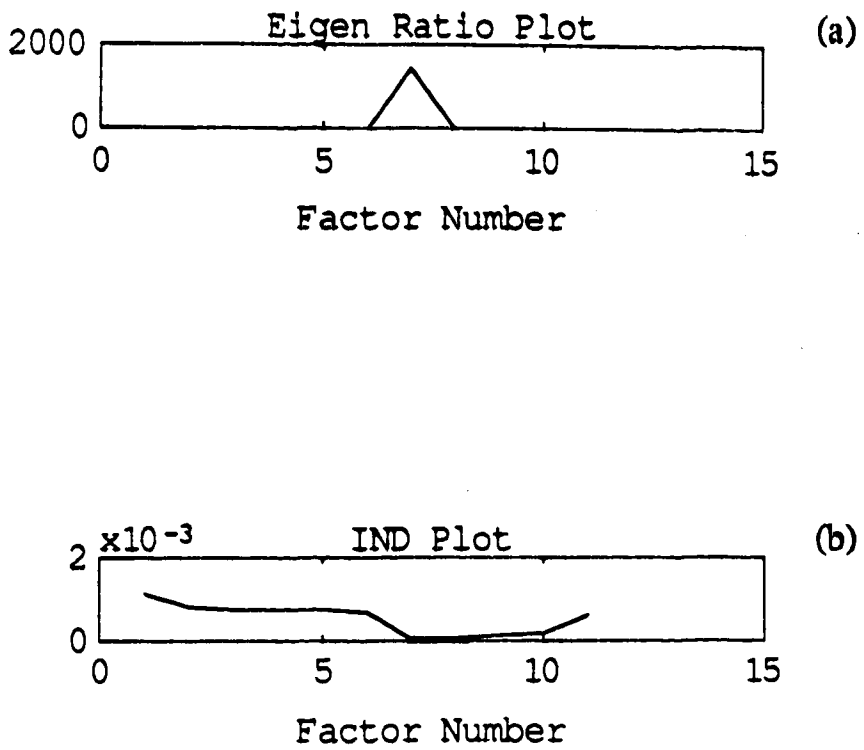

Figure 4.5 Typical eigenratio plot (a) and IND plot (b) obtained from abstract factor analysis.

system. We also have these factors (elements) separated in space. The problem that exists at this point is that there is no physical significance to the data. A transformation step is now needed in order to obtain a set of factors that are physically significant. We must rotate the abstract factors from an abstract factor space into an element space. This is done by target transformation [16]. The requirements of target transformation are straight forward. A transformation matrix is required to rotate the abstract data into element space. In order to obtain the transformation matrix a set of test vectors that are independent and cover the factor space are required. In this application these are the individual mass spectra for the elements in the system; in this example, the spectra displayed in Figures 4.1 and 4.2. The target matrix has the same form as the data matrix and consists of target vectors composed of the spectra of the single element standards. The same masses that were used in the original data matrix are required here.

If the test vectors are good they will not introduce excess error into the system. If they are inappropriate, however, they will add excessive error to the system and spoil the results. Malinowski and Howery describe an indicator function called SPOIL [16] which provides an indication of whether or not the test vector is applicable to a given system. A small SPOIL value suggests that the test vector should be used and a large SPOIL indicates that it should be discarded. The SPOIL values for the seven pure element standards used as test vectors are plotted in Figure 4.6a. All seven SPOIL values are less than 2.5 and are acceptable. Malinowski and Howery [16] suggest a SPOIL of 6 as the maximum for a cutoff between acceptable and unacceptable test vectors. The SPOIL values for nine test vectors are plotted in Figure 4.6b. In this set of test vectors the first seven are the pure element standards and vectors 8 and 9 are

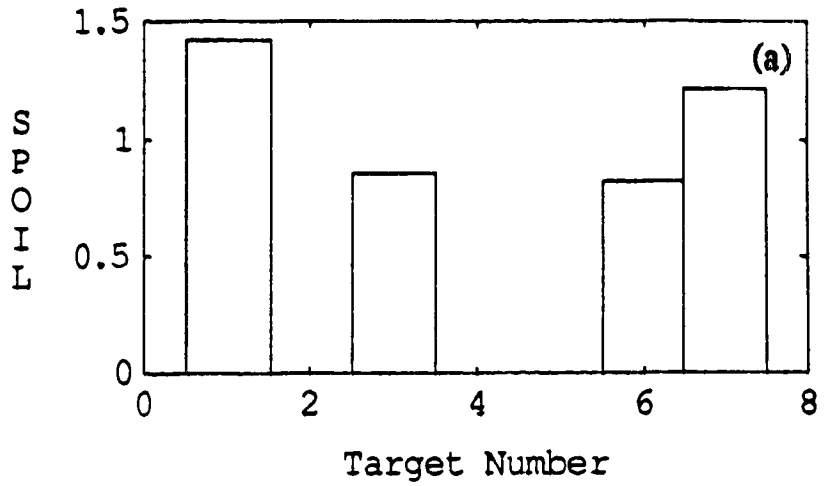

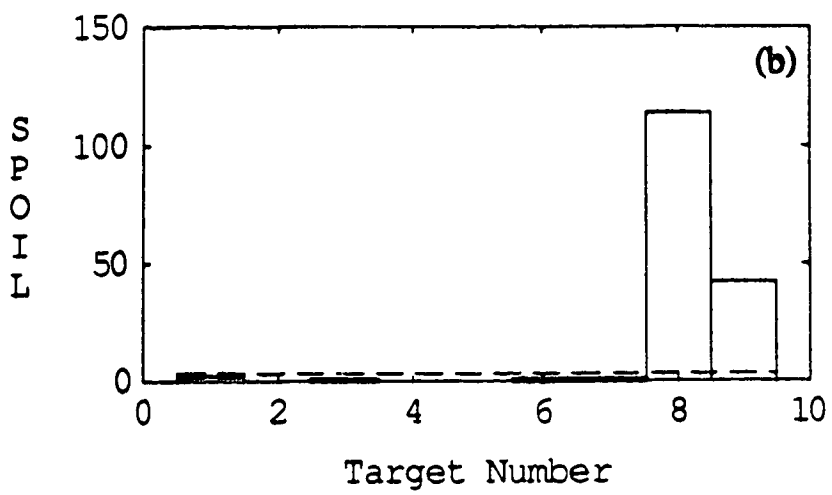

Figure 4.6 Typical SPOIL plot for target transformation analysis. Plot (a) corresponds to seven applicable target vectors. Plot (b) includes two inappropriate target vectors, 8 and 9.

synthetic and unrelated to the data; that is they consist of a set of numbers unrelated to any element spectrum. It is clear from the large SPOIL values associated with them that they are inappropriate for use in this system.

Once all the test vectors are found a transformation matrix may be built and the target factors may be calculated. These factors are obtained by using the transformation matrix to rotate the abstract factors into element space. Thus we obtain an axis in hyperspace for each element and a set of factors projected onto each of these axes which give an indication of the element concentration. Following this step, the actual concentration of each element in each sample may be obtained by multiplying the target factors by the concentration of the appropriate rare earth element standard. The measured concentrations for this set of data are presented in Table 4.6. In this data set all 22 masses (Table 4.2) were used in the principal components analysis and the standards were all 0.50μg/mL. An internal standard of 0.50μg/mL Cs was used.

3. Comparison of Gauss Elimination and PCA.

In the previous section using PCA, the system was well overdetermined using measurements made at 22 masses, as listed in Table 4.2. Although one of the requirements of PCA is that the system must be overdetermined, the data analysis can be successful when fewer masses are employed. PCA was employed on the data used in the Gauss elimination section using the same masses (Table 4.3) required for the algebraic equations listed in Table 4.4. The results are presented in Table 4.7. The "0" entries indicate that a negative target score was obtained in the factor analysis process. A small negative number eg. -0.0003 was usually obtained. Large negative

numbers indicate a problem in the system such as the use of an inappropriate target vector.

In general, the results obtained with the principal components analysis are acceptable, in agreement with the Gauss elimination results and with the prepared concentrations. As with the Gauss results the Sm concentration in sample 4 is low since it is beyond the linear dynamic range for the element. The Ce concentration in sample 1 was low but in agreement with the Gauss results.

Also included in Table 4.7 are the PCA results for the analysis of the same solutions using a different set of ten masses than the set of ten masses required for Gauss elimination. The alternate mass set is presented in Table 4.8. The results are essentially the same, demonstrating the greater flexibility of the PCA method. If a required mass for Gauss elimination cannot be measured the concentrations of the affected elements cannot be determined. With PCA the loss of a single mass may not be as critical unless of course the mass is that of a mono-isotopic element of interest.

To illustrate the point, the concentrations of the elements Gd, Dy, Er, Ho and Yb were determined by PCA for the 550μg/mL Sm solution, sample 5, Table 4.5. Data for all masses listed in Table 4.2 were used except for the masses associated with Sm^+. The Gauss elimination technique cannot yield the concentrations for these elements because Sm^+ intensities are required in the equations for the oxide corrections. The desired information, namely the element concentrations, can be obtained through PCA, however. The results are presented in Table 4.9. The measured concentrations are in agreement with the prepared concentrations.

Table 4.7 Results from principal components analysis. (Concentration in μg/mL)

Elm.	Sam.	Prep.	Gauss Masses	Alternate Masses
Ce	1	10.0	9.5	9.5
	2	0	0*	0
	3	10.0	9.8	9.8
	4	0	0	0
Sm	1	8.0	8.1	8.1
	2	10.0	9.7	9.8
	3	10.0	9.6	9.6
	4	100	90	90
Gd	1	6	5.9	5.9
	2	0.0	0	0
	3	0.0	0.03	0.036
	4	0.0	0	0
	5	0.0	-	-
Dy	1	4.0	4.0	4.1
	2	0.0	0.005	0
	3	5.0	5.0	5.0
	4	5.0	4.8	4.8

Elm.	Sam.	Prep.	Gauss Masses	Alternate Masses
Er	1	0.0	0.001	0
	2	6.0	6.2	6.2
	3	1.0	1.1	1.0
	4	5.0	5.0	5.0
Ho	1	0.0	0	0
	2	8.0	8.1	8.1
	3	1.0	1.1	1.1
	4	5.0	4.9	4.9
Yb	1	0.0	0	0
	2	4.0	3.8	3.8
	3	1.0	0.97	0.97
	4	0.0	0	0

* Factor analysis result was a negative number.

- Not able to calculate.

Table 4.8 Alternate PCA Mass Set.

^{140}Ce	^{165}Ho
^{152}Sm	^{166}Er
^{158}Gd	^{168}Er
^{162}Dy	^{172}Yb
^{164}Dy	^{174}Yb

Table 4.9 PCA results in a 550μg/mL Sm matrix. (Concentration in μg/mL)

Elem.	Prep.	Meas.
Gd	0	0
Dy	2.5	2.5
Er	2.5	2.4
Ho	2.5	2.5
Yb	0	0

Conclusions.

The classical approach to correcting oxide overlap problems, that of Gauss elimination, may be employed in ICP-MS although it does have limitations. Separate standards must be run for each element in order to obtain the needed oxide ratios under the operating conditions used. These would have to be re-measured each day the analysis is to be done since the oxide ratios are sensitive to instrumental conditions. Abundance ratios are required either from tables or calculated from data measured for the individual element the standards. The correction equations become more complicated as more elements are included in the system and if a required intensity is above shutdown calculation of the element concentration is not possible.

In contrast the principal components analysis approach is more flexible. It, too, needs individual pure element standards to be used as targets and these must be run every day an analysis is done. This approach, however, removes the need for abundance ratios as the correction for isobaric overlap occurs automatically with the oxide correction due to the nature of the method. As the system becomes larger, ie. more elements are included, the matrices become larger but no new algebra is required. Another attractive feature is the flexibility in choosing the masses to be used in the analysis. There is more than one combination that may be used. The ability to determine some elements in the presence of high concentrations of interfering oxide formers is also an advantage.

References.

1. M. A. Vaughan and G. Horlick, Applied Spectrosc. **40**, 434-445, (1986).

2. E. Roaldset, Talanta, **17**, 593-598, (1970).

3. J.R. Bacon and A. M. Ure, Analytica Chimica Acta **105**, 163-176, (1979).

4. D. W. Zachmann, Anal. Chem. **60**, 420-427, (1988).

5. M. E. Tremblay, B. W. Smith and J. D. Winefordner, Analytica Chimica Acta **99**, 111-118, (1987).

6. A. R. Date and D. Hutchison J. Anal. Atom. Spectrom. **2**, 269-276, (1987).

7. T. Hirata, H. Shimizu, T. Akagi, H. Sawatari and A. Masuda, Analyt. Sci. **4**, 637-643, (1988).

8. H. P. Longerich, B. J. Fryer, D. F. Strong and C. J. Kantipuly, Spectrochim. Acta, **42B**, 79-92, (1987).

9. F. E. Lichte, A. L. Meier and J. C. Crock, Anal. Chem. **59**, 1150-1157, (1987).

10. D. F. Wirsz and M. W. Blades, Anal. Chem **58**, 51-57, (1986).

11. M. Otto and W. Wegscheider, Anal. Chem. **57**, 63-69, (1985).

12. F. Cahn and S. Compton, Applied Spectrosc. **42**, 865-872, (1988).

13. M. P. Fuller, G. L. Ritter and C. S. Draper, Applied Spectrosc. **42**, 228-236, (1988).

14. B. G. M. Vandeginste, W, Derks and G. Kateman, Analytica Chimica Acta, **173**, 253-264, (1985).

15. M. F. Devaux, D. Bertrand, P. Robert and M. Qannan, Applied Spectrosc. **42**, 1020-1023, (1988).

16. E. R. Malinowski and D. G. Howery, "Factor Analysis in Chemistry", John Wiley and Sons, 1980, New York.

17. P. Geladi and B. R. Kowalski, Analytica Chimica Acta, **185**, 1-17, (1986).

Chapter 5

Analysis of Steels Using Inductively Coupled Plasma Mass Spectrometry*

Inductively coupled plasma-mass spectrometry (ICP-MS) has now been used for the trace metal analysis of a variety of sample types. These include geological materials [1-5], sediments [6, 7], natural waters [8-11] and biological samples [12-14]. As experience has been gained with the technique the important areas to address during method development have now been delineated. These include compromise instrument settings [15-18], spectral interferences [16, 19] and matrix effects [20-23]. In addition, the analytical methodology normally incorporates the use of internal standardization. In this report these areas are addressed with respect to the analysis of steel samples.

Experimental

All analyses were carried out using a SCIEX (Perkin Elmer-Sciex) Elan Model 250 ICP-MS. A standard MAK optical emission ICP torch was used in conjunction with a Meinhard nebulizer and a Scott-type spray chamber. Referring to the study carried out by Vaughan et al. [18], it can be seen that compromise conditions of power and nebulizer flowrate are easily obtained for a range of elements. Indeed, the flow rate yielding maximum ion count

---

* A version of this chapter has been published. M. A. Vaughan and G. Horlick, J. Anal. Atom. Spectrom.,4, 45-50, (1989).

for a given power and sampling depth is essentially the same for the majority of elements. For this work a sampling depth of 15 mm from the load coil and a plasma forward power of 1.5 kW were chosen. A plasma power of 1.5 kW was used because of the high sensitivity that can be obtained at that power. The ion focusing lens voltages were a compromise chosen to cover a large mass range. Some sacrifice in intensity for the lighter elements was accepted in order to obtain stronger signals for the heavier elements. The ion lens voltages used are listed in Table 5.1.

Six National Bureau of Standards (NBS) Standard Reference Material (SRM) steel samples in chip form were chosen for this work. Three stainless steels; SRM 121d, SRM 123c and SRM 160b were selected along with SRM 361 and the modified steels SRM 362 and SRM 363. These steels were dissolved using a high temperature, high pressure decomposition method described by Fernando [24]. A 1 g sample was weighed into a 100 mL plastic beaker and 2 mL of concentrated HNO_3 was slowly added. This was followed by the slow addition of 4 mL of concentrated HCl. The mixture was warmed, 2 mL of HF was added and the mixture was warmed again until the reaction subsided. The contents of the beaker were transferred to the PTFE cup of a Parr bomb using a few milliliters of water and heated at 180°C for 1 h. The cooled mixture was diluted with deionized water, typically to 100 mL. All acids used were reagent grade. All standards were prepared from SPEX Industries Inc. standard solutions.

Table 5.1 Ion lens voltage settings.

Lens	Setting	Voltage (V)
Bessel Box Barrel (B)	50	5
Bessel Box Plates (P)	30	-18
Einzel Lens (E1)	80	-16
Photon Stop (S2)	50	-10

Results and Discussion

1. Qualitative Spectral Scans

One of the key features of ICP-MS is the ease with which qualitative analysis of a sample can be carried out. Mass spectra for one of the stainless steel samples (NBS 160b) are shown in Figures 5.1 and 5.2. The spectrum shown in Figure 5.1 is for a solution that had a total steel composition of 0.01%. The certified values for Ni, Cu and Mo are 12.26%, 0.172% and 2.38% thus the concentration of these species in this solution were 12.26 μg/mL, 0.172 μg/mL and 2.38 μg/mL. The spectra shown in Figure 5.2 are for a 0.1% solution of the NBS 160b stainless steel. Cd, Sn, Sb, Ba, W, and Pb were all readily identified. Of these, only Pb has a certified value (0.001%).

The simplicity of these spectra is in marked contrast to the corresponding atomic emission spectrum for this sample. The complexity of the atomic emission spectra of steels and stainless steels is well known and these mass spectra clearly illustrate the ease with which the elemental composition of such samples can be determined. This is further illustrated in Figure 5.3. Among the more difficult elements to determine in steels by atomic emission spectrometry are the rare earth elements. A mass spectrum of a low alloy steel (NBS 361) is shown in Figure 5.3a, illustrating the presence of a number of rare earth elements (La, Ce, Pr, and Nd) in this sample. The solution run to obtain this spectrum was 1% in steel. This steel (NBS 361) has certified values for Ce and Nd of 0.004% and 0.0007% and uncertified values for La and Pr of 0.001% and 0.0003%. These elements, often difficult to identify by emission spectrometry, can be easily verified and determined by ICP-MS.

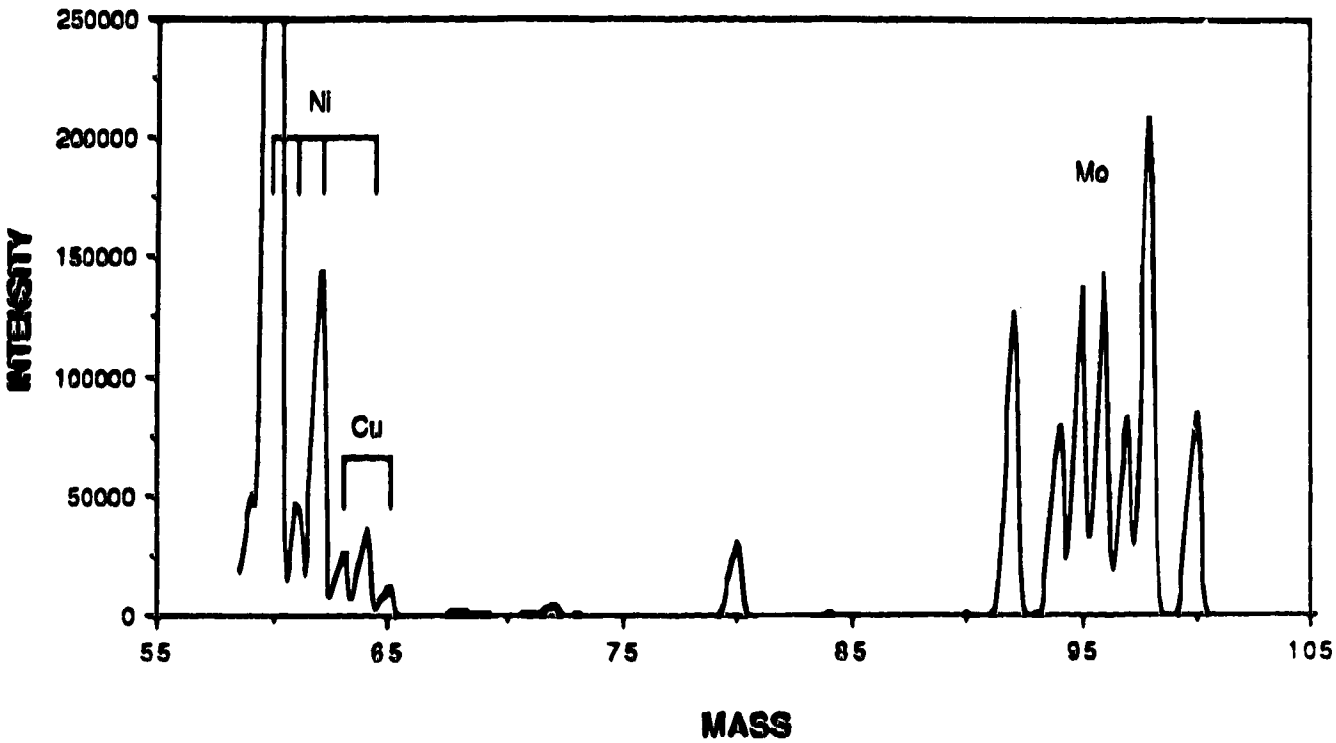

Figure 5.1. Spectrum of 0.01% stainless steel solution (Standard Reference Material NBS 160b).

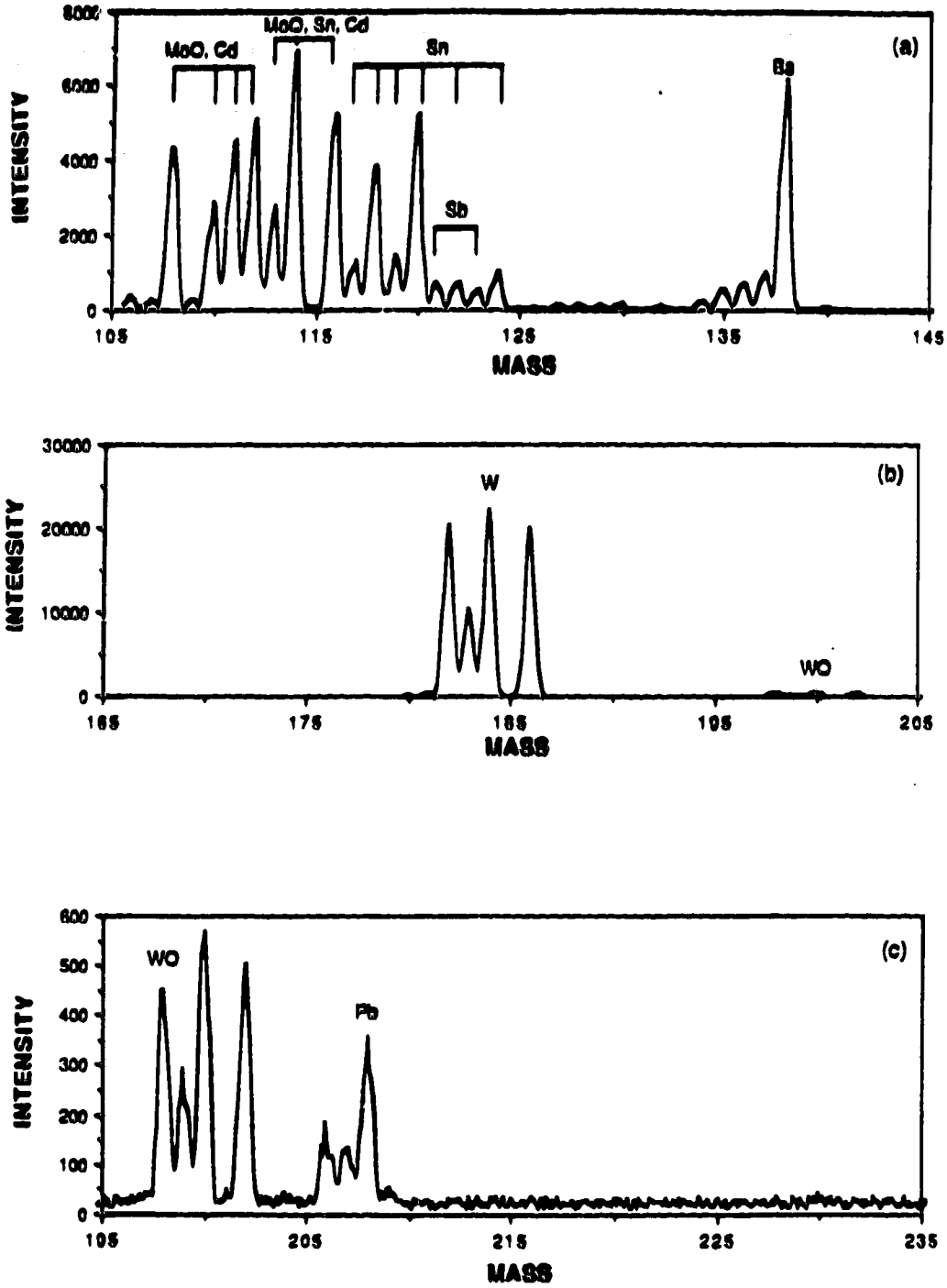

Figure 5.2. Spectra of 0.1% stainless steel solution (Standard Reference Material NBS 160b).

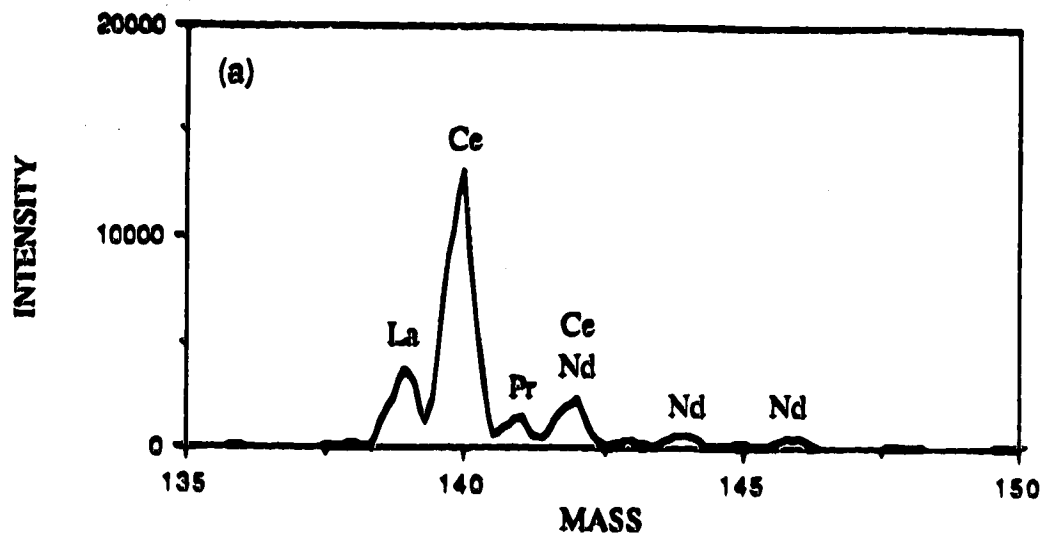

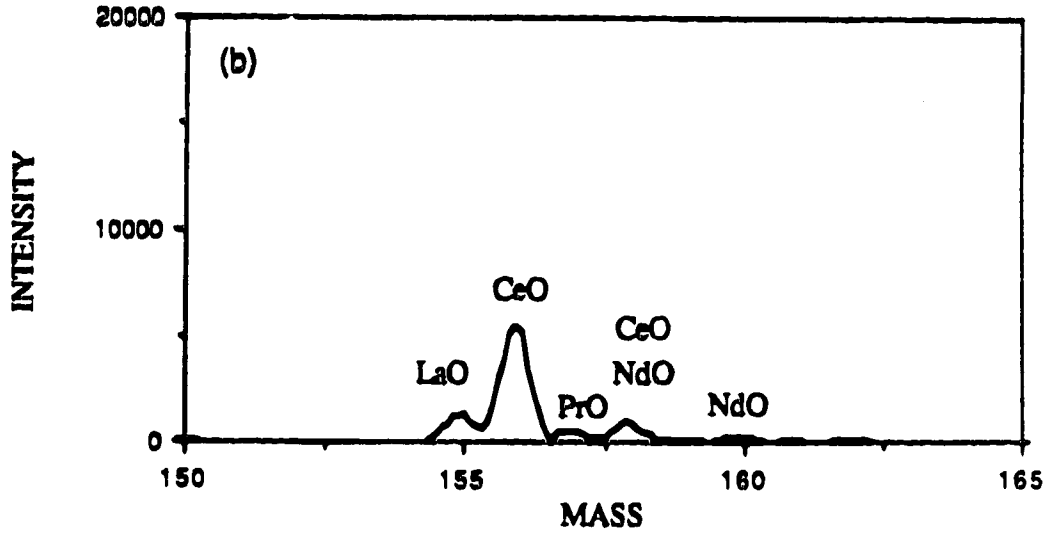

Figure 5.3. Spectrum of 1% steel solution showing rare earths and the associated oxides (Standard Reference Material NBS 361).

The mass spectra shown in Figures 5.1-5.3 also illustrate some potential problems when using ICP-MS for the analysis of steel samples. In particular, spectral interference problems can arise from metal oxide species as shown in Figures 5.2 and 5.3 This problem and additional spectral interference problems are discussed in the next section.

2. Evaluation of Potential Spectral Interferences

The basic isobaric and background spectral interferences in ICP-MS are well documented [16, 19]. Some of the major problem species are summarized in Table 5.2 for Fe and the more common elements determined in ferrous alloys. Only the major background species are listed for water, and dilute nitric acid, sulfuric acid and hydrochloric acid solutions, and the tables of Tan and Horlick [19] should be consulted for more details.

Unfortunately, some of the key elements of interest in ferrous metallurgy (S, Si, P and S) cannot readily be determined because of spectral overlaps with species basic to the ICP discharge. These include $^{14}N^{+}_{2}$, $^{14}N^{16}OH^{+}$ and $^{16}O^{+}_{2}$ which affect the major isotopes of Si, P and S. Iron itself is a problem, with its major isotope (^{56}Fe) affected by $^{40}Ar^{16}O^{+}$, and its next two most abundant isotopes ^{54}Fe and ^{57}Fe affected by $^{40}Ar^{14}N^{+}$ and $^{40}Ar^{16}OH^{+}$. That leaves only ^{58}Fe which, alas, has an isobaric overlap with the major Ni isotope.

Molecular background ions can also be formed from the components of the overall sample matrix. Sulfur and chlorine containing components can be particularly troublesome [19]. For example, with the dissolution procedure

Table 5.2 Basic spectral interferences for elements of major interest in ferrous alloys.

Element	Isobaric Overlaps	Background Species		
		H_2O, HNO_3	H_2SO_4	HCl
^{27}Al (100)				
^{28}Si (92.21)		$^{14}N_2$, $^{12}C^{16}O$		
^{31}P (100)		$^{14}N^{16}OH$		
^{32}S (95.02)		$^{16}O_2$	^{32}S	
^{48}Ti (73.98)	^{48}Ca (0.19)		$^{34}S^{14}N$, $^{32}S^{16}O$	
^{51}V (99.76)				$^{37}Cl^{14}N$, $^{35}Cl^{16}O$
^{52}Cr (83.76)		$^{40}Ar^{12}C$, $^{36}Ar^{16}O$	$^{36}S^{16}O$	$^{35}Cl^{16}OH$
^{54}Fe (5.82)	^{54}Cr (2.38)	$^{40}Ar^{14}N$		$^{37}Cl^{16}OH$
^{55}Mn (100)		$^{40}Ar^{14}NH$		
^{56}Fe (91.66)		$^{40}Ar^{16}O$		
^{57}Fe (2.19)		$^{40}Ar^{16}OH$		
^{58}Ni (67.77)	^{58}Fe (0.33)			
^{62}Ni (3.66)				
^{59}Co (100)				
^{63}Cu (69.1)				
^{98}Mo (32.5)	^{98}Ru (1.87)			

used in this study, the use of HCl presents some major potential problems. Two key elements that can be affected are V and As. A chloride containing matrix results in the formation of ClO^+ and $ArCl^+$. $^{35}Cl^{16}O^+$ interferes with $^{51}V^+$. This is a serious problem because $^{50}V^+$ is the only other naturally occurring isotope of vanadium and it has an abundance of only 0.25%. As well, $^{50}V^+$ suffers from isobaric overlaps from $^{50}Ti^+$ and $^{50}Cr^+$ and $^{36}Ar^{14}N^+$, $^{35}Cl^{15}N^+$ and $^{34}S^{16}O^+$ background species. $^{40}Ar^{35}Cl^+$ interferes with $^{75}As^+$ and as arsenic is monoisotopic this can be a major problem. These are just two of the problems with a chloride matrix; other chlorine-based background species have been tabulated by Tan and Horlick [19]. Should such species cause problems for elements of interest, as illustrated for V and As above, chloride must be eliminated from the sample dissolution procedure or removed from the final solution matrix.

Elements within the sample itself can also contribute to spectral interference problems. For steels, potential spectral interferences can occur because of FeO^+ and $FeOH^+$ formation. A spectrum of FeO^+ and $FeOH^+$ species is shown in Figure 5.4. With an oxide bond dissociation energy of 92 kcal/mol, iron is not a strong oxide former and it took a solution of 2000 μg/mL of Fe to produce the spectrum shown in Figure 5.4. At most the FeO^+/Fe^+ ratio was about 0.5%. Even so, the FeO^+ and $FeOH^+$ species can result in spectral interferences. These are summarized in Table 5.3. The most serious problem concerns Ge, where four out of five of its isotopes are affected, including the major Ge isotope at mass 74. The one remaining isotope (^{76}Ge) suffers an interference from $^{36}Ar^{40}Ar^+$. Thus, determinations of trace Ge in steels cannot readily be done by ICP-MS.

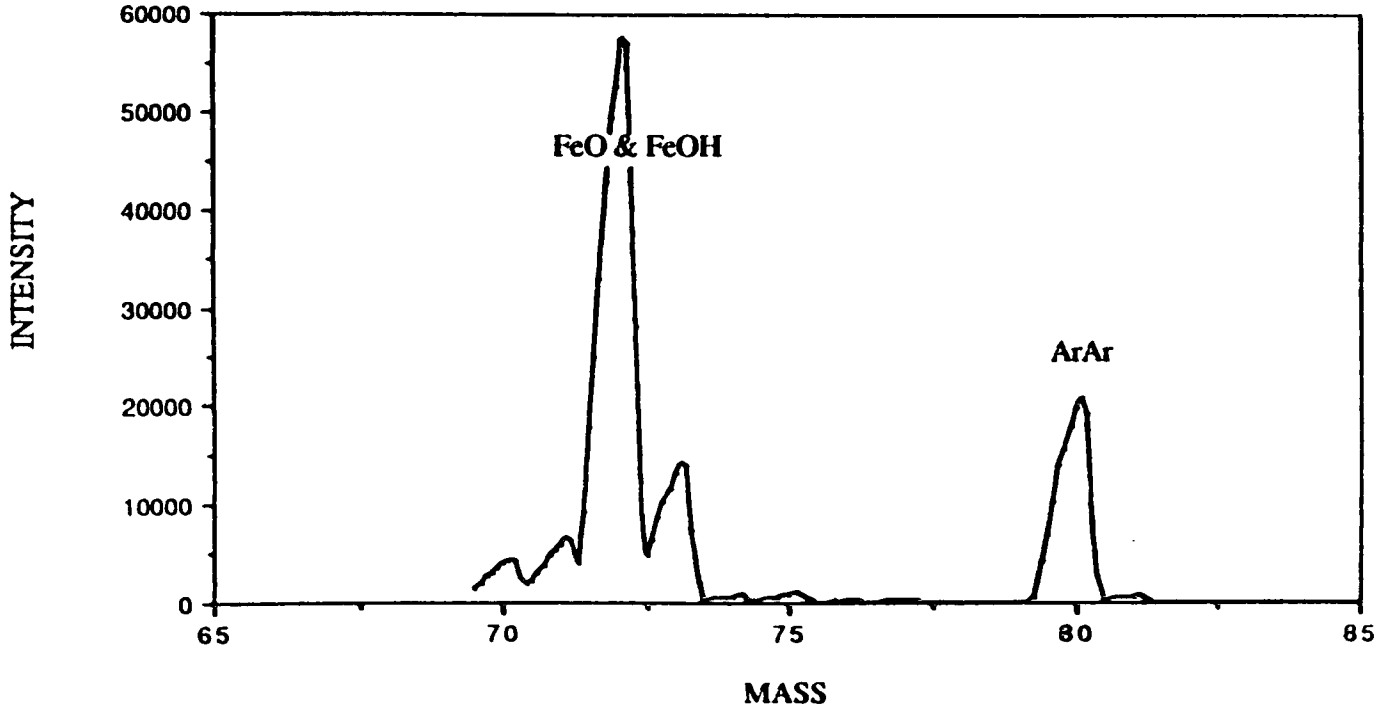

Figure 5.4. Spectrum of FeO and FeOH for a 0.2% Fe solution.

Table 5.3 Spectral interferences due to FeO and FeOH

Species	Mass	% Abund. of Fe Isotope	Affected Species
FeO	70	5.82	Zn (0.62), Ge (20.51)
	72	91.66	Ge (27.4)
	73	2.19	Ge (7.76)
	74	0.33	Ge (36.56), Se (0.87)
FeOH	71	5.82	Ga (39.84)
	73	91.66	Ge (7.76)
	74	2.19	Ge (36.56), Se (0.87)
	75	0.33	As (100)

In addition to Fe, other sample components may cause MO^+ and MOH^+ spectral interference problems. For example, it can be seen in Figure 5.2 that some masses of both Cd and Sn suffer spectral overlap from MoO^+'s. Also, as shown in Figure 5.3b, the rare earth elements are particularly strong oxide forming elements as the oxides of La, Ce, Pr, and Nd are all readily observed. These oxides present spectral overlap problems for some masses of Gd (LaO), Gd, Sm (CeO's), Gd (PrO) and Gd, Tb, Dy, Er (NdO's). Detailed tables of these interferences have been published by Vaughan and Horlick [16].

Finally, major sample components (X) can combine with argon to form ArX^+ species. An example of this is $ArCl^+$ formation, discussed earlier, in samples having hydrochloric acid as one of the major components. Another of these species, $ArFe^+$, should be considered when doing ferrous analysis, however, this ion was not observed even with Fe levels of 2000 ug/mL.

3. Instrument Stability and Internal Standardization

The short term stability of the ICP-MS was measured over a period of 11 min for Cu^+, Mo^+ and W^+ in a 0.1% steel solution which was aspirated continuously. The standard deviation of the signal over that time period was, on average, 3.5%. Rh, added to the sample at 1 µg/mL level to act as an internal standard, was also monitored and the stability of the response using the internal standard was measured. The standard deviation was 3.2% on average, comparable to the results obtained without using the internal standard.

The change in signal intensity over a longer period of time was also investigated. Data for the medium term drift were acquired over a period of

30 min while the 0.1% steel solution was aspirated. Plots of the medium term drift with and without the use of Rh as an internal standard are shown in Figure 5.5 The unratioed ion counts show a continuous downward drift with respect to time. However, when Rh is used as an internal standard, the drift in signal intensity with time is greatly reduced. The drift in signal is not as severe as presented in Figure 5.5 if a rinse solution is aspirated periodically during analysis, a practice which is routinely employed. The standard deviations for both short term and medium term drifts are presented in Table 5.4. In the medium term, the internal standard reduces the standard deviation of the signal significantly, from 10.9% on average to 2.3%.

Rh was chosen as the internal standard for steel work for several reasons. It is not present in the steel samples at significant levels. It is monoisotopic so there are no extra isobaric corrections to be made on account of the internal standard. It is not a strong oxide former, indeed no RhO^+ was observed in this work. Finally, it is in the mid-mass range, 103, a compromise position for any mass effects.

4. Matrix Effects

In ICP-MS, large amounts of concomitant elements are known to affect analyte sensitivity and most often signal suppressions are observed [20-23]. Thus, for steel analyses, the effect of high iron concentrations on analyte sensitivity must be evaluated. A set of plots illustrating the effect of 1000 μg/mL Fe on Zr, Ce and Ta signals is shown in Figure 5.6. Signal intensities are plotted as a function of nebulizer flowrate with the solid line corresponding to the analyte solution (0.1 μg/mL) containing no iron and the hatched line corresponding to a solution containing 1000 μg/mL Fe in

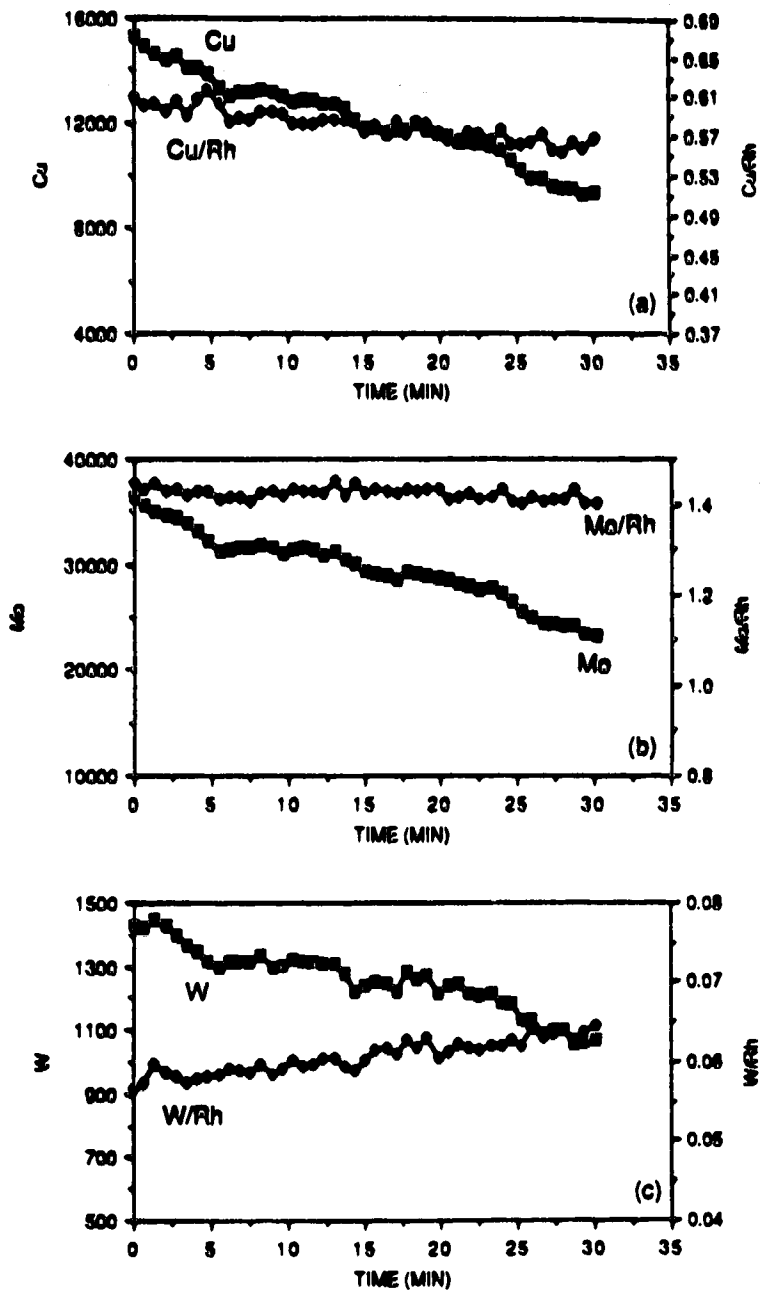

Figure 5.5. Signal intensity changes as a function of time for Cu, Mo and W in a 0.01% steel solution with and without the use of the Rh internal standard.

Table 5.4 RSD's for short (11 min) and medium term (30 min) measurement times with and without internal standardization.

Short Term

Element	% RSD
Cu	3.5
Cu/Rh	2.4
Mo	3.5
Mo/Rh	3.4
W	3.4
W/Rh	3.8

Medium Term

Element	% RSD
Cu	13.2
Cu/Rh	2.5
Mo	11.4
Mo/Rh	1.0
W	8.1
W/Rh	3.4

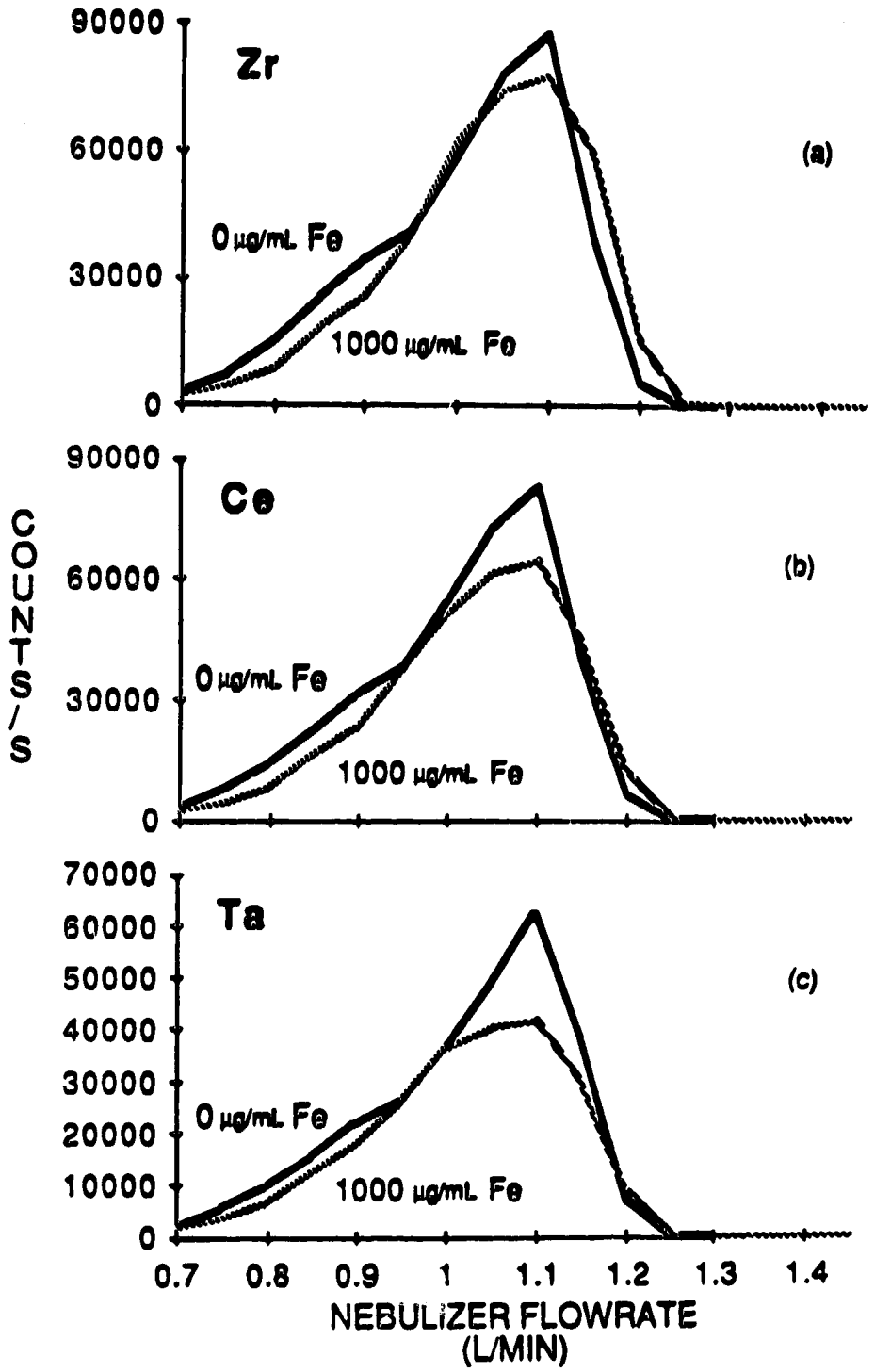

Figure 5.6. Ion count as a function of nebulizer flowrate for Zr, Ce and Ta in 5% HNO_3 and in a matrix of 1000 µg/mL Fe.

addition to 0.1μg/mL analyte. As shown by Tan and Horlick [20], the most severe suppression occurs at the nebulizer flowrate corresponding to the maximum analyte signal intensity. Overall though, suppressions are not too severe as iron is a relatively light matrix ion [20].

The matrix effect due to the high concentration of Fe can be minimized by a small reduction in the nebulizer flowrate from that which results in the maximum analyte signal. The dependence of the matrix effect on nebulizer flowrate and iron concentration is shown in Figure 5.7 for Zr^+. At the nebulizer flow rate for maximum analyte signal, the Zr^+ signal is suppressed by increasing amounts of Fe, but the matrix effect is eliminated at the lower nebulizer flowrate. This reduction in matrix effect does, however, come with a minor loss in analyte sensitivity. The loss in signal intensity resulting from the lower nebulizer flowrate is listed in Table 5.5 for a number of analytes. In the worst case the sacrifice in signal intensity was only 50%.

In ICP-MS, this type of matrix effect is a general effect [20] and mass trends have been observed for the matrix effect. Heavy matrix elements cause more severe matrix effects and light analytes are more seriously affected. However, the degree of the matrix effect changes slowly as a function of mass and over a modest mass range of analytes and for a relatively light matrix element (such as Fe) all analytes experience a similar matrix effect. One important consequence of this is that the use of internal standard methodology (as mentioned earlier, required to compensate for drift problems) will also compensate for matrix effects. Matrix effect data are shown in Figure 5.8 for Rh (internal standard) and two analytes (Nd and Ce) as a function of Fe concentration. These data were taken at a nebulizer flowrate corresponding to maximum signal response. The matrix effect is

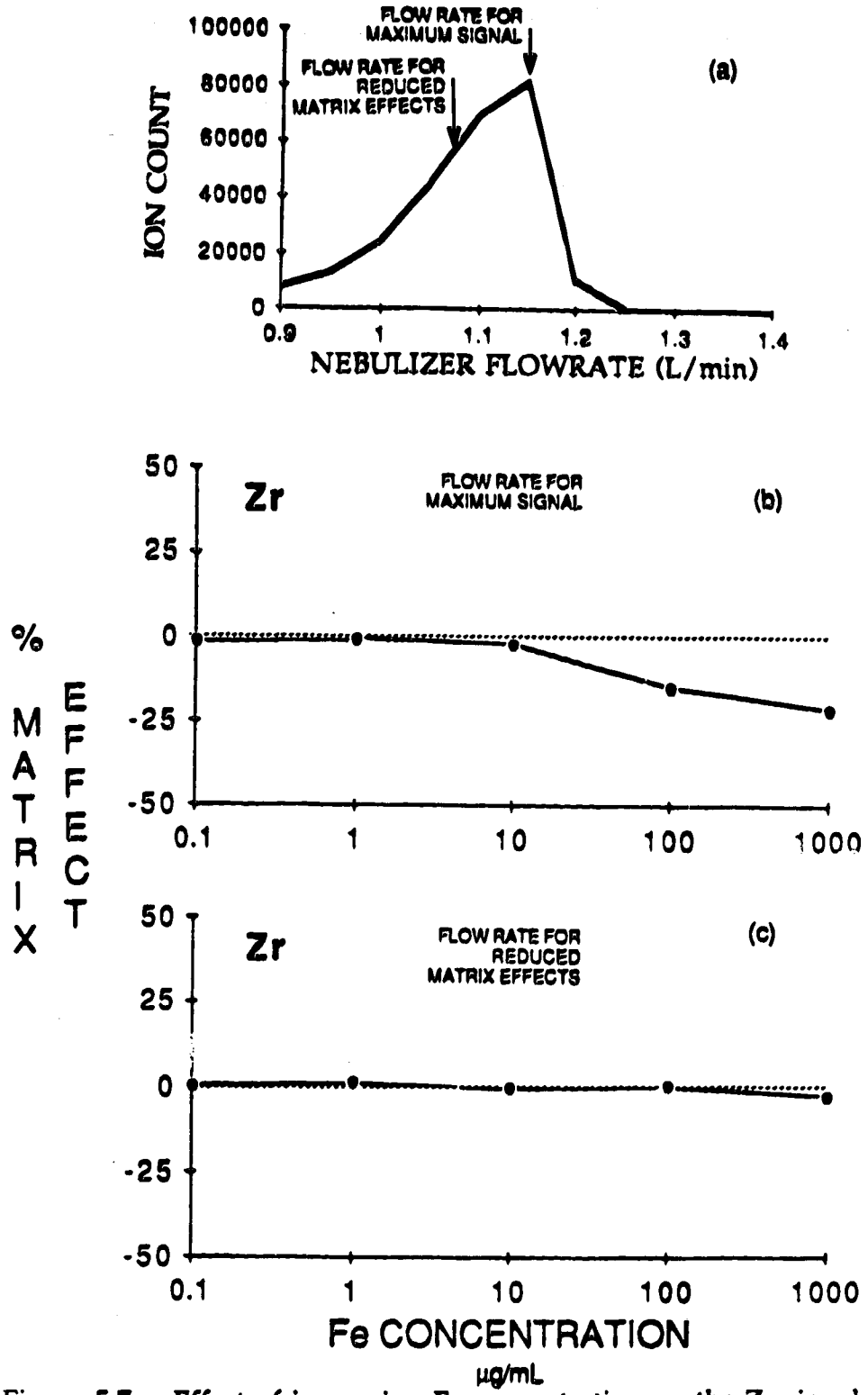

Figure 5.7. Effect of increasing Fe concentration on the Zr signal at the nebulizer flowrate yielding maximum signal intensity and at a reduced nebulizer flowrate.

Table 5.5 A comparison of signal intensities at nebulizer flowrates yielding maximum signal or reduced matrix effects.

Element	Flowrate for maximum intensity	Flowrate for reduced matrix effects	% Loss in signal intensity
Ce	22000	12500	43
Nd	6600	3600	45
Zr	20000	11500	43
Ta	12000	6000	50
Rh*	310000	190000	39

*The concentrations of all elements are 0.1 μg/mL except for Rh which is 1 μg/mL.

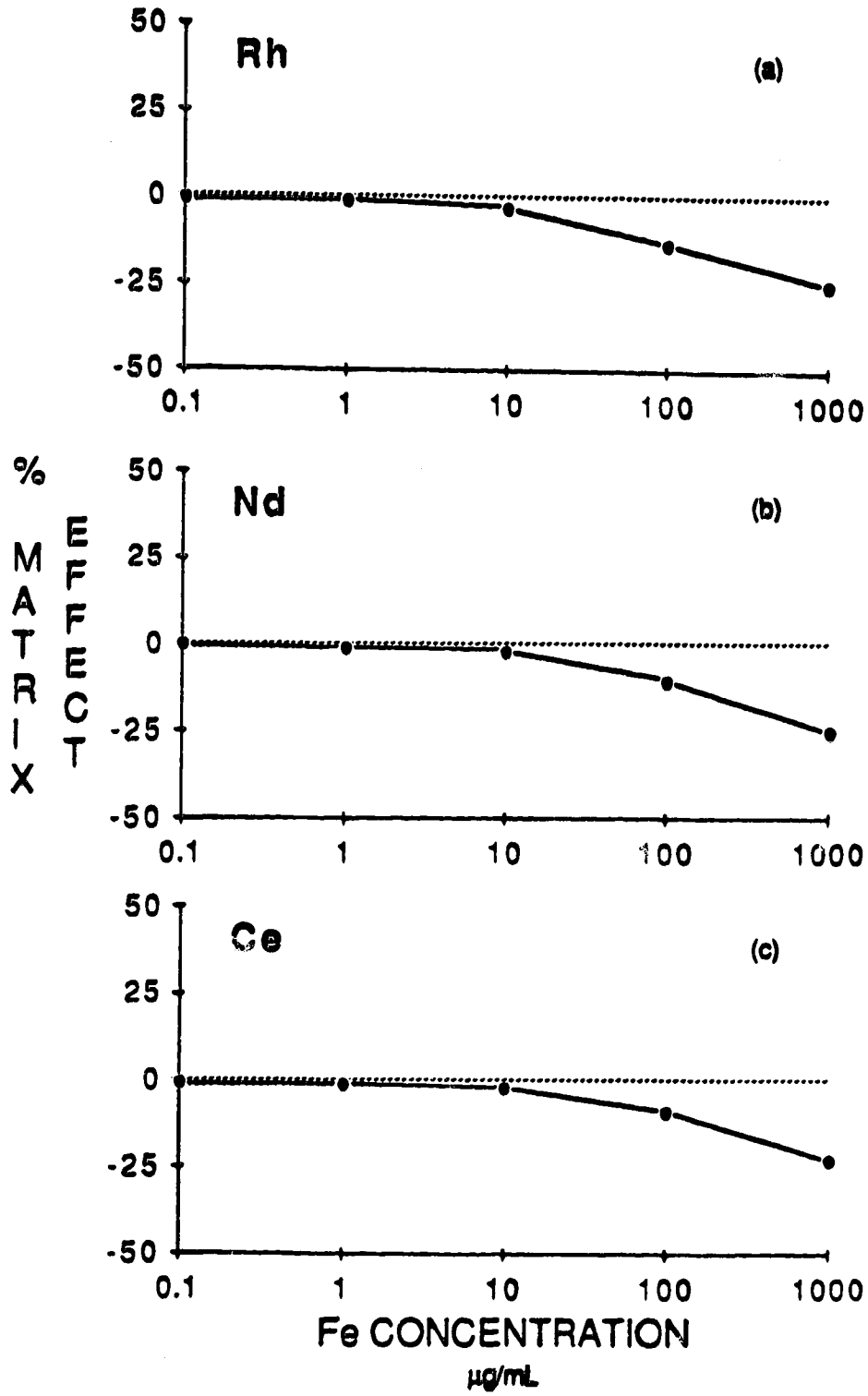

Figure 5.8. Effect of increasing Fe concentration on Rh, Nd and Ce signals plotted as percent matrix effect.

clearly similar for all species. Thus, when Rh is used as an internal standard (Figure 5.9) it compensates for the Fe induced matrix effect.

This method of compensating matrix effects is only effective if the analyte and the internal standard experience the same matrix effect. Ta, a heavier analyte, does not experience the exact same matrix effect and as such, Rh is not quite as effective in correcting for the matrix effect as it was for the lighter elements closer in mass to Rh. This is shown in Figure 5.10. Overall, however, the combined utilization of a reduced nebulizer flowrate and an internal standard provides robust compensation for matrix effects in ICP-MS.

It should be pointed out that while most published ICP-MS analyses have used internal standard methodology, the authors have either not realized or underestimated the extent to which the internal standard is compensating for matrix effects. They have emphasized the traditional role of the internal standard in compensating drift, 1/f noise and multiplicative noises in general. As a result, the real extent and universal existence of matrix effects in ICP-MS has been under appreciated.

5. Analytical Results

Aqueous calibration curves (i.e. no matrix matching) were used for the determination of Cu, Co, Ni, and Mo in the steel samples. Rh (1 μg/mL) was used as the internal standard. The calibration curves were linear over the three orders of magnitude needed for the samples. A calibration curve for Mo is presented as an example in Figure 5.11. All of the samples were 0.01% steel. The concentration ranges and the slopes of the log-log plots for the calibration curves are presented in Table 5.6. The analytical results plus the certified

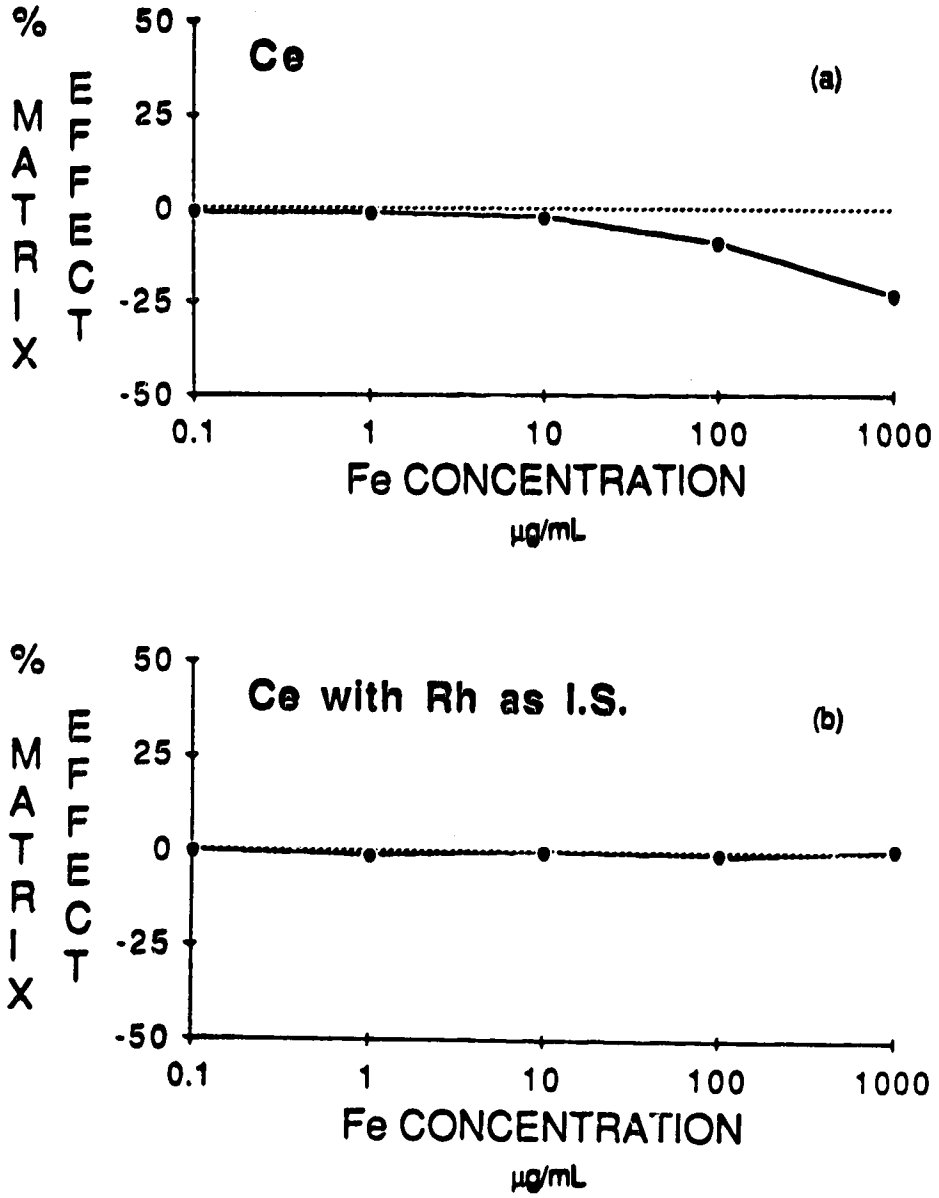

Figure 5.9. Effect of increasing Fe concentration on the Ce signal with and without the use of Rh as an internal standard.

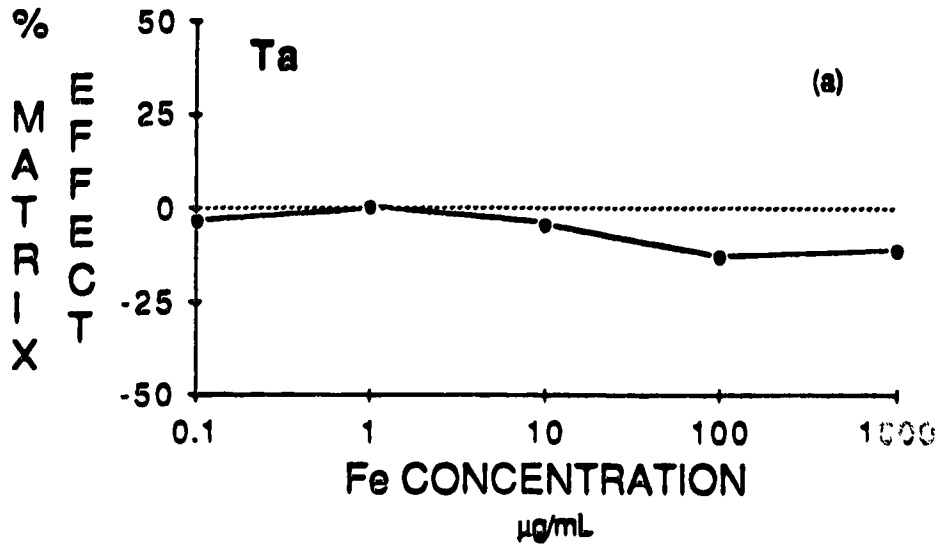

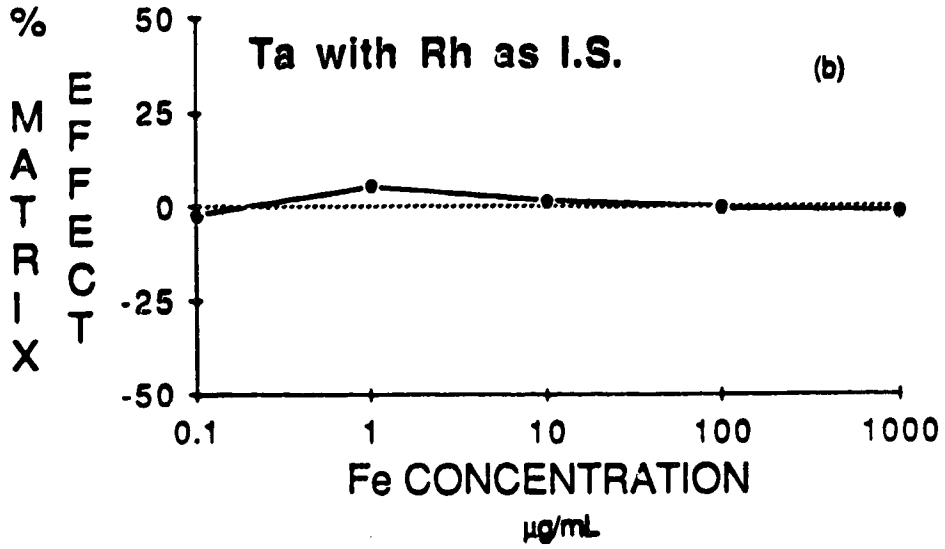

Figure 5.10. Effect of increasing Fe concentration on the Ta signal with and without the use of Rh as an internal standard.

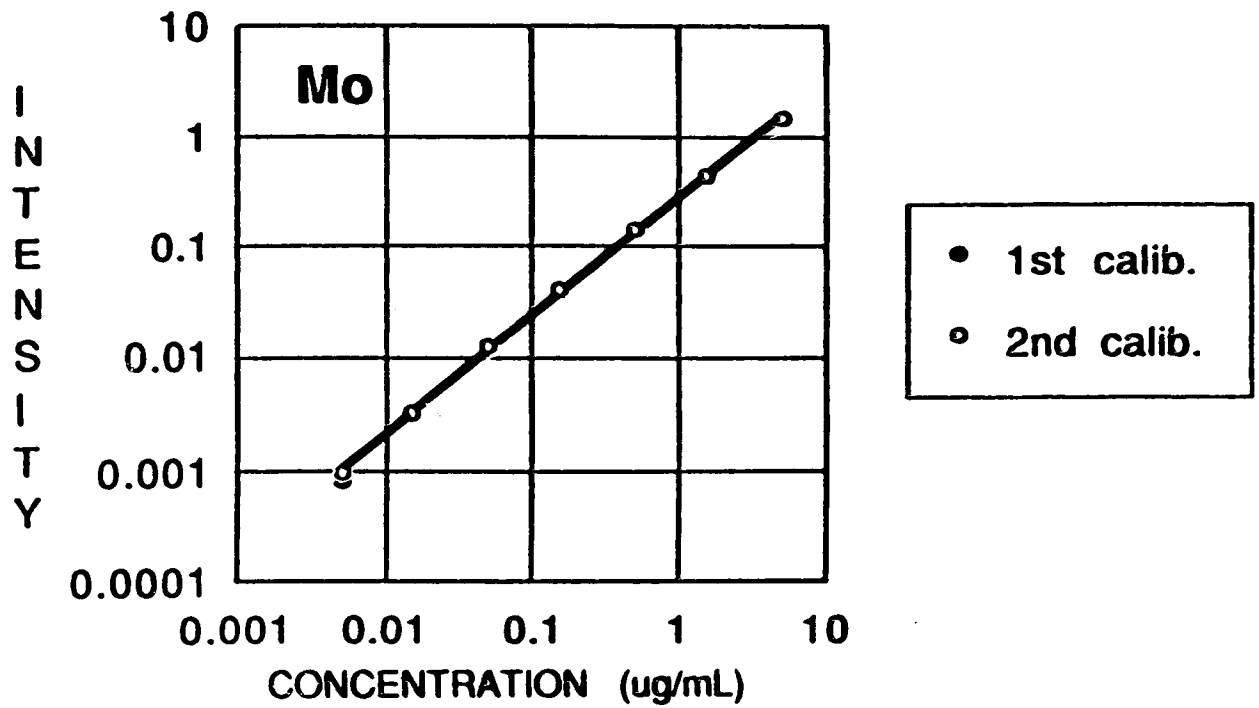

Figure 5.11. Aqueous calibration curve for Mo. Two calibrations acquired 0.5h apart. Rh used as an internal standard.

Table 5.6 Concentration ranges and slopes for aqueous calibration curves.

Element	Concentration range (μg/mL)	Slope of log-log plot
^{63}Cu	0.001000-1.000	1.01
^{59}Co	0.001001-1.001	1.01
^{62}Ni*	0.02090-20.10	1.01
^{98}Mo	0.005015-5.015	1.07

*Minor isotope ^{62}Ni was used.

values are presented in Table 5.7. The agreement between the experimental and the certified value was good with errors between 2 to 5%.

For a series of elements found in steels at lower concentrations, the method of standard additions was employed. Table 5.8 contains the results for two steels, NFS SRM 363 and 361. The sample solutions were 0.1% steel and again Rh was used as an internal standard. The standard addition curves were linear and yielded reasonable results although in the case of Ce the results were low. A sample standard addition plot, for W, is displayed in Figure 5.12.

Aqueous calibration curves were also used for the analysis of the major component of steel, namely iron. The analyses were done using a minor isotope of iron, ^{57}Fe 2.19% abundant. Background subtraction was used to correct for the interfering species $^{40}Ar^{16}OH^{+}$. The concentration range of the calibration curve was from 50 to 120 μg/mL Fe and a 0.1 μg/mL Rh internal standard was used. The results are presented in Table 5.9. Only three of the six steel samples had NBS values for % Fe in steel. There was good agreement between the reported values and the measured values with an error of only 1% on average.

Table 5.7 Analysis of 0.01% solutions of the standard reference steels. Results reported as % in steel; precision expressed as the standard deviation (n = 4). Aqueous calibration solutions used with Rh used as an internal standard.

% In Steel

	Cu		Co	
Sample	Measured	Certified Value	Measured	Certified Value
121	0.115 ± 0.002	0.121	0.100 ± 0.003	0.10
123	0.103 ± 0.002	0.103	0.128 ± 0.003	0.12
160	0.162 ± 0.002	0.172	0.110 ± 0.002	0.101
361	0.0400 ± 0.001	0.042	0.0293 ± 0.0005	0.032
362	0.476 ± 0.008	0.50	0.285 ± 0.008	0.30
363	0.0921 ± 0.001	0.10	0.00424 ± 0.001	0.048

% In Steel

	Ni		Mo	
Sample	Measured	Certified Value	Measured	Certified Value
121	10.74 ± 0.27	11.17	0.168 ± 0.008	0.165
123	11.05 ± 0.21	11.34	0.2316 ± 0.005	0.22
160	11.88 ± 0.20	12.26	2.324 ± 0.010	2.38
361	1.91 ± 0.02	2.00	0.204 ± 0.013	0.19
362	0.552 ± 0.006	0.59	0.0743 + 0.007	0.068
363	0.271 ± 0.003	0.30	0.038 ± 0.006	0.028

Table 5.8 Analysis of 0.1% solutions of the NBS standard reference steels 361 and 363 by the method of standard additions. Results reported as % in steel. Precision expressed as the standard deviation for one standard additions curve. Rh used as an internal standard.

	SRM 361		SRM 363	
Elem.	Exp.	Cert.	Exp.	Cert.
Pb	--	0.000025	0.0017±0.001	0.00186
Sb	0.0047±0.02	0.0042	0.0020±0.002	0.002
Zr	0.013±0.02	0.009	0.055±0.07	0.049
W	0.019±0.007	0.017	0.049±0.03	0.046
Ce	0.0034±0.001	0.0040	0.0012±0.02	0.003
Sn	0.0094±0.004	0.010	--	0.104
Ta	0.022±0.01	0.020	--	--

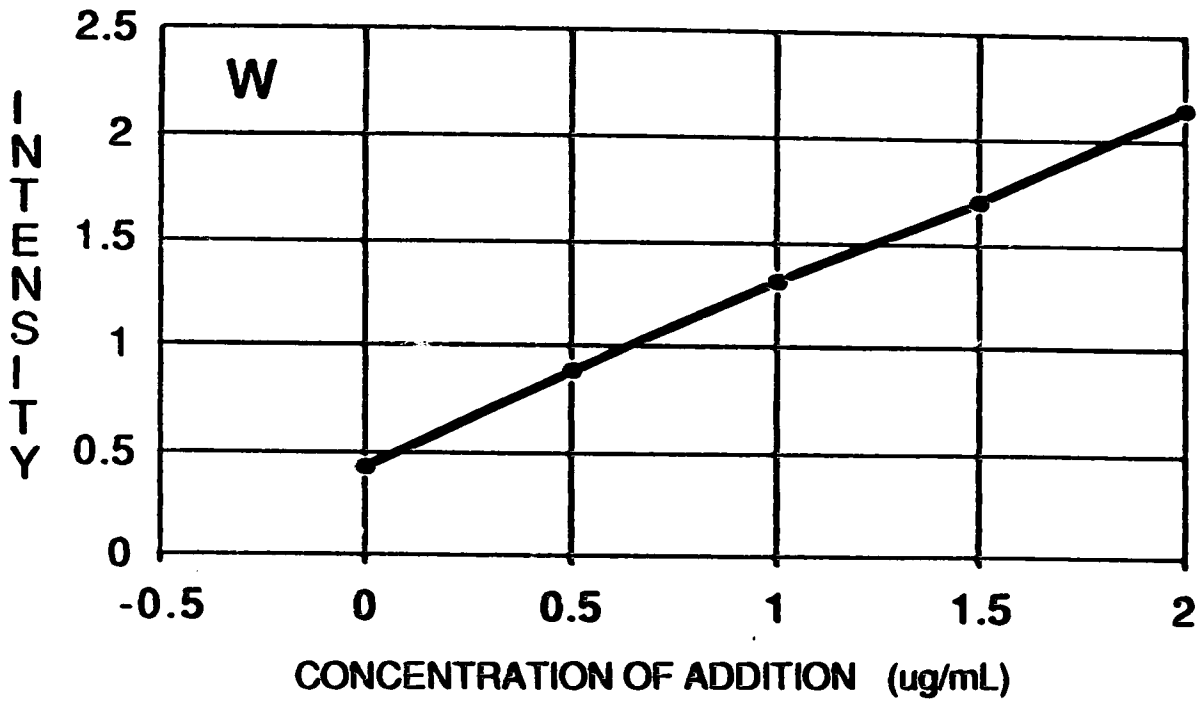

Figure 5.12. Standard Addition Calibration for W. Rh used as an internal standard.

Table 5.9 Analysis of standard reference steels. results reported as % in steel. Aqueous calibration solutions used with Rh used as an internal standard.

SRM	% Fe in Steel	NBS Value (by difference)
361	94.0	95.6
362	93.9	95.3
363	93.9	94.4
121	68.4	68.2*
123	66.5	67.7*
160	63.1	64.3*

*No NBS values by difference reported. The tabulated values above were obtained by difference upon summing the amounts of the certified values.

Conclusions.

ICP-MS can be successfully applied to the analysis of steel samples. However, basic spectral interferences make the determination of some important elements (Si, P and S) difficult if not impossible. In addition MO^+ and MOH^+ species from the sample (M = Fe, Mo, W, rare earth elements) and from the solution matrix (M - Cl, S) may cause important spectral interferences that must be evaluated on an individual basis as part of method development.

Suppressive matrix effects are an important aspect of ICP-MS analyses and it was shown that a nebulizer flowrate setting of slightly less than that producing the maximum analyte signal was advantageous in reducing matrix effects. In addition it was seen that internal standardization was important, not only from the point of view of compensating for instrumental drift, but also for helping to compensate for matrix effects. With due attention to instrument settings, spectral interferences, matrix effects, and internal standardization excellent results can be obtained for most transition metals and the lanthanides (rare earths) in steel samples.

References.

1. H.P. Longerich, B.J. Fryer, D.F. Strong and C.J. Kantipuly, Spectrochim. Acta, **42B**, 75-92, (1987).

2. F.E. Lichte, A.L. Meier and J.G. Crock, Anal. Chem., **59**, 1150-1157, (1987).

3. A.R. Date and D. Hutchinson, J. Anal. Atom. Spectrom., **2**, 269-276, (1987).

4. A. R. Date and D. Hutchinson, Spectrochim. Acta, **41B**, 175-181, (1986).

5. D.C. Gregoire, J. Anal. Atom. Spectrom., **3**, 309-314, (1988).

6. J.W. McLaren, D. Beauchemin and S.S. Berman, J. Anal. Atom. Spectrom., **2**, 277-281, (1987).

7. J.W. McLaren, D. Beauchemin and S.S. Berman, Anal. Chem., **59**, 610-613, (1987).

8. J.R. Garbarino and H.E. Taylor, Anal. Chem., **59**, 1568-1575, (1987).

9. D. Beauchemin, J.W. McLaren, A.P. Mykytiuk, and S.S. Berman, Anal. Chem., **59**, 778-783, (1987).

10. J.W. McLaren, , A.P. Mykytiuk, S.N. Willie and S.S. Berman, Anal. Chem., **57**, 2907-2911, (1985).

11. D. Beauchemin, J.W. McLaren, A.P. Mykytiuk and S.S. Berman, J. Anal. Atom. Spectrom., **3**, 305-308, (1988).

12. T.P.B. Lyon, G.S. Fell, R.C. Hutton and A.N. Eaton, J. Anal. Atom. Spectrom., **3**, 265-279, (1988).

13. B.T.G. Ting and M. Janghorbani, Anal Chem., **58**, 1334-1340, (1986).

14. H.T. Delves and M.J. Campbell, J. Anal. Atom. Spectrom., **3**, 343-348, (1988).

15. G. Horlick, S.H. Tan, M.A. Vaughan and C.A. Rose, Spectrochim. Acta, **40B**, 1555-1572, (1985).

16. M.A. Vaughan and G. Horlick, Appl. Spectrosc., **40**, 434-445, (1986).

17. G. Zhu and R.F. Browner, Appl. Spectrosc., **41**, 349-359, (1987).

18. M.A.Vaughan, G. Horlick and S.H. Tan, J. Anal. Atom. Spectrom., **2**, 765-772, (1987).

19. S.H. Tan and G. Horlick, Appl. Spectrosc., **40**, 445-460, (1986).

20. S.H. Tan and G. Horlick, J. Anal. Atom. Spectrom., **2**, 745-763, (1987).

21. D.C. Gregoire, Spectrochim. Acta, **42B**, 895-907, (1987).

22. H. Kawaguchi, T. Tanaka, T. Nakamura, M. Morishita and A. Mizuiki, Anal. Sci., **3**, 305-308, (1987).

23. D. Beauchemin, J.W. McLaren and S.S. Berman, Spectrochim. Acta, **42B**, 467-490, (1987).

24. L.A. Fernando, Anal. Chem., **56**, 1970-1973, (1984).

Chapter 6

ICP-MS Ion Lens Simulations.

The success of ICP-MS depends upon the ability to sample ions from the plasma, to direct the ions to the quadrupole, to separate the ions in the quadrupole and to detect the ions as they exit. Ion separation and detection in ICP-MS is accomplished using conventional quadrupole mass spectrometry methods. The sampling procedure, which allows atmospheric pressure sampling of the plasma into a vacuum, has its basis in molecular beam studies. The step between these two, directing the ions to the quadrupole, is done with electrostatic lenses and is the part of the process of interest here.

A very general study of the ion lenses in ICP-MS is not possible due to differences in instrument design. Lens design varies from manufacturer to manufacturer. Also of importance is the interface between the ICP and the MS which also varies with manufacturer. The interface affects the ion energy and therefore the ion behaviour in a given electrostatic lens system. Ion kinetic energies have been measured by Olivares and Houk [1] and by Fulford and Douglas [2]. The results obtained by the two groups differ primarily due to the center tapped grounded load coil on the Sciex system used by Fulford and Douglas. This design eliminated any detectable discharge between the plasma and the sampler or skimmer and the resulting ion kinetic energies were lower than those measured for the system not having a center tap ground on the load coil.

There has been a limited amount of ion lens modeling published relating specifically to the ICP-MS. Kawaguchi [3], in his review, discusses ion lens systems and presents some ion trajectories for a somewhat simplified model of the lenses used in their instrumentation. Gillson et al. [4] also employed ion lens modeling in their study of non-spectroscopic interelement interferences in ICP-MS. Their work involved a comparison of ion trajectories through the einzel lens elements of a Sciex Elan 250 with and without the effect of space charge.

The ion lenses modeled in this study are based on the Sciex Elan 250 ICP-MS. The numerical simulation program MacSimion (Montech Pty. Ltd.) was used to model the lenses and calculate the ion trajectories. The model included the entire set of electrostatic lenses from the skimmer to the back of the bessel box. No space charge effects were considered.

Theory

All of the properties of motion of a particle in a potential field depend on a function of the velocity and particle position. In ion optics the ion velocity is proportional to the square root of the potential experienced by the ion. Snell's Law, which is commonly written for light optics as:

$$\frac{\sin\theta_1}{\sin\theta_2} = \frac{n_2}{n_1} \qquad 6.1$$

may also be written for ion optics as [5]:

$$\frac{\sin\theta_1}{\sin\theta_2} = \left(\frac{\phi_1}{\phi_2}\right)^{1/2} \qquad 6.2$$

where θ is the angle of the particle's path, n is the refractive index and ϕ is the potential. From this we can see that the square root of the potential affects the ion path in the same manner as the refractive index affects the path of light. Ion trajectories depend on the potential experienced by the ion and, therefore, on the electrostatic field established by the lenses. Although in theory, once the electrostatic field is known, Snell's Law could be employed directly to determine ion trajectories, in practice cumulative errors grow rapidly. Consequently a numerical methods approach is used to calculate ion trajectories.

Programs such as MacSimion are available for ion lens simulations. First the ion optics are modeled and the voltages are assigned to each element. The program then calculates the electrostatic field. Once this is accomplished, ions with different initial parameters, such as energy and angle, may be introduced into the system and the trajectories are calculated and displayed on the computer screen. The equipotential lines for a simple einzel lens as calculated by MacSimion are displayed in Figure 6.1a. The ion trajectories for two 7.5eV ions through this lens system are presented in Figure 6.1b. The initial angles of the ions are 9° and -9° from a horizontal axis of symmetry running through the center of the figure. An important characteristic of electrostatic ion optics is that ion trajectories depend on energy not on mass/charge. The trajectory is the same for any charged particle no matter what its mass to charge ratio provided it enters the field with the same initial kinetic energy. Ions with different charges but the same energy come to the same focus but arrive there at different times.

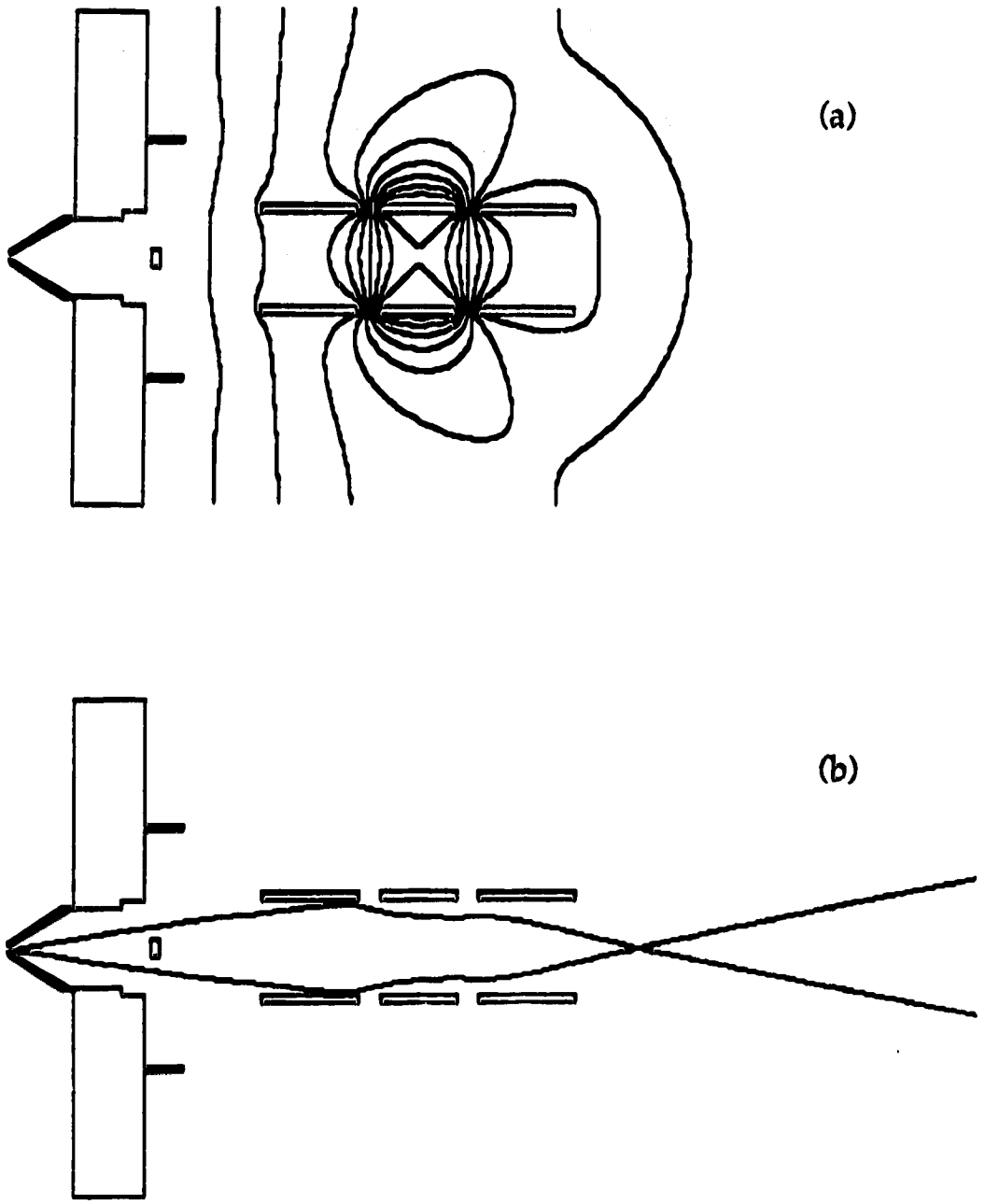

Figure 6.1 Equipotential lines for the einzel lens (a) and ion trajectories through the einzel lens (b). Ion energy, 7.5eV. Entry angles, 9° and -9°. E1 = -30V, central einzel element, -130V.

Since the lenses discriminate on the basis of kinetic energy we must consider the kinetic energies of the ions entering the ICP-MS in order to understand their behaviour in the lens system. Fulford and Douglas [2] have measured ion kinetic energies in the Sciex Elan 250. Following their work, we can establish an equation for calculating the kinetic energies of the ions in the ICP-MS. From the assumption that the ions get most of their energy from the supersonic expansion we may calculate the kinetic energy. In the expansion the ions move at the speed of the Ar neutrals.

Since

$$E = \frac{1}{2} mv^2 \qquad 6.3$$

we have

$$E_{Ar} = \frac{1}{2} m_{Ar} v_{Ar}^2 \qquad 6.4$$

$$E_M = \frac{1}{2} m_M v_M^2 \qquad 6.5$$

assuming that the velocity of the ions equal the velocity of Ar ($v_{Ar} = v_M$) we get:

$$E_s(M) = E_{Ar} \frac{M}{M_{Ar}} \qquad 6.6$$

The value of E_{Ar} is usually obtained from consideration of the terminal velocity in the supersonic expansion. The terminal velocity is given as:

$$U_\infty = \sqrt{5/2}\, \alpha \qquad 6.7$$

where α is defined as:

$$\alpha = \sqrt{\frac{2kT}{m}} \qquad 6.8$$

substitution into 6.4 yields:

$$E_{Ar} = \frac{5}{2}kT \qquad 6.9$$

Assuming a reasonable value for T, the gas kinetic temperature in the ICP, (4900K for this work) we can calculate E_{Ar} and E_S. Fulford and Douglas report a plasma potential of approximately 2V which must be added to the kinetic energies of the ions. Thus taking this into consideration we get:

$$E = E_s + P \qquad 6.10$$

where P = 2.0eV.

According to these equations the kinetic energy of an ion sampled using a supersonic expansion such as the one used in the ICP-MS, depends, in a linear fashion, upon the ion mass. With T = 4900K the kinetic energy of the ions may be calculated by E = 0.026M+2.0eV. From this ^{48}Ti will have a calculated kinetic energy of 3.26eV and ^{208}Bi a kinetic energy calculated to be 7.46eV. This explains why there is an apparent mass effect when studying ion signal intensities as a function of lens voltages. (See Chapter 2.)

Experimental

The lens system from a P.E. Sciex Elan 250 ICP-MS was disassembled and measured. The information obtained was used in the ion lens simulation program MacSimion (Montech Pty. Ltd. Australia) to model the ion lenses in

this ICP-MS. MacSimion was run on a MacII Macintosh computer. The calculations for determining the electric field were done using cylindrical symmetry. Ion trajectories were determined for a variety of initial conditions for a variety of ions plus the effects of varied potentials on individual lens elements were studied. In all cases no space charge was assumed.

Results and Discussion

A schematic of the ICP-MS system for a P.E. Sciex Elan 250 is presented in Figure 6.2. Ions formed in the ICP are extracted by the sampler, through the skimmer into the ion focussing optics. The ion optics of interest in this study are those elements from the skimmer down to and including the bessel box. The quadrupole, although an ion lens itself, is a special line focussing lens which has been studied extensively and is described in detail elsewhere [6-8]. A schematic of the lenses as they were drawn in MacSimion is shown in Figure 6.3. The skimmer and the first photon stop were at ground potential at all times. Element 2 of the einzel lens was kept at -130V. Elements 1 and 3 of the einzel lens are tied together and have the same potential. This is also true for the front and back plates of the bessel box. The lenses where the voltages were varied shall be referred to as follows: E1 shall indicate the einzel lens elements 1 and 3; P shall indicate the front and back bessel plates; B shall represent the bessel box barrel; and S2 shall represent the photon stop in the bessel box.

1. Basic Lens Behaviour.

Equipotential lines for the lens system with the following voltages: E1 = -30V, P = -18V, B = 4V and S2 = -9V are displayed in Figure 6.4. The first

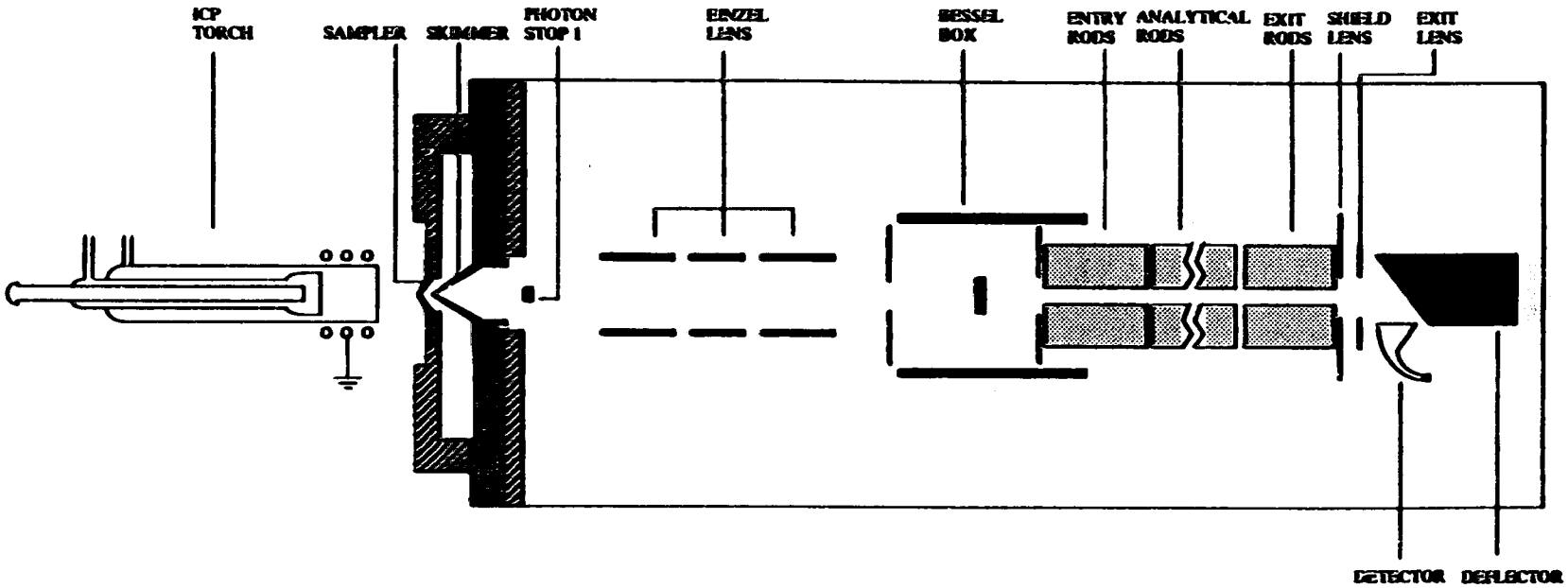

Figure 6.2 Schematic of a P.E. Sciex Elan 250 ICP-MS.

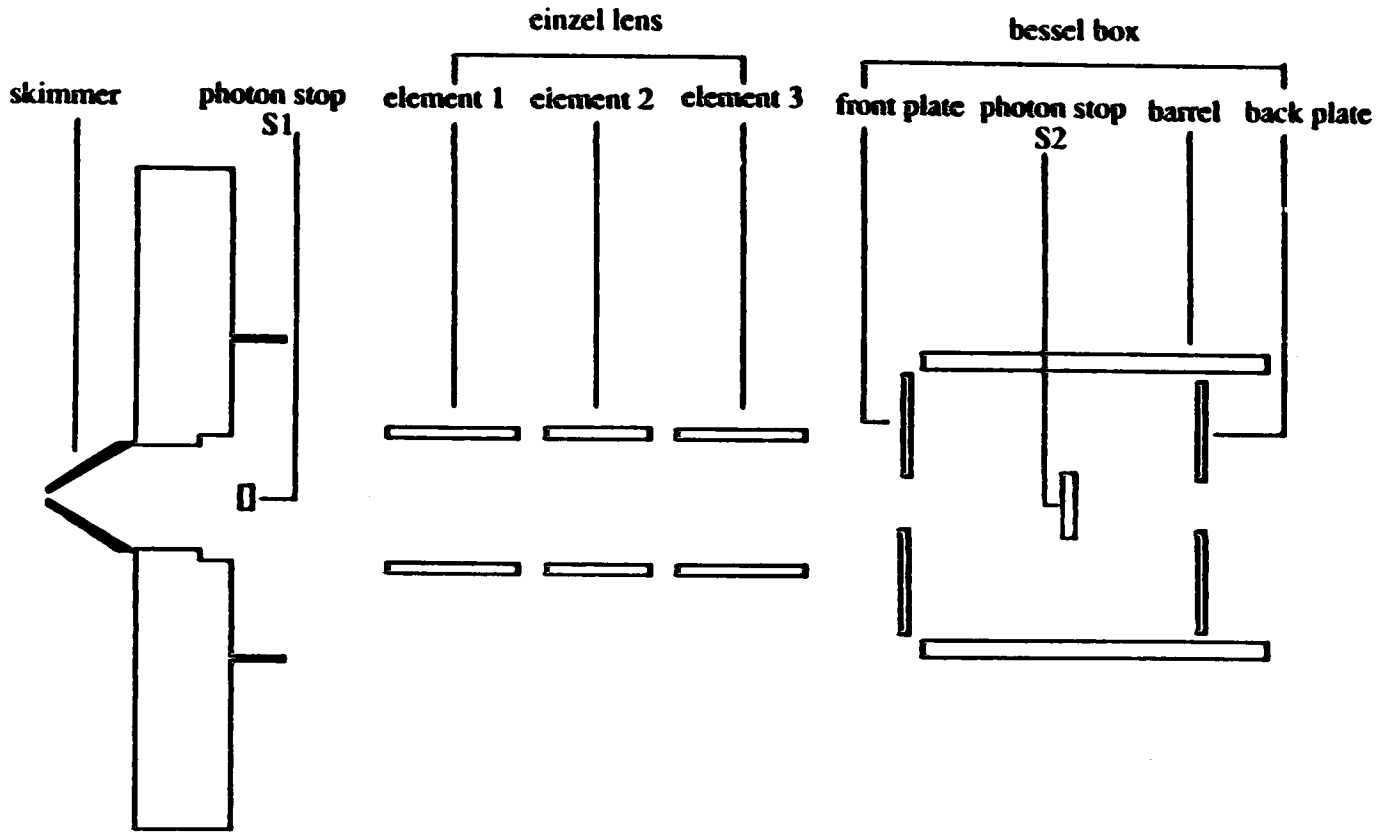

Figure 6.3 Schematic of the ion lenses as drawn in MacSimion.

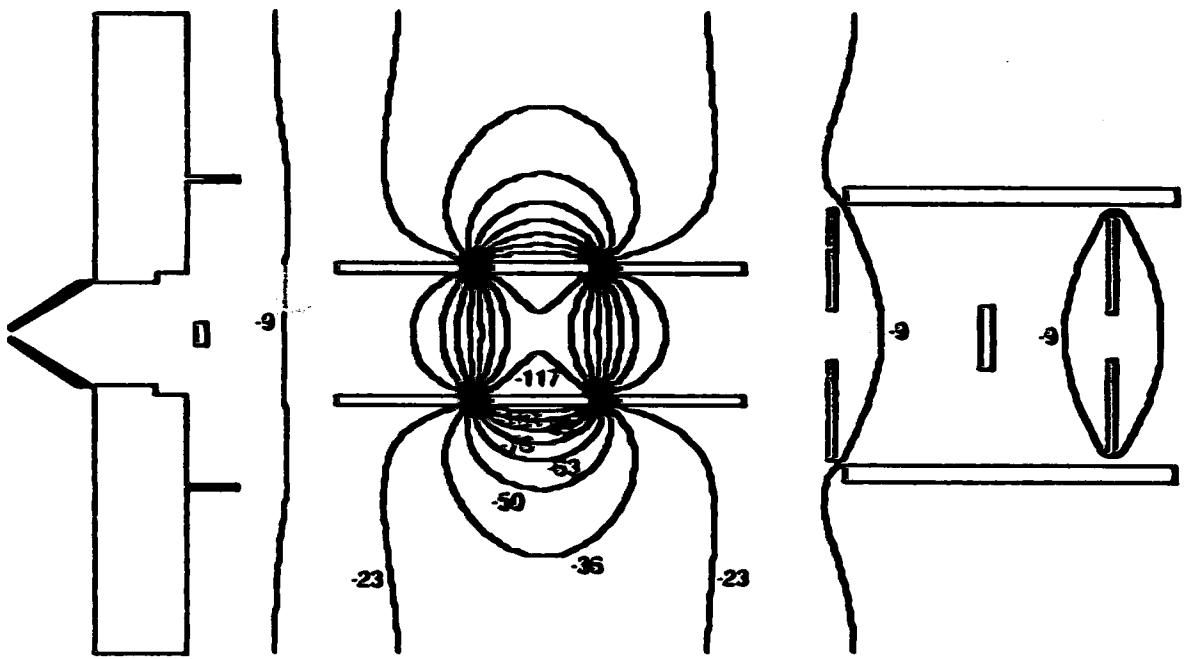

Figure 6.4 Equipotential lines generated for the ion lenses with E1 = -30V, P = -18V, B = 4V and S2 = -9V.

thing to catch the eye is the characteristic equipotential distribution around the einzel elements. The region of interest is inside the cylindrical lens elements. Provided the potentials are properly adjusted for the kinetic energy of the ion of interest, the ion trajectory shall be such that the ion passes through the einzel lens and into the bessel box through the hole in the front plate. There are only two equipotential lines drawn in the bessel box but it is enough to get a feel for the ion behaviour. Again, depending on the field strength and ion kinetic energy, the first set of equipotentials, inside the bessel box behind the front plate, serve to deflect the ions away from the photon stop. The ions are forced around the sides of the photon stop and then the field established around the back plate serves to bend the ion trajectory towards the exit of the bessel box. Ions with the appropriate kinetic energy will exit the bessel box through the hole in the back plate and enter the AC entry rods of the quadrupole system. A trajectory for an ion successfully traversing the lens system is shown in Figure 6.5. Actually the figure contains the trajectories for three singly charged ions with masses of 48, 148 and 248 amu. In agreement with the theory discussed, these trajectories are overlapped because ion trajectories under these conditions are independent of mass/charge depending only on kinetic energy. A kinetic energy of 3.3eV for each of the three masses was used in this simulation.

The effect of changing the kinetic energy under these lens conditions may be observed in Figure 6.6. From the top set of ion trajectories, Figure 6.6a, we see that a range of kinetic energies may successfully exit the lens system. Ion paths for ions with a larger range of kinetic energies are displayed in Figure 6.6b. The ion with the lowest kinetic energy, 1eV, gets deflected too much in the back of the bessel box and crashes into the back plate. The higher

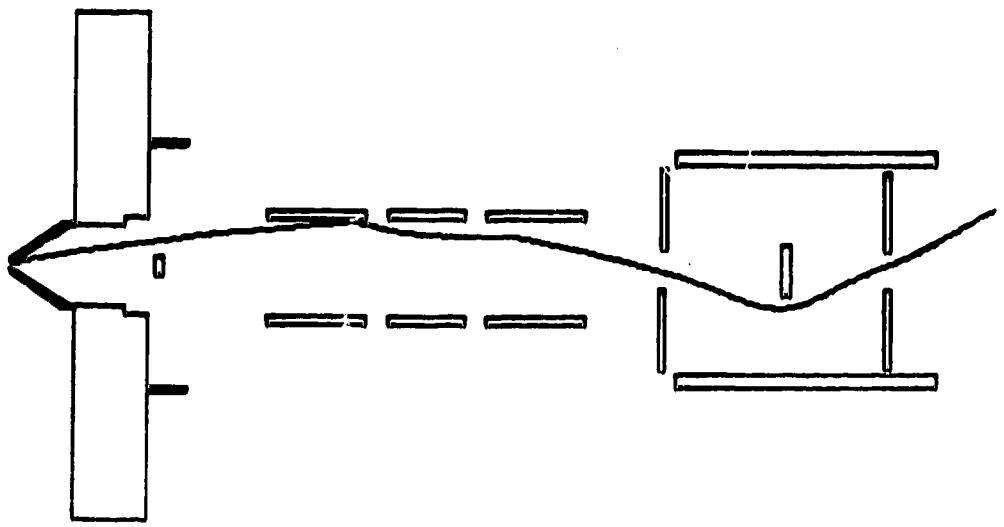

Figure 6.5 Typical ion trajectory. Ion energy is 3.3eV, entry angle is 9°. Lens settings: E1 = -30V, P = -18V, B = 4V and S2 = -9V.

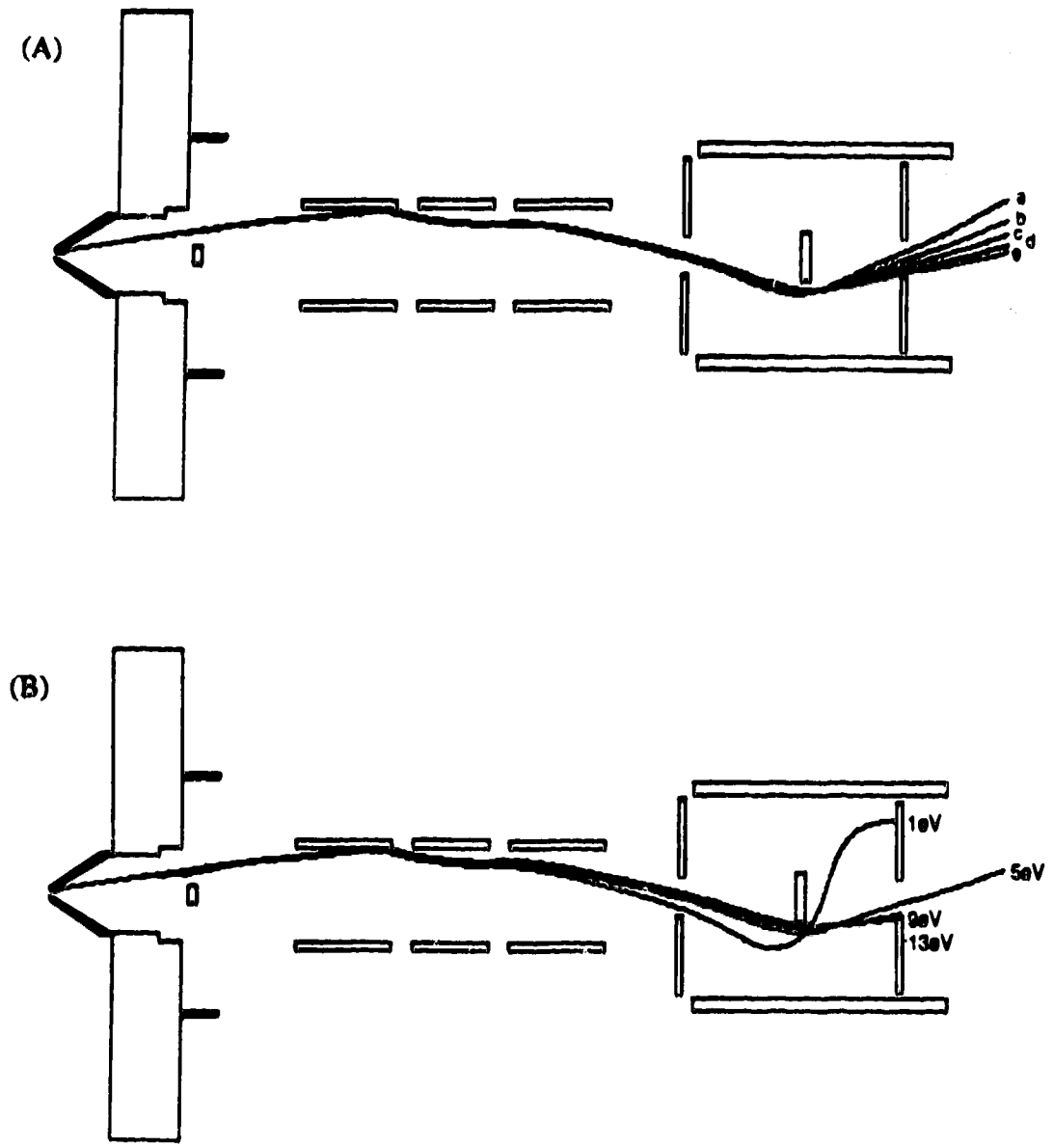

Figure 6.6 Trajectories for ions of varying kinetic energies. (A) small energy range: (a) 3.3eV, (b) 4.3eV, (c) 5.3eV, (d) 6.3eV and (e) 7.3eV. (B) larger energy range. Lens settings: E1 = -30V, P = -18V, B = 4V and S2 = -9V. Entry angle is 9°

energy ions, 9eV and 13eV, are not deflected enough and also crash into the back plate of the bessel box. The 5eV ion, for which the lens voltages are correct, exits properly from the lens system. The ion energies can be selected in the bessel box by proper adjustment of the lens potentials.

Another characteristic of cylindrically symmetrical systems is that the charge on the ion does not affect the ion trajectory. Trajectories for the Ba^{+} and Ba^{2+} ions are plotted in Figure 6.7. Mass 138 and a kinetic energy of 5.62eV were used for these ions. Clearly the two trajectories overlap, in agreement with theory.

One final consideration to discuss, before we proceed to a more detailed look at the ion behaviour through these lenses, is that of the ion entry angle. Since there is a photon stop, S1, directly behind the skimmer (see Figure 6.3) ions from the skimmer travelling straight down along the axis of symmetry shall crash into the photon stop and be lost. Likewise, ions exiting the skimmer at too large an angle will hit the walls or, depending on the E1 voltage, will crash into the first einzel element. Thus only ions whose paths fall within a certain range of angles will successfully enter the lens system. Of those, not all will successfully exit. Referring to Figure 6.8 we can see that ions with initial angles of 9° and 12° made it through the lenses but ions entering at angles of 6° and 15° crashed into the plates of the bessel box. Thus in order for an ion to successfully traverse the lens system the potentials must be set according to the kinetic energy of the ion and the ion must enter the lenses at the proper angle.

The original plan for this study was to simulate the ion lenses in the ICP-MS and study ion trajectories for the conditions, ie. lens voltages, used in

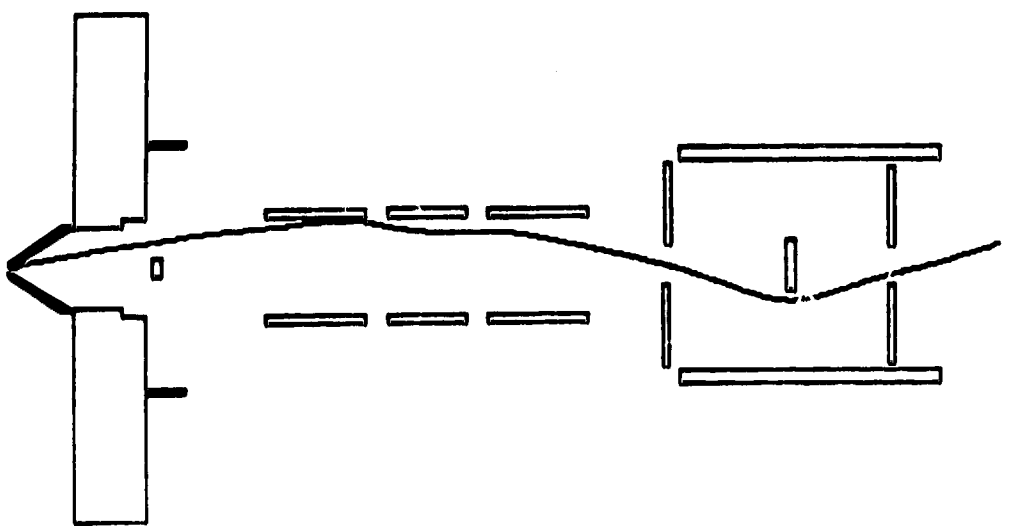

Figure 6.7 Ion trajectories for Ba^{+} and Ba^{2+} (5.62eV). Lens settings: E1 = -30V, P = -18V, B = 4V and S2 = -9V. Entry angle is 9°.

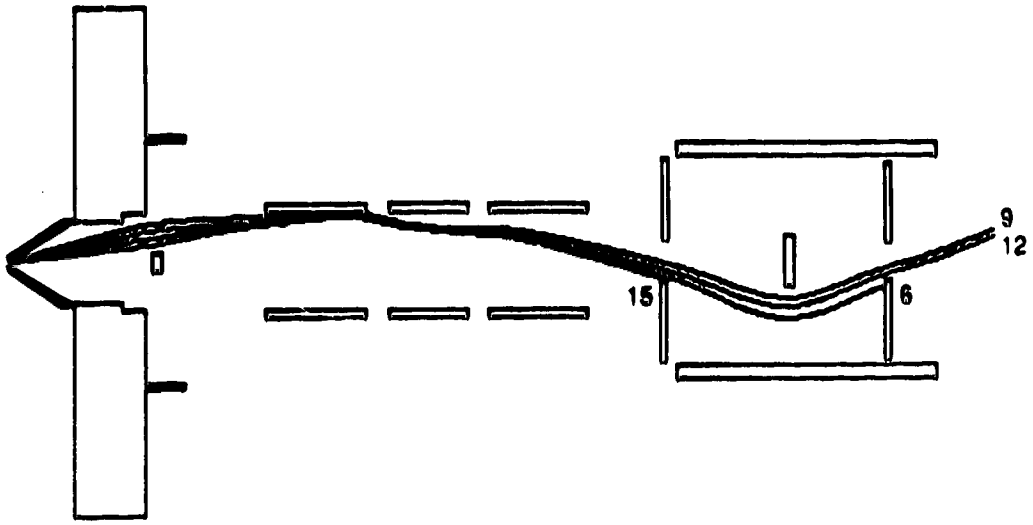

Figure 6.8 Ion trajectories for a 4.8eV ion with entry angles of 6°, 9°, 12° and 15°.

the parameter study done on this instrument (see Chapter 2). The lens settings used in the parameter study were B=4V, S2 = -9V, P = -18V and E1 = -16V. When these settings were used in the lens modeling we found that for the ion kinetic energies calculated the ion paths did not lead out of the lens system and into the quadrupole. Instead, the ions were deflected too much by the einzel lens and crashed into the front plate of the bessel box. In order to get ions in the calculated kinetic energy range into the bessel box, the einzel lens voltage had to be increased. A value of E1= -30V was found to be acceptable.

In an attempt to understand the discrepancy between the experimental results and the simulation, we tried to get ions through the lens system by modifying the parameters other than the einzel lens voltage. The position of the first photon stop was varied but this did not help. If the stop was removed completely the ions made it through the lens system. This constituted a large change in the ion optics, however, and was not acceptable. Making small changes in the positions of the rest of the lenses with respect to each other did not improve the ion throughput either. Since the ion trajectories depend on ion kinetic energy our next step was to assign larger kinetic energies to ions in the simulation. In the range of 16eV, ions successfully traversed the lens system so it may be possible that the assumption about the ion energies discussed earlier is incorrect. This is disturbing because with the higher kinetic energies it is difficult to associate ion energy with mass. This also disagrees with the measurements made by Fulford and Douglas. There is some circumstantial evidence supporting the idea that the kinetic energies are in the 2eV to 8eV range. Once the ions enter the bessel box, the voltage ranges for the bessel box lens elements that result in successful trajectories are

closer to experimental voltage ranges for the ions in the 2eV to 8eV range compared to those ions in the 14eV to 17eV range. Although this problem is essentially unresolved we are still able to get, at least, a qualitative feel for the ion behaviour in this lens system, to understand how the voltage changes alter ion trajectories and to see why compromise lens settings are sometimes required.

2. Effects of Individual Lens Elements.

A systematic study of each of the lens elements - the einzel lens (E1), the bessel box barrel (B), the bessel box plates (P), and the photon stop (S2) - was carried out. Each lens was set at a default value as follows: B = 4V, S2 = -9V, P = -18V and E1 = -30V. Then, varying the voltage of only one lens in the set of four, a series of ion trajectories were obtained. This was repeated for all four lenses. A series of trajectories for four different einzel lens settings ranging from -25 to -45V are shown in Figure 6.9. At each potential, the trajectories for 1eV, 5eV and 9eV ions are shown. For the default set of voltages the ion trajectory for 13eV is also included. With a potential of -25V on the einzel lens, E1, the 1eV ion is deflected too much in the einzel field and is lost to the front plate of the bessel box. Both the 5eV and 9eV ions enter the bessel box. Due to the field within the bessel box only the 5eV ion exits toward the quadrupole. For both the -30V and the -35V einzel lens (E1) settings, the ions in the range 1eV to 9eV enter the bessel box with only the 5eV ion making it through. Finally the E1 = -45V setting resulted in a series of ion trajectories where only the 1eV ion enters the bessel box and it crashes into the photon stop. The other ions, 9eV and 5eV, are not deflected sufficiently in the einzel field to enter the bessel box.

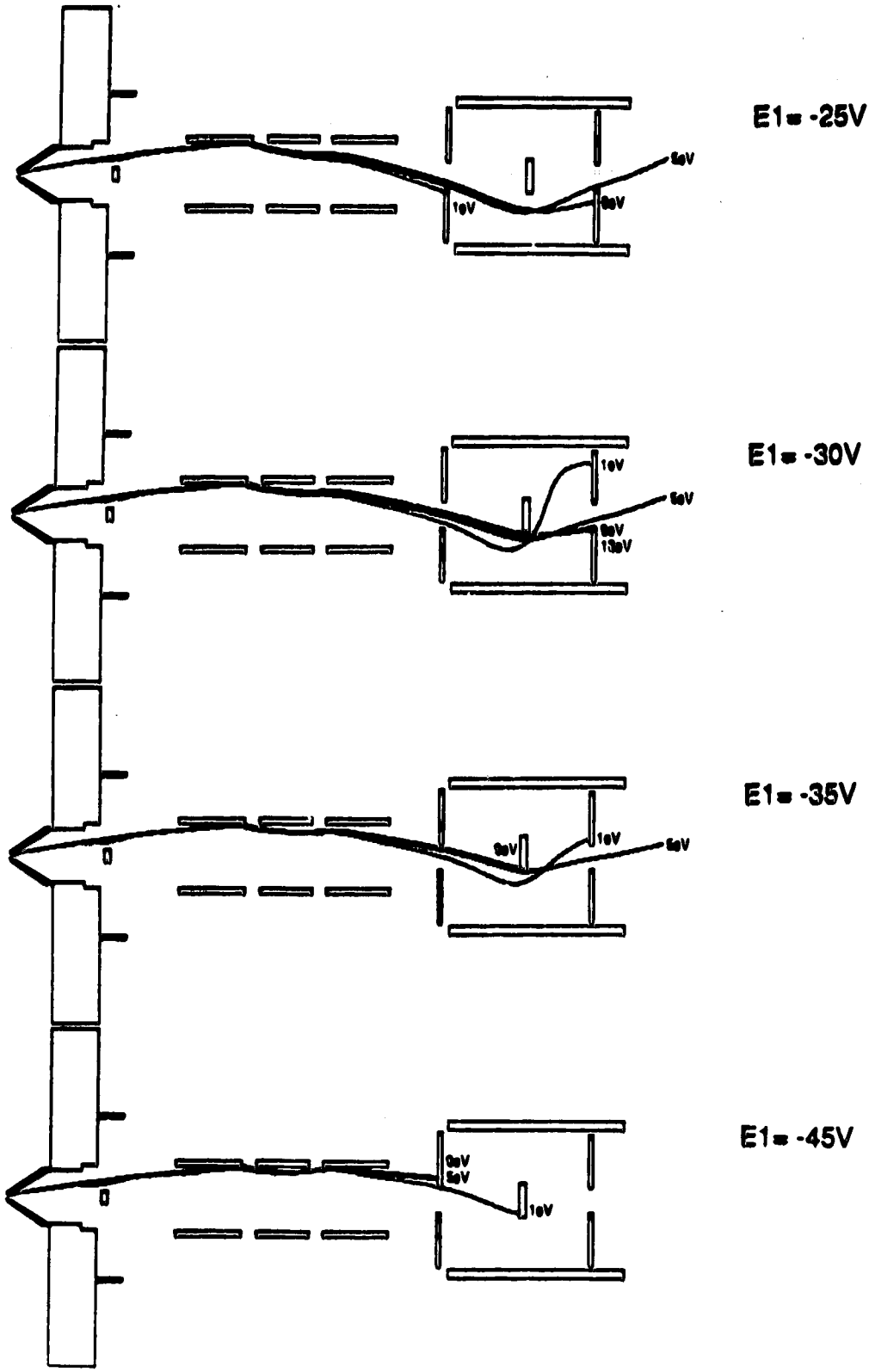

Figure 6.9 Trajectories for 1, 5 and 9eV ions at varied E1 voltages. Lens settings: P = -18V, B = 4V and S2 = -9V. Entry angle is 9°.

The ion trajectories presented in Figure 6.10 demonstrate the effect of the photon stop voltage, S2. At a voltage of -3V a 1eV ion is deflected into the photon stop. The ions of higher kinetic energy, 5eV and 9eV, are deflected around the photon stop but do not get deflected enough in the back of the bessel box to bring them through the exit. The set of conditions where the photon stop voltage = -9V are the default conditions and have already been described. This set of conditions (default conditions) has been included in Figures 6.9 - 6.12 for the sake of comparison. The conditions where the photon stop voltage = -15V results in both the 5eV and the 9eV ions traversing the lens system and entering the quadrupole. In contrast, the 1eV ion crashes into the back plate of the bessel box. When S2 =-18V the potential is high enough that the 5eV ion, like the 1eV ion, crashes into the back plate as a result of being deflected too strongly in the field. The 9eV ion trajectory still exits the bessel box successfully.

The next lens to look at is the bessel box barrel. Trajectories for different potentials on this lens are displayed in Figure 6.11. When B=2V the only ion with a trajectory passing through the entire lens system is the 1eV ion. The 5eV and 9eV ions were not deflected enough to get to the exit in the back plate. The B=4V plot is the plot of default conditions. Changing the bessel box barrel to 6V results in acceptable trajectories for 5eV and 9eV ions where both exit the bessel box. The 1eV ion crashes into the photon stop. When B= 12V none of the ions 1eV, 5eV or 9eV exit. The 5eV and 9eV ions get deflected too much and crash into the photon stop or the back plate respectively. The 1eV ion enters the bessel box, is repelled by the field, changes direction and crashes into the back of the front plate of the bessel box.

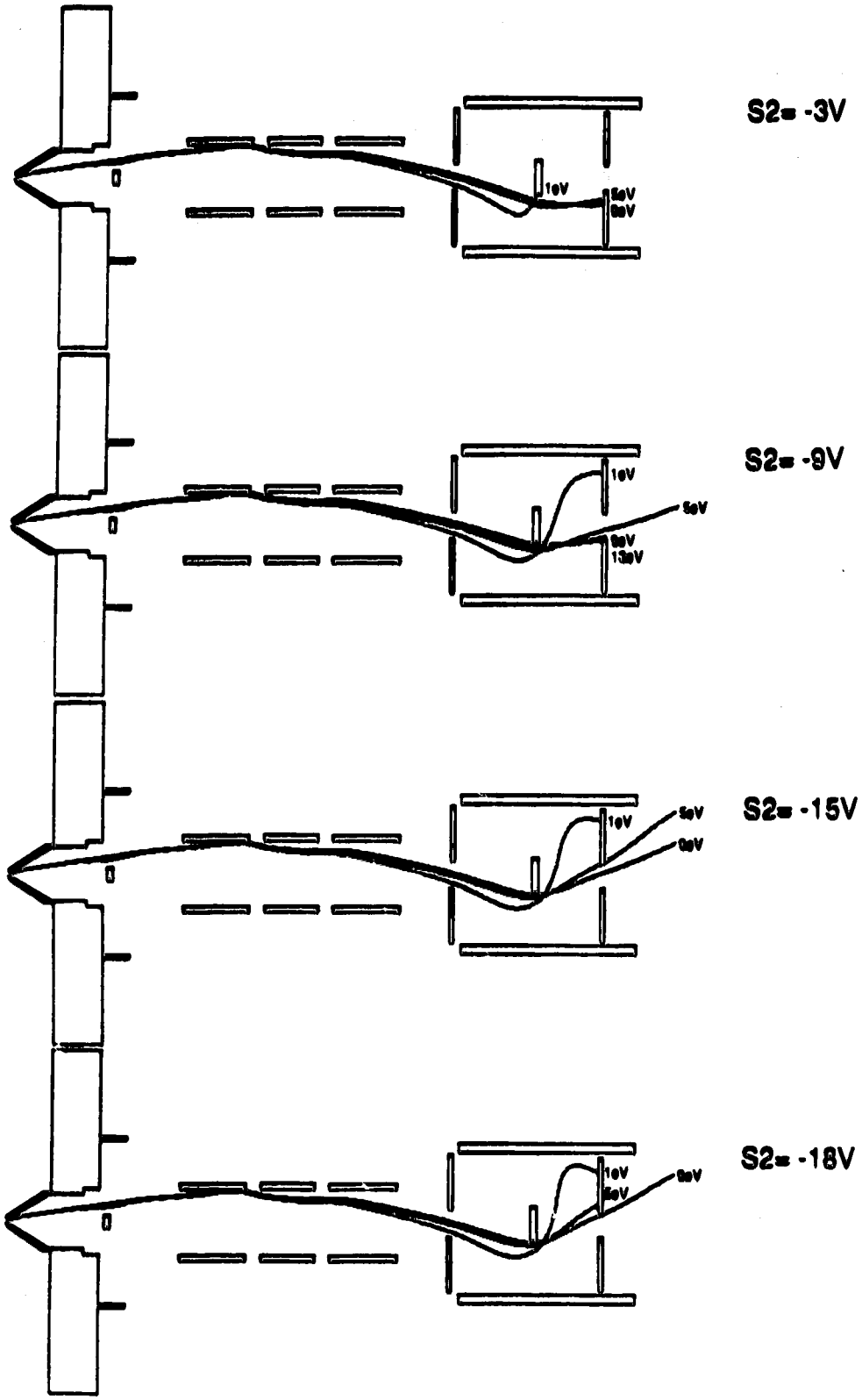

Figure 6.10 Trajectories for 1, 5 and 9eV ions at varied S2 voltages. Lens settings: E1 = -30V, P = -18V and B = 4V. Entry angle is 9°.

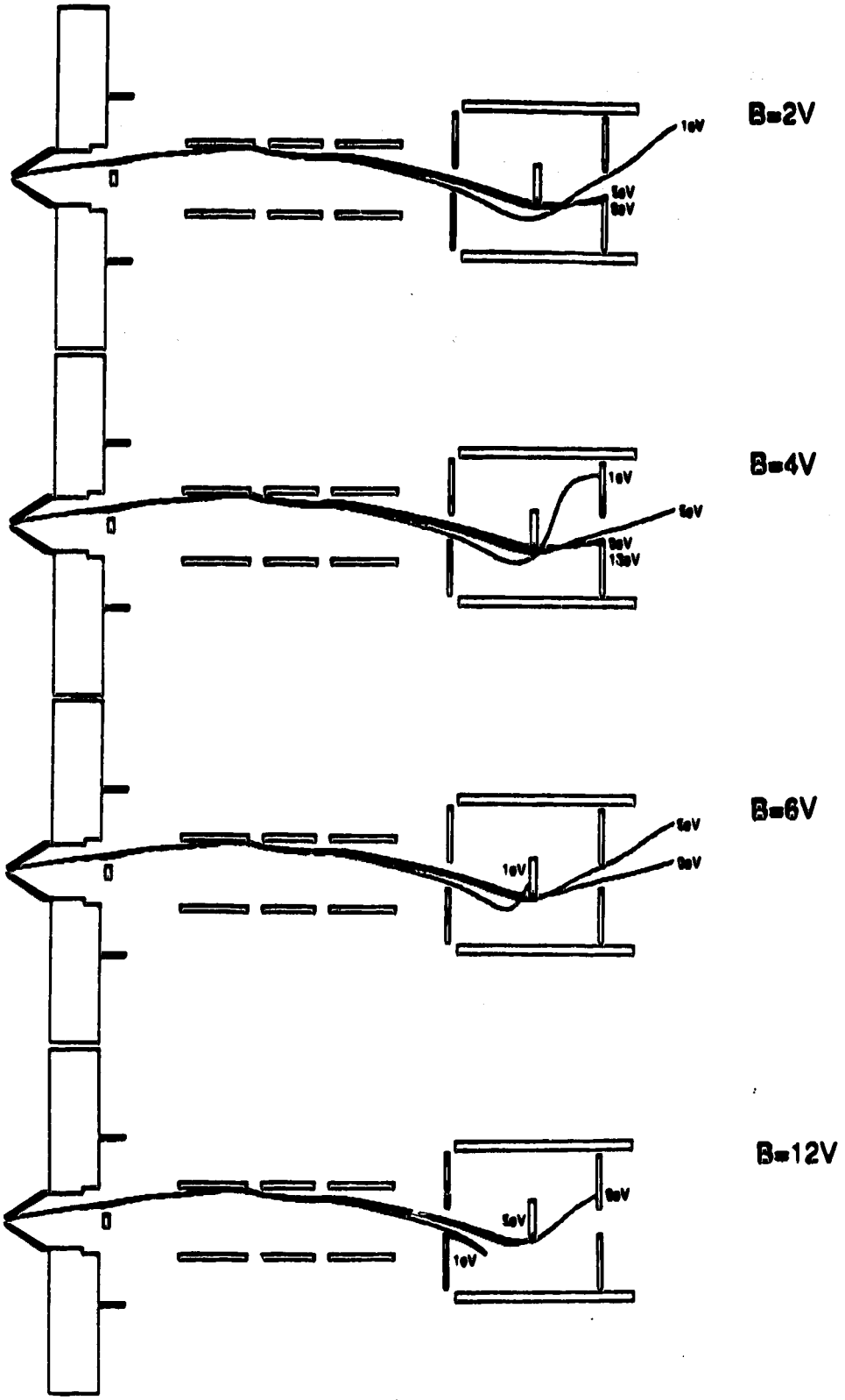

Figure 6.11 Trajectories for 1, 5 and 9eV ions at varied B voltages. Lens settings: E1 = -30V, P = -18V and S2 = -9V. Entry angle is 9°.

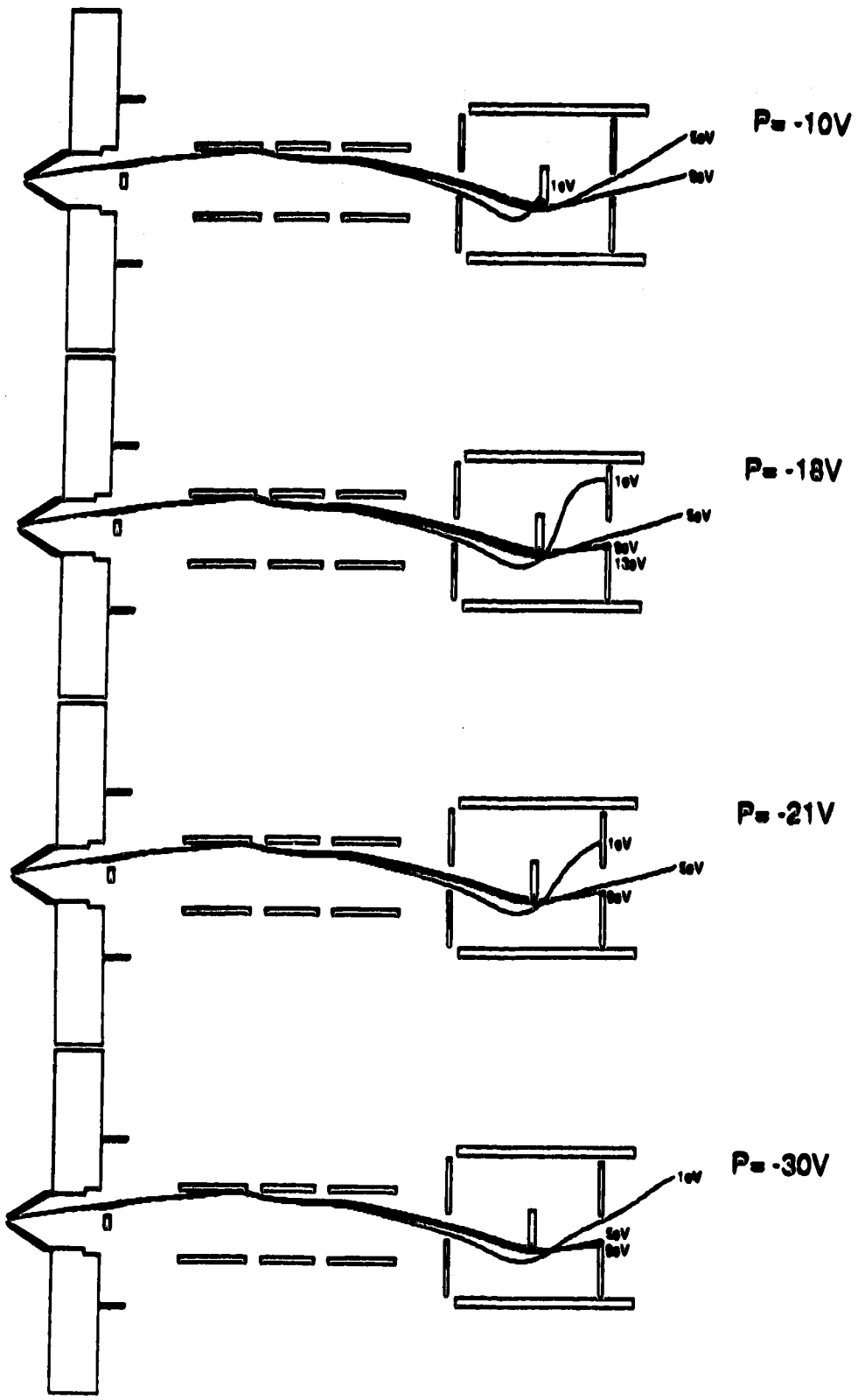

Figure 6.12 Trajectories for 1, 5 and 9eV ions at varied P voltages. Lens settings: E1 = -30V, B = 4V and S2 = -9V. Entry angle is 9°.

The final lens of the four consists of the bessel box plates. The trajectories for changes in this lens voltage are shown in Figure 6.12. At P= -10V ions with energies of 5eV and 9eV will exit the bessel box but the 1eV ion crashes into the photon stop. P = -18V is the default set of conditions. The trajectories for P= -21V are similar to those for the default conditions although all the ions are deflected a little less. At a bessel box plate voltage of -30V only the 1eV ion exits; the 5eV and 9eV ions do not get deflected enough to avoid the back plate of the bessel box.

From this simulation of the behaviour of the ions of various energies under different lens potentials a list of trends can be compiled. The trends observed for this lens system are presented in Table 6.1. Condition 1a deals with the case where the ions are deflected too much by the field established by the einzel lens. The ions are deflected past the bessel box opening and crash into the front plate. The 1eV ion at E1 = -25V, Figure 6.9, is an example of this. By increasing the einzel lens (E1) potential to -30V, the 1eV ion enters the bessel box. Condition 1b describes the opposite problem. Ions do not get deflected enough to enter the bessel box. The 5eV and 9eV ion trajectories for E1 = -45V (Figure 6.9) are not deflected enough. Reducing the potential to -35V allows both the 5eV and the 9eV ions to pass into the bessel box. An example of condition 1c, the conditions where ions crash into front of the photon stop following a fairly straight trajectory, is also displayed in Figure 6.9. When E1 = -35V the 9eV ion crashes into the photon stop. Reducing the einzel lens (E1) voltage to -30V results in an ion trajectory for the 9eV ion that passes around the photon stop toward the back of the bessel box.

The second set of trends relate to the bessel box. Consequently there may be more than one way to correct a condition; not every correction

Table 6.1 Major Behaviour Trends.

The larger the voltage on einzel lens elements 1 and 3, (E1), the smaller the angle of deflection in the ion trajectory moving from the einzel lens toward the bessel box.

1a.Condition	Ions deflected too much by the field established by the einzel lens voltage to enter the bessel box.
Correction	Increase the einzel lens (E1) voltage.
b.Condition	Ions not deflected enough by the field established by the einzel lens voltage to enter the bessel box.
Correction	Decrease the einzel lens (E1) voltage.
c. Condition	Ions crash into front of the photon stop following a fairly straight trajectory.
Correction	Decrease the einzel lens (E1) voltage.

The larger the photon stop (S2) voltage or the larger the bessel box barrel (B) voltage or the smaller the bessel box plate (P) voltage the more curved the ion trajectory becomes through the bessel box.

2a.Condition	Once inside the bessel box, ions are not deflected enough to exit.
Correction	1. Increase photon stop (S2) voltage. 2. Increase bessel box barrel (B) voltage. 3. Decrease bessel box plate (P) voltage.
b.Condition	Once inside the bessel box ions are deflected past the exit into the back plate.
Correction	1. Decrease photon stop (S2) voltage. 2. Decrease bessel box barrel (B) voltage. 3. Increase bessel box plate (P) voltage.
c. Condition	Ions crash into photon stop following a curved trajectory.
Correction	1. Decrease bessel box barrel (B) voltage. 2. Increase bessel box plate (P) voltage.

method will apply in every case and changing the potential on more than one lens element may counteract the effect obtained by only changing one. Condition 2a describes the situation where ions, once inside the bessel box, do not get deflected around the back of the photon stop to the hole in the back plate of the bessel box. To correct for this we may increase the photon stop (S2) voltage, increase the bessel box barrel (B) voltage, or decrease the bessel box plate (P) voltage. In Figure 6.10, where S2 = -3V, the 5eV and 9eV ions end up on the back plate of the bessel box. By increasing the photon stop (S2) voltage to -9V the 5eV ion exits. When the photon stop (S2) voltage is increased further to -15V both the 5eV and the 9eV ion exit properly. Note how the angle of exit increases as the potential increases. The same situation for the 5eV and 9eV ions exists for the bessel box barrel setting of B=2V, displayed in Figure 6.11. The ions end up on the back plate of the bessel box. Increasing the bessel box barrel (B) voltage to 4V allows the 5eV ion to exit and a further increase to 6V allows both the 5eV and the 9eV ions to exit. The bessel box plate (P) voltage also effects the degree of deflection an ion undergoes in the bessel box. Looking first at the trajectories for P = -30V in Figure 6.12 we see that the 5eV and 9eV ions are not deflected enough. Changing the bessel box plate voltage to -21V allows 5eV ions to exit and P= -10V allows both 5eV and 9eV ions to exit to the quadrupole.

Condition 2b, where once inside the bessel box ions are deflected past the exit into the back plate, is the opposite of condition 2a discussed above and consequently the corrections are also opposite. In Figure 6.10 where S2 =-18V the 5eV ion crashes into the back plate because it has been deflected too much. Reducing the photon stop (S2) voltage to -15V corrects the problem. Similarly, referring to Figure 6.11, B=12V, the 9eV ion trajectory terminates on the back

plate of the bessel box after being deflected past the exit. Reducing the bessel box barrel (B) voltage to 6V results in the trajectory which passes through the bessel box and exits successfully. The ion trajectory for a 1eV ion which has been deflected past the exit and into the back plate of the bessel box is shown in Figure 6.12 (P = -21V). Increasing the bessel box plate (P) voltage to -30V resulted in an acceptable trajectory for the 1eV ion.

Condition 2c, where ions crash into photon stop following a curved trajectory, and condition 1c, where the ions crash into the photon stop following a fairly straight trajectory, differ in the amount of curvature in the trajectory and in the type of the correction applied. An ion trajectory for the 1eV ion which crashes into the photon stop is presented in Figure 6.11 (B=6V). Note how curved the trajectory is compared to the 9eV trajectory in Figure 6.9 (E1=-35V). When the bessel box barrel (B) voltage is reduced to 2V the 1eV ion trajectory passes through the exit of the bessel box. Similarly, in Figure 6.12 (P = -10V) the 1eV ion crashed into the photon stop. When the bessel box plate (P) potential was changed to -30V the 1eV ion trajectory passed through the exit of the bessel box.

Using these trends, predictions may be made on how to better adjust the lenses for ions of a given energy. Take, for example, the case where the bessel box plate voltage =-21V. This set of trajectories is displayed again in Figure 6.13a. In this figure the 9eV ion is not deflected enough to exit the bessel box. One possible correction for the problem is to increase the voltage on the photon stop, S2. The trajectory for an increase in this voltage from -9V to -15V is plotted in Figure 6.13b. This change is sufficient to correct the the ion path through the bessel box. Another option is to increase the bessel box barrel (B) voltage. The results of changing this voltage from 4V to 6V are

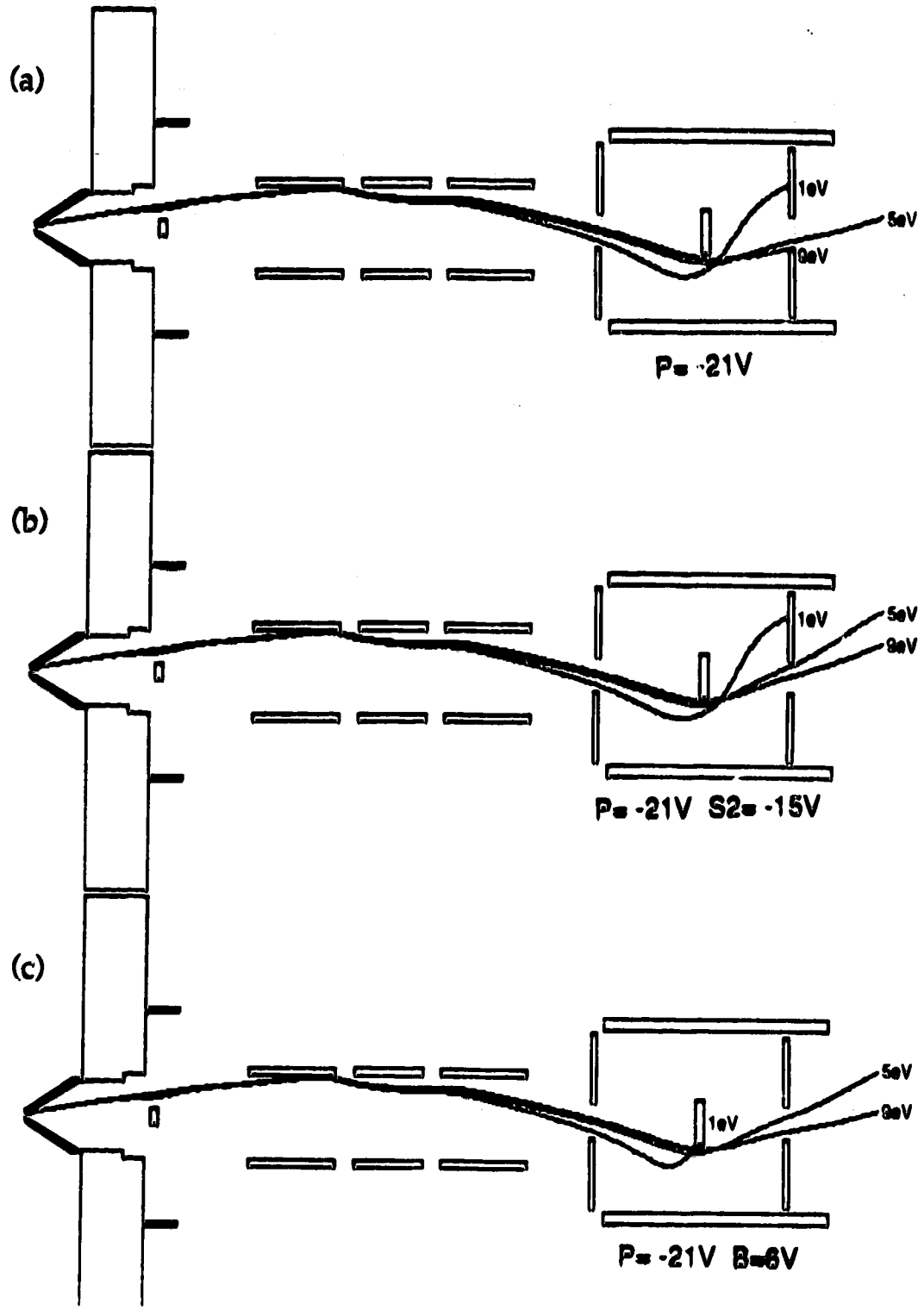

Figure 6.13 Trajectories for 1, 5 and 9eV ions. Lens settings: E1 = -30V, B = 4V, S2 = -9V and P = -21V (a). Lens settings:E1 = -30V, B = 4V, S2 = -15V and P = -21V (b). Lens settings:E1 = -30V, B = 6V, S2 = -9V and P = -21V (c). Entry angle is 9°.

shown in Figure 6.13c. Again the trajectory of the 9eV ion is sufficiently modified to enable the ion to exit toward the quadrupole. Thus either of these adjustments would improve the high mass response of the Sciex instrument.

The trajectory for the 1eV ion in Figure 6.14a provides an example of an ion inside the bessel box that gets deflected too much. By decreasing the bessel box barrel (B) voltage to 2V, Figure 6.14b, the 1eV ion trajectory passes through the bessel box exit. If the bessel box barrel (B) voltage of 2V is maintained and the photon stop voltage, S2, is increased to -12V, the changes in the 1eV ion trajectory caused by reducing the bessel box barrel (B) voltage is partially counteracted, Figure 6.14c. This demonstrates the interactive behaviour of the ion lenses, which is something we have observed experimentally.

3. Higher Energy Ions.

Thus far, all the ion trajectories have been acquired for ions of 1eV, 5eV and 9eV with the lens voltages chosen around a default set of conditions where E1 = -30V, P = -18V, B = 4V and S2 = -9V. For these ion energies successful ion trajectories required the einzel lens elements 1 and 3 (E1) to be set in the range of -30V. This setting differs from the settings used in experimental measurements where E1 = -16V. In order to investigate the lens settings exactly as they were set in the experimental work, higher energy ions were studied. Ion trajectories for ions with energies of 14eV, 15eV, 16eV and 17eV were generated for the lens settings E1 = -16V, P = -18V, B = 4V and S2 = -9V. In the same manner as before, the voltage of each lens was varied in turn to see how it affected the ion trajectories. The results were in agreement with the general trends summarized in Table 6.1.

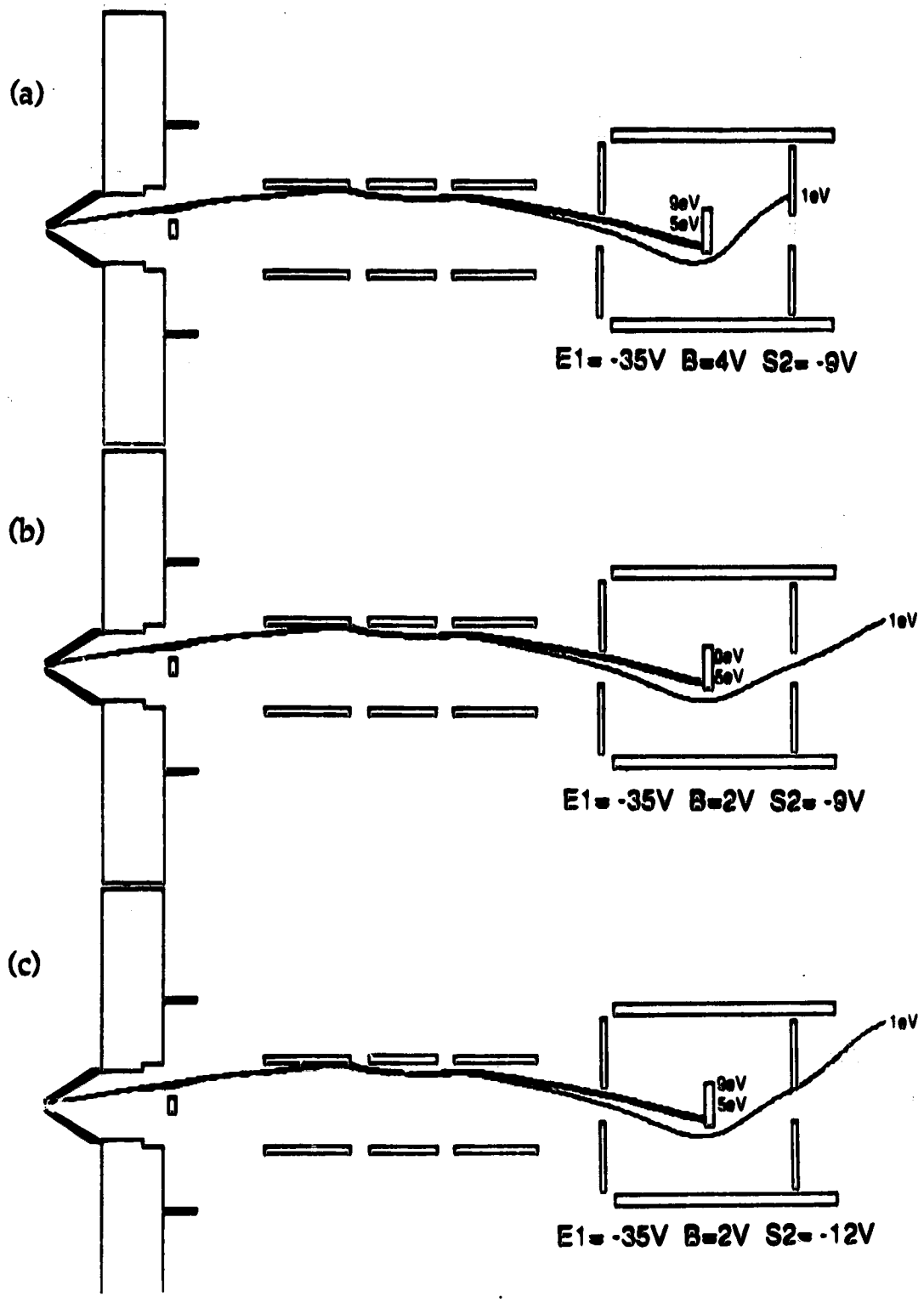

Figure 6.14 Trajectories for 1, 5 and 9eV ions. Lens settings: E1 = -35V, B = 4V, S2 = -9V and P = -18V (a). Lens settings: E1 = -35V, B = 2V, S2 = -9V and P = -18V (b). Lens settings: E1 = -35V, B = 2V, S2 = -12V and P = -18V (c). Entry angle is 9°.

A set of trajectories for three einzel lens settings is shown in Figure 6.15. As with the lower energy ions, the lower the voltage on the einzel lens, E1, the greater the deflection of the ion path from the einzel lens to the front of the bessel box. It is interesting to note that in this energy range the ion paths are not bent around the photon stop as much as in the case of the lower energy ions. A series of ion trajectories for a series of photon stop voltages is presented in Figure 6.16. For these ions, the larger the photon stop voltage the more bent the trajectory of the ions becomes in the back of the bessel box. The same is true for the bessel box barrel, B, lens. The larger the the barrel lens voltage the more the ion trajectory curves in the back of the bessel box. The trajectories supporting this are plotted in Figure 6.17. Figure 6.18 rounds out the set with trajectories generated for two bessel box plate, P, lens settings. As above, the results support the data acquired for the lower energy ions. The lower the plate voltage the greater the trajectory curvature in the bessel box.

4. Signal Intensity as a Function of Lens Potential.

An attempt was made to estimate relative signal intensities as a function of lens potentials. To this end the following argument was used. In these simulations there is a range of entry angles a to b where ions will successfully traverse the lens system. Due to the cylindrical symmetry these angles will cut a ring in space the area of which should be proportional to signal intensity. Via basic trigonometry the area of the ring may be given by:

$$\beta = \tan^2 b - \tan^2 a \qquad 6.11$$

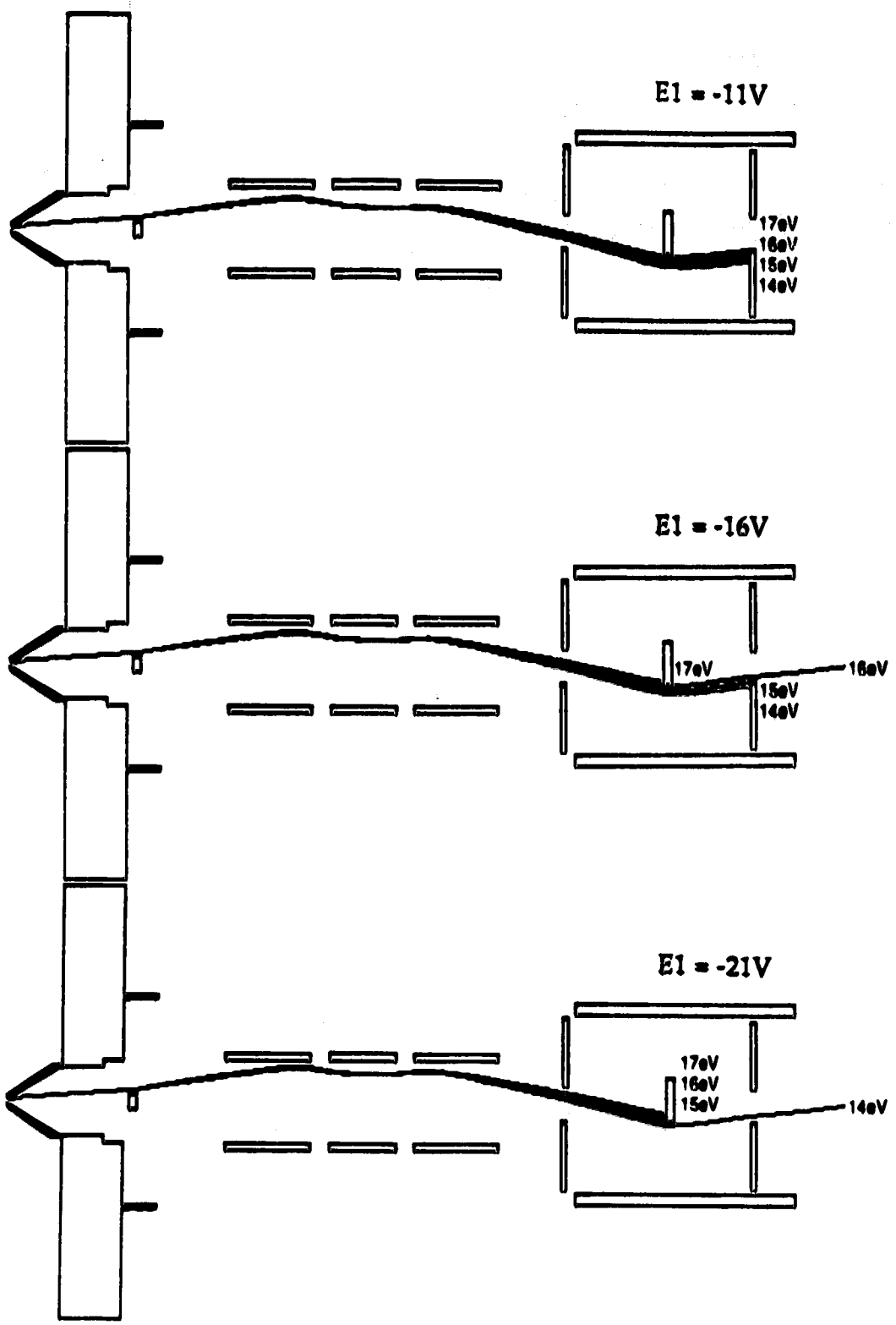

Figure 6.15 Trajectories for 14, 15, 16 and 17eV ions at varied E1 voltages. Lens settings: P = -18V, B = 4V and S2 = -9V. Entry angle is 9°.

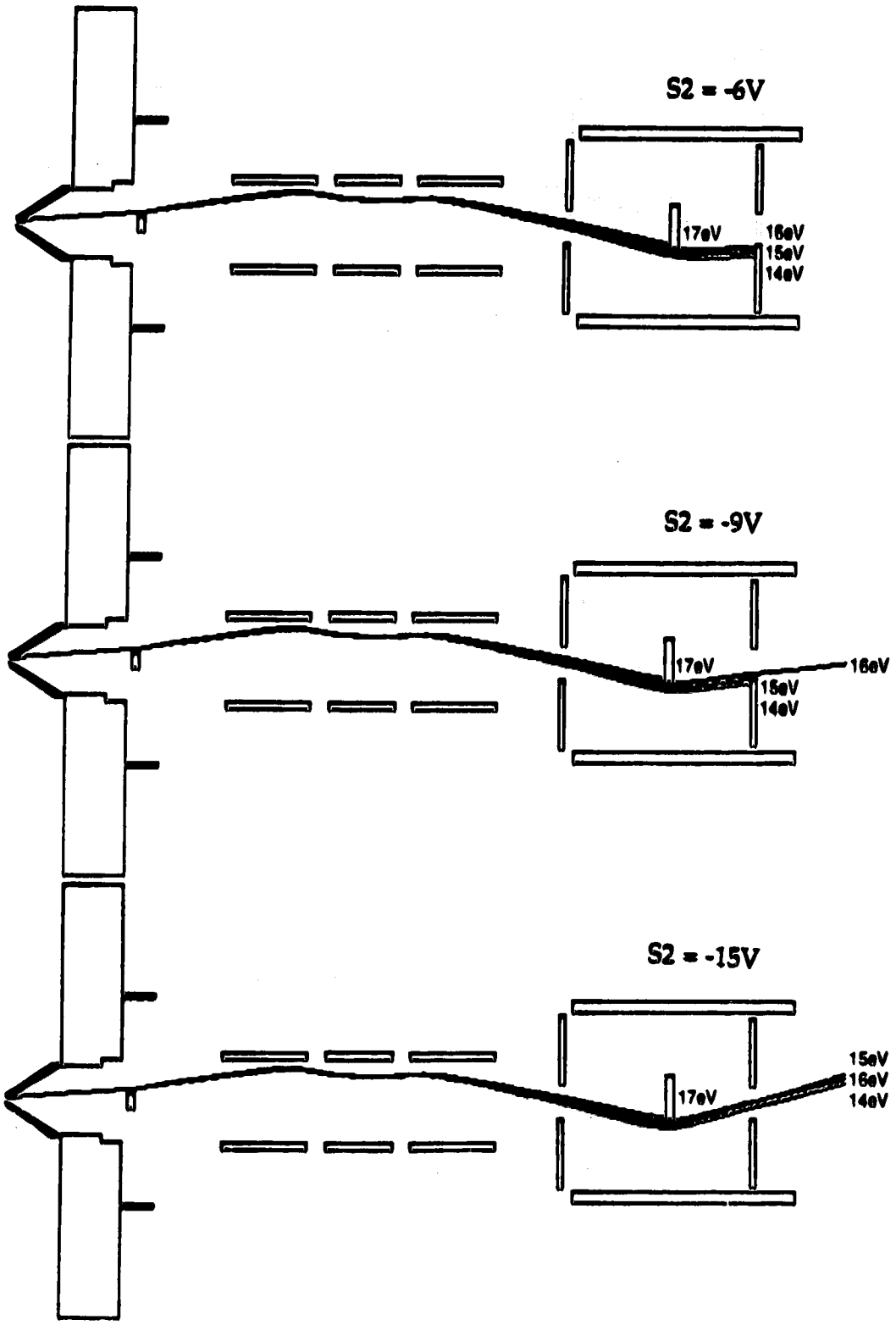

Figure 6.16 Trajectories for 14, 15, 16 and 17eV ions at varied S2 voltages. Lens settings: E1 = -16V, P = -18V and B = 4V. Entry angle is 9°.

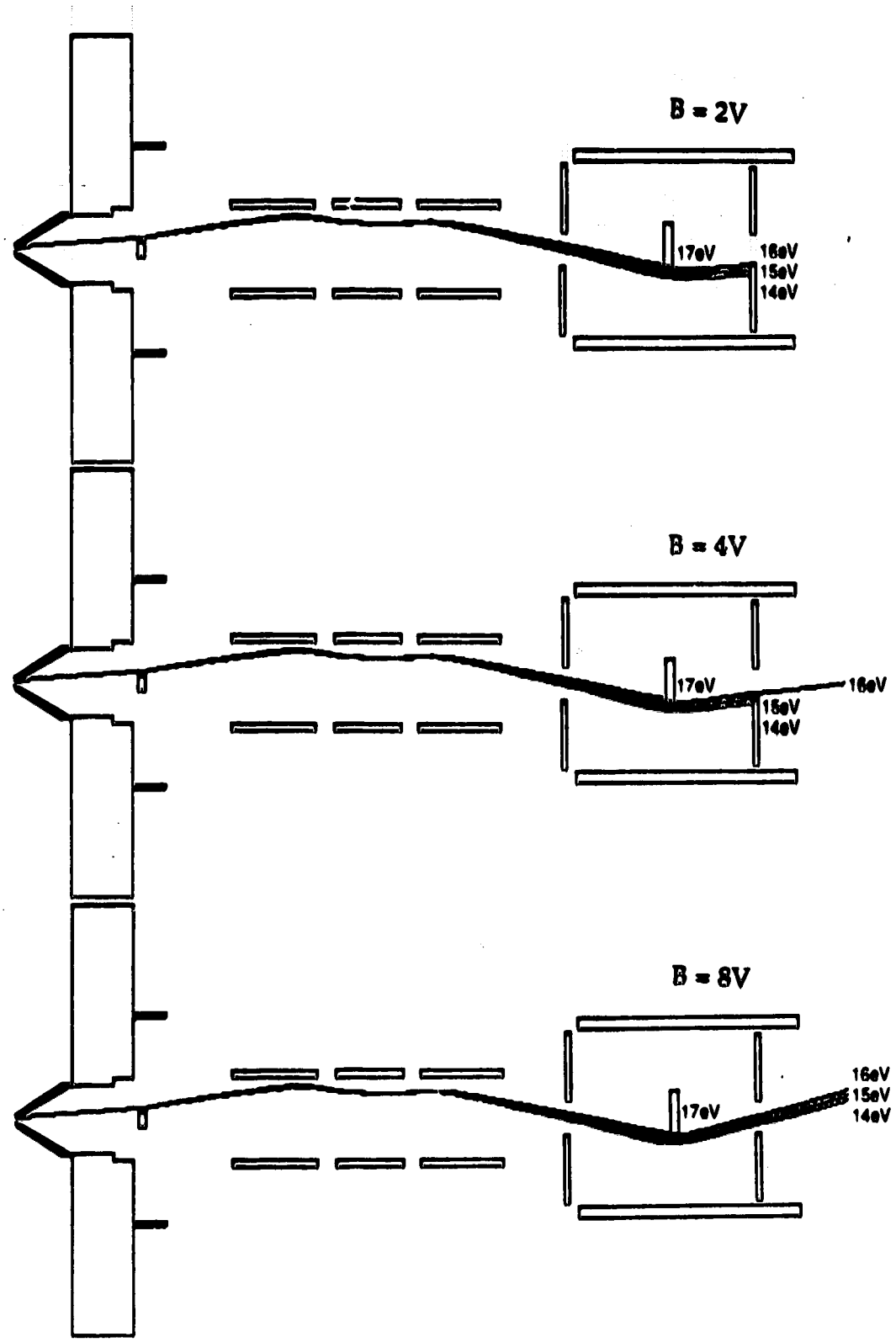

Figure 6.17 Trajectories for 14, 15, 16 and 17eV ions at varied B voltages. Lens settings: E1 = -16V, P = -18V and S2 = -9V. Entry angle is 9°.

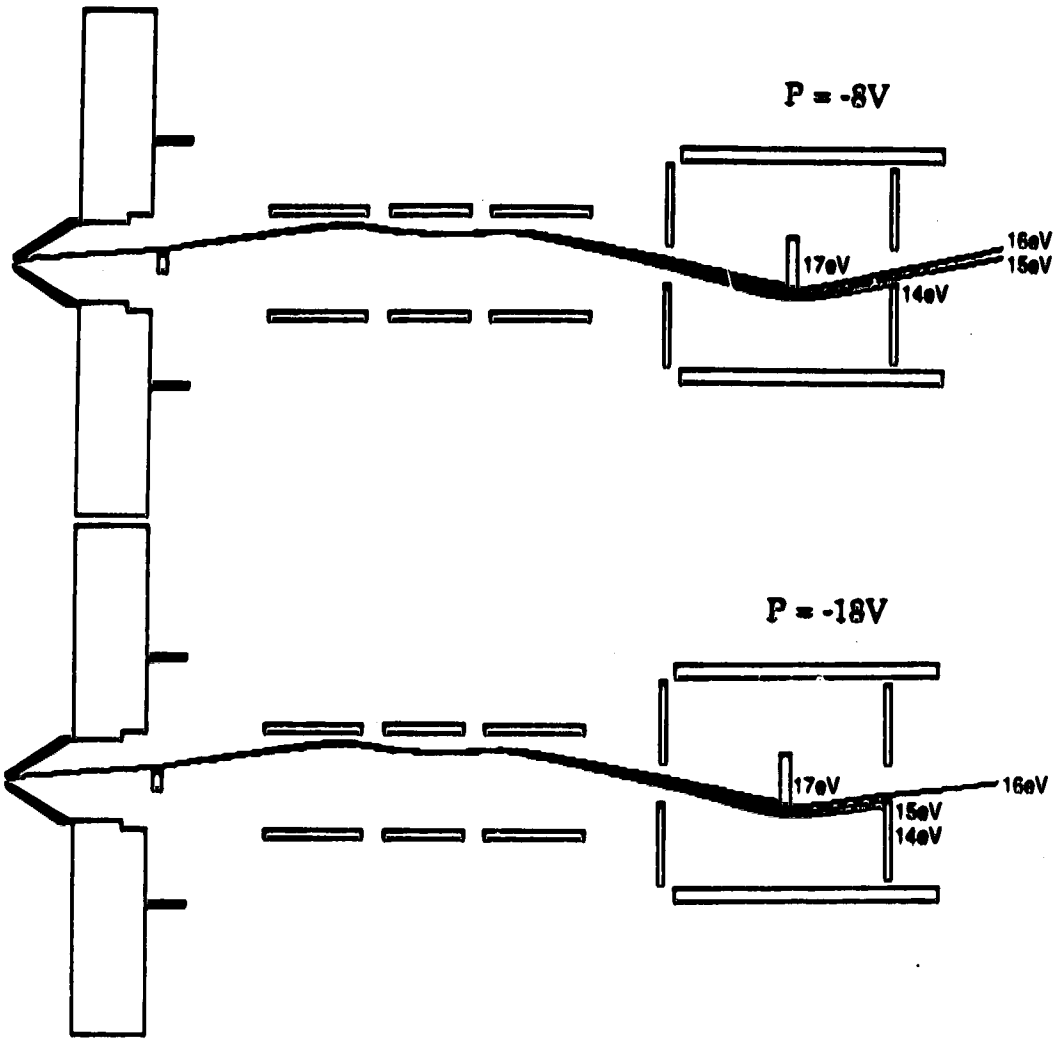

Figure 6.18 Trajectories for 14, 15, 16 and 17eV ions at varied P voltages. Lens settings: E1 = -16V, B = 4V and S2 = -9V. Entry angle is 9°.

This β value was used as an estimate of lens throughput. The results of estimated ion throughput in arbitrary units versus the photon stop voltage is shown in Figure 6.19 . For plot (a) the other potentials were set at E1 =-30V, P = -18V and B = 4V. The maximum range of angle throughput was 7° - 18° for Ti, 6° - 14° for Pd and 5° - 11° for Bi. These element assignments are based on the assumptions relating energy to mass as reported by Fulford and Douglas [2]. The results obtained by repeating the experiment with E1 = -25V, keeping all other conditions the same is presented in the bottom plot, Figure 6.19b. With the reduced einzel lens voltage the 3.3eV ion corresponding to Ti did not successfully exit the system. Of the remaining two, Pd, (4.8eV) had a solid angle range of 7.2° - 8.9° and Bi (7.5eV) had a range of 4.4° -9.5°. These ranges are much smaller than those obtained with the einzel lens setting of E1 = -30V and the resulting area values, β, are of reduced magnitude. The effect is more severe for the lower energy ions. The Pd signal is reduced by 83% while the Bi signal is reduced by 27%. It is important to note the effect the einzel lens voltage has on the relative magnitudes of the ion throughput. It is tempting to look at the top plot in Figure 6.19 and compare it to the experimental results from the ICP-MS since the intensities for both go as Ti>Pd>Bi. We cannot draw any conclusions from this, however, because of the large number of factors that affect experimental signal intensities such as the quadrupole, the degree of analyte ionization in the plasma, the natural abundances of the elements and so on.

The ion throughput, calculated as β (equation 6.11), was determined as a function of ion lens voltage for the photon stop, S2, the bessel box barrel, B, and the bessel box plates, P, using the two sets of default conditions and the two sets of ion energies. The signal versus lens voltage plots for the three

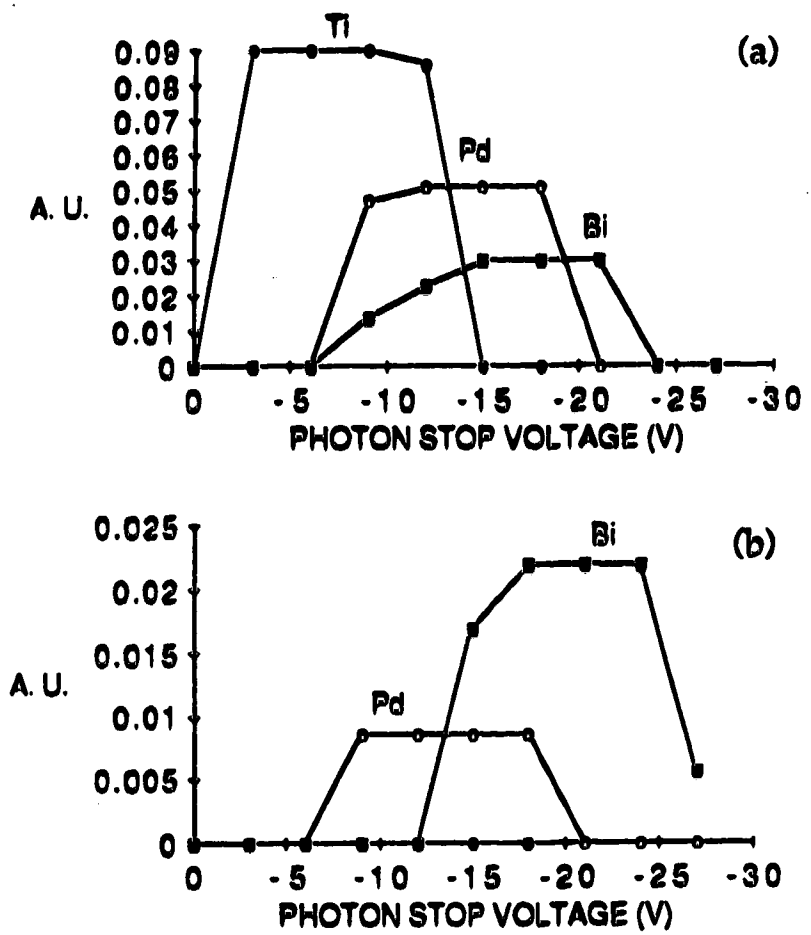

Figure 6.19 Estimated ion throughput (arbitrary units) as a function of photon stop voltage. Lens settings: E1 = -30V, P = -18V and B = 4V (a). Lens settings: E1 = -25V, P = -18V and B = 4V (b). Entry angle is 9°.

lenses when E1 = -30V is shown in Figure 6.20. The signal versus lens voltage plots for E1 = -16V may be found in Figure 6.21. The behaviour of the ion signal with respect to the lens voltage as measured on the ICP-MS closely resembles the solid angle transmitted as a function of voltage when E1 = -30V. The signal maxima are reached within the voltage ranges tested. When E1 = -16V it appears that the voltage ranges may need to be extended to reach maximum signal intensities.

Using the results from the E1 =-30V then, the response to the voltage changes for experimental and simulated data were compared. All the data were normalized to the peak value in each case for the following reasons. The peak amplitude can be a function of other lens settings and, in the case of the experimental results, the intensity fluctuation from element to element is so large that Bi, for example, would be lost on the baseline if the appropriate scale for Ti were used. In Figure 6.22 the simulated results (Figure 6.22a) and the experimental results (Figure 6.22b) for intensity as a function of photon stop voltage are presented. In both cases the response takes the shape of a peak, however, the experimental results cover a smaller voltage range. Similarly, in Figure 6.23, the results for the plate voltage, P, are given. The simulated data are presented in Figure 6.23a and Figure 6.23b contains the experimental results. Again the experimental results are not exactly like the simulated data, especially for Bi, but there are similarities in general shape. Finally, to complete the set, the results for the barrel voltage are presented in Figure 6.24. In this case too, there are similarities in shape of the curves generated by simulation and by experiment.

In all three sets the comparison between simulated and experimental results must be done with caution. In the ICP-MS the ions for each mass have

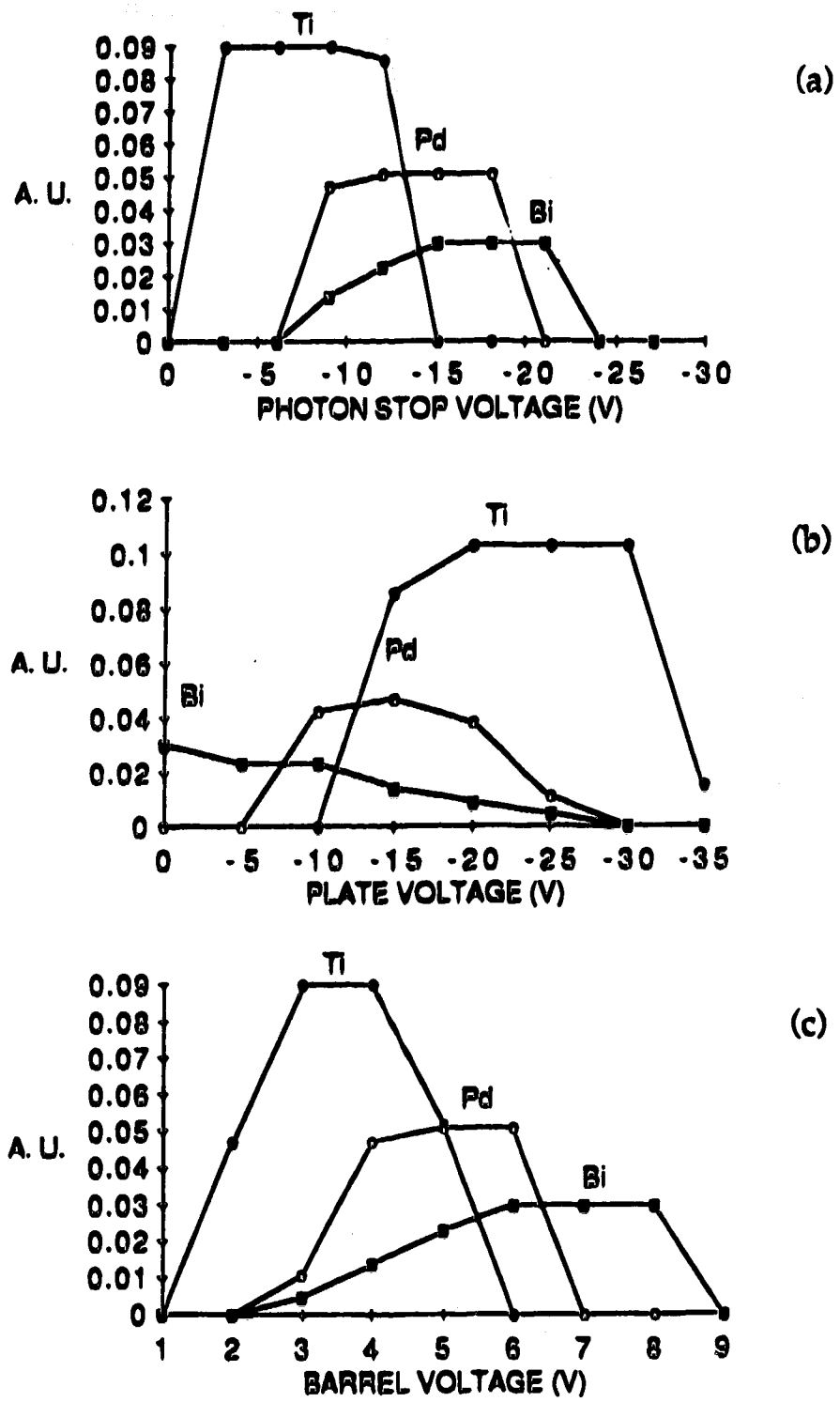

Figure 6.20 Estimated ion throughput (arbitrary units) as a function of photon stop voltage (a), plate voltage (b) and barrel voltage (c). E1 = -30V.

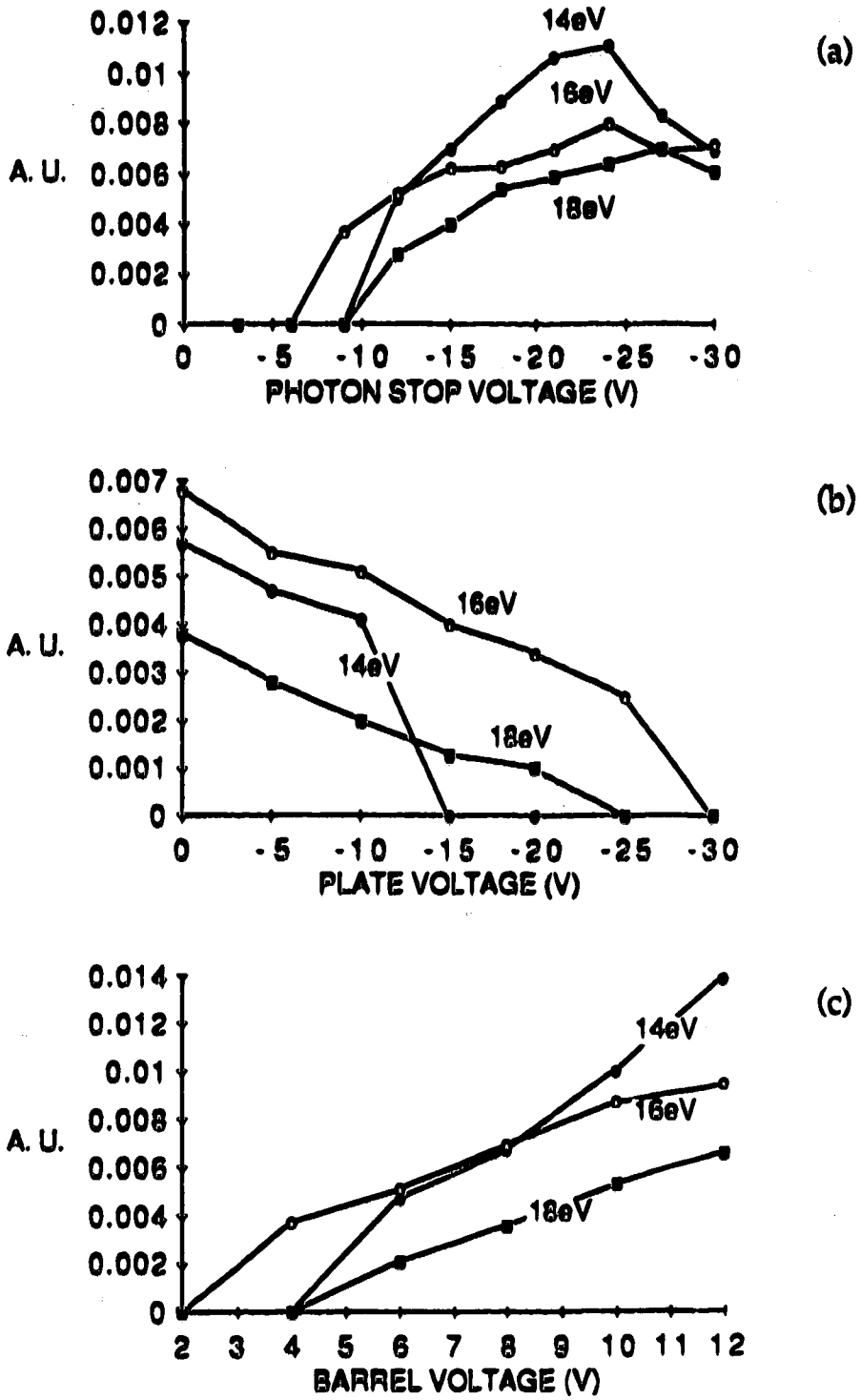

Figure 6.21 Estimated ion throughput (arbitrary units) as a function of photon stop voltage (a), plate voltage (b) and barrel voltage (c). E1 = -16V.

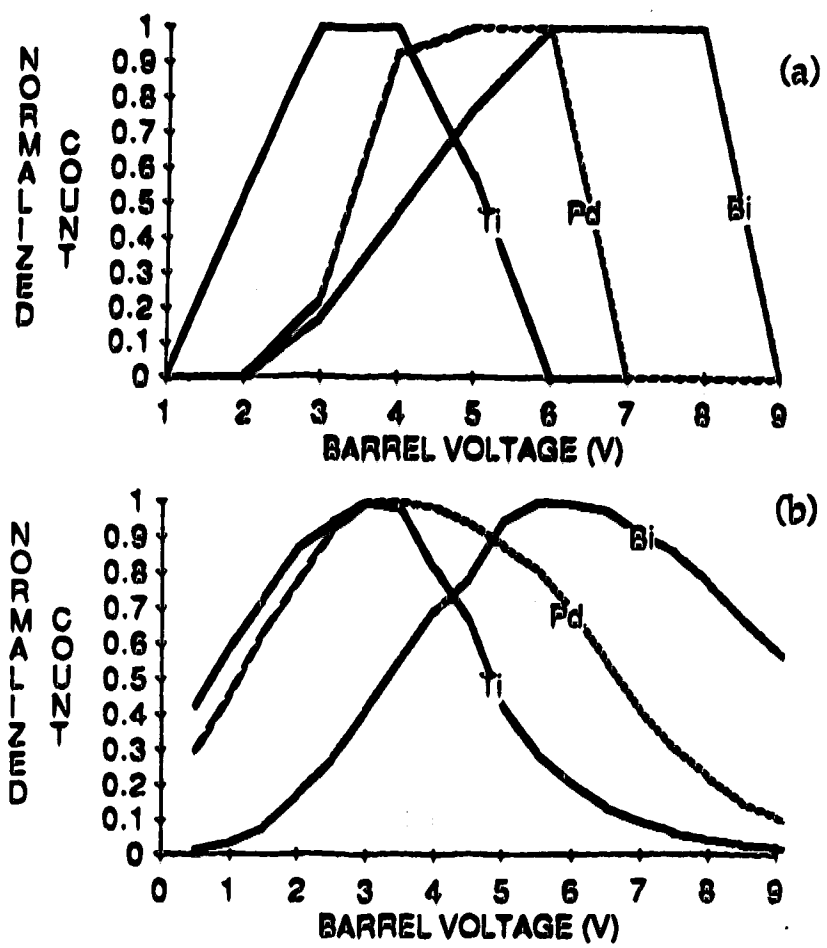

Figure 6.22 Estimated ion throughput (arbitrary units, normalized for each element) as a function of barrel voltage (a). Experimental results of intensity as a function of barrel voltage, normalized for each element (b).

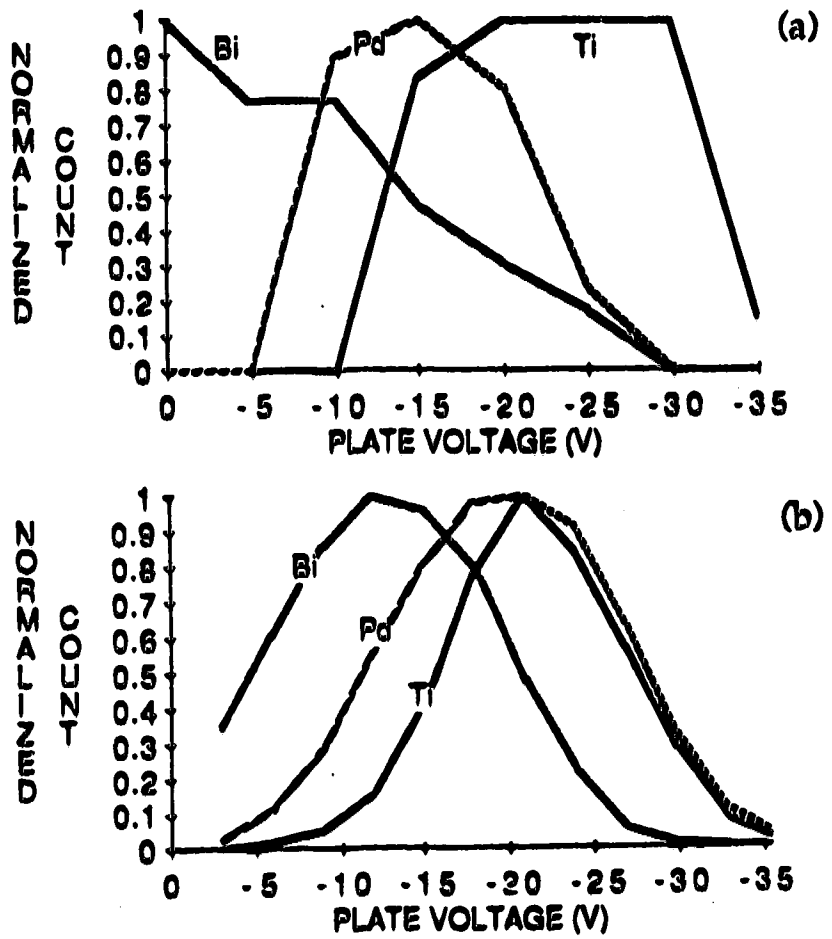

Figure 6.23 Estimated ion throughput (arbitrary units, normalized for each element) as a function of plate voltage (a). Experimental results of intensity as a function of plate voltage, normalized for each element (b).

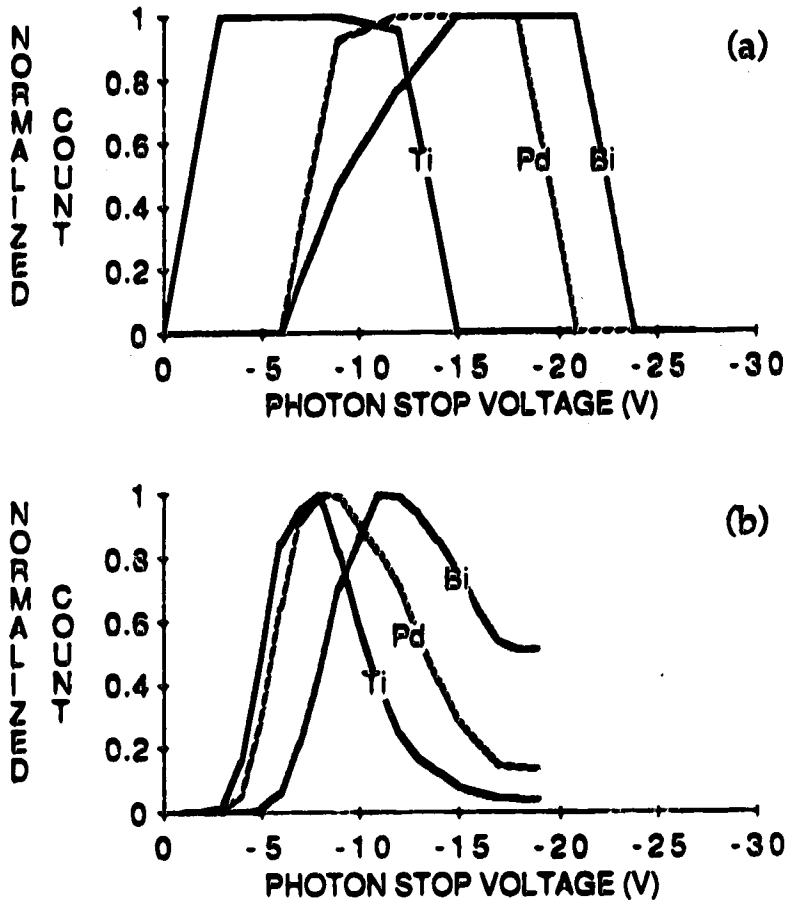

Figure 6.24 Estimated ion throughput (arbitrary units, normalized for each element) as a function of photon stop voltage (a). Experimental results of intensity as a function of photon stop voltage, normalized for each element (b).

a range of energies while only one energy is considered in the simulation. There is also a question as to the validity of assigning ion energies to masses as discussed earlier. However, keeping that in mind, it is interesting to see that for both the experimental and simulated results the order in which the peaks appear are the same; eg. Ti before Pd before Bi for the photon stop, and there is a general similarity in the shape of the response curves.

5. Effect of Photon Stop Voltage on Parameter Plots.

The effect of changing the photon stop voltage on the nebulizer flowrate power parameter plots was first mentioned in Chapter 2. Although voltage changes did not affect the general mountain shape of the plots, in some cases the position of the peak maxima shifted for a given power. Parameter plots for Ni^+ obtained at photon stop voltages of -9V and -13V are presented in Figure 6.25. Changing the photon stop voltage from -9V to -13V resulted in an overall drop in signal intensity and the nebulizer flowrate corresponding to the peak maxima at each power has been reduced by 0.05L/min typically.

From the lens studies involving the photon stop we know that changing the voltage from -9V to -13V causes a larger deflection of the ions around the photon stop in the back of the bessel box. This results in ions of higher energy successfully traversing the bessel box. Since we have to lower the nebulizer flowrate to regain the maximum ion count for Ni after the photon stop voltage is changed it would appear that lowering the nebulizer flowrate causes an increase in the ion energy. If this is true, however, then why are the positions of the nebulizer flowrate power parameter plot maxima so insensitive to mass? For example, at 1.5kW, both the Ti (3.26eV) and the Pt

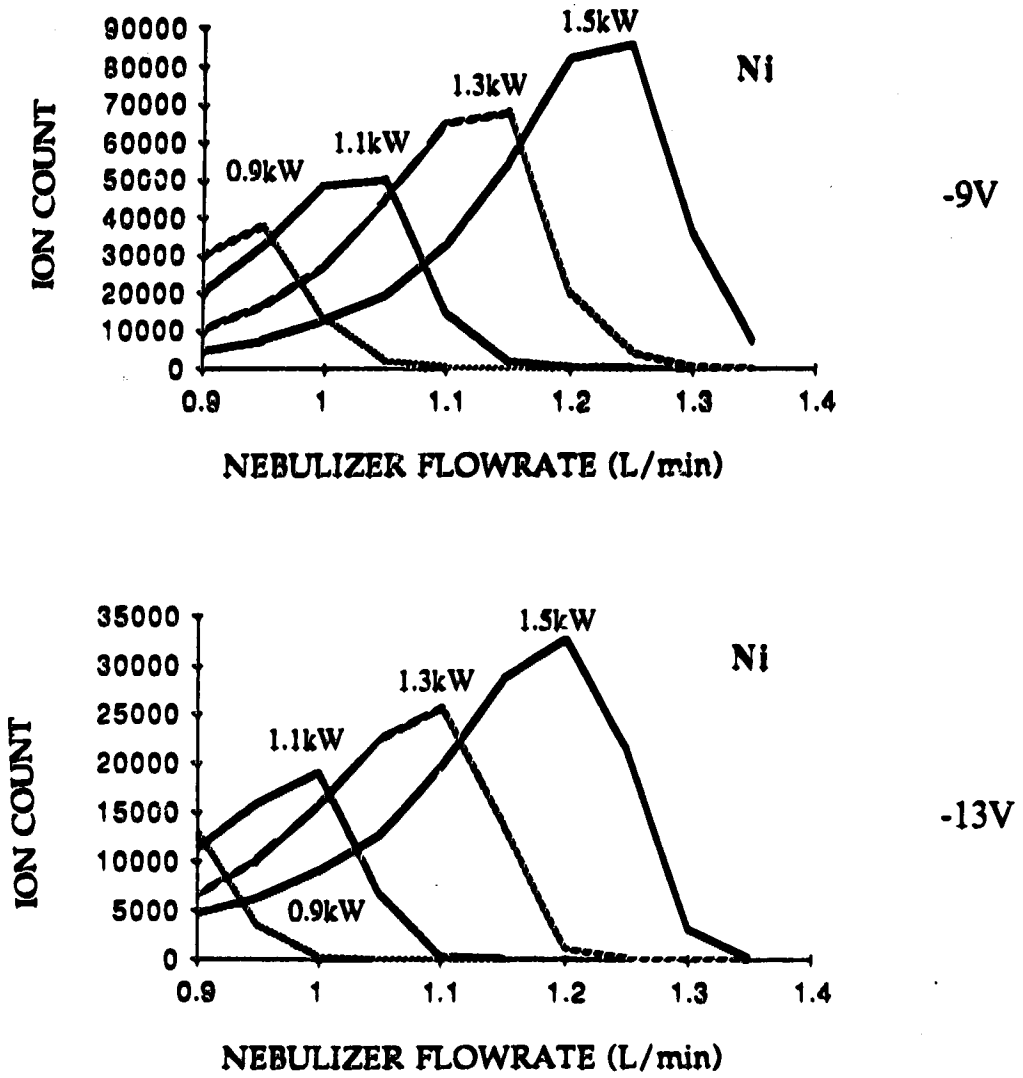

Figure 6.25 Nebulizer flowrate power parameter plots for Ni^+ at two photon stop voltages, -9V and -13V. Power in kW shown on each line.

(7.12eV) ion signal intensities reach a maximum at 1.30L/min (Chapter 2, Figure 2.1). If there was a simple relationship between the nebulizer flowrate and the ion energy, ions of higher energy (ie. larger mass) should reach a maximum signal at lower nebulizer flowrates. While it appears that ion energy and the ion optics have some effect on the parameter plots the reason for the mountain shape has not yet been determined. Since the parameter plots are affected by so many factors, it is not easy to pin-point the cause of the mountain shape. Clearly this is an area requiring further study.

Conclusions

The series of ion trajectory simulations through this lens system has proven beneficial from the viewpoint of the basic understanding of the ion lenses. It has become clear that ion trajectories through the lenses are independent of mass/charge and of absolute ion charge or mass. The apparent mass effect on ion lens behaviour observed experimentally may be explained by considering the individual ion energies. Since ions traveling through the molecular beam expansion attain the velocity of the Ar neutrals, there is a kinetic energy spread in the ions which is a function of mass. This is why compromise conditions are needed in ICP-MS when a large mass range is to be covered.

Ideally the ions entering the ion optics in ICP-MS should have a low energy spread; this would remove the need for compromise lens settings. The ion energy should also be independent of the ICP conditions. This is not what is observed for the ICP-MS systems which have a secondary discharge between the plasma and the interface to the mass spectrometer. Obviously

there is more work to be done on instrument design addressing these problems.

Ion trajectories through the lens system depend on ion energy entrance angle and lens potential. Despite our inability to get the simulation to work under the exact experimental conditions general trends were observed which aid in our understanding of how these ion optics work. In general, the larger the E1 voltage, the smaller the angle of deflection in the ion trajectories from the einzel lens toward the bessel box. Also the larger the photon stop (S2) voltage or the larger the bessel box barrel (B) voltage or the smaller the bessel box plate (P) voltage the more curved the trajectory becomes inside the bessel box.

References.

1. J. A. Olivares and R.S. Houk, Applied Spectrosc. **39**, 1070-1077, (1985).

2. J. E. Fulford and D. J. Douglas Applied Spectrosc. **40**, 971-974, (1986).

3. H. Kawaguchi, Analytical Sciences, **4**, 339-345, (1988).

4. G. R. Gillson, D. J. Douglas, J. E. Fulford, K. W. Halligan, and S. D. Tanner, Anal. Chem. **60**, 1472-1474, (1988).

5. A. B. El-Kareh and J. C. J. El-Kareh, "Electron Beams , Lenses and Optics Vol.I", Academic Press, N. Y. 1970.

6. J. E. Campana, Int, J. Mass Spec. Ion Phys. **33**, 101-117, (1980).

7. P.H. Dawson, Quadrupole Mass Spectrometry and its Applications, Elsevier Scientific Publishing Co. 1976, Chapter 2.

8. G. Lawson and J. F. J. Todd, Chemistry in Britain, **8**, 373-380, (1972).

Chapter 7

Effect of Sampler and Skimmer Orifice Size on Parameter Behaviour and Oxide Formation

Ideally the sampling of an inductively coupled plasma (ICP) into a mass spectrometer would involve obtaining material from a known point in the plasma followed by immediate quenching of any chemical reactions that might occur in the sampled material. In this way the composition of the plasma would be accurately represented by the mass spectra obtained. Unfortunately such an ideal situation does not exist. As well as reactions occurring in the supersonic expansion of the sampled material, the insertion of a relatively cool metal sampling cone into the plasma results in changes in the composition of the plasma gases that come in contact with the metal surface. A boundary layer of cooler gases is formed along the surface of the metal. This is a region rich in ion molecule reactions.

The earliest reports of work in inductively coupled plasma mass spectrometry (ICP-MS) by Houk et al. [1] and Date and Gray [2] involved ion extraction after transport through a boundary layer. It was estimated that an ion could undergo up to ~10^6 collisions [1] in the 1 - 2ms it took to traverse the boundary layer. Sampling through such a boundary layer can produce a variety of molecular ions causing interelement interferences and an increase in mass spectral complexity. To get around this problem, continuum flow ion extraction of the ICP into the mass spectrometer was developed. Gray and Date [3] reported that larger orifices than those in the 50 - 80μm diameter range used in boundary layer sampling were needed in the samplers for

sampling of the bulk plasma. They stated that sampling apertures of at least 0.2mm diameter were required. With these larger orifices another problem appeared. A secondary discharge between the plasma and the sampling cone developed [3]. The formation of this discharge is discussed in detail by Hieftje and Vickers [4] who point out that from a fundamental point of view an orifice linked discharge produces a distorted view of species that intrinsically exist in the plasma.

Douglas and French [5] describe an interface for the ICP-MS that reduces such a discharge to negligible proportions. Thus with this interface and with sampling orifices with diameters in the range of 0.2 - 1.0mm it should be possible, in principle, to have continuum sampling of the plasma through the sampler. Even though continuum sampling is obtained it is important to know if the ions sampled are truly representative of the plasma or if there are processes occurring that modify the sampled plasma material. Longerich et al. [6] reported that the design and condition of the sampler and skimmer have an effect on oxide formation and on the shape of the intensity versus nebulizer flowrate plots. Hayhurst et al. [7], in their report on MS sampling of ions from atmospheric pressure flames state that the composition of the sampled flame may be affected by reactions occurring on the surface of the cone as well as by reactions occurring during the expansion. These observations suggest that changes in the sampled plasma gas caused by the ICP-MS sampling interface are possible and even likely.

In this study we will discuss the effect of simple changes in the sampling interface of the ICP-MS, namely changing the orifice size in the samplers and skimmers used. Intensity versus nebulizer flowrate data shall

be presented and discussed for the various orifice sizes as well as a discussion of the dramatic changes in oxide formation that result.

Experimental

All measurements were made on a Sciex Elan 250 ICP-MS. A MAK torch was positioned such that the tip of the sampler was 15mm from the load coil. All data were collected with the ICP power set at 1.3kW and the central plasma and auxiliary Ar gas flows set at 12L/min and 1.4L/min respectively. The Ar nebulizer flowrate was varied between 0.75 and 1.25L/min and was controlled by a Matheson Model 8240-0423 mass flow controller. The ion lenses were optimized for ions in the rare earth element mass range. Data were acquired in low resolution, multichannel mode using 3points/peak, 0.1s integration time, 50ms dwell time and 6 repeats.

The samplers and skimmers were made in house from Cu and stainless steel respectively. The design of the samplers, modeled after those provided with the instrument, was kept the same except for the orifice size. Orifice diameters used were 0.51, 0.64, 0.76, 0.89 and 0.94mm. Similarly, the skimmer design, modeled after the skimmer provided with the instrument, was unchanged except for the orifice diameters which were 0.76, 0.89 and 1.0mm. Except where otherwise stated a skimmer with a 0.89mm diameter orifice was used.

Multi-element solutions were prepared from Spex Industries Inc. standards and were 1μg/mL in each element.

Results and Discussion

1. Effect of sampler orifice diameter on intensity versus flowrate plots.

The intensity as a function of nebulizer flowrate was measured for a series of nine elements, Zn, Ge, As, Sr, Y, Zr, Ru, Te and Ba at five sampler orifice diameters, 0.51, 0.64, 0.76, 0.89 and 0.94mm. The oxides for Sr, Y, Zr, Ru, Te and Ba were also measured. There were some interesting changes in the shape of the plots for the different samplers, especially for the smaller orifice sizes. The narrowest intensity versus nebulizer flowrate peaks were obtained with the 0.51mm diameter orifice. See Figure 7.1. The maxima for the nine elements occurred at 1.15L/min except for As^+ and Te^+ which had maxima at 1.10L/min. The intensity versus nebulizer flowrate plots all seem to have low but moderately flat tails on the low flowrate end. The plot for As^+ contains a tail that appears larger than the rest but it is exaggerated because of the low ion count of only 9000counts/s maximum. Of the oxides measured strong YO^+ and ZrO^+ signals were obtained while signals were moderate for SrO^+ and BaO^+ and small for ReO^+ and TeO^+. Oxides for Ge and As were not measured due to interferences with ^{90}Zr and ^{91}Zr respectively.

From the intensity versus nebulizer flowrate plots for a sampler orifice diameter of 0.64mm, displayed in Figure 7.2, we can see a loss of distinct peak structure so commonly seen under normal operating conditions (0.89mm). Compared with the results from the 0.51mm sampler the Sr^+, Ru^+ and Ba^+ signals have decreased while the signals for Zn^+, As^+, Ge^+ and Te^+ have increased. Signals have also increased for Y^+ and Zr^+ although the YO^+ and

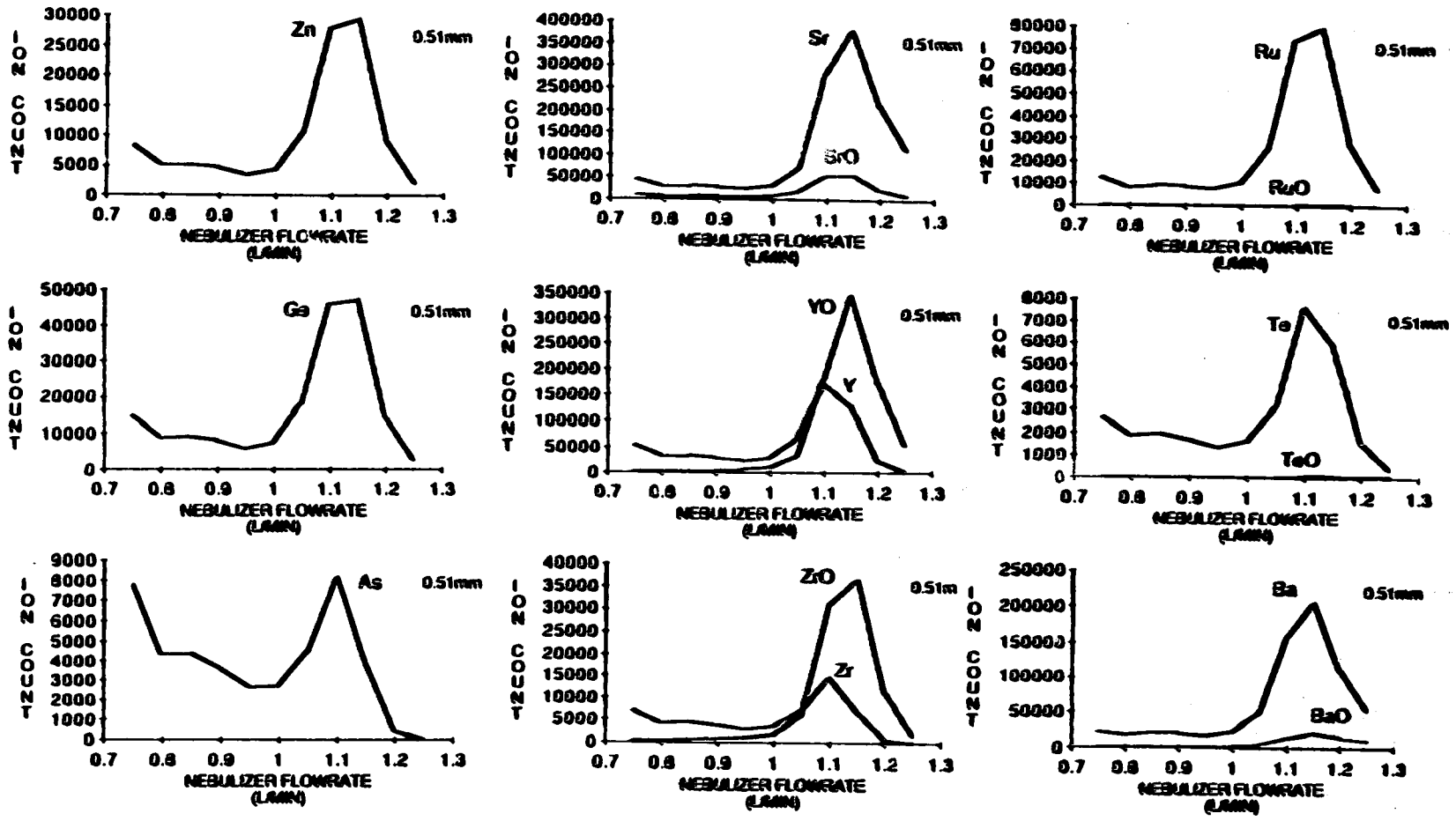

Figure 7.1 Nebulizer flowrate parameter plots for Zn^+, Ge^+, As^+, Sr^+, Y^+, Zr^+, Ru^+, Te^+ and Ba^+. Sampler orifice diameter, 0.51mm.

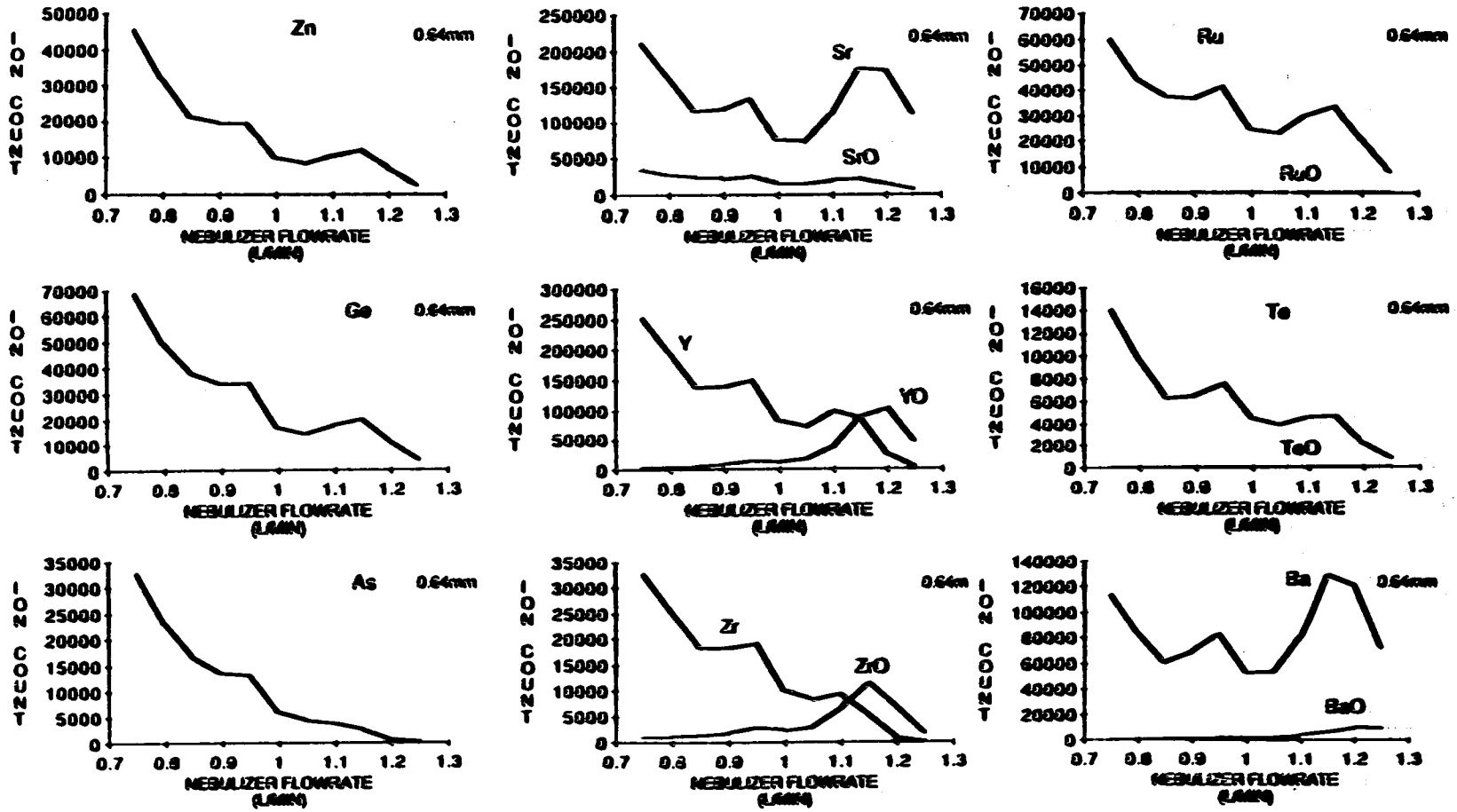

Figure 7.2 Nebulizer flowrate parameter plots for Zn^+, Ge^+, As^+, Sr^+, Y^+, Zr^+, Ru^+, Te^+ and Ba^+. Sampler orifice diameter, 0.64mm.

ZrO^+ signals have dropped considerably. There has been a general decrease in oxide levels with this orifice.

A further increase in sampler orifice diameter to 0.76mm, Figure 7.3, resulted in the re-establishment of a peak shape in the intensity versus nebulizer flowrate plots. The peaks seen here are broad and double humped. There is an intensity increase for all nine elements and although the absolute ion count is up the relative oxide levels are down for SrO^+, YO^+ and ZrO^+. Such double humped peaks have been observed from time to time in our laboratory using a 0.89mm diameter orifice sampler. Longerich et al. [8] have also reported bimodal curves, specifically for Bi^+ and Pb^+ (figure 1a, reference 8), but could not explain why they were obtained.

A sampler orifice diameter of 0.89mm resulted in intensity versus nebulizer flowrate plots which have a peak shape with a shoulder on the low flowrate side, Figure 7.4. The signal intensity increases for all M^+ and MO^+ ions and the shape of the oxide plots resemble those observed at 0.76mm. It should be noted that this is the usual sampler orifice size used in this laboratory.

Finally, the results for the 0.94mm orifice diameter sampler are displayed in Figure 7.5. The intensity versus nebulizer flowrate plots are peak shaped and the peaks are fairly smooth. The levels of the YO^+ and ZrO^+ are increased a little with respect to Y^+ and Zr^+ compared with the results obtained with the 0.89mm sampler. There is not much change in signal intensity for Sr^+ and Ba^+ although the signal decreases for the seven other elements.

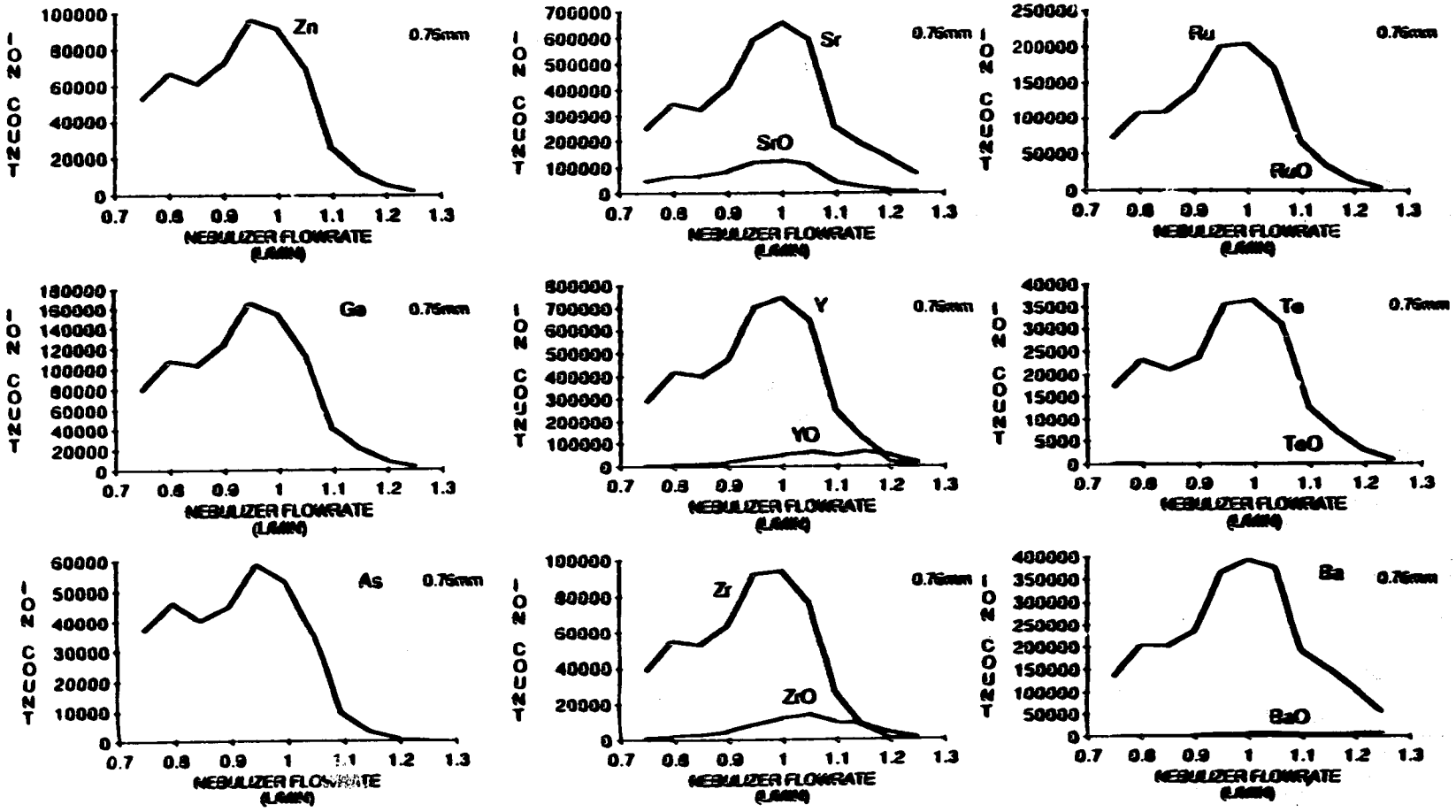

Figure 7.3 Nebulizer flowrate parameter plots for Zn^+, Ge^+, As^+, Sr^+, Y^+, Zr^+, Ru^+, Te^+ and Ba^+. Sampler orifice diameter, 0.76mm.

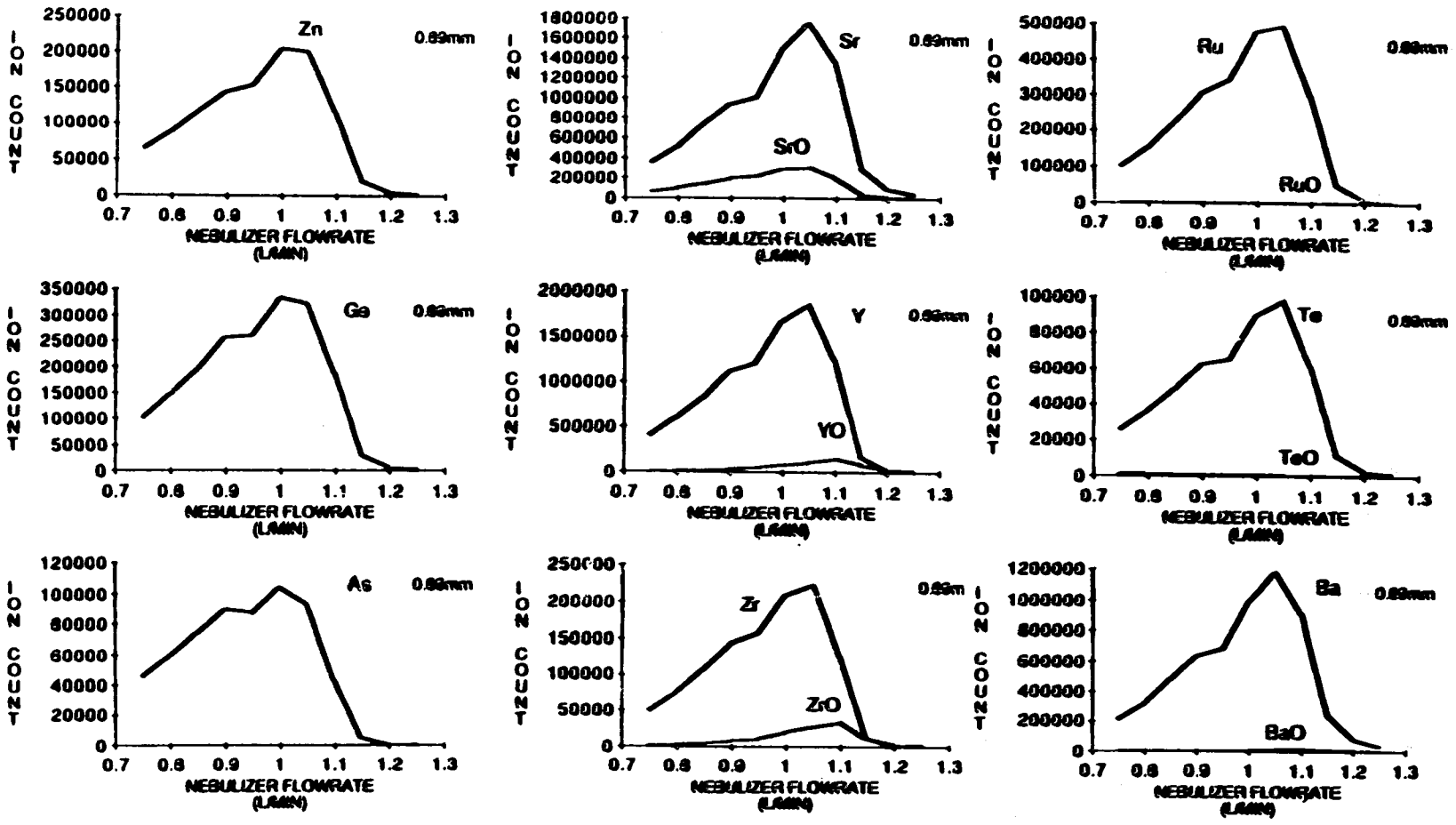

Figure 7.4 Nebulizer flowrate parameter plots for Zn^+, Ge^+, As^+, Sr^+, Y^+, Zr^+, Ru^+, Te^+ and Ba^+. Sampler orifice diameter, 0.89mm.

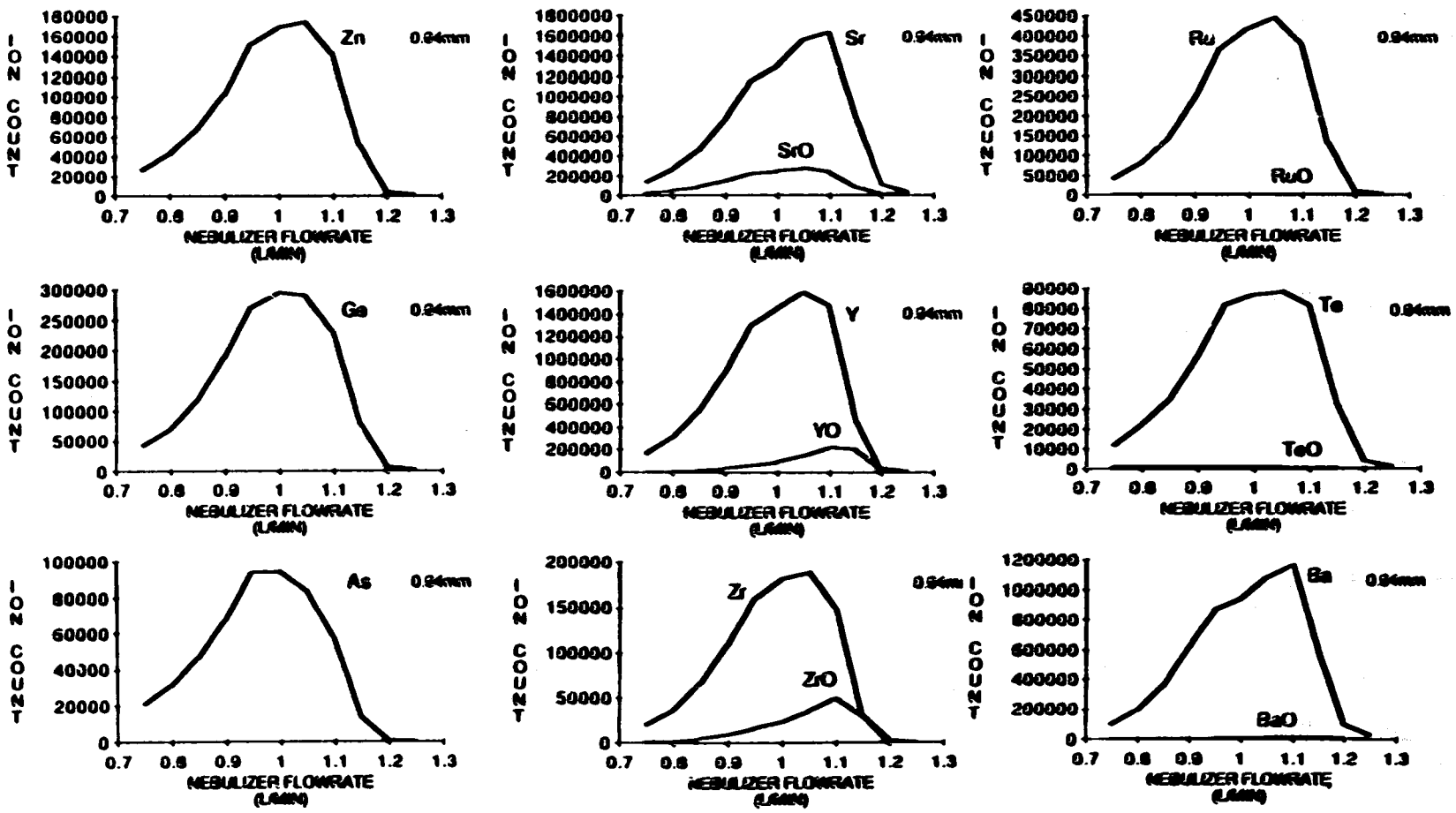

Figure 7.5 Nebulizer flowrate parameter plots for Zn^+, Ge^+, As^+, Sr^+, Y^+, Zr^+, Ru^+, Te^+ and Ba^+. Sampler orifice diameter, 0.94mm.

2. Orifice Size Effects on Oxide Formation.

From the results above it is clear that the effect of orifice size on oxide formation warrants further attention. Consider then the four elements, La, Ho, Lu and Yb, which have oxide dissociation energies of 8.90, 6.12, 5.51 and 3.81eV respectively. These four elements include a strong oxide former, La, moderate oxide formers, Ho and Lu, and a relatively poor oxide former, Yb. The intensity versus nebulizer flowrate plots for La^+ and LaO^+ are presented in Figure 7.6. At an orifice diameter of 0.51mm LaO^+ is the dominant ion, being roughly seven times the intensity of the La^+ signal. At 0.64mm, the LaO^+ signal is still dominant but the La^+ ion signal is stronger in both absolute and relative terms and has its peak maximum at a much lower nebulizer flowrate. When the orifice size is increased to 0.76mm diameter the La^+ signal is dominant and reaches its maximum at a lower flowrate than the LaO^+ signal. The La^+ signal has a more distinct peak shape compared to the La^+ signal for the 0.64mm sampler. The results for the 0.89 and 0.94mm diameter orifice are similar in shape and intensity except the LaO^+ signal reaches a higher intensity with the 0.94mm sampler. The plots for both the La^+ and LaO^+ signals have peak shapes. The peak maximum for LaO^+ falls between 1.15L/min and 1.20L/min for the orifice diameters 0.51, 0.64 and 0,76mm but then shifts to 1.10L/min, closer to the La^+ peak when the larger orifices 0.89 and 0.94mm diameter are used. The position of the La^+ peak shifts more than the LaO^+ peak. The La^+ signal reaches a maximum at 1.10L/min for the 0.51mm diameter orifice, the same flowrate at which the LaO^+ maximum is reached. The La^+ maximum then shifts farthest to the left to 0.95L/min with the 0.64mm sampler. The remaining maxima occur at 0.95,

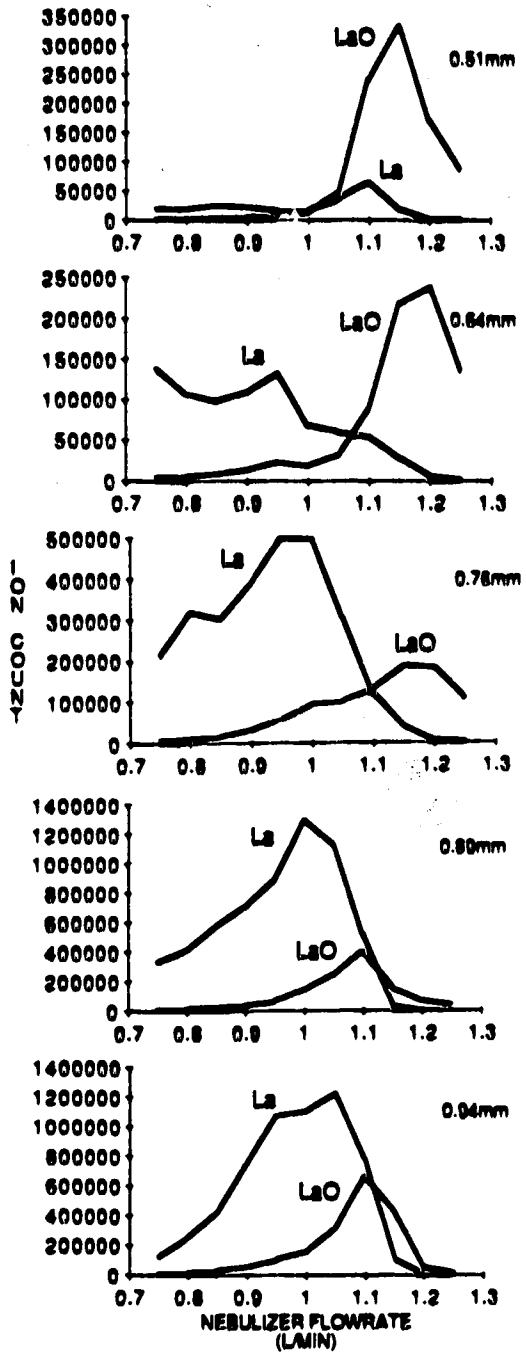

Figure 7.6 Nebulizer flowrate parameter plots for La^+ and LaO^+. Sampler orifice diameters: 0.51, 0.64, 0.76, 0.89 and 0.94mm.

1.00 and 1.05 L/min for the 0.76, 0.89 and 0.94mm diameter orifices respectively.

The data for Ho^+ and HoO^+ are presented in Figure 7.7. For this moderate oxide former, the Ho^+ and HoO^+ signals are approximately equal at their maxima which occur at the same flowrate for the 0.51mm sampler. When the orifice size is increased to 0.64mm diameter the Ho^+ signal takes on a double humped shape, one local maximum at 0.95L/min and the other at 1.15L/min. The Ho^+ signal is now stronger than the HoO^+ signal. At the 0.76mm diameter orifice, a broad Ho^+ peak with a maximum at 1.00L/min is observed and the HoO^+ intensity is reduced although its maximum still occurs in the 1.15 - 1.20 L/min range. For orifice diameters of 0.89 and 0.94mm the Ho^+ signal is dominant and the HoO^+ signal is low. The signal intensity increased with orifice size and the oxide peak shifted to a lower nebulizer flowrate of 1.10L/min.

The results for Lu^+ and LuO^+ are presented in Figure 7.8. Lu is another moderate oxide former and the results are much like those observed for Ho except the oxide levels are lower.

The fourth in this set is Yb, a relatively poor oxide former. It is easy to see from Figure 7.9 that little YbO^+ was measured. The largest amount was 1000counts/s at 0.51mm; all other levels were less than 500counts/s. The shapes of the plots of intensity versus nebulizer flowrate for Yb^+ are similar to those obtained for Ho^+ and Lu^+ although there are some differences. Consider, for example, the data obtained using the 0.64mm orifice diameter. The Yb^+ plot (Figure 7.9) has two peaks, a small one at 0.95L/min and a larger one at 1.20L/min. The Lu^+ plot (Figure 7.8) has a similar shape except the

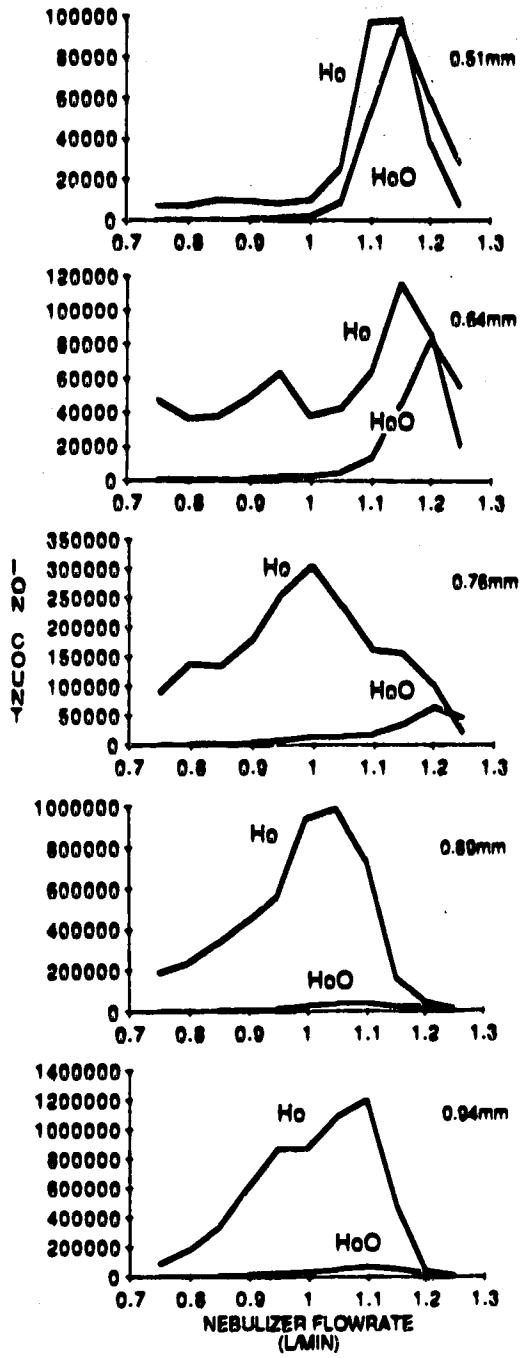

Figure 7.7 Nebulizer flowrate parameter plots for Ho^+ and HoO^+. Sampler orifice diameters: 0.51, 0.64, 0.76, 0.89 and 0.94mm.

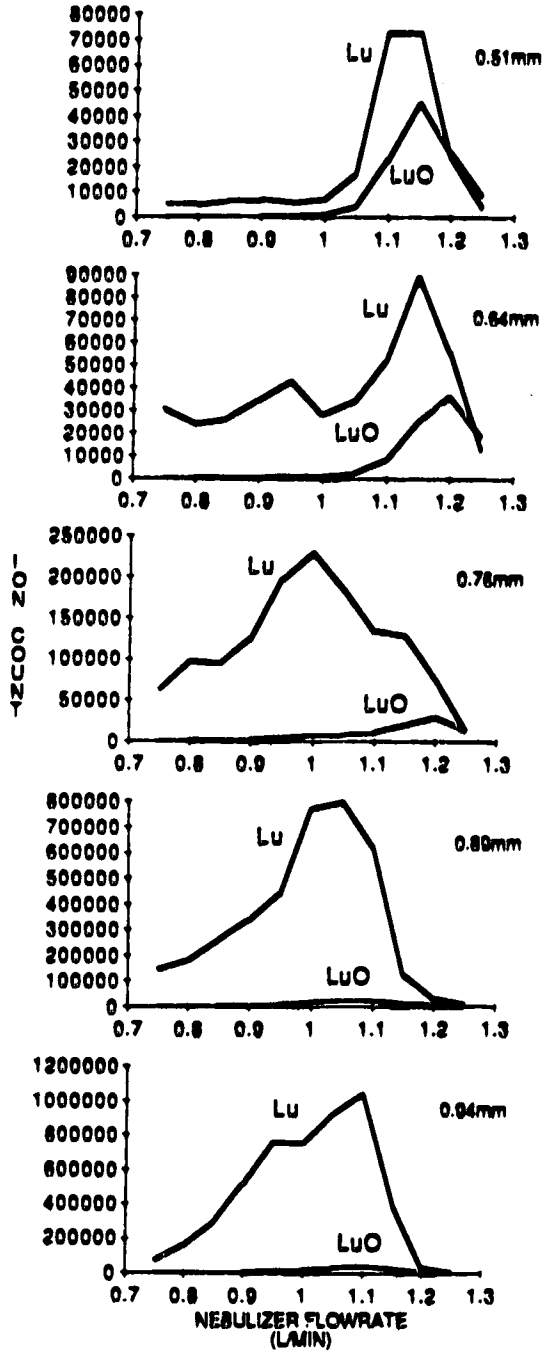

Figure 7.8 Nebulizer flowrate parameter plots for Lu^+ and LuO^+. Sampler orifice diameters: 0.51, 0.64, 0.76, 0.89 and 0.94mm.

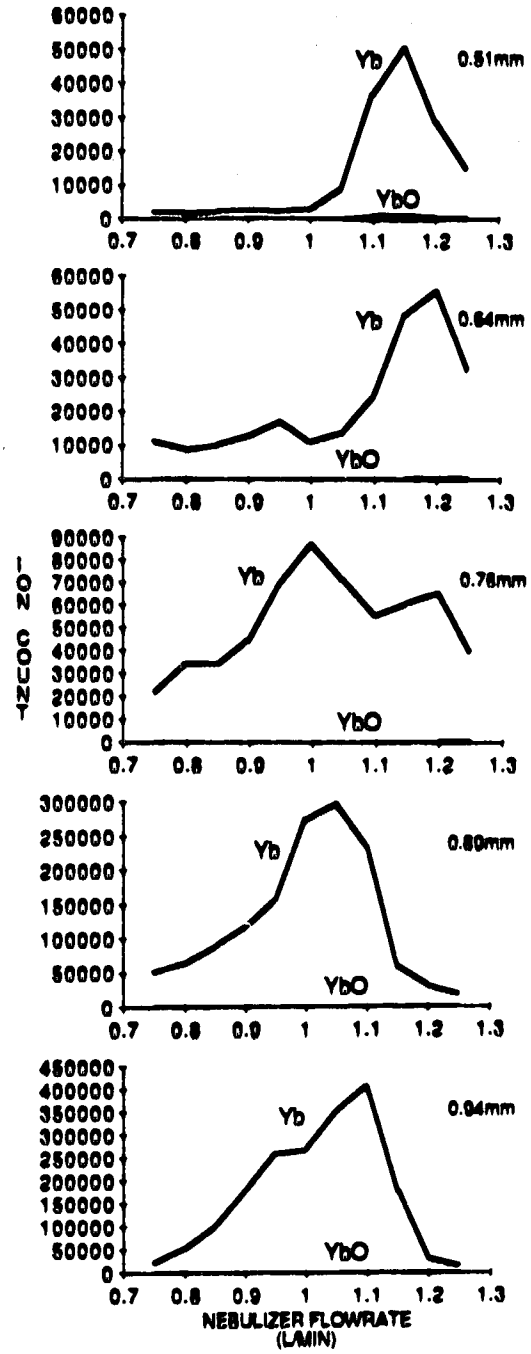

Figure 7.9 Nebulizer flowrate parameter plots for Yb^+ and YbO^+. Sampler orifice diameters: 0.51, 0.64, 0.76, 0.89 and 0.94mm.

second Lu^+ peak occurs at 1.15L/min and is closer in size to the peak at 0.95L/min. The shape of the Ho^+ plot (Figure 7.7) resembles the Lu^+ plot. The shape of the La^+ plot, (Figure 7.6) however, is distinctly different from the Yb^+ plot. The peak at 0.85L/min is the larger one and the signal at 1.10L/min is no more than a shoulder on the curve. Actually the best comparison of peak shapes occurs between Yb^+ and Bi^+. If you look at the Bi^+ data for 0.64mm in Figure 7.10, you will see that it most closely matches the shape the Yb^+ plot. This is in fact true for Yb^+ and Bi^+ at all five orifice sizes. It does not hold true for Lu^+, Ho^+ or La^+, however, but this appears to be due to the presence of the oxides.

Thus the shape of the nebulizer flowrate parameter plots for M^+ are similar for non-oxide forming elements of similar mass. The shapes of the M^+ nebulizer flowrate parameter plots become more diverse as the degree to which M^+ forms oxides increases. The smaller sampler orifice sizes (0.51mm diameter) result in conditions which yield larger relative amounts of oxides for the oxide forming elements. At these small orifice sizes the parameter plot peaks occur at higher nebulizer flowrates, typically 1.15L/min, for both the M^+ and the MO^+ species. The intermediate sized sampler orifices (0.64mm diameter) yielded double humped peaks, the predominant one at higher flowrates. Where MO^+ was formed, this species was formed almost exclusively at the higher flowrates of the second peak. The M^+ ion is the predominant ion in the peak at the lower flowrate. At the larger orifice sizes, 0.89mm and 0.94mm the M^+ peak moves to a higher nebulizer flowrate and the MO^+ peak moves to a lower flowrate. It appears that some sort of relationship between the M^+ and the MO^+ species exists and that the sampler orifice size has a strong influence on the species distribution.

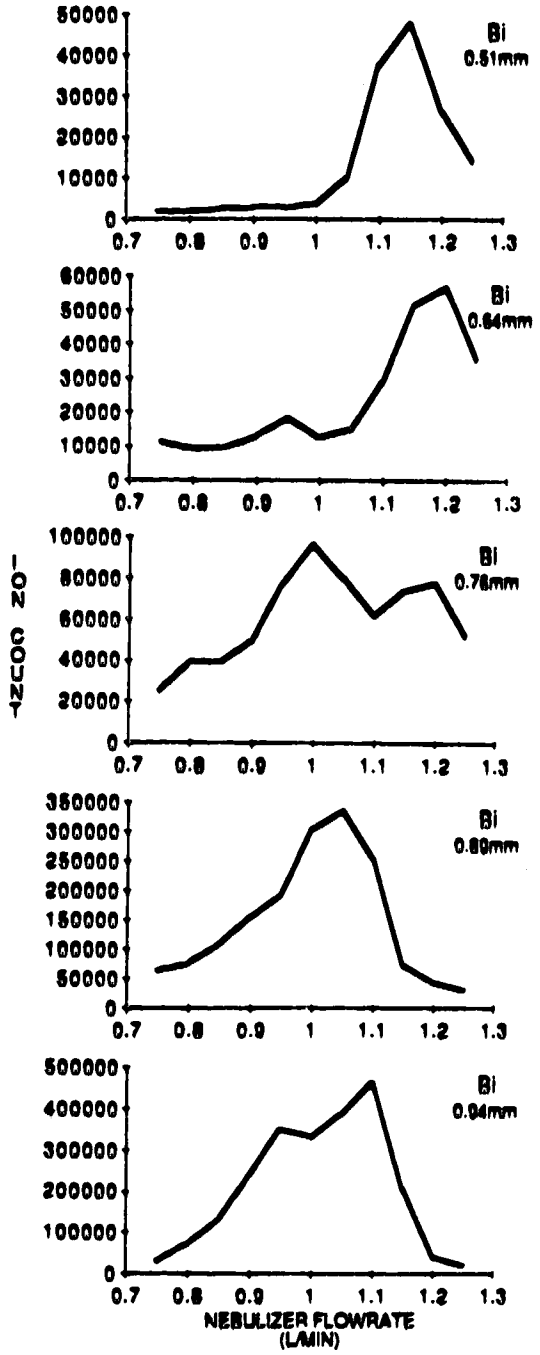

Figure 7.10 Nebulizer flowrate parameter plots for Bi^+. Sampler orifice diameters: 0.51, 0.64, 0.76, 0.89 and 0.94mm.

3. The (M + MO) Phenomenon.

Longerich et al. [6] have presented similar intensity versus nebulizer flowrate plots (figure 3, reference 6) for one orifice size for the rare earths and their oxides. They observed differences in the peak maxima for M^+ and MO^+ signals and noticed that the sum of the Ce^+ and CeO^+ signals reached a maximum at the same flowrate as the Cs^+ signal. Based on this they suggested an equilibrium between the the elemental ion and its oxide ion. This observation led us to try summing the M^+ and MO^+ signals at each flowrate and plotting the sum as a function of nebulizer flowrate. The plots of (Lu^++LuO^+) versus nebulizer flowrate are presented in Figure 7.11. The shapes of the summed data resemble the shapes of the plots for Bi^+ closely except at 0.76mm. The (Ho^++HoO^+) plots, Figure 7.12, are also close in shape to Bi^+ except, once again, for the results at 0.76mm. The two plots at 0.76mm for (Lu^++LuO^+) and (Ho^++HoO^+) resemble each other, however.

When the summed signals for La^+ and LaO^+, Figure 7.13, are compared to the Bi^+ signal the shapes are close for 0.51, 0.89 and 0.94mm orifice diameters but not for 0.64 or 0.76mm. Actually a much better correlation exists between the (La^++LaO^+) shapes and the shapes of the Cs^+ plots, Figure 7.14. This is probably because La^+ and Cs^+ are closer in mass (139 and 133) than are La^+ and Bi^+ (139 and 209). With the Cs^+ data we can go back to (Lu^++LuO^+) and (Ho^++HoO^+) at 0.76mm and suggest that the plots may resemble a combination of the Bi^+ and Cs^+ plots at that orifice size.

The observation that the sum of the singly charged ion and its oxide as a function of nebulizer flowrate results in a plot where not only the peak maximum but the general peak shape correlate to that of a plot of intensity

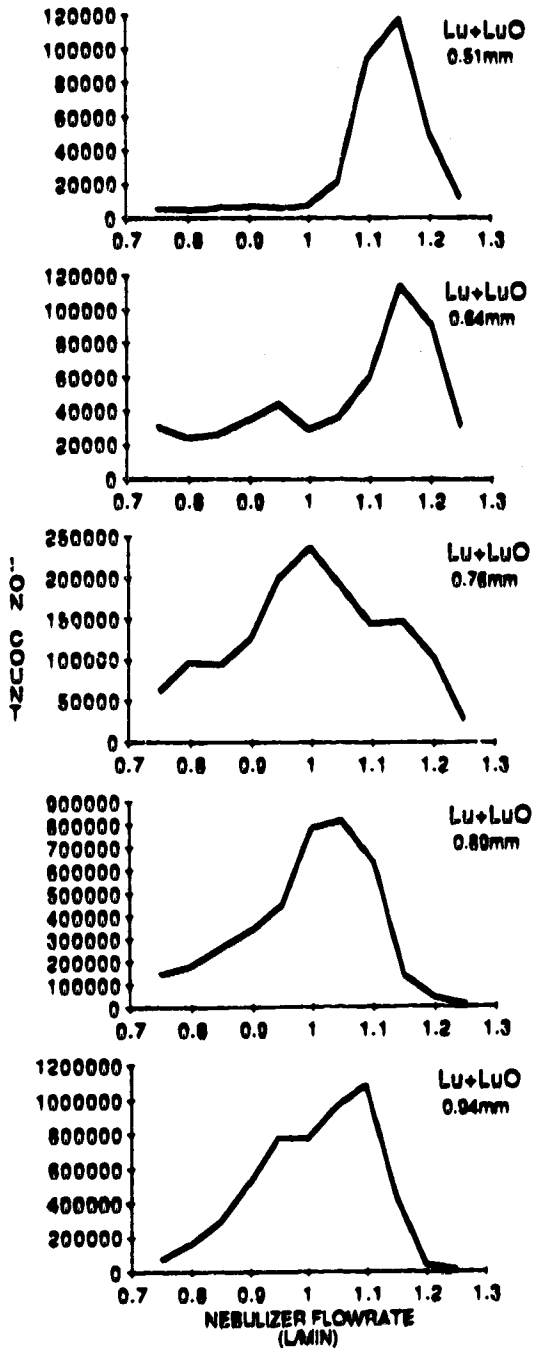

Figure 7.11 Nebulizer flowrate parameter plots for the sum of (Lu^+ + LuO^+) signals. Sampler orifice diameters: 0.51, 0.64, 0.76, 0.89 and 0.94mm.

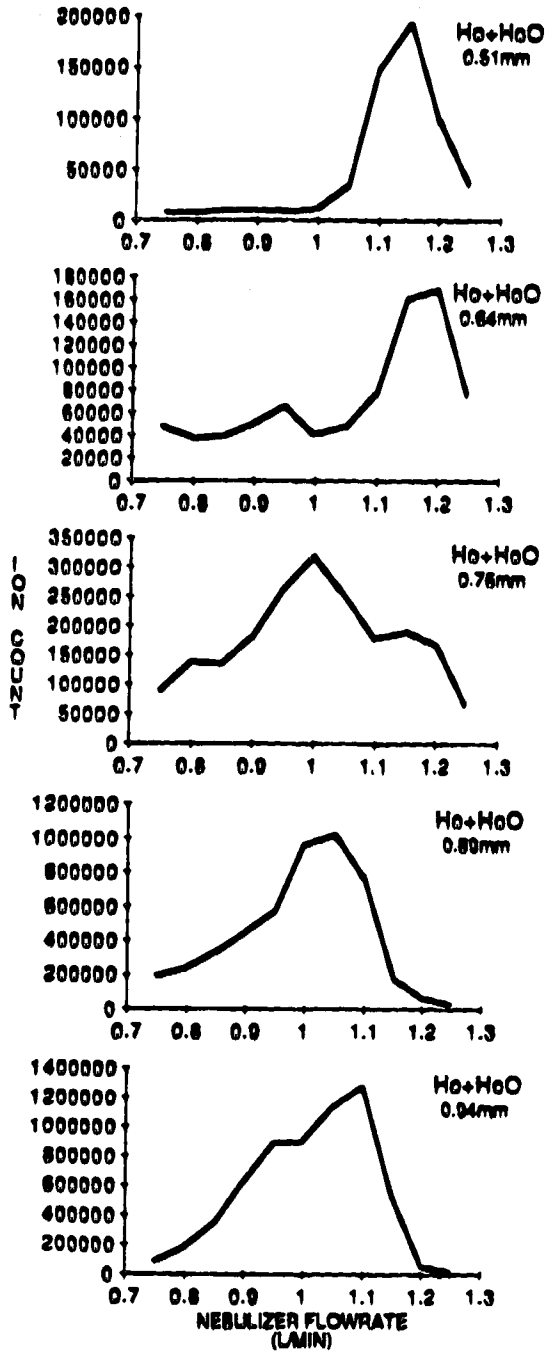

Figure 7.12 Nebulizer flowrate parameter plots for the sum of (Ho^+ + HoO^+) signals. Sampler orifice diameters: 0.51, 0.64, 0.76, 0.89 and 0.94mm.

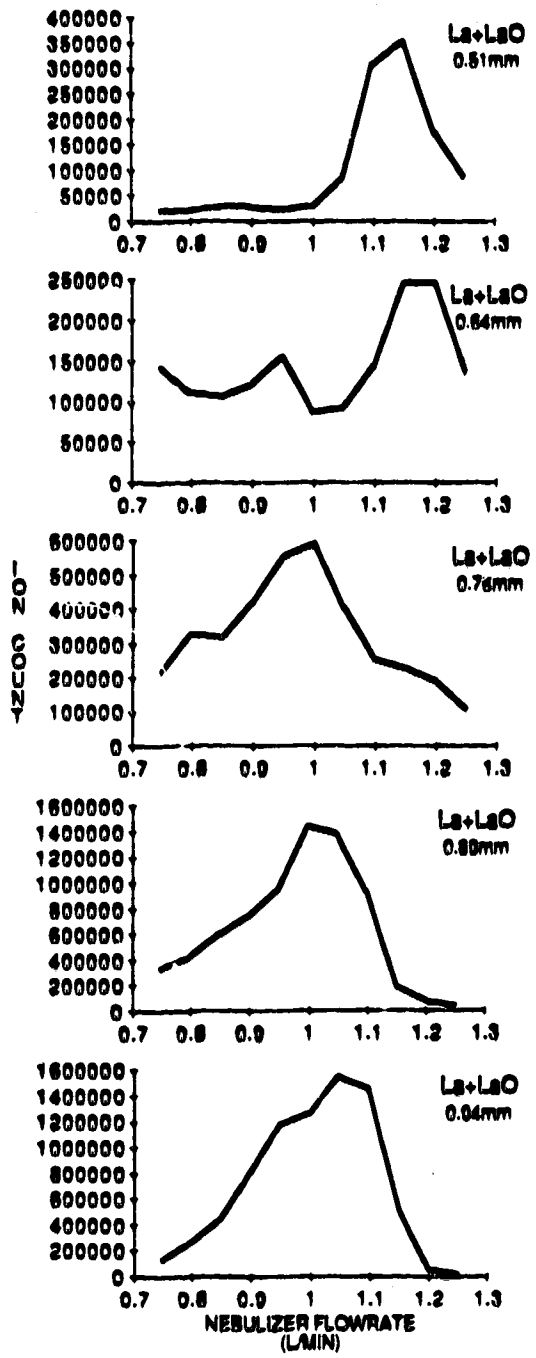

Figure 7.13 Nebulizer flowrate parameter plots for the sum of (La^+ + LaO^+) signals. Sampler orifice diameters: 0.51, 0.64, 0.76, 0.89 and 0.94mm.

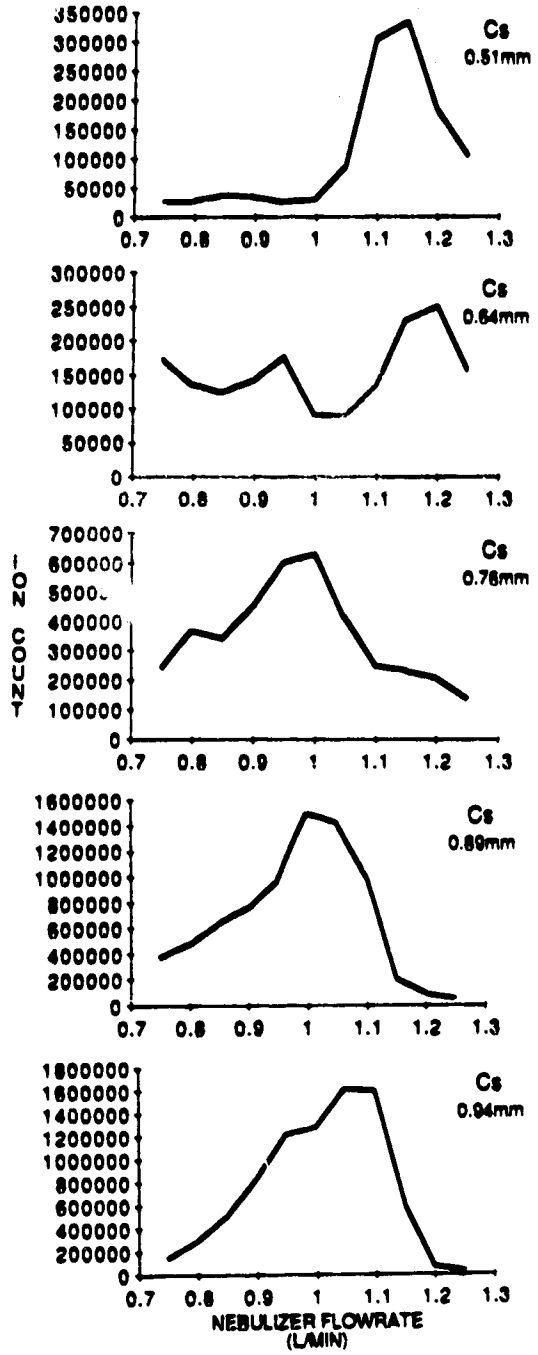

Figure 7.14 Nebulizer flowrate parameter plots for Cs^+. Sampler orifice diameters: 0.51, 0.64, 0.76, 0.89 and 0.94mm.

versus nebulizer flowrate for a non-oxide former of similar mass is a curious phenomenon that is not limited to the rare earth oxides. There are a series of plots in Figure 7.15, comparing Ru^+ to (Y^++YO^+); Cs^+ to (Ce^++CeO^+) and (Pr^++PrO^+); and Bi^+ to (Ho^++HoO^+), (Tm^++TmO^+) and (Th^++ThO^+). In all cases the similarity is striking.

4. Temperature Estimates from Oxide Formation.

Although the source of the oxides in ICP-MS is still debated, oxide ratios have been used to calculate temperatures based on a Boltzmann distribution. Temperatures in the range of 6000 - 8000K would be expected if the oxides are derived from undissociated MO^+ in the plasma. The reported temperatures calculated in this manner have been rather high. Longerich et al. [6] reported a temperature of 10100K and Douglas and French calculated an even larger temperature of 21000K. Douglas and French concluded that given such a large temperature the oxides could not be derived from undissociated MO^+ in the plasma but probably occur in the sampling process. Since the oxide formation is so clearly affected by the sampler orifice size we decided to look at the resulting temperatures for the five orifice sizes. A flowrate of 1.15L/min was chosen for these calculations since the $\ln(MO^+/M^+)$ versus dissociation energy is non-linear at lower flowrates. The plots of (MO^+/M^+) versus dissociation energy for all five orifices are displayed in Figure 7.16. The temperatures are presented in Table 7.1 along with the oxide count and oxide ratios for La.

The values for the temperature obtained here are closer to what would be expected for an ICP than are the values reported by Longerich et al. [6] and Douglas and French [5]. It is disturbing, however, that the values vary over a

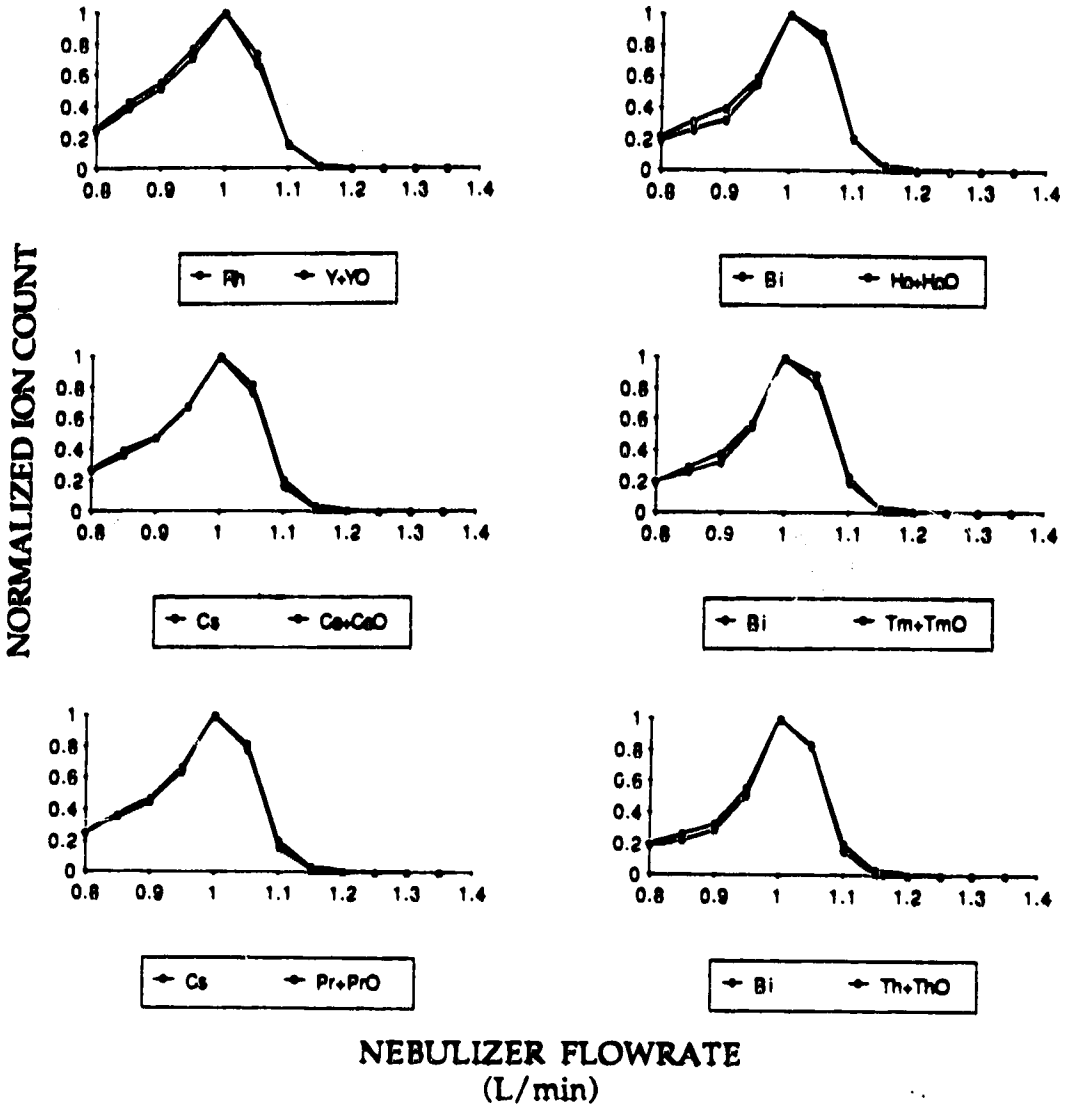

Figure 7.15 Normalized nebulizer flowrate parameter plots comparing Rh^+ and (Y^+ + YO^+), Cs^+ and (Ce^+ + CeO^+), Cs^+ and (Pr^+ + PrO^+), Bi^+ and (Ho^+ + HoO^+), Bi^+ and (Tm^+ + TmO^+) and Bi^+ and (Th^+ + ThO^+). Sampler orifice diameter, 0.89mm.

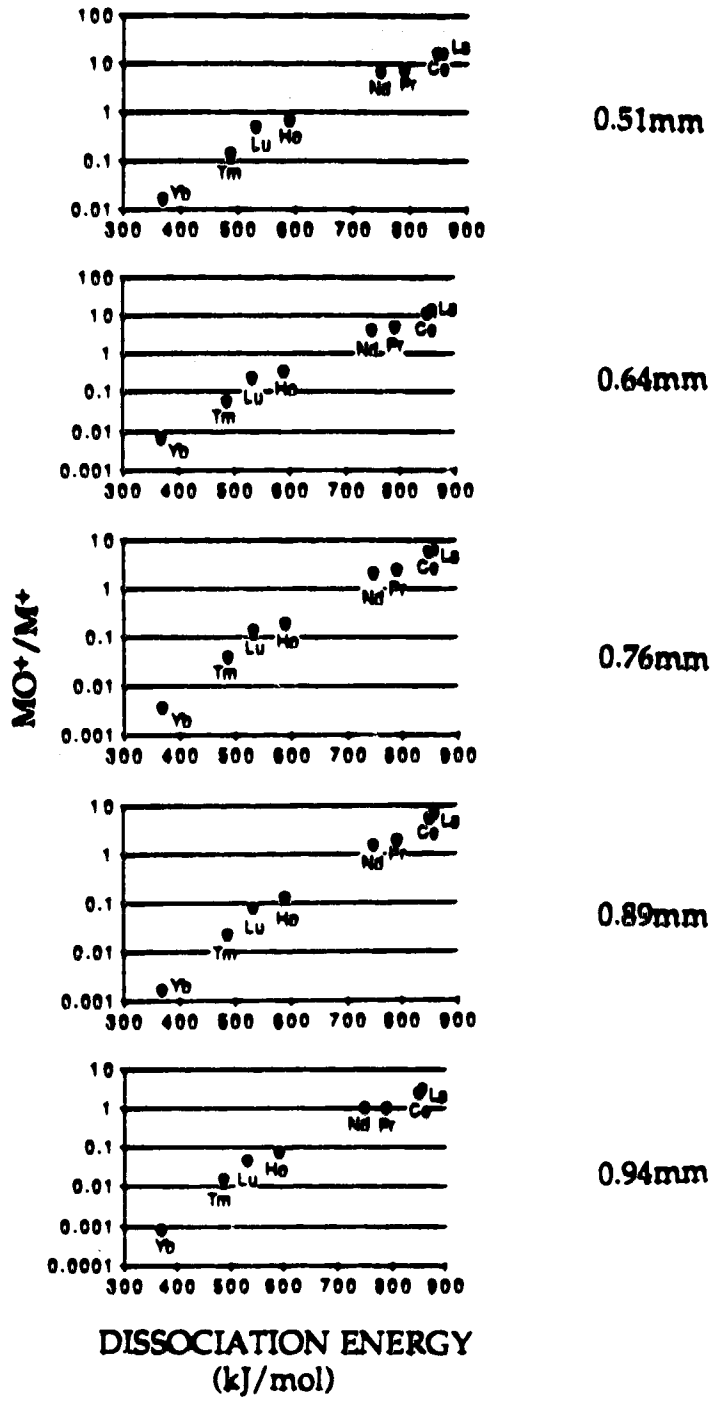

Figure 7.16 MO^+/M^+ versus dissociation energy for sampler orifice diameters 0.51, 0.64, 0.76, 0.89 and 0.94mm. Nebulizer flowrate, 1.15L/min.

Table 7.1 Calculated temperature based on oxide ratios (MO^+/M^+) for different sampler orifice sizes.

Diameter (mm)	LaO^+	LaO^+/La^+	Temperature (K)
0.51	918200	16.3	8900
0.64	318400	13.6	8200
0.76	180800	6.4	8300
0.89	280100	6.8	7600
0.94	366600	3.2	7700

range of 1300K simply as a result of changes in orifice size. It is also disturbing that the highest temperature, 8900K, obtained when the 0.51mm sampler was used, corresponded to the largest absolute and relative levels of oxide; for example, a LaO^+ count of 918200 and a LaO^+/La^+ ratio of 16.3. If the plasma were the primary source of MO^+ the higher temperatures should correspond to lower absolute values of oxide. Based on these observations it seems unlikely that the primary source of MO^+ is from undissociated oxide species in the plasma.

5. Skimmer Orifice Size Effects.

Since the effect of the sampler orifice size can be so dramatic, the skimmer orifice size was also varied to determine its effect on the intensity versus nebulizer flowrate behaviour for singly charged ions and oxides. Since the skimmer data were collected on different days the absolute ion intensities cannot be compared. However, the intensity versus nebulizer flowrate plot shape and relative M^+ and MO^+ formation may be. As an example of the skimmer effect the results for La^+ and LaO^+ at each sampler orifice size and for skimmer orifice sizes of 0.76 and 1.0mm are presented in Figure 7.17. These results may be compared to the La^+ and LaO^+ results in Figure 7.6. From a comparison of the results obtained for the three skimmers at a sampler orifice diameter of 0.51mm we can see that in all cases the LaO^+ peak is dominant. The plots for the 0.89mm skimmer (Figure 7.6) and the 1.0mm skimmer (Figure 7.17) have similar shapes and although the results obtained with the 0.76mm skimmer (Figure 7.17) are also similar the LaO^+ peak did not drop off on the high flowrate end for the flowrate range covered. For all three skimmers and the 0.64mm sampler the shape of the intensity versus

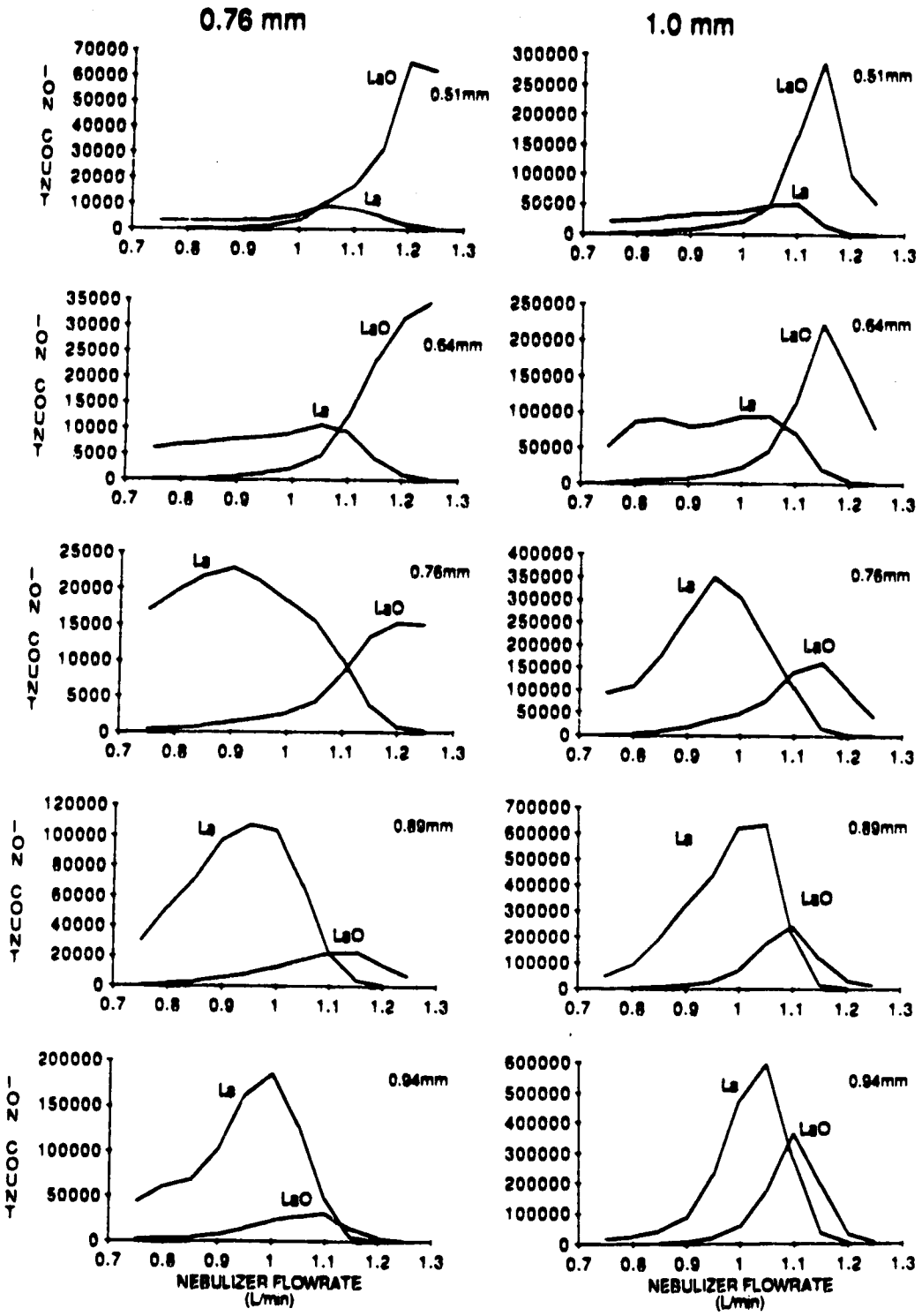

Figure 7.17 Nebulizer flowrate parameter plots for La^+ and LaO^+. Sampler orifice diameters: 0.51, 0.64, 0.76, 0.89 and 0.94mm. Skimmer orifice diameters 0.76 and 1.0mm.

nebulizer flowrate plots are dominated by the LaO^+ peak while the La^+ signal is lower, broad and does not have a distinct peak shape. The more familiar mountain shape of the intensity versus nebulizer flowrate plot is observed for the sampler orifice diameter of 0.76mm. The plot shape is similar for all three skimmer orifice sizes except that the plots are broader and the oxide level is higher, in a relative sense, for the 0.76mm skimmer. The same basic shape is observed for the plots corresponding to each skimmer and the 0.89 and 0.94mm samplers. With both of these samplers we see an increase in the oxide level and a narrowing of the peaks as the skimmer orifice size increases.

In general it appears as though there are not many drastic changes in the intensity versus nebulizer flowrate plots for the M^+ or the MO^+ ions as a function of skimmer orifice diameter, especially compared to the changes corresponding to changes in the sampler orifice size. It is interesting to note that the (M^++MO^+) intensity versus nebulizer flowrate plots still have a similar shape to intensity versus nebulizer flowrate plots for non-oxide formers of similar mass for all skimmer orifice sizes tested. The (La^++LaO^+) data presented for the 0.76 and 1.0mm skimmers in Figure 7.18 can be compared with the Cs^+ data in Figure 7.19. The shapes of the curves are are very close especially for the 1.0mm diameter skimmer orifice. There are some differences in the shapes of the curves but the differences are not large. In a similar fashion (Yb^++YbO^+) data (Figure 7.20) may be compared to Bi^+ data (Figure 7.21). Once again the shapes of the curves are similar.

The curves corresponding to (Lu^++LuO^+) (Figure 7.22) and (Ho^++HoO^+) (Figure 7.23) are also close to the Bi^+ results, especially for the 1.0mm skimmer and the 0.51, 0.89 and 0.94mm samplers. Again the plots for these elements and their oxides appear as if they are some sort of combination

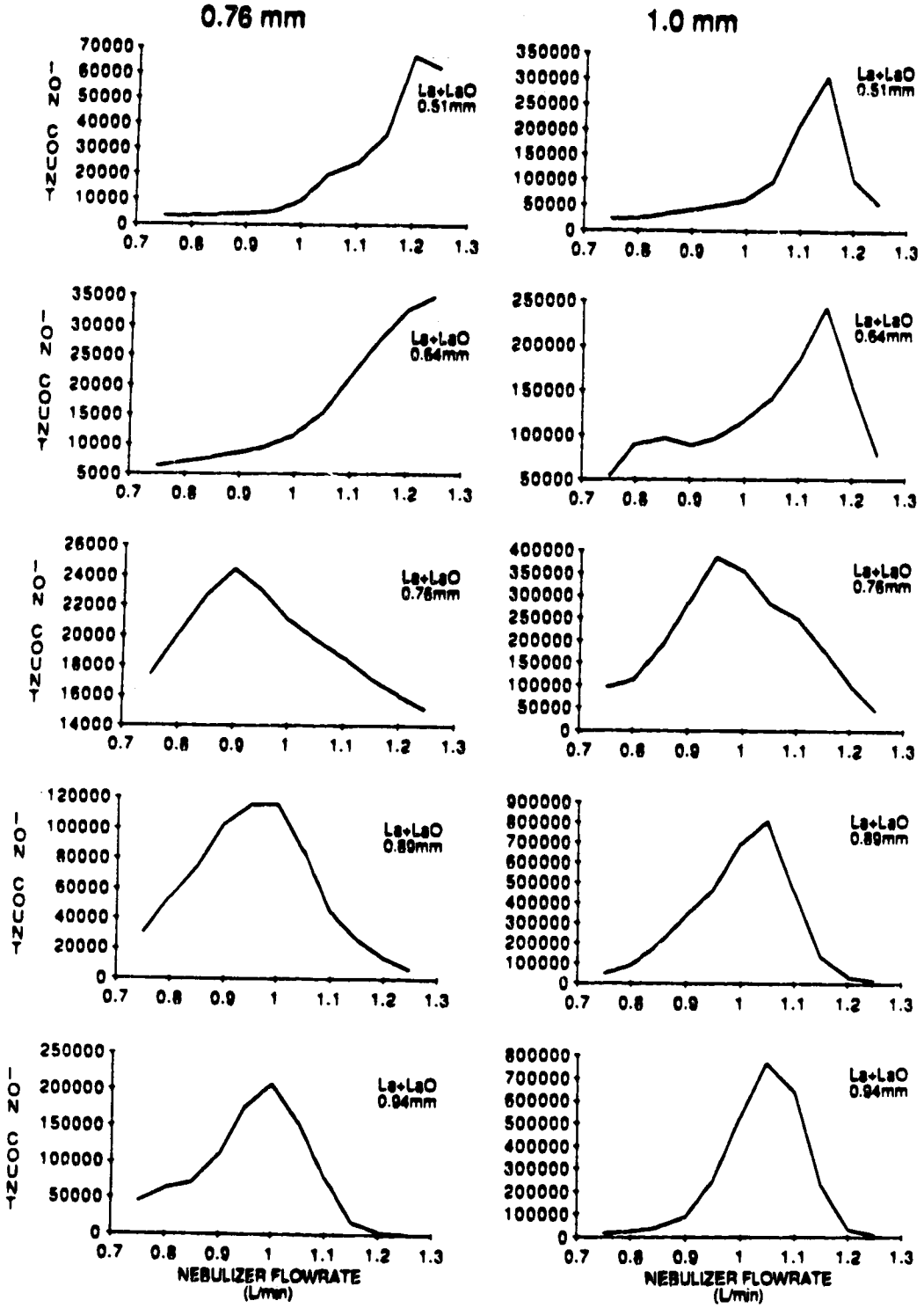

Figure 7.18 Nebulizer flowrate parameter plots for (La^+ + LaO^+). Sampler orifice diameters: 0.51, 0.64, 0.76, 0.89 and 0.94mm. Skimmer orifice diameters 0.76 and 1.0mm.

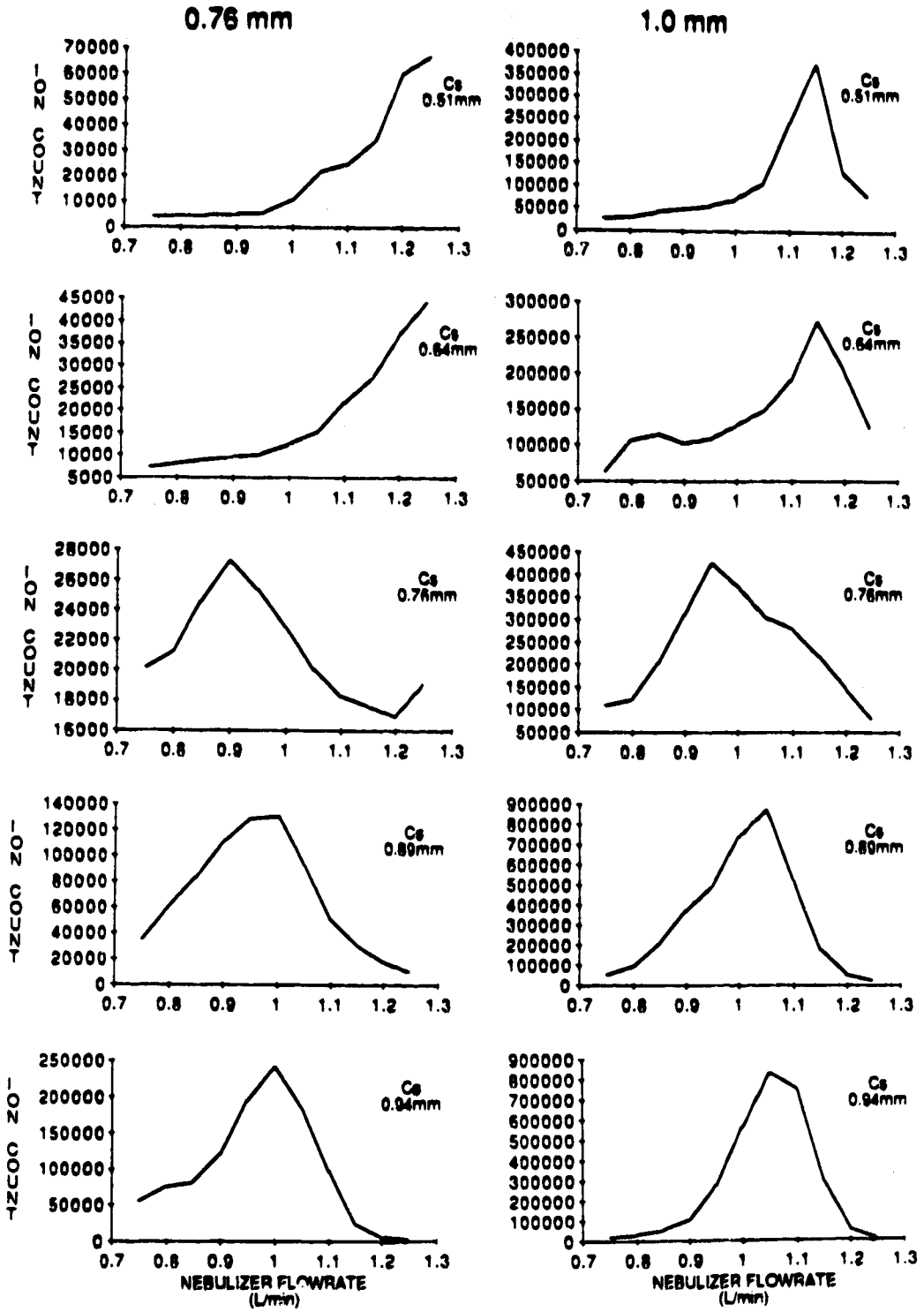

Figure 7.19 Nebulizer flowrate parameter plots for Cs^+. Sampler orifice diameters: 0.51, 0.64, 0.76, 0.89 and 0.94mm. Skimmer orifice diameters 0.76 and 1.0mm.

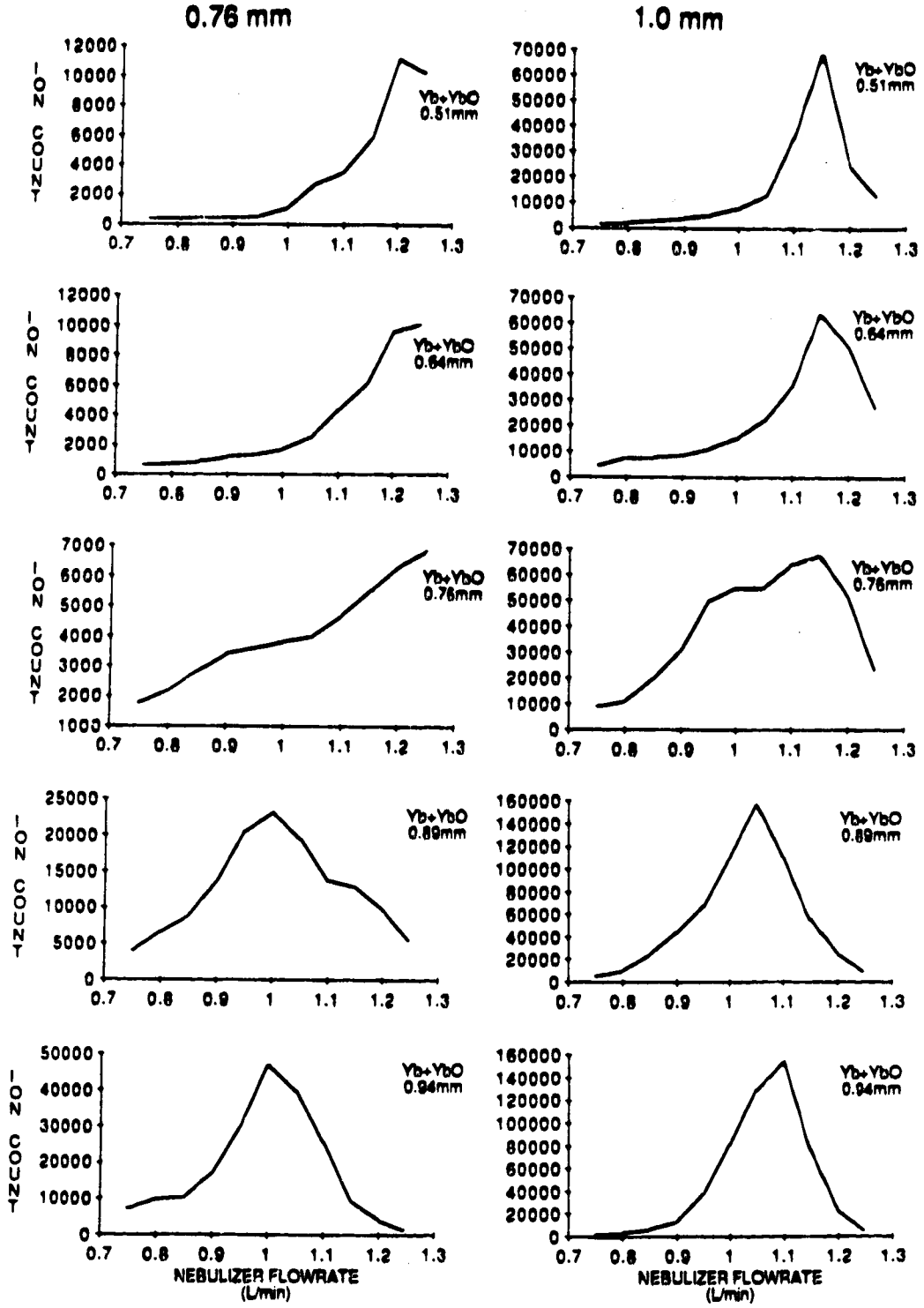

Figure 7.20 Nebulizer flowrate parameter plots for (Yb^+ + YbO^+). Sampler orifice diameters: 0.51, 0.64, 0.76, 0.89 and 0.94mm. Skimmer orifice diameters 0.76 and 1.0mm.

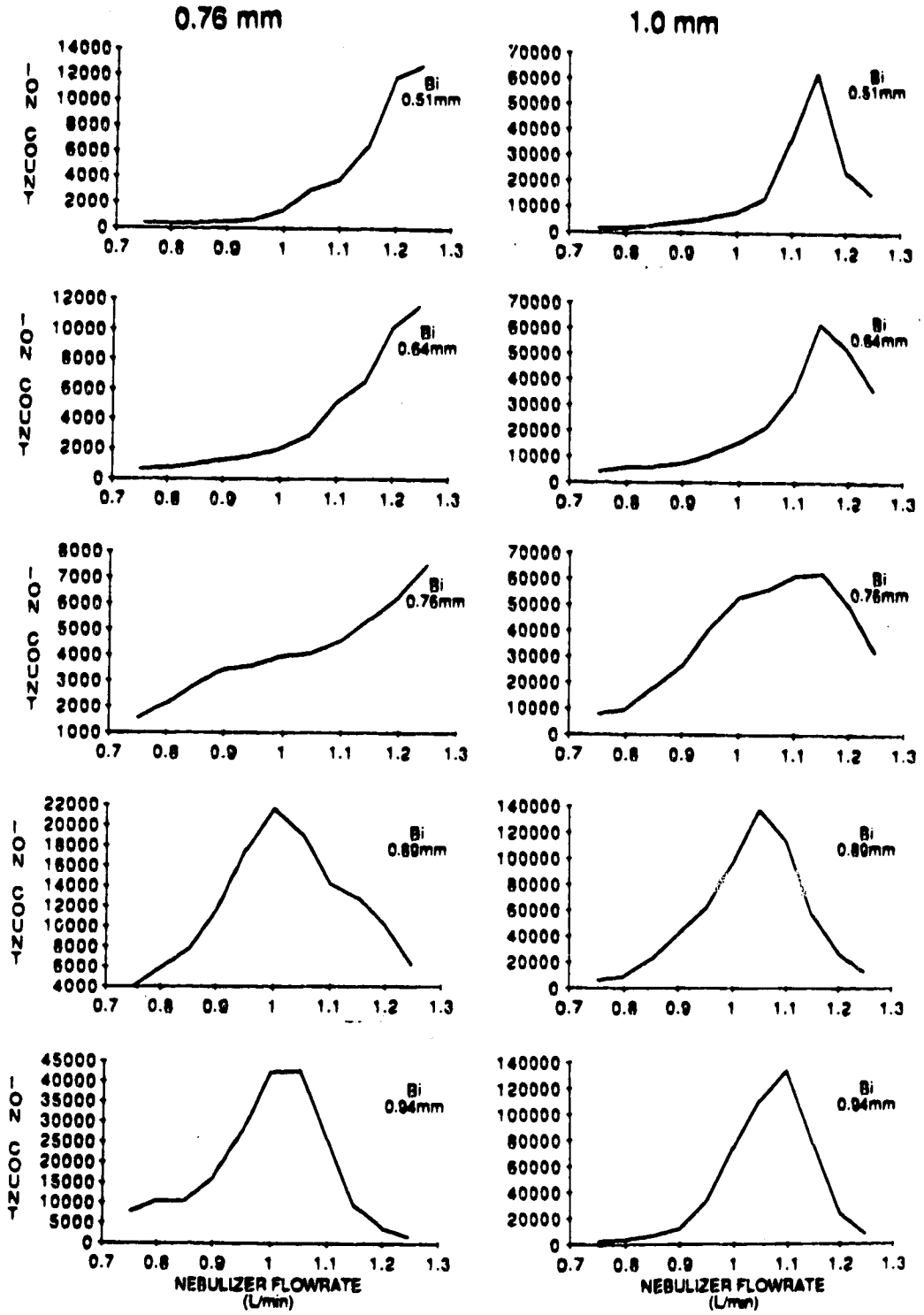

Figure 7.21 Nebulizer flowrate parameter plots for Bi^+. Sampler orifice diameters: 0.51, 0.64, 0.76, 0.89 and 0.94mm. Skimmer orifice diameters 0.76 and 1.0mm.

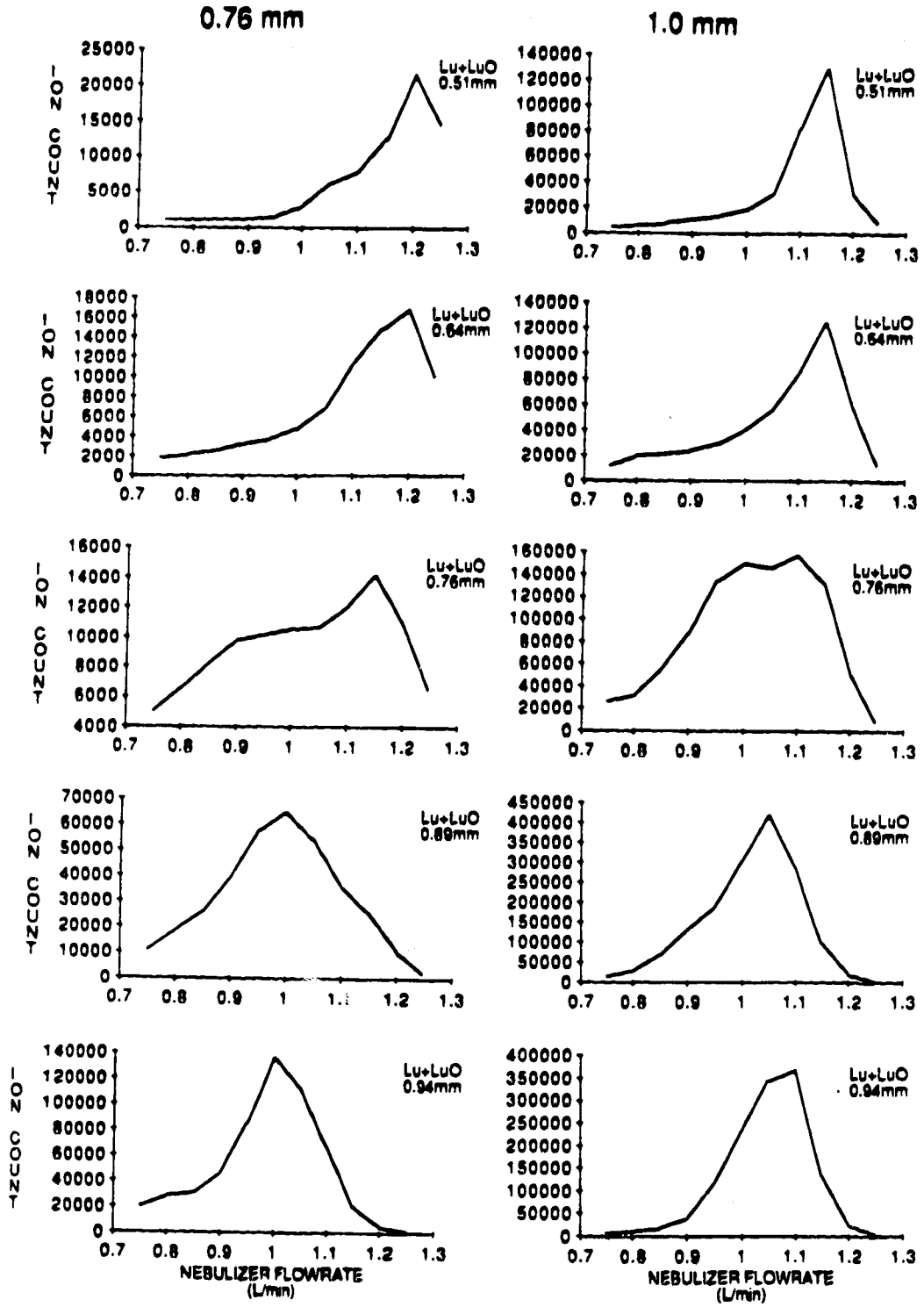

Figure 7.22 Nebulizer flowrate parameter plots for (Lu^+ + LuO^+). Sampler orifice diameters: 0.51, 0.64, 0.76, 0.89 and 0.94mm. Skimmer orifice diameters 0.76 and 1.0mm.

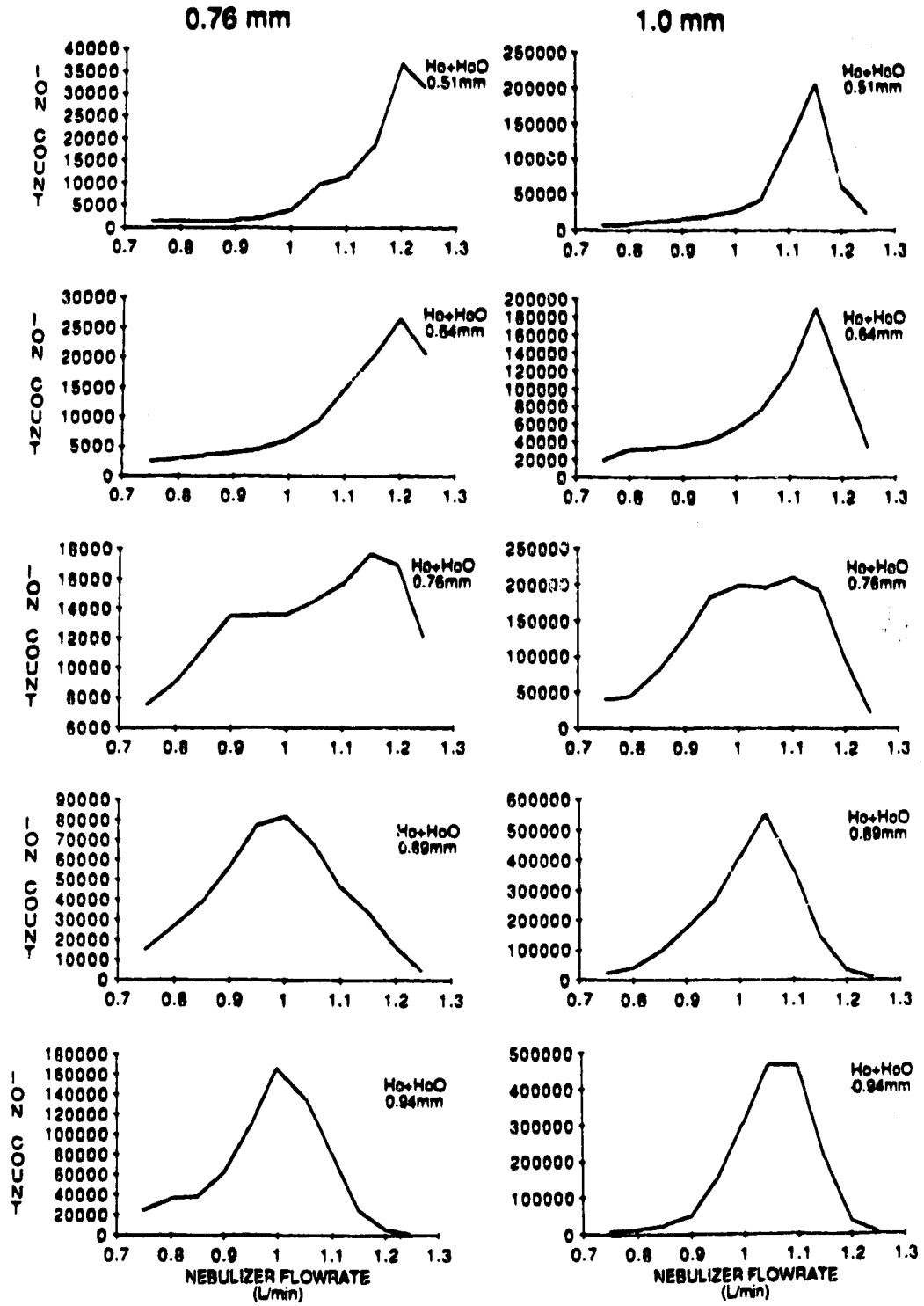

Figure 7.23 Nebulizer flowrate parameter plots for (Ho^+ + HoO^+). Sampler orifice diameters: 0.51, 0.64, 0.76, 0.89 and 0.94mm. Skimmer orifice diameters 0.76 and 1.0mm.

of the results for Cs^+ and Bi^+, especially the results for sampler and skimmer orifice diameters of 0.76mm and 0.76mm. However, regardless of whether they are a combination of the Cs^+ and Bi^+ patterns the curves for (Lu^++LuO^+) and (Ho^++HoO^+) for a given skimmer size resemble each other very closely. This holds for all three skimmer sizes and seems too consistent to dismiss as mere coincidence.

6. General Discussion.

The number of collisions occurring in the supersonic expansion increases with increasing sampler orifice size and may be estimated by [9]:

$$N_{tot} = 0.116 D_o n_o \sigma \qquad 7.1$$

If the majority of oxides were formed in this process we would see more oxides at large orifice diameters. Since the larger amounts of oxides are detected using the smaller orifice sizes it is unlikely that reactions in the expansion are responsible for most of the oxide formation. Since it is also unlikely that the oxides are due to undissociated species in the plasma, the oxides must be formed in the boundary layer around the edge and along the sides of the sampler cone. Although the sampler orifice sizes used in this work are large enough to allow continuum sampling of the plasma, some of the material from the boundary may be swept into the mass spectrometer. How this might occur is demonstrated by the flow field around the sampler [11], displayed in Figure 7.24. The boundary layer is formed around the edge of the cone as the hot plasma comes in contact with the cooler sampler. Not all of the material that enters the sampler orifice comes directly from the plasma; some of the boundary layer is drawn in from around the sides of the orifice.

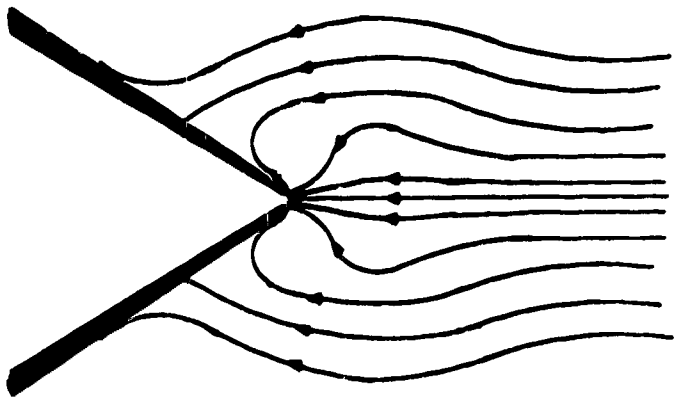

Figure 7.24 Flow field around the sampling cone. (Modified from reference [11]).

Hayhurst et al. [7] in their discussion of boundary layers stated that a larger orifice diameter results in a larger total flowrate into the sampler which causes a reduction in boundary layer thickness. This would result in lower oxide levels for larger sampler orifice sizes which is what has been observed. The effect of skimmer orifice size on oxide levels is less clear. At smaller sampler orifice diameters the oxide decreases with increasing skimmer orifice diameter while at larger sampler orifice sizes oxide levels increase with increasing skimmer orifice diameter.

We usually see mountain shaped intensity versus nebulizer flowrate plots in ICP-MS but the reason for this has not been determined. We do know that the shape of the plots can be affected by the diameter of the sampler orifice and the positions of the mountains on the nebulizer flowrate axis can be affected by ion lens voltages (see Chapter 2 and Chapter 6). The position changes, as a function of lens voltage, hints that the mountain may be related to ion energies. Consider for a moment the energy of an ion sampled in ICP-MS. It is assumed that the energy of the ions will be the same as the energy of the argon neutrals because of supersonic expansion [10].

$$E_S(M) = E_{Ar}(M/M_{Ar}) \qquad 7.2$$

We know that $E_{Ar} = mv^2/2$ and it is often assumed that in ICP-MS $E_{Ar} = 5kT/2$ [10]. This assumption is based on the terminal velocity of the expansion being :

$$U = \sqrt{\frac{5}{2}}\,\alpha \qquad 7.3$$

where

$$\alpha = \sqrt{\frac{2KT}{m}} \qquad 7.4$$

The characteristic velocity in the reservoir, α, comes from classical molecular beam work [11]. In ICP-MS we do not have a simple reservoir of atoms; we have a directed flow toward the sampler orifice and, therefore, the velocity of the atoms change as a function of nebulizer flowrate. There may also be a cooling effect on the material in the central analyte channel when the nebulizer flowrate is increased. This would serve to decrease E_{Ar}. If the velocity of Ar and E_{Ar} change with flowrate so should $E_S(M)$. Perhaps this is why the ion lenses have an effect on the position of the mountain.

It is not as easy to relate the orifice size to an energy change in the ions. We do know that the ion energy depends upon the terminal velocity reached in the expansion and that the velocity depends on the temperature in the ion reservoir. We also know that the boundary layer is cooler than the bulk plasma. When the small orifice samplers are used more ions travel through the boundary layer so perhaps their energy is reduced which is reflected in the position and shape of the intensity versus nebulizer flowrate plots. This may be why bimodal character is sometimes observed. One hump may correspond to ions from continuum sampling while the other hump (including the oxides) is related to those ions passing through the boundary layer.

Regardless of whether ion energy is the cause of the mountain shaped intensity versus nebulizer flowrate plots, the plots can be considered as windows for ion detection across the nebulizer flowrate range. All of the ions,

oxide formers and non-oxide formers sampled from the ICP follow the same flow fields around the sampler. Some ions would flow directly into the sampler while others would pass through the boundary layer formed around the sampler edge. For oxide forming ions such as La^+ some of the collisions in the boundary layer would result in the formation of monoxide ions LaO^+ while collisions with non-oxide formers such as Cs^+ would not produce oxide ions. Thus for a given mass there is a window across the nebulizer flowrate range where ion detection is possible. The analyte species detected in this window may be in the form M^+ or may be distributed between the singly charged ion, M^+ and other species such as MO^+ . Ions of similar mass may have similar shaped "windows" as seen when the intensity versus nebulizer flowrate plots for Cs^+ and (La^++LaO^+), for example, are compared.

Conclusions

Parameter plots of intensity versus nebulizer flowrate are affected by the size of the orifice in the sampler in ICP-MS. The larger orifices yield larger signals although oxide levels are larger for the smaller orifice sizes. It appears likely that the boundary layer around the edges of the sampler is the region where most oxide formation occurs. A portion of the boundary layer material gets drawn into the sampler even when there is continuum sampling of the plasma.

The shape of the intensity versus nebulizer flowrate plot appears to be significant. A similarity in shape for (M+MO) intensity versus nebulizer flowrate plots and intensity versus nebulizer flowrate plots for non-oxide formers of similar mass has been observed. It is as if there is a window for ion

detection along the nebulizer flowrate axis and the analyte species may be detected in more than one form within the window.

The effect of the orifice size of the skimmer is not as dramatic as the effect of the sampler orifice size. The intensity versus nebulizer flowrate plots remained much the same with the different skimmers although some changes in oxide levels were noticed.

References

1. R. S. Houk, V. A. Fassel, G. D. Flesch, H. J. Svec, A. L. Gray and C. E. Taylor, Anal. Chem. **52**, 2283-2289, (1980).

2. A. R. Date and A. L. Gray, Analyst, **106**, 1255-1267, (1981).

3. A.L. Gray and A. R. Date, Analyst, **108**, 1033-1050, (1983).

4. G. M. Hieftje and G. H. Vickers, Analytica Chimica Acta **216**, 1-24, (1989).

5. D. J. Douglas and J.B. French, Spectrochim. Acta, **41B**, 197-204 (1986).

6. H. P. Longerich, B. J. Fryer, D. F. Strong and C. J. Kantipuly, Spectrochim. Acta, **42B**, 75-92, (1987).

7. A. N. Hayhurst, D. B. Kittleson and N.R. Telford, Combust. Flame, **28**, 123-135, (1977).

8. H.P. Longerich, B. J. Fryer and D. F. Strong, Spectrochim. Acta, **42B**, 101-109, (1987).

9. D. J. Douglas and J.B. French, J. Anal. Atom. Spectrom. **3**, 743-747, (1988).

10. H. C. W. Beijerinck, R. J. F. Van Gerwen, E. R. T. Kerstel, J. F. M. Martens, E. J. W. Van Vliembergen, M. R. Th. Smits and G. H. Kaashock, Chem. Phys. **96**, 153-173, (1985).

11. A. Hoglund and L.-G. Rosengren, Int. J. Mass Spec. Ion Process. 60, 173-187, (1984).

Chapter 8

The Use of Inductively Coupled Plasma Mass Spectrometry Results for Plasma Diagnostics

There is interest in gaining a fundamental understanding of the inductively coupled plasma (ICP) and a great effort has been applied in this area. With the development of inductively coupled plasma mass spectrometry (ICP-MS) as an analytical tool it has been tempting to try and use the mass spectral information obtained to help gain insight into the workings of the ICP [1-3]. The mass spectrometer gives us access to ion populations such as M^+ analyte ions and a variety of other species. Since the M^+ signal measured with the ICP-MS does not depend on the excited electronic state of the element the information obtained is different in nature than the information obtained through ion emission.

If data obtained with the ICP-MS are to be used in plasma diagnostics we must be sure that the results obtained from ICP-MS measurements are representative of the undisturbed plasma. Unlike emission measurements, sampling ions for mass spectrometry is an invasive technique and there is evidence that the measurements made by ICP-MS are affected by the sampling system and the ion lenses. We shall look at the comparison of emission and mass spectrometer measurements in this regard. We shall also discuss the use of CsI temperature estimates for the plasma based on the measurement of Cs^+ and I^+ with the ICP-MS.

Experimental

A Sciex Elan 250 ICP-MS was run in the standard fashion for aqueous samples using a MAK torch, a Meinhard nebulizer and a Scott spray chamber. Except where otherwise indicated sampling of the plasma was done 15mm from the load coil and the ICP power was 1.3kW. The central plasma gas and the auxiliary gas flowrates were 12L/min and 1.4L/min Ar respectively.

A Plasma -Therm ICP with a MAK torch, a Meinhard nebulizer and a Scott spray chamber was used for separate emission measurements. The SrII emission was measured at 407.7nm using a Minuteman monochromator. Simultaneous mass spectrometric and emission measurements were made using the ICP-MS fitted with a fiber optic probe leading to a monochromator. The system has been described in detail elsewhere [4]. For the simultaneous measurements SrII was measured at 421.6nm. The fiber optic was positioned such that the emission measurements were measured 1mm in front of the sampler which corresponded to 14mm from the load coil.

The solutions were prepared from SPEX industries Inc. standard solutions and were 1μg/mL in each element. The CsI solution was prepared from Aldrich 99.999% pure CsI powder.

Results and Discussion

1. Simultaneous Emission and Mass Spectral Measurements.

The data for Sr^+ as measured with the ICP-MS are presented in Figure 8.1 in a common nebulizer flowrate - power parameter format often used in ICP-MS. The plots of intensity versus nebulizer flowrate yield mountain-like peaks at each power. As the power increases the maxima move to greater flowrates. This is typical signal behaviour in ICP-MS. Although the ion emission measured from the ICP has been traditionally presented in an intensity versus height above the load coil format [5,6], the data may be presented in the nebulizer flowrate power parameter format used in ICP-MS. Emission data from SrII measured 15mm above the load coil are presented in such a format in Figure 8.2. It is obvious immediately that the change in signal intensity as a function of nebulizer flowrate is different for emission compared to ICP-MS. In emission the peaks at each power are much broader and the signal increases with increasing power at all flowrates covered in the data set.

These two sets of results are different but they were acquired on different instruments. Making simultaneous emission and mass spectrometric measurements can help determine whether the presence of the sampler in the plasma changes the emission profile of the plasma. Simultaneous emission and mass spectral measurements were made for Sr^+ using the ICP-MS and a fiber optic and monochromator. The results for Sr^+ and SrII are presented in Figure 8.3. It appears that the emission data measured 1mm in front of the sampler are similar to the data obtained using

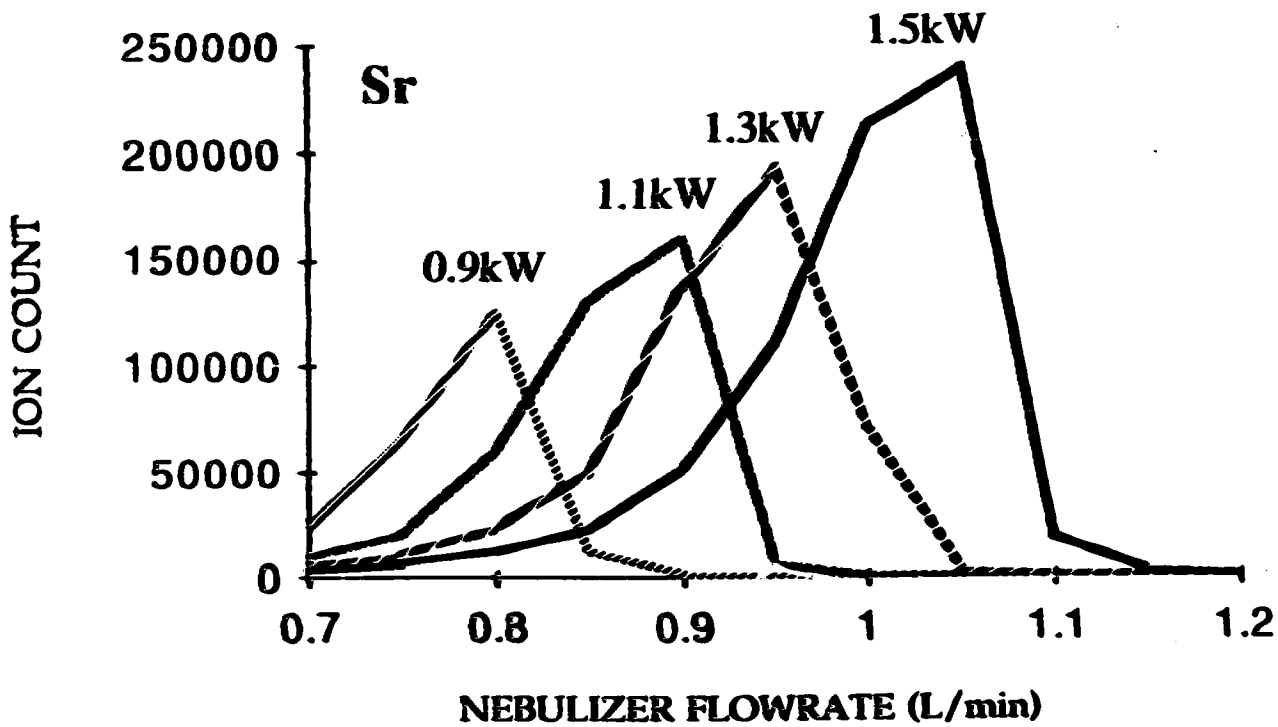

Figure 8.1 Nebulizer flowrate power parameter plot for Sr^+. Power in kW shown on each line.

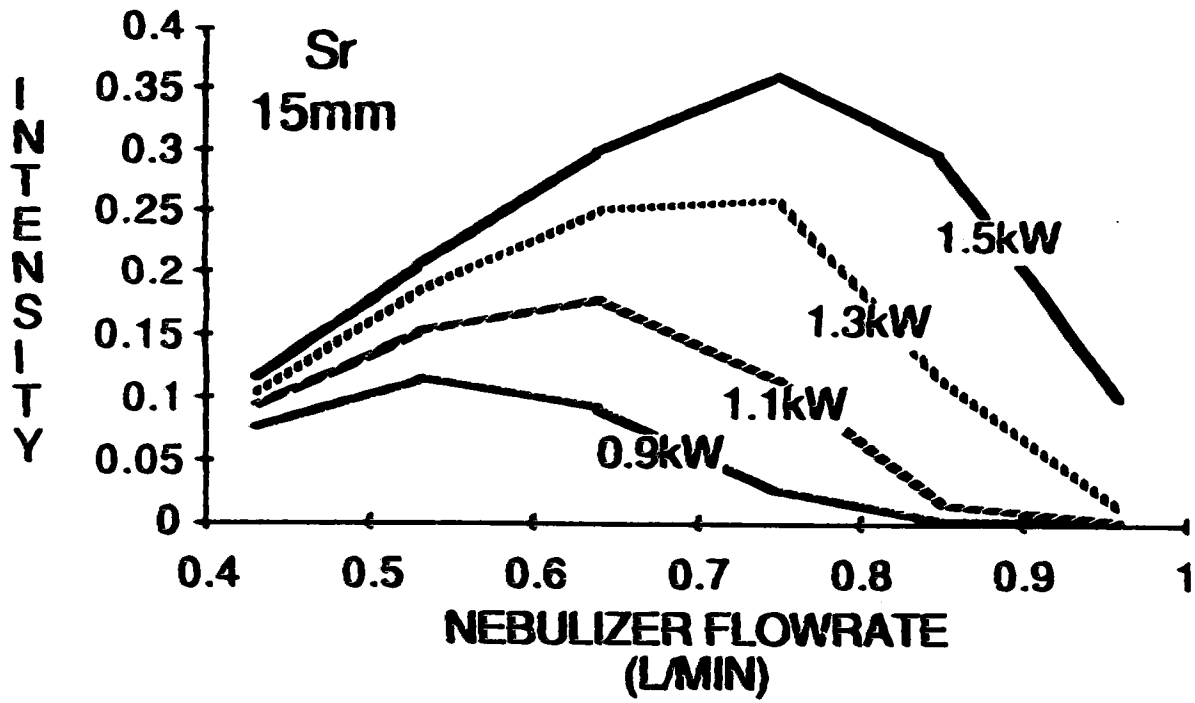

Figure 8.2 Nebulizer flowrate power parameter plot for SrII emission. Power in kW shown on each line. Intensity in arbitrary units.

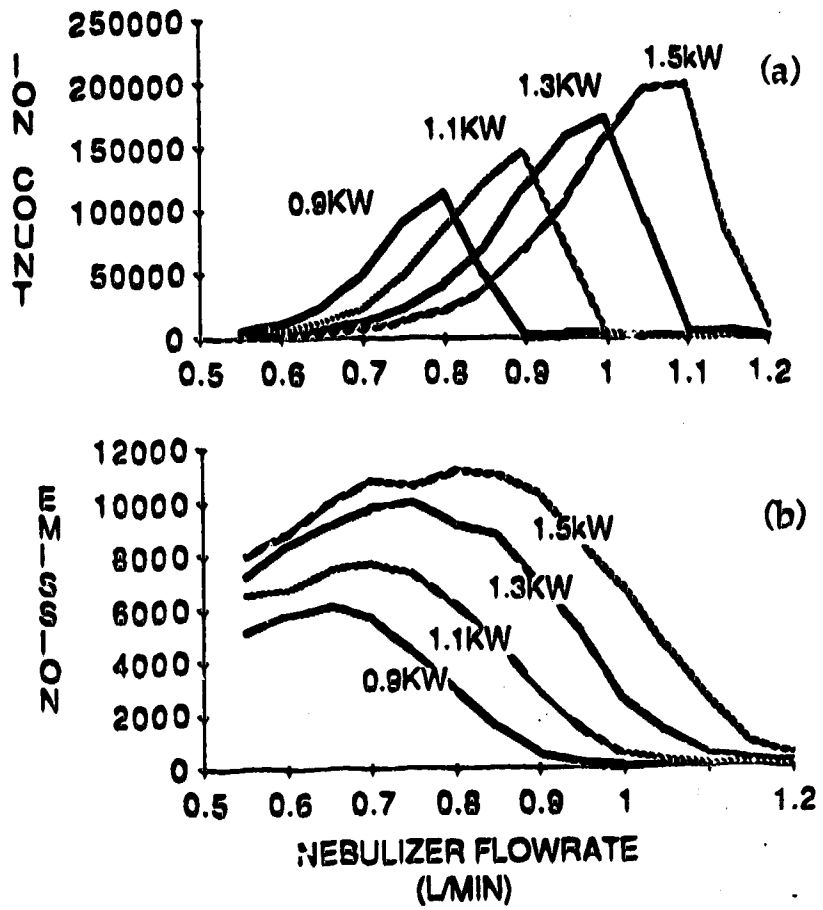

Figure 8.3 Nebulizer flowrate power parameter plot for Sr^+ (a) and SrII (b). Power in kW shown on each line. Measurements made simultaneously from same ICP.

the ICP emission system (Figure 8.2). Under these conditions the presence (the sampler does not appear to cause large changes in emission behaviour a a function of nebulizer flowrate.

The differences in the plots for emission and mass spectral results ma be attributed in part to the different populations being measured. Sr emission results are related to the population of the first excited electron state of the Sr^+ ion while Sr^+ mass spectral results are dependent on the Sr population regardless of electronic state. Although the populations fro which the measurements are taken are different, the species, singly charge ions, are the same and because of this it is reasonable to assume that tl results should somehow be related.

Relating the emission and mass spectral results could be difficu however, because of the effect of the sampling and lens systems in ICP-M Unlike the emission measurements the ion sampling for MS analyses is a invasive technique. While the extent to which this modifies the plasma unimportant when employing the ICP-MS as an analytical tool, it important if statements about the plasma itself are made based on ICP-M measurements. The presence of the sampler may not effect the emissi profiles but we have seen previously (Chapter 7) that the orifice diameter the sampler can effect the shape and position of the signal intensity vers nebulizer flowrate. We can also re-position the mountain on the nebuliz flowrate axis by changing the photon stop voltage (Chapters 2 and 6).

Thus the position of the mountain in the nebulizer flowrate paramet plots depends not only on power but also on ion lens voltages and on orifi diameter of the sampler. The general shape of the nebulizer flowrate pow

parameter plots in ICP-MS appear to reflect less the plasma from which the material is sampled and more the conditions under which the sampling occurred. If this is so then there is little that can be said based on the relative positions of the emission and mass spectrometric data on the nebulizer flowrate axis.

2. CsI Measurements.

The ratio of I^+/Cs^+ measured from a CsI solution has been used in a number of cases as an indicator for estimating α, the degree of ionization in the ICP [3]. In a solution prepared from CsI there are equal amounts of Cs and I atoms and since Cs is easily ionized it is assumed to be 100% ionized in the ICP. In contrast the I, being harder to ionize, will be less than 100% ionized. Assuming that the Cs^+ count represents the total I level, the ratio I^+/Cs^+ should give an indication of the degree of ionization for I. From the degree of ionization the Saha equation is used to calculate an ion temperature. The calculated values are often compared to temperatures obtained from emission measurements and have been studied as a function of distance above the load coil [3]. Figure 8.4 contains a series of three plots composed of combinations of intensity versus distance from the load coil and the I^+/Cs^+ ratio versus distance from the load coil. The I^+/Cs^+ ratio is plotted instead of temperature because we do not have values of electron density as a function of distance from the load coil. The I^+/Cs^+ plot has a minimum at 12mm from the load coil. Wilson et al. [3] included similar results (Figure 1, reference 3) in their work. They explained that the drop in temperature corresponded to the normal working position in the plasma. At lower heights they were in the fireball where the temperature is higher and at greater heights they attributed

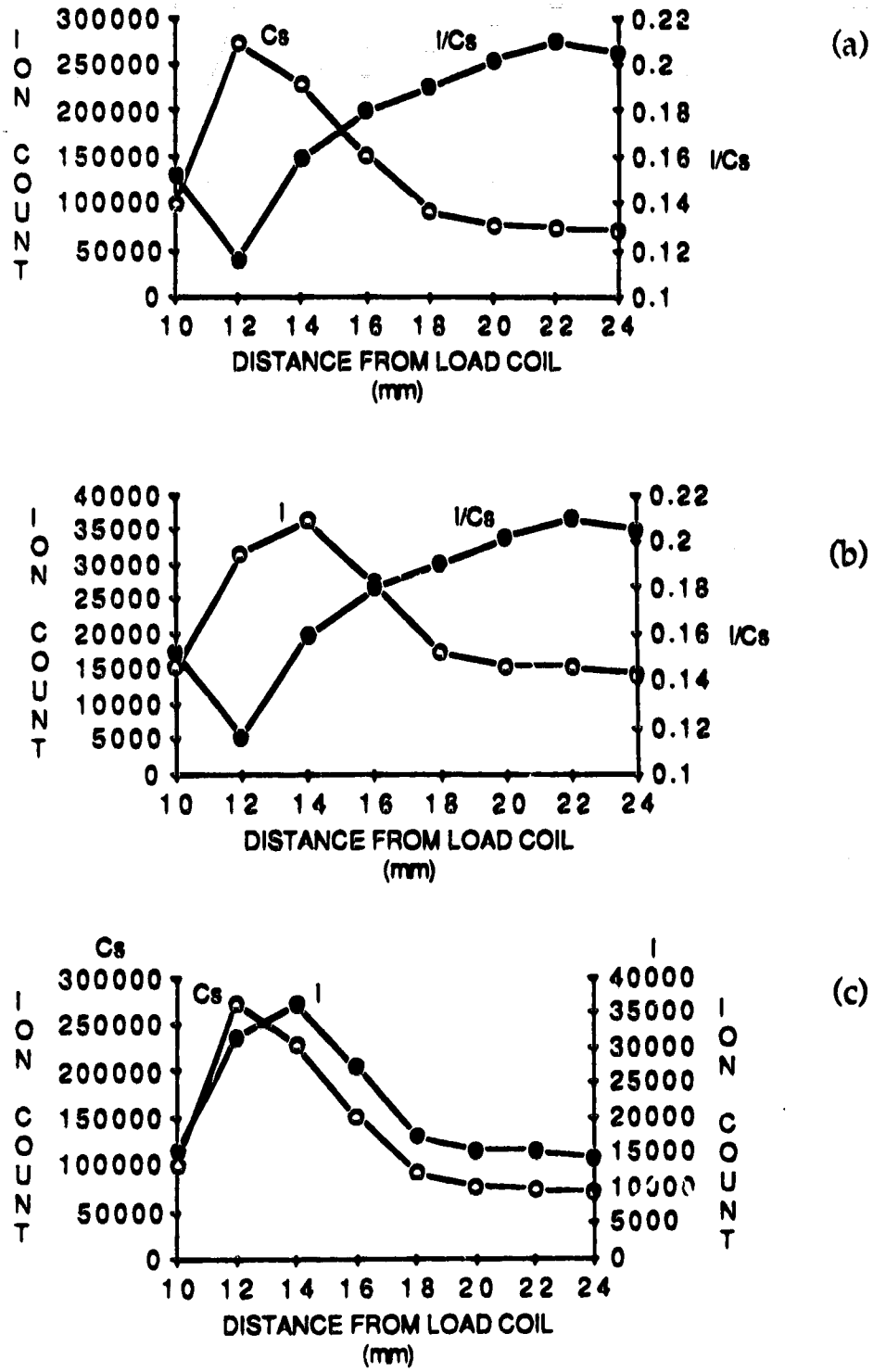

Figure 8.4 Ion count versus distance from the load coil plots for Cs^+ (a) and I^+ (b) plus overlay plots of I^+/Cs^+ versus distance from the load coil. Ion count versus distance from the load coil plots for Cs^+ and I^+ (c). Nebulizer flowrate, 0.95L/min.

the increasing temperature to a secondary discharge between the plasma and the sampler. It is generally held that with the Sciex Elan ICP-MS, there is negligible discharge between the plasma and the sampler [7] so the increase in I^+/Cs^+ at distances greater than 12mm cannot be explained that way for our system. The minimum in the I^+/Cs^+ ratio we measured corresponds to the maximum in the Cs^+ signal. The maximum in the I^+ signal occurred at a greater distance from the load coil. The Cs^+ and the I^+ signals are plotted together in Figure 8.4c. The dip in the I^+/Cs^+ ratio may be a result of the different positions of the signal maxima for the two ions.

Returning to our more usual format for ICP-MS data, the I^+/Cs^+ ratio was studied as a function of nebulizer flowrate. A set of plots of intensity versus nebulizer flowrate for Cs^+ and I^+ along with overlay plots of I^+/Cs^+ ratio versus nebulizer flowrate is presented in Figure 8.5. The ratio of I^+/Cs^+ seems fairly constant at low flowrates and starts to drop as the Cs^+ and I^+ signal intensities increase. The Cs^+ and I^+ peaks do not reach their maxima at the same nebulizer flowrate which is clearly displayed in Figure 8.5c.

We know from previous studies that we can move the intensity versus nebulizer flowrate mountain by changing the photon stop lens voltage so the effect of such a lens voltage change on the I^+/Cs^+ ratio was investigated. The intensity versus nebulizer flowrate plots for Cs^+ and I^+ at photon stop voltages of -9V and -5V are displayed in Figure 8.6. The peak position and signal intensities for Cs^+ and I^+ are dependent on the voltage. The bottom frame, Figure 8.6c, contains I^+/Cs^+ versus nebulizer flowrate for -9V and -5V lens settings. The ratios are lower for the photon stop voltage setting of -5V. If we assume an electron density of 10^{15} then at 0.95L/min we get an I^+/Cs^+ ratio of 0.1790 ± 1.5% corresponding to a temperature of 7200K for -5V and an

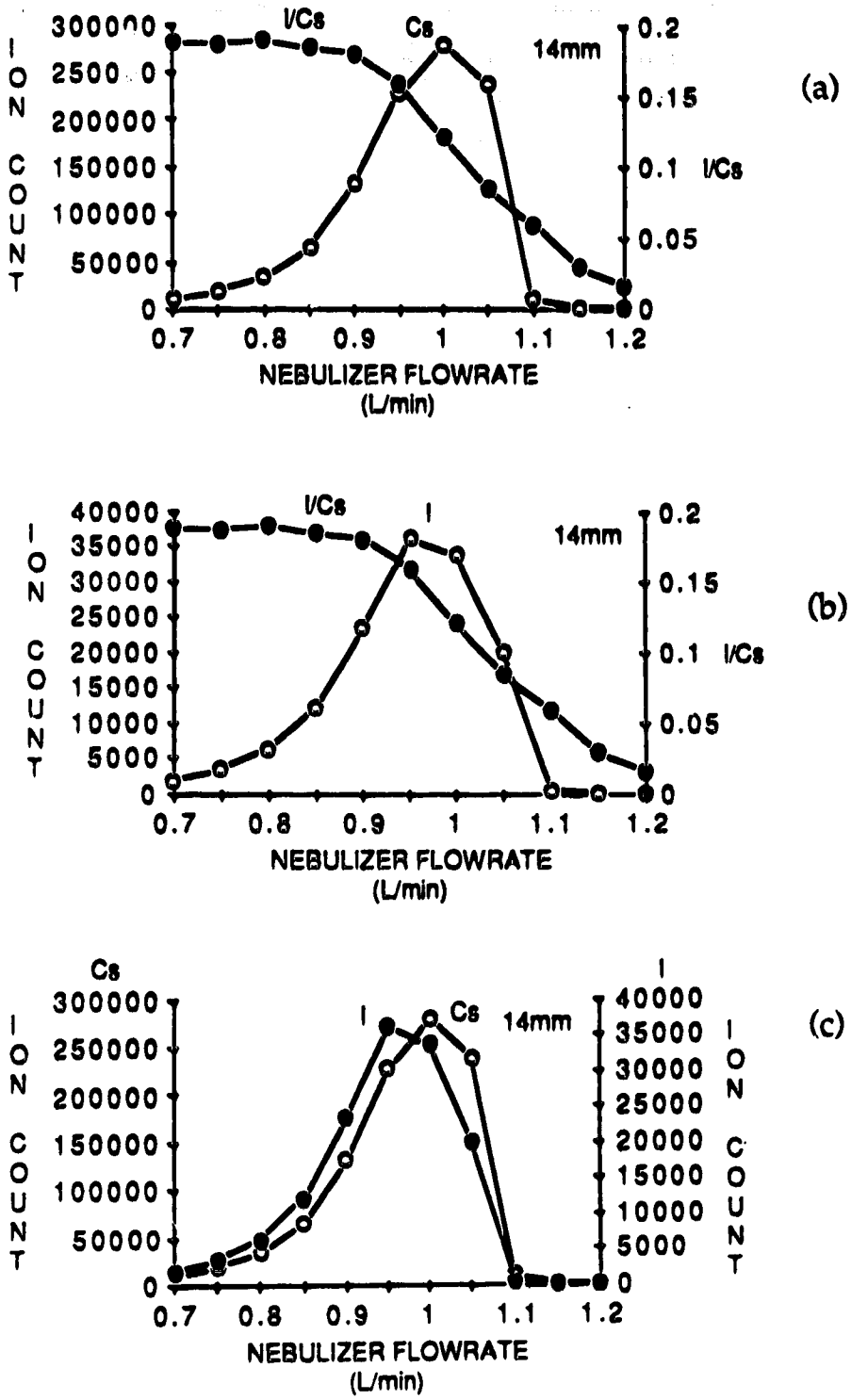

Figure 8.5 Nebulizer flowrate parameter plots for Cs^+ (a) and I^+ (b) plus I^+/Cs^+ versus nebulizer flowrate overlay plots. Nebulizer flowrate parameter plots for Cs^+ and I^+ (c). Sampling depth, 14mm.

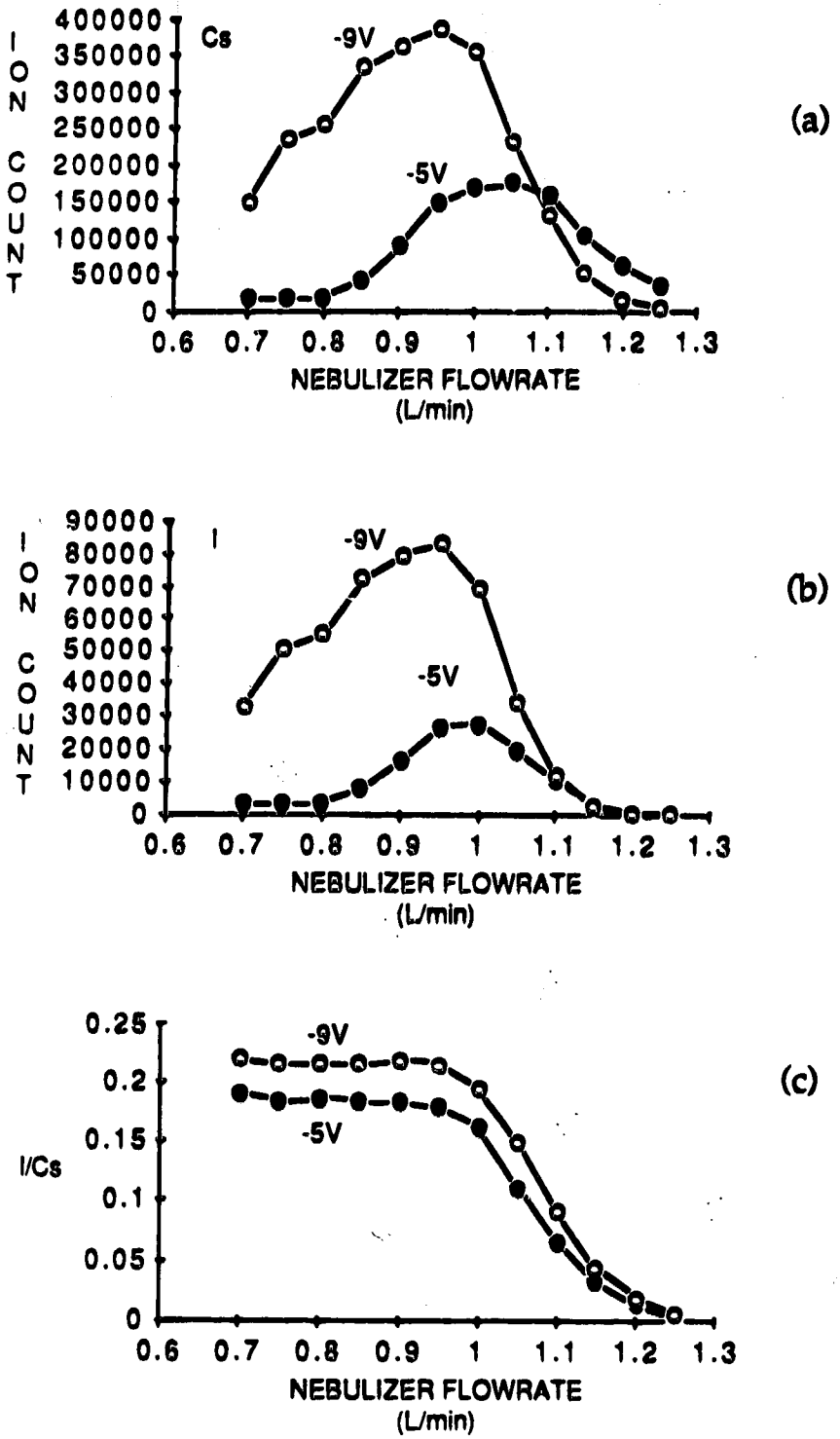

Figure 8.6 Nebulizer flowrate parameter plots for Cs^+ (a) and I^+ (b) for photon stop voltages of -9V and -5V. I^+/Cs^+ versus nebulizer flowrate plots (c) for photon stop voltages of -9V and -5V.

I^+/Cs^+ ratio of 0.2145 ± 0.34% corresponding to a temperature of 7300K when the photon stop is -9V. For a 17% difference in I^+/Cs^+ we have a 1.4% difference in temperature.

The orifice diameter of the sampler can also affect the power flowrate peaks in ICP-MS. The signal intensity for a range of flowrates was measured using a series of samplers with orifice diameters ranging from 0.94mm to 0.51mm. Figure 8.7 contains the plot of I^+/Cs^+ versus nebulizer flowrate for the series of orifice diameters. Although the same basic shape is maintained, in general the smaller orifices yield lower I^+/Cs^+ ratios and drop off at lower flowrates. Table 8.1 lists the I^+/Cs^+ ratios and calculated temperatures for the various orifice diameters at 1.05L/min. Although the I^+/Cs^+ ratio is doubled when the 0.94mm diameter orifice is used instead of the 0.51mm diameter orifice, the temperatures vary by less than 5%.

It is puzzling that the I^+/Cs^+ ratio has such a consistent shape when measured with the different samplers since the Cs^+ and the I^+ intensity versus nebulizer flowrate plot shapes are so varied. The results plotted in Figure 8.5 are for a sampler orifice diameter of 0.89mm. The Cs^+ signal maximum occurred at 1.00 L/min and the I^+ signal maximum at 0.95L/min. The shoulder of the I^+/Cs^+ plot occurred at 0.95L/min. In Figure 8.8, the I^+/Cs^+, Cs^+ and I^+ data obtained using a sampler with a 0.51mm diameter orifice are presented. The maxima for Cs^+ and I^+ occur at 1.15 and 1.10L/min respectively and the shoulder of the I^+/Cs^+ plot occurs at 0.95L/min. With this orifice size the I^+/Cs^+ ratio drops at a flowrate farther away from the Cs^+ or the I^+ maxima compared to the results obtained with the 0.89mm diameter orifice. Figure 8.9 contains a similar set of plots for CsI data taken

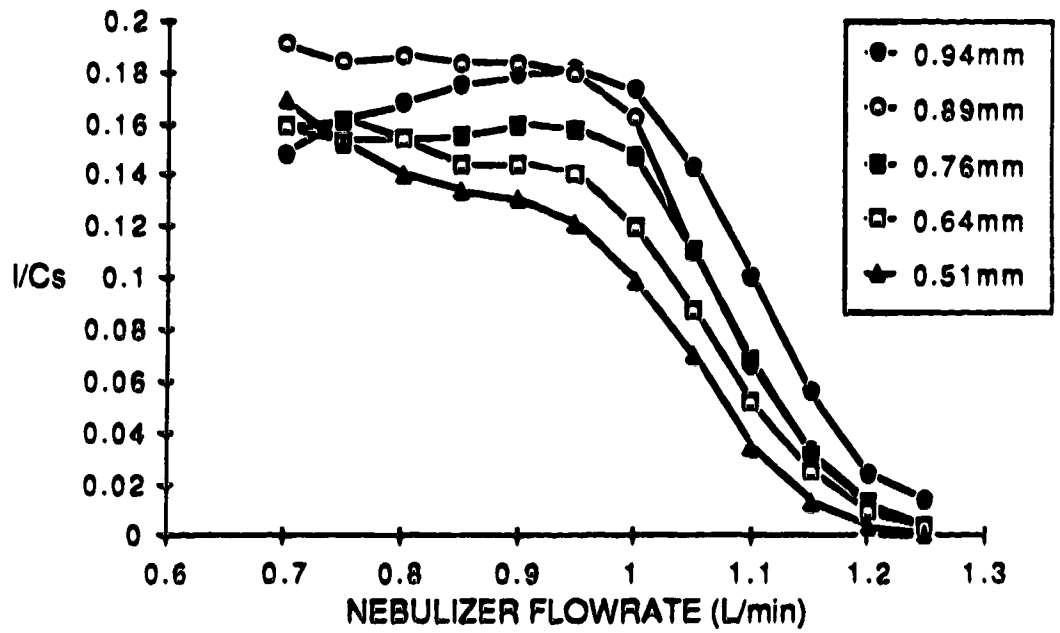

Figure 8.7 I^+/Cs^+ ratio versus nebulizer flowrate for five sampler orifice diameters.

Table 8.1 I^+/Cs^+ Ratios and Temperature Estimates for a 1.3kW Plasma with Different Sampler Orifice Sizes (Assuming $n_e = 10^{15}$).

Diam. (mm)	I^+/Cs^+	%RSD (I^+/Cs^+)	Temp. (K)
0.94	0.1433	4.1	7100
0.89	0.1116	7.2	7000
0.76	0.1106	7.0	7000
0.64	0.0880	6.6	6900
0.51	0.0704	6.2	6800

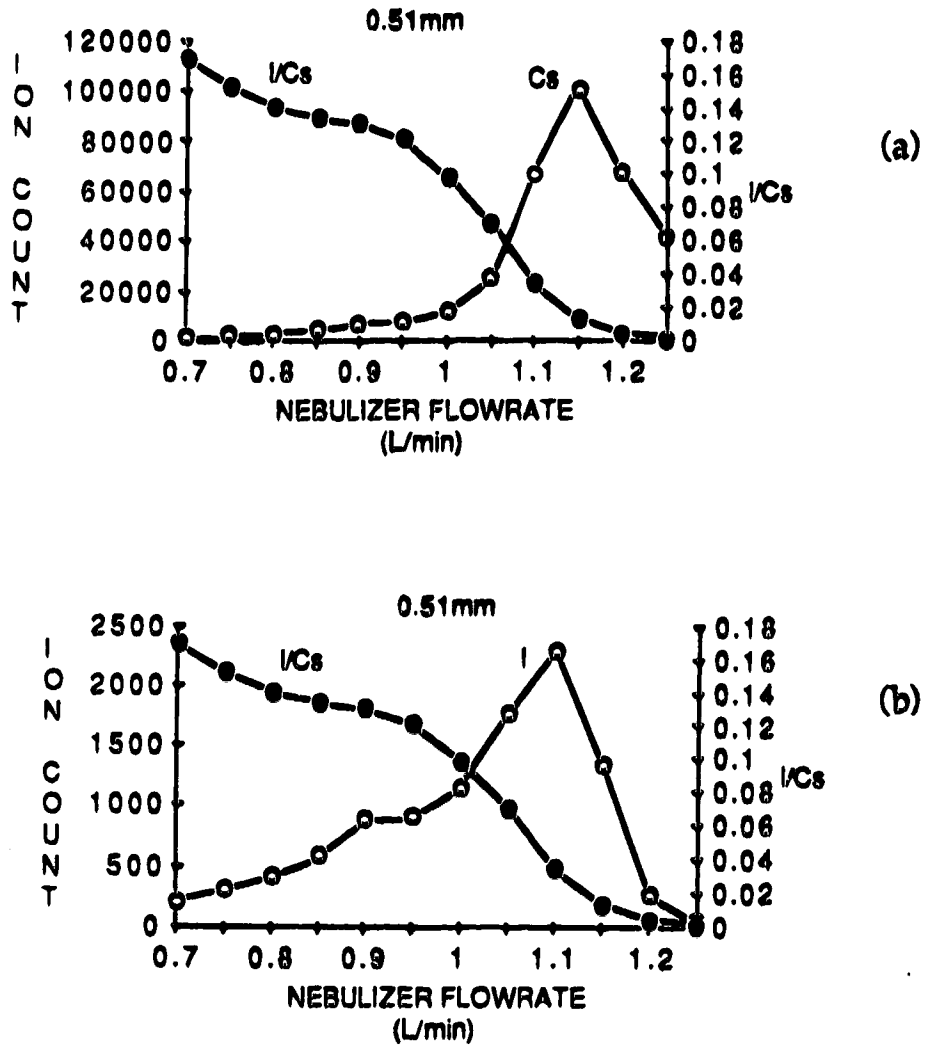

Figure 8.8 Nebulizer flowrate parameter plots for Cs^+ (a) and I^+ (b) plus I^+/Cs^+ versus nebulizer flowrate overlay plots. Sampler orifice diameter, 0.51mm.

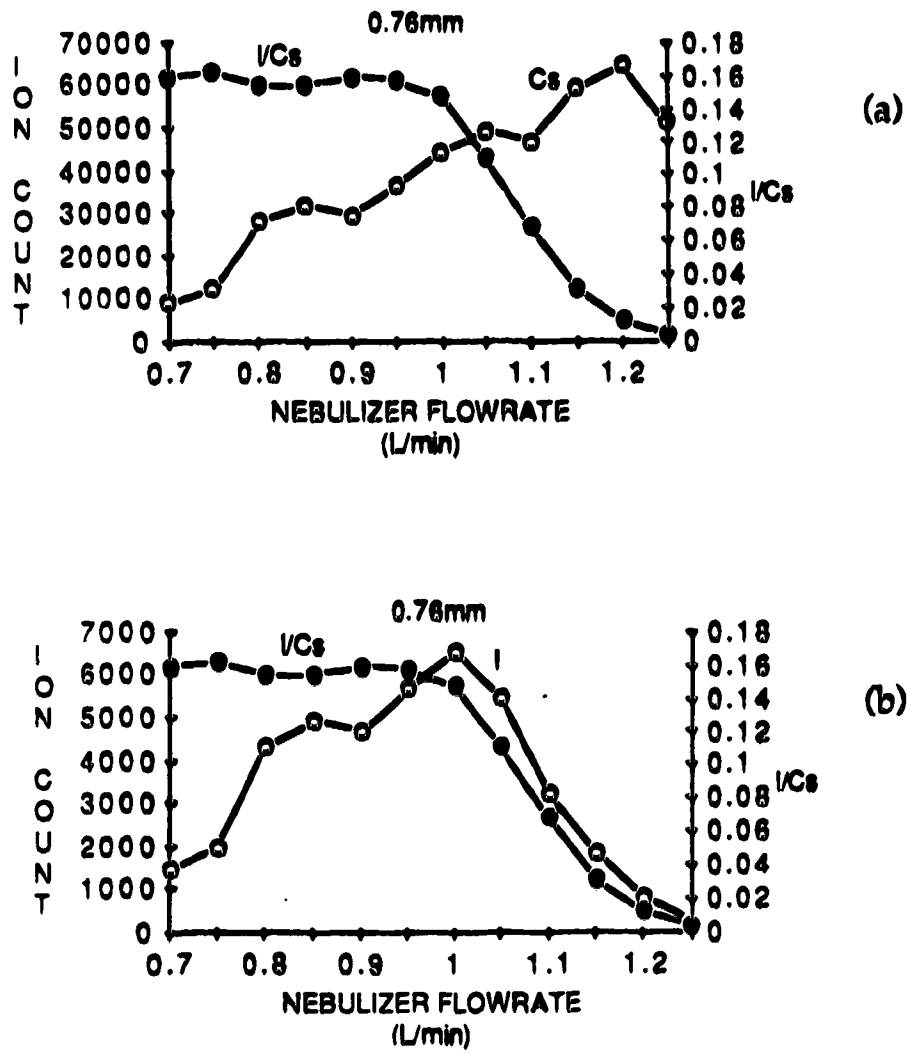

Figure 8.9 Nebulizer flowrate parameter plots for Cs^+ (a) and I^+ (b) plus I^+/Cs^+ versus nebulizer flowrate overlay plots. Sampler orifice diameter, 0.76mm.

with a 0.76mm diameter orifice. In this case the Cs^+ and I^+ signal intensities as a function of nebulizer flowrate are significantly different in shape yet the plot of I^+/Cs^+ versus nebulizer flowrate still resembles the plots obtained for the other sampler orifice sizes.

Conclusions

The signals measured with the ICP-MS may be modified by changing the ion lens voltages and by changing the sampler orifice size. Because we can move and change the shape of the intensity versus nebulizer flowrate plots in this manner we must be cautious about what we conclude about the plasma based on simultaneous mass spectrometric and ion emission measurements.

The I^+/Cs^+ ratio is also affected by the orifice size and the photon stop lens voltage. The effect of these parameters on the I^+/Cs^+ ratio is seen primarily as a change in magnitude with the basic shape of the I^+/Cs^+ ratio as a function of nebulizer flowrate remaining unchanged. Although the I^+/Cs^+ ratio can be doubled by some of these changes only small changes in temperature result. Consequently it seems to be a rather insensitive method for temperature determinations and care should be taken when using I^+/Cs^+ ratios to estimate the degree of ionization in the ICP.

It is clear that we must understand more fully the sampling process in the ICP-MS and why we get the nebulizer flowrate power parameter plot mountains. Until this is understood we must be cautious about drawing too many conclusions about the fundamentals of the ICP based on ICP-MS measurements.

References

1. R. S. Houk, H. J. Svec and V.A. Fassel, Applied Spectrosc. **35**, 380-384, (1987).

2. R.S. Houk, A. Montaser and V. A. Fassel, Applied Spectrosc. **37**, 425-428, (1983).

3. D. A. Wilson, H. G. Vickers and G. M. Hieftje, Applied Spectrosc. **41**, 875-880, (1987).

4. K. Lepla Ph.D. Dissertation, Univ. of Alberta (1989).

5. M.W. Blades and G. Horlick, Spectrochim. Acta, **36B**, 861-880, (1981).

6. N. Furuta and G. Horlick, Spectrochim. Acta, **37B**, 53-64, (1982).

7. D. J. Douglas and J. B. French, Spectrochim. Acta **41B** 197-204, (1986).

Chapter 9

Conclusions and Future Directions

The inductively coupled plasma mass spectrometer (ICP-MS) has been available commercially now for five years and many of its features and limitations are being realized. It is a very sensitive technique with detection limits in the sub-ng/mL range and the calibration curves are linear over 4 -5 orders of magnitude [1] on average. The spectra are simple, especially when compared to atomic emission, and the majority of elements can be detected. It is not interference free, however, and matrix effects, both spectroscopic and non-spectroscopic [1], can be serious. The ICP-MS is a complicated piece of instrumentation and it is no surprise that the signal variation with instrumental parameters is complex.

The basic parameter behaviour of the ICP-MS, changes in signal intensity as a function of power, nebulizer flowrate, sampling depth and ion lens potential, has been presented in Chapter 2. A standard intensity versus nebulizer flowrate parameter plot format was chosen to present the data. Under useful analytical conditions, the parameter plots have the shape of a mountain. The position of the mountain can be varied by changing the ICP forward power, sampling depth and the photon stop lens voltage. Similar mountain shaped plots have been reported by Zhu and Browner [2] and by Gray and Williams [3] on instruments built by other manufacturers so it appears that this is not a characteristic specific to the Sciex Elan used in this work.

The signal intensity also varies with the voltages on the ion lenses, the einzel lens, the bessel box plates and barrel and the photon stop. An apparent mass effect was observed when these lenses were studied. The signals for different masses reached their maxima at different lens voltages. This means that compromise lens settings are required if a large mass range is to be covered. This apparent mass effect is actually an energy effect (see Chapter 6) and results from the kinetic energy spread of the ions sampled in the ICP-MS as a function of mass.

Although for the majority of elements the main analyte species is the singly charged positive ion, M^+ , the analyte may be distributed among several species including oxides, hydroxides and doubly charged species. These species display similar power - nebulizer flowrate parameter behaviour although the position of the mountain may vary with the species under consideration. The presence of oxides, hydroxides and doubly charged species reduce the sensitivity of the M^+ signal but the more serious problem is the spectral overlap that results from the presence of these species. Such overlaps can cause direct interference with another M^+ of interest or can cause inappropriate isobaric corrections to be made. An extensive list of the overlaps is included in Chapter 3.

While it is true that the oxide or hydroxide ratios for an element may be small, <1%, the interference may be significant if the element is present in large enough quantities in the sample. The oxide and hydroxide levels may be reduced by lowering the nebulizer flowrate but it may be necessary to correct the data for the presence of the interfering species, if the signal intensity is above the background level. This may be accomplished by using gauss

elimination (an algebraic correction scheme) or by abstract factor analysis. The two schemes yield comparable results but the advantages of abstract factor analysis include flexibility in choosing the masses to be measured and the ease with which the system may be expanded.

The parameter and species information described above is useful when developing an analysis method for various sample types. The proper parameter settings yielding strong signal intensities are determined first, followed by qualitative spectral scans to give preliminary information about the contents of the sample and to help evaluate the potential spectral interferences. These preliminary scans also help in choosing a proper internal standard for the process. The internal standard corrects for instrumental drift and helps compensate for moderate non-spectroscopic matrix effects. The development of an analytical method has been described for steel in Chapter 5.

Although ICP-MS is suitable for both qualitative and quantitative analysis as is, it is interesting to try and determine where species such as oxides are formed. Toward this end, the effect of the sampler and skimmer orifice sizes was investigated. Changes in orifice size in the sampler had a much more dramatic effect on the nebulizer flowrate parameter plots compared to the effect of the skimmer orifice size. The plot shapes changed quite dramatically with the changes in sampler orifice diameter. The relative amounts of oxide detected also varied with sampler orifice size. Although the larger orifice sizes yielded larger signal levels, the relative amount of oxide formed was smaller. It seems likely that the majority of oxide formation occurs in the boundary layer formed around the edge of the sampler and part of the boundary layer is drawn into the sampler orifice. The actual shape of

the nebulizer flowrate parameter plot appears important. It may be thought of as a window for ion detection where the ions detected may be distributed among several species. This is supported by the observation that the plot of the sum of the intensities (M^++MO^+) versus nebulizer flowrate has a peak shape similar to that of an intensity versus nebulizer flowrate plot for a non-oxide former of similar mass.

It is clear then that there are many instrumental parameters that affect the signal obtained from ICP-MS, including power, nebulizer flowrate, sampling depth, sampler and skimmer orifice size and ion optic lens voltages. While changes in signal intensity associated with changes in power, nebulizer flowrate and sampling depth may reflect changes in the plasma, changes corresponding to different sampler and skimmer orifice sizes or different ion lens voltages do not. One must be cautious in the interpretation of the ICP-MS data at a fundamental level and clearly the sampling process in the ICP-MS must be more fully understood.

It would be interesting to continue studying the ICP-MS interface, both optically and with the mass spectrometer. The interface material and geometry are areas which could be explored further along with the effect such changes would have on the optimum ion lens settings and non-spectroscopic matrix effects. It may be of use to somehow equalize the ion energies after the expansion through the ICP-MS interface. Although this would modify the sampled plasma even further, it would remove the mass effect observed with the ion lens settings. It would be interesting to see how that would effect the nebulizer flowrate parameter plots. Further study is also warranted in the modeling of the ion optics. The discrepancies between simulated and real lens

data could be investigated and a study of the effects of space charge would be beneficial in trying to understand the non-spectroscopic matrix effects.

The study of ICP-MS has reached a point where we have a basic understanding of how the instrument will respond to changes made in instrument settings. We are also aware of many potential interferences, both spectroscopic and non spectroscopic, that limit aqueous samples to low levels of total dissolved solids. People are trying to get around the limitations set by the total dissolved solids problem by using alternate sample introduction methods such as flow injection [4-6], laser ablation [7] and direct sample insertion [8,9]. The disadvantage with these methods is the transient nature of the signals that limits the total measurement time for each sample. The problems of spectroscopic interferences are being addressed at this time by studying alternate plasma gas compositions [10,11] and by dry sample introduction [8,9]. It is likely that the matrix effect problems will receive much attention in the next while for if they can be reduced significantly while maintaining the sensitivity of the ICP-MS we shall have a powerful technique available to us.

References

1. S. H. Tan Ph.D. Dissertation, Univ. of Alberta (1987).

2. G. Zhu and R.F. Browner,Appl. Spectrosc., **41**, 56349-359, (1987).

3. A. L. Gray and J.G. Williams, J. Anal. Atom. Spectrom., **2**, 599-606,(1987).

4. J. R. Dean, L. Ebdon, H. M. Crews and R. C. Massey, J. Anal. Atom. Spectrom. **3**, 349-354, (1988).

5. D. Beauchemin, K. W. M. Siu and S. S. Berman, Anal. Chem. **60**, 2587-2590, (1988).

6. R. C. Hutton and A. N. Eaton, J. Anal. Atom. Spectrom. **3**, 547-550, (1988).

7. P. Arrowsmith, Anal. Chem. **59**, 1437-1444, (1987).

8. G. E. M. Hall, J.-C. Pelchat, D. W. Boomer and M. Powell, J. Anal. Atom. Spectrom. **3**, 791-797, (1988).

9. D. W. Boomer, M. Powell, R. L. A. Sing and E. D. Salin, Anal. Chem. **58**, 975-976, (1986).

10. R. S. Houk, A. Montaser and V. A. Fassel, Applied Spectrosc. **37**, 425-428, (1983).

11. D. W. Koppenaal and L. F. Quinton, J. Anal. Atom. Spectrom. **3**, 667-672, (1988).